Polysulfones for Sustainability Related Applications

by

Hoda Shokrollahzadeh Behbahani

A Dissertation Presented in Partial Fulfillment
of the Requirements for the Degree
Doctor of Philosophy

Approved April 2024 by the
Graduate Supervisory Committee:

Matthew D. Green, Chair
Klaus S. Lackner
Benny D. Freeman
Marylaura Lind Thomas
Gary F. Moore

ARIZONA STATE UNIVERSITY

May 2024

ABSTRACT

This dissertation investigates the pressing issue of climate change, identifying carbon dioxide as its main driver and introduces Direct Air Capture (DAC) as a crucial technology for achieving significant reductions in net global emissions. Through an extensive review of existing literature on DAC, it examines various methods and materials developed for this purpose, highlighting the ongoing efforts, advancements, and potential for real-world application. A novel sorbent, quaternary ammonium-functionalized poly(arylene ether sulfone) is explored for DAC via the moisture swing process. This sorbent exhibited the ability to capture and release atmospheric CO_2 by a swing in moisture. Effects of form factors of powder, free standing dense membrane and thin film composite membrane were also evaluated for DAC. Furthermore, the dissertation explores modifications to poly(arylene ether sulfones) – polymers primarily used in desalination processes – to enhance water scarcity solutions by improving desalination membrane hydrophilicity and reducing fouling. This enhancement is achieved through the incorporation of zwitterionic groups into the polymer structure. Additionally, it investigates the synthesis of polysulfone polymers from lignin-derivable monomers, offering a greener alternative to traditional polysulfones used in desalination due to their environmental and health concerns. Polysulfones derivable from lignin exhibited comparable thermal properties and enhanced hydrophilicity compared to petroleum-derived polymers, showing considerable promise. Lastly, this dissertation investigates a potential hybrid system for desalination and direct ocean capture by integrating redox-active compounds into desalination membranes. This aims to achieve a pH swing that facilitates the formation of dissolved CO_2.

DEDICATION

My journey towards this PhD has been enlightening, challenging, and immensely rewarding. This path has been filled with many lessons, taught by the challenges faced and achievements unlocked along the way. It has taught me resilience, dedication, sacrifice, and the value of hard work, enriching my life in ways I had never imagined. I could not have reached this point without the invaluable support, guidance, and encouragement from a constellation of remarkable people.

To my advisor and mentor, Dr. Matthew D. Green, whose insight, expertise, and patience laid the foundations upon which this work stands. Your guidance was not just academic but life-changing, shaping my perspective and approach to both challenges and opportunities. I am very thankful for the financial support and the nurturing environment you provided, which played a pivotal role in my professional and personal development. Thank you, Matt, for guiding me through this journey and helping me evolve into the person I am today.

To my committee members Dr. Klaus Lackner, Dr. Benny Freeman, Dr. Marylaura Lind and Dr. Gary Moore, whose expertise and insightful feedback have been critical to my research and personal growth. Your guidance has provided me with invaluable learning opportunities, which have helped me refine my work and thinking, for which I am very grateful. And to many other faculty members who have influenced my journey, whether through direct collaboration, casual conversations, or by simply being exemplary figures in the field, I owe a debt of gratitude.

To my dearest family: my mother, Mehri, my father Hassan, my sisters Sara and Houria, and my amazing nephew Elia. You have enveloped me in an endless ocean of love and support every single day. You have sacrificed so much for me, and never once faltered in your belief in me. In every word of encouragement and every gesture of comfort, you have given me the strength to rise, to persevere, to excel. For all this and for the unwritten chapters of support yet to come, my gratitude to you knows no bounds.

To my partner, Ali Ghahramani, whose love and partnership have been a source of constant inspiration and comfort. You have stood by me with unwavering support, sharing in every challenge and triumph, making this journey beautiful. Your presence has been a haven of peace and motivation, encouraging me to aim higher and dream bigger.

To all my lab mates and friends, especially Ani Nazari, Mani Korah, Husain Mithaiwala, Brad Grim, Jae Sang Lee, Yuta Kaneko, and Yi Yang for the camaraderie, discussions and teachings, and moments of relief amidst the rigors of research. Your presence made the tough moments bearable and the achievements more joyful. Special thanks to Mr. Fred Pena, not just for your role in sustaining a conducive lab environment but also for the positive energy and encouragement you share whenever we cross paths. I also wish to express my gratitude to my co-authors, whose insights and expertise were vital to the success of our joint papers.

And to my cherished friends, who have transformed into family in this journey of mine: Zahra Soltani, Zahra Sheibani, Atefeh Sedaghat, Arezoo Esrafili, Parisa Jahangiri, Mohammad Ghaljehei, Behrouz Azimian, and Mohammad Mousavi. Your unwavering support, care and kindness has made it a delightful adventure.

ACKNOWLEDGMENTS

I would like to acknowledge the support of my funding sources, including the US Advanced Research Projects Agency-Energy (ARPA-E), US Department of Energy, Office of Basic Energy Sciences (BES), National Science Foundation, division of Chemical, Bioengineering, Environmental and Transport systems (NSF CBET), and the Office of Naval Research (ONR), National Oceanic and Atmospheric Administration (NOAA) Ocean Acidification Program. The views and opinions expressed herein do not necessarily state or reflect those of the United States Government or any agency thereof.

As a student at Arizona State University, I acknowledge that the Tempe campus sits on the ancestral homelands of American Indian tribes that have lived in this area for centuries, including the Akimel O'odham (Pima) and Pee Posh (Maricopa) peoples.

TABLE OF CONTENTS

Page

CHAPTER Page

CHAPTER Page

CHAPTER Page

CHAPTER Page

LIST OF TABLES

Table Page

LIST OF FIGURES

Figure Page

LIST OF SCHEMES

Scheme Page

1 CHAPTER 1: THE CHANGING CLIMATE

In this introductory chapter one of the most pressing challenges of our era, climate change, is presented. I begin by reviewing climate change and some of the significant events related to climate change that are occurring on our planet right now. Then, I look at why climate change is happening and how the rise of greenhouse gases, mainly CO_2, is responsible for many climate change-related natural disasters. Direct Air Capture (DAC) is introduced as a pivotal strategy for mitigating climate change, offering hope and a potential path forward in our efforts to slow its progression. The chapter concludes with an overview of this dissertation.

1.1 Introduction

Realization of climate change occurred through the first world climate change conference held in Geneva in February 1979 by the World Meteorological Organization. More than 350 scientists participated in this meeting to review climatic changes observed as the result of human activities and future risks and impacts.[1] From then, there has been growing recognition towards climate change. We now understand that increasing atmospheric greenhouse gas (GHG) levels can shift climate patterns and cause environmental degradation in many ways around the globe. Climate change-related impacts such as global warming, shrinking of the cryosphere, increased flooding, more extreme heatwaves,

drought, ocean acidification and worsening wildfires are already affecting the lives of many people worldwide.

The center for research on epidemiology of disasters reports 432 natural disasters, affecting 101.8 million people, resulting in 10,492 deaths and $252 billion in economic damages only for the year of 2021. The majority of the natural disasters are climate-related, ~51% of the 432 reported natural disasters is from floods, ~30% is from storms and ~12% is from wildfires, drought, extreme temperatures and landslides.[2] Compared to the 2001-2020 annual average, a 25% and 64% increase is observed for 2021 in number of climate-related disasters and economic losses, respectively. The progress and severity of these climate-related events in the future will depend on the volume of future emissions and control and management of GHGs driving climate change. Further emissions of GHGs will lead to more extreme, pervasive, and irreversible damage to different parts of our planet. Our social communities will also be affected by climate change. Food and water security, economic growth, and international peace and security will be in danger. In this section, some of the major climate change crises are described.

1.1.1 Melting of the Cryosphere

The cryosphere is home to roughly 10% of the human population and many unique living organisms such as polar bears, penguins, and arctic cods. The cryosphere is a component in Earth's climatic system and is our planet's refrigerator.[3] The white ice from the cryosphere cools the planet by reflecting the excess heat from sun radiation back to space, balancing other parts of Earth which mostly absorb the heat. The cryosphere controls global sea levels and impacts water resources.[4] The cryosphere is thawing and disappearing

rapidly, retreating in area, length and thickness as the result of climate change (**Figure 1.1**).[4] According to literature, 400 billion tons of ice is lost from glaciers since 1994, 294 billion metric tons of ice is lost from Greenland and Iceland per year, ~13% of ice is lost per decade from the Arctic sea ice since 1979 and 127 billion metric tons is lost from Antarctica per year.[5–10]

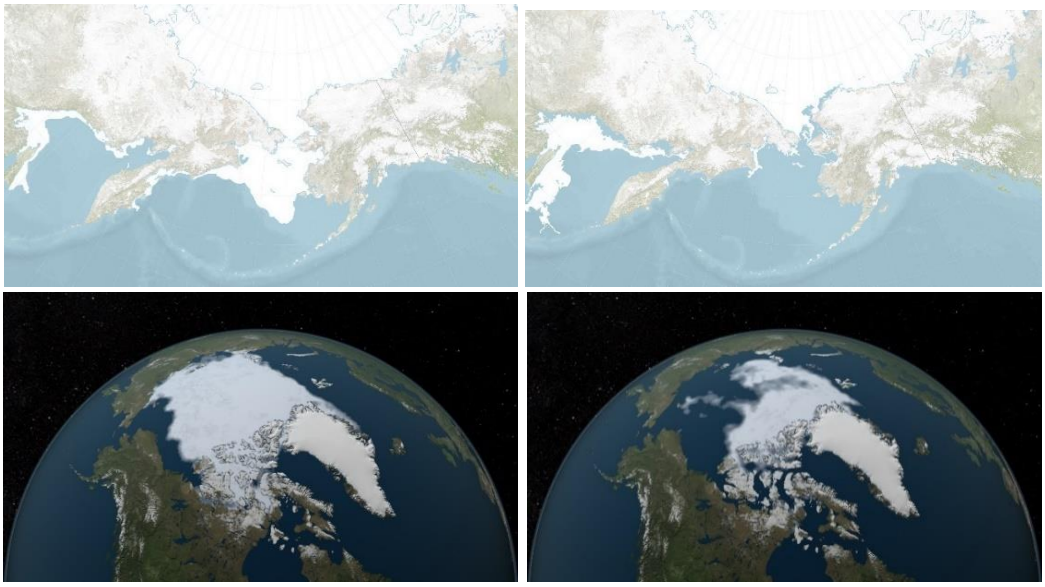

Figure 1.1 Changes in the cryosphere. Bering Sea ice decrease, left image taken Apr. 29th, 2013, and right Apr. 29th, 2018[11] (top) and Arctic Sea ice loss, left image taken Sep. 14th, 1984 and right Sep. 13th, 2012[12] (bottom).

1.1.2 Rising Sea Levels

The melting and runoff of mountain glacier ice and icebergs in oceans and thermal expansion of oceans from global warming result in rising sea levels. This results in land loss, higher coastal erosion, extreme wave height, flooding and more frequent and intense storms and typhoons occurring further inland (**Figures 1.2**).[13] Rise of sea level is disruptive, threatening local jobs and industrial activities, bridges, historical landmarks and built environment, roads and oil and gas drilling activities along coastlines.[14–17] Change in

coastal water levels and climate could re-distribute wildlife, force adaptation and migration, and change native wildlife in low-lying coastal areas.[18–21] As an example, egg incubation, hatching, emergence, mortality and body mass of sea turtles is significantly influenced by location (humidity, temperature, and nutrient and water availability) of nest site, altering as the result of floods and sea level rise.[22]

Global mean sea level rise is accelerating with continued GHG emission.[23] The Intergovernmental Panel on Climate Change (IPCC) reports the annual global average sea level rise from 1901 to 1990 which was 1.4 mm, more than doubled, reaching 3.6 mm during 2006 to 2015.[24] It is reported that the global mean sea level rise throughout 2006 – 2015 is more influenced by melting of glaciers and icebergs (1.9 mm/year) than thermal expansion as the result of rise in ocean temperature (1.4 mm/year).[24] Tide gauge measurements and satellite observations report non-uniform sea level rise around the world but within ±30% of the global mean average, with areas with invasive vertical land movement encountering harsher impacts.[24,25] Greenland ice sheet has an area of 1.7 million km^2 and ice with thickness up to 3 km. It is estimated that the global sea level will rise 7.2 m if the Greenland ice sheet is fully thawed.[26] Furthermore, sea level rise from climate change is a major threat to low lying islands.[27,28] The Small Island Developing States (SIDS) in the Pacific, Atlantic and Indian ocean and the Caribbean Sea are considerably vulnerable to sea level rise. The Tuvalu island in the South Pacific Ocean (population approx. 12,000) and the Marshall Islands in the Central Pacific Ocean (population approx. 42,000) are completely within 5 m above sea level, and will disappear with continued sea level rise.[29] More than 88% of land of the Kiribati island in the Central Pacific Ocean and

the Cook islands in the south Pacific Ocean are within 5 m above sea level.[28] The Caribbean islands of Bahamas, Cuba, and Dominican Republic, the Solomon islands, Fiji and Tahiti in the Pacific Ocean are also in danger with rising sea levels.[30–34]

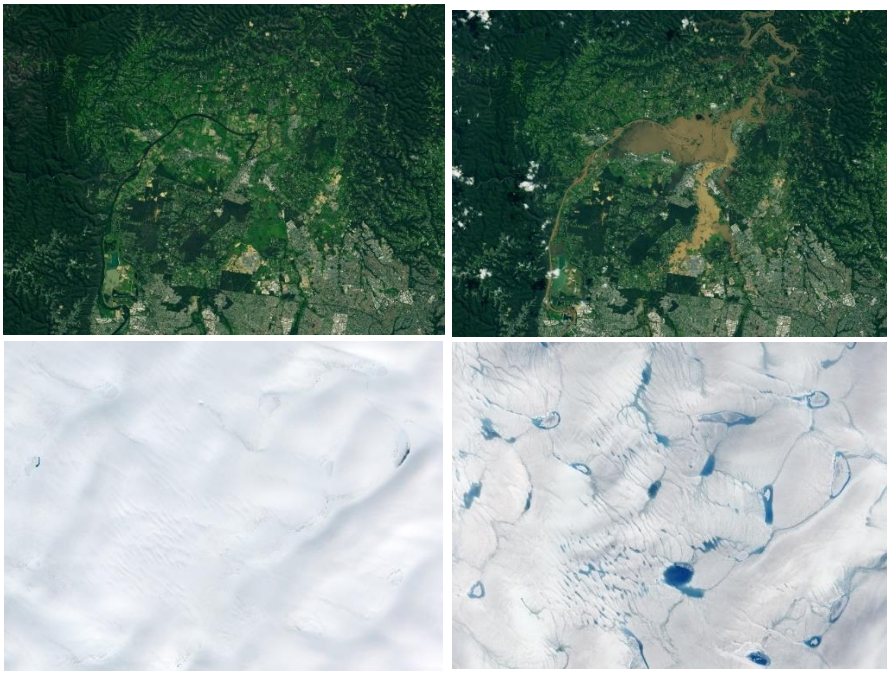

Figure 1.2 Flooding in Hawksbury-Nepean River near Sydney, Australia, left image taken Apr. 5th, 2020 and right Mar. 23rd, 2021 (top), and Premature melting of Greenland ice sheets, left image taken Jun. 10th, 2014 and right Jun 15th, 2016.[35] (bottom)

1.1.3 Changing Ocean Currents

The thermohaline circulation (global ocean conveyor belt) is the recognized continuous circulation (loop) of surface and deep water between the Pacific, Atlantic and Indian oceans driven by water density, which is determined by water temperature and salinity of the local water.[36,37] As shown in **Figure 1.3**, The circulation "starts" from the Norwegian sea, where the ocean water is much denser and saltier than ocean water around the equator due to lower temperatures. As the ocean water freezes to ice, the salt is rejected in the ice formation and is released back to the ocean, resulting in a locally higher salt content. The

"heavy" water sinks deep into the ocean and moves south in the Atlantic Ocean. Ocean water along the equator (Indian ocean) absorbs sun's heat and becomes lighter from higher temperatures. The difference in density promotes the continuous sinking of heavier water to the bottom of the ocean, to make room for the lower density water and establish the ocean current.

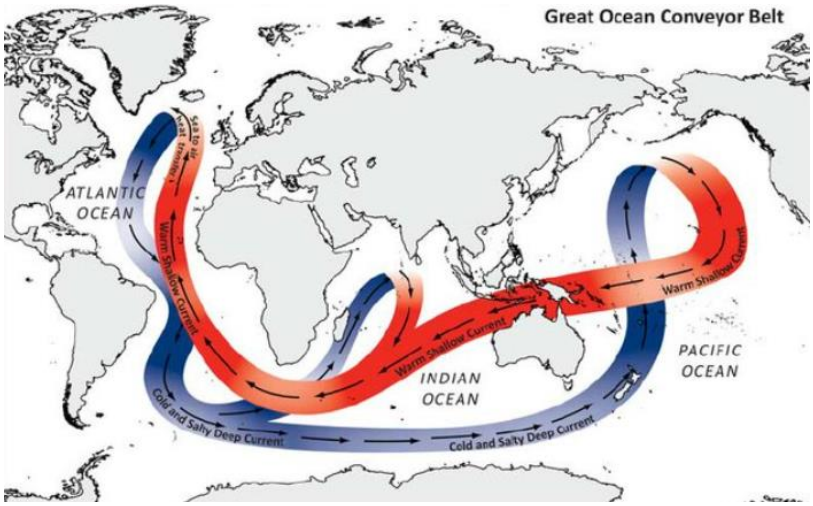

Figure 1.3 The global ocean conveyor belt[38]

The ocean current controls the climate by transferring the heat along the equator toward the colder climates. Without ocean currents, Earth will observe higher number of intense heatwaves along the equator in summers, and more extreme winters along the poles. This current is also important to living organisms deep in the oceans, as their permanent habitats and oxygen and nutrient availability depends on the established ancient ocean currents.[39]

Sea ice and ice sheets impact global weather systems by affecting ocean currents. As the result of rising global temperatures, longer summer melting and delayed winter freezing, broad and bulky sea ice has transitioned to young and small clusters of thin ice.[40,41] Addition of freshwater from thawed ice to, for example, the Atlantic Ocean saltwater,

decreases its salinity and density. Continued addition may lower the density difference driving force and halt the ocean current completely.[42] Studies have shown that with prolonged melting of sea ice, the ocean currents are now at a critical level to collapse.[43] Data shows that Arctic sea ice volume has decreased with a rate of 12.5% per year between 2018 and 2021.[44] Another study has concluded that the Petermann sea ice and ice sheets, located in the Greenland Ice sheet in the Arctic ocean, will permanently thaw and irreversibly lose 50 km in length in a scenario in which the global average temperature increase 2 °C above the pre-industrial level and reverse back to present-day conditions.[44]

1.1.4 Warming Permafrost

Water which is trapped between cracks, rocks, and soil in layers beneath the ground freezes in cold seasons, and thaws in warm seasons. The deeper layer in land that remains permanently frozen for at least two consecutive years, mostly observed in subzero climates, is known as permafrost. On about a fourth of Earth's northern hemisphere, ~23 million km^2, permafrost exists.[45] Siberia, Canada, Alaska, China, and Greenland all consist of permafrost layers. With elevated temperatures as the result of global warming, the permafrost thaws (**Figure 1.4**). Effectively, the infrastructure built on frozen permafrost may be destroyed. Previously frozen organic waste in permafrost layers decompose and generate GHGs and ancient virus and bacteria frozen in deep layers may plague humans, animals, and plants.[46–49] Furthermore, arctic permafrost is estimated to hold 1,700 billion metric tons of frozen carbon, and feedback emission from permafrost thawing will accelerate climate change.[50]

Figure 1.4 Collapsed and thawing permafrost, left in Drew Point, Alaska (Credit: Benjamin Jones, U. S. geological survey (USGS)) and right in Kolyma River in the Siberian arctic (credit: Chris Linder).

1.1.5 Changes in Global Biodiversity

Climate change disturbs ecosystems and natural habitats that are fundamental to life on our planet. Change in ocean pH, ocean and atmospheric temperature, precipitation cycle, and higher frequency of wildfires, heat waves, storms and drought threaten the livelihoods of many species. Ecosystems on Earth are inter-connected, and a loss or alteration of a single species may have a ripple effect upon the function of the global ecosystem.[51] Many living organisms are vulnerable to environmental conditions.[52,53] Upon changes in their climate envelope, the species are forced to either migrate, physiologically evolve through genetic mutation and adapt, or be wiped out. Migration is not always a possibility due to many environmental or geographical restrictions, specifically for mountain-restricted or polar-restricted species.[54] Oceans have always been a source of CO_2, but nowadays, with increasing rates of CO_2 emissions to the atmosphere, oceans are shielding our planet from a rapid climate change, and absorbing close to a third of all emission.[55] Oceans can store around 38 Gt CO_2 due to their natural buffering carbonate/bicarbonate/carbonic acid system. However, higher ocean water acidity is corrosive to the calcium carbonate shells

endangering marine species.[56,57] Higher ocean water temperatures also enable the spread of disease among marine organisms.[56,58]

We are already late. The International Union for Conservation of Nature red list of threatened species reports that as of August 2022, at least 35 living organisms are extinct, 1635 are critically endangered and 5680 are endangered, vulnerable and threatened as the result of only climate change and severe weather events.[49] The Golden toad (*Incilius periglenes*) of Costa Rica and *Pachnodus velutinus* land snail from Seychelles island in East Africa are among the animals now extinct from climate change (**Figure 1.5**). The Staghorn Corals (*Acropora cervicornis*) native to reefs in the Caribbean, southern Gulf of Mexico, and the Bahamas, and the Mountain Pygmy Possum (*Burramys parvus*) native to Australia are among the current critically endangered species, decreasing in population due to climate change (**Figure 1.6**).[49] Polar bears (*Ursus maritimus*) depend on sea ice to hunt ice seals, breed, and rest. Global polar bear population size is estimated to significantly decline in 35 to 41 years due to climate change, hunt and harvest for subsistence and oil spills.[59–62]

Figure 1.5 Extinct species due to climate change. Left: Golden toad (*Incilius periglenes*), last seen in 1989 and declared extinct in 2004 from climate change (credit: US fish and wildlife) and right: *Pachnodus velutinus* land snail, last seen in 1994 (credit: Dr. Justin Gerlack)

Figure 1.6 Endangered species left to right: The Staghorn Corals (Acropora cervicornis) (credit: Wikipedia), Mountain Pygmy Possum (Burramys parvus) (credit: Zoos Victoria), and Polar bears (Ursus maritimus) (credit: Katharina M Miller/Polar Bears International)

1.1.6 Social and Economic Impacts

Climate change not only influences the planet we live on, but also societies and economies. Many systems such as social ties, industries, retail and commercial activities, and tourism will be affected from climate change-related disasters. Climate-related disasters such as rising sea level, heatwaves, change in rainfall patterns, flooding and erosion of coastal ports and beaches, and water and food scarcity and contamination, may cause loss of revenue, shipping and trade issues, fishing limitations, and tourism decline. Greater competition between nations for available resources may fuel socioeconomic tensions and discord.[63] Physical, reproductive and mental health of human beings may also be threatened with climate change related disasters.[64–66] 143 million people from three regions of sub-Saharan Africa, South Asia and Latin America will be forced to migrate to escape rising sea levels and water scarcity.[67] Forced displacement and migration of "climate refugees" drives cutting of social ties with family, relative and friends and is disruptive to mental health.[68] Higher frequency of extreme weather events and rise of sea levels may affect tourism destination choices, spending and length of stay, upsetting tourism-dependent economies.[69] The Great Barrier Reef in Australia, Venice city and Lipari in Italy, the Spanish Canary Islands, Glacier National Park, the Amazon rainforest, Maldives, Key West in Florida, The

Alps, Rio de Janeiro, sub-Saharan Africa and Madagascar are among the tourist destinations that will be impacted by climate change.[70–73]

Retail and commercial services and the supply chain are vulnerable to climate change.[74] Raw material, component parts and packaging supplies, distribution and transportation, storage, and energy supply may be disrupted by climate change.[75] Significant portions of the US transportation network, mostly situated in the Northeast, are evaluated to be at high risk of shutting down due to climate change.[76] The Boston Logan international airport is projected to be paralyzed and to experience a significant number of storms by 2050, and worsen if climate change management fails.[77]

1.1.7 Role of CO_2 in climate change

CO_2 is the fourth most abundant gas in dry air, after nitrogen, oxygen, and argon for up to 80 km up in Earth's atmosphere. This gas is essential for the survival of ecosystems and living organisms on our planet. It plays an important role in keeping the Earth's temperature hospitable by acting as a blanket wrapped around Earth, trapping the heat from the sun in the atmosphere with the GHG effect. However, the concentration of this GHG is rising relentlessly as the result of human activities. Paleoclimatologists report that the current excessive level of CO_2 was last seen on Earth around three million years ago.[78] This unprecedented rise amplifies our planet's natural GHG effect and contributes to climate change, a serious existential threat to humanity. Climate change has already begun and caused changes to our planet. Some of these changes are irreversible for generations, some can be slowed down or reversed through potent, sustained, and swift actions.[79]

The GHG effect, the reason behind climate change, was identified in the early 1800s when scientists were searching for the reason behind ice ages, and a clear correlation was observed with the time of glacial periods and time of when CO_2 concentrations of the atmosphere were at their lowest.[78] Solar energy is continuously radiated on Earth from the sun as mostly visible light, with shortwave radiation. Some of this energy is immediately reflected to space by the clouds, snow and ice and some airborne particles, and the majority passes through to the surface of the earth and heats our planet. The energy is then reflected from the land and oceans back to space as longwave radiation or infrared energy. While some of this infrared energy continues to exit Earth's atmosphere to space, almost 90% is absorbed by GHGs. This absorbed energy is re-emitted back to Earth, causing further warming. Without GHGs, the average temperature of Earth would be -18 °C (0 °F), our planet will be mostly frozen, and life as we know it would not exist.[80]

Several natural and anthropogenic gases are responsible for the greenhouse effect. Water vapor (H_2O), methane (CH_4), carbon dioxide (CO_2), nitrous oxide (N_2O) and fluorinated gases are among the most influential GHGs. These gases, due to their chemical composition and geometry, can stop the escape of longwave radiation back to space by absorbing the infrared energy, and re-emit them back in all directions. But why is CO_2 portrayed as the main driver of climate change?

The influence of a GHG on climate change depends on two factors of energy (heat) absorption capacity per molecule and concentration of the gas The concentration of gas depends on emission rate and residence time in the atmosphere. Fluorinated gases are extremely potent GHGs used in air conditioning, refrigeration, and aerosol sprays. On a

molecule-by-molecule basis, these gases have up to 20,000-fold higher energy absorption capacity compared to CO_2 and can reside in the atmosphere for several hundreds of years.[81] However, use of this gas has been phased out through the Montreal protocol set in 1987.[82] CH_4 is emitted mainly during extraction, distribution and transportation of oil and natural gas, from agriculture (rice farming, cattle breeding etc.) and biogas combustion.[83] This greenhouse gas has 25-fold higher potency compared to CO_2 in trapping heat but has a much lower residence time.[84] CH_4 molecules react with hydroxyl radicals in the troposphere and degrade in a decade, whereas CO_2 molecules can last up to centuries in the atmosphere. N_2O emitted through agriculture, animal and human waste and industrial activities, has a 300-fold higher potency compared to CO_2 in energy absorption capacity, but is also relatively short lived, and lingers around for only up to 125 years before degrading through a photochemical reaction.[85,86] Water vapor is the most abundant GHG in the atmosphere, by both volume and weight. However, the increase of atmospheric water vapor is not directly attributed to human activities. The concentration of water vapor depends on the climate, thus, water vapor does not control Earth's temperature, as the amount of water vapor is controlled by temperature. Higher temperatures lead to more evaporation from water sources which will lead to higher water vapor content, having amplifying feedback with the greenhouse effect. Residence time of water vapor in the atmosphere is only a couple of days before precipitating out, so human effort to reduce water vapor content would not be worthwhile. It is also noteworthy to mention that higher water vapor content can lead to more cloud formation, which would potentially reflect solar radiation and reduce radiation on Earth's surface and inflict a cooling effect.

In the last two decades, anthropogenic emission increased for all GHGs.[87] According to the latest IPCC report,[87] between the years of 2000 – 2009, the average annual anthropogenic GHG emissions were 46.9 ± 6.0 Gt $CO_{2\text{-eq}}$. Throughout 2010 – 2019, , average annual emissions increased to 56.0 ± 6.0 Gt $CO_{2\text{-eq}}$. In 2019, 59.0 ± 6.6 Gt $CO_{2\text{-eq}}$ emission was recorded, where fluorinated gases, N_2O, CH_4 and CO_2 have contributed 1.4 ± 0.4 Gt $CO_{2\text{-eq}}$, 2.7 ± 1.6 Gt $CO_{2\text{-eq}}$, 11.0 ± 3.2 Gt $CO_{2\text{-eq}}$, 44.6 ± 7.6 Gt CO_2, respectively. As can be seen, CO_2 with more than 75% share is the largest contributor to GHG emissions. It is projected that CO_2 will still be the dominant GHG in terms of concentration over the next century, as it is the foremost GHG emitted through human activities. Ultimately, even though CO_2 has the lowest energy absorption capacity relative to other major GHGs, most reactive GHGs trap a large amount of heat but disappear "quickly" whereas a higher number of CO_2 molecules trap a smaller amount but continuously, over a large period of time. Therefore, when looking far into the future, CO_2 is the most important GHG with the largest contribution to climate change.[88]

1.1.8 Highest CO_2 levels in human history

CO_2 emissions consistently occur in nature from sources such as gases released from the decomposition of organic matter, volcanic activity and eruptions, wildfires, hot springs, ocean-atmosphere exchange, and respiration. Through nature's carbon cycle, the emitted CO_2 is readily circulated and recycled through natural sinks such as sedimentation, photosynthesis, and absorption by oceans.[89] However, the carbon cycle is disrupted with human interference. Burning of fossil fuels, which is carbon which had been tucked away for millions of years, releases a vast and sudden volume of CO_2 to the atmosphere. Human

activities can also lower the capacity of natural sinks with land use and deforestation. This results in current volume of natural sinks not sufficient and fast enough to remove the fast-increasing rate of CO_2 emissions, and CO_2 is accumulated in the atmosphere.

The Keeling curve, named after its creator Dr. Charles David Keeling, is the uninterrupted record of atmospheric CO_2 levels since 1958 at Mauna Loa in Hawaii (**Figure 1.7**). This plot shows that the CO_2 level has an overall upward trend, and varies throughout the year with a daily and seasonal pattern.[90,91] Plants are a major sink to CO_2, decreasing atmospheric CO_2 levels with photosynthesis, but contribute to rise of CO_2 levels as leaves fall and turn into decomposing matter. The Keeling curve illustrates that the lowest CO_2 levels are detected in autumn, just as plants are no longer taking CO_2 for photosynthesis, and highest in spring just before plant growth, leafing and vegetation kicks off in the northern hemisphere. Specifically, the months of May and September show the highest and lowest annual CO_2 levels, respectively. To study the CO_2 trend further back in Earth's history, paleoclimatologists investigate air trapped in ice or proxies, such as chemicals found in fossilized shells which would have been affected by ocean acidity induced from CO_2 in the atmosphere.[92] The CO_2 concentrations of the past are studied along with modern CO_2 recordings to assess climate change.

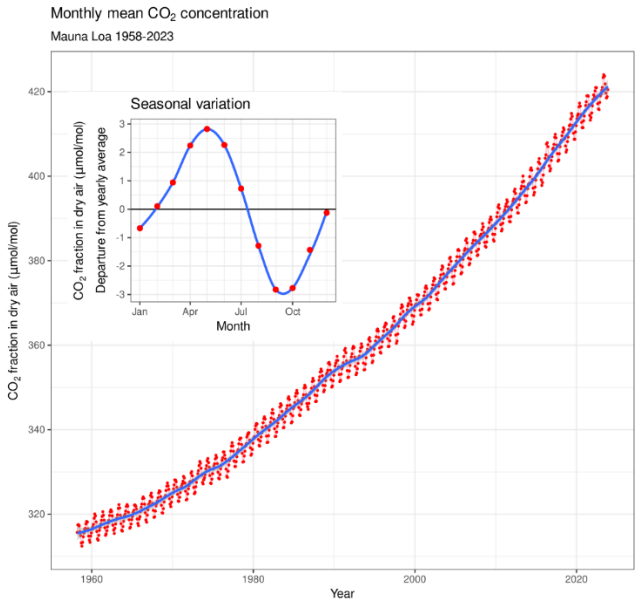

Figure 1.7 Keeling Curve showing atmospheric CO_2 levels from 1958 to 2023[93]

The National Oceanic and Atmospheric Administration (NOAA) is actively measuring the CO_2 levels of Earth at Mauna Loa in Hawaii. This site in the Pacific Ocean is chosen as it is far enough away from major pollution sources and industrial activities to detect an accurate level of Earth's CO_2. With an altitude of ~3.4 km above sea level, NOAA measures the CO_2 level in the well mixed troposphere layer, representing global atmospheric levels.

Investigations show that before the industrial revolution, Earth's CO_2 levels fluctuated between 180 and 280 ppm. In March 2024, NOAA reported CO_2 levels of 425 ppm, double the CO_2 concentration from pre-industrial levels (**Figure 1.8**).[94] One might think 425 ppm is still a very low value, corresponding to only 0.0425% of the atmosphere so why is this a significant increase? Let's look at some numbers.

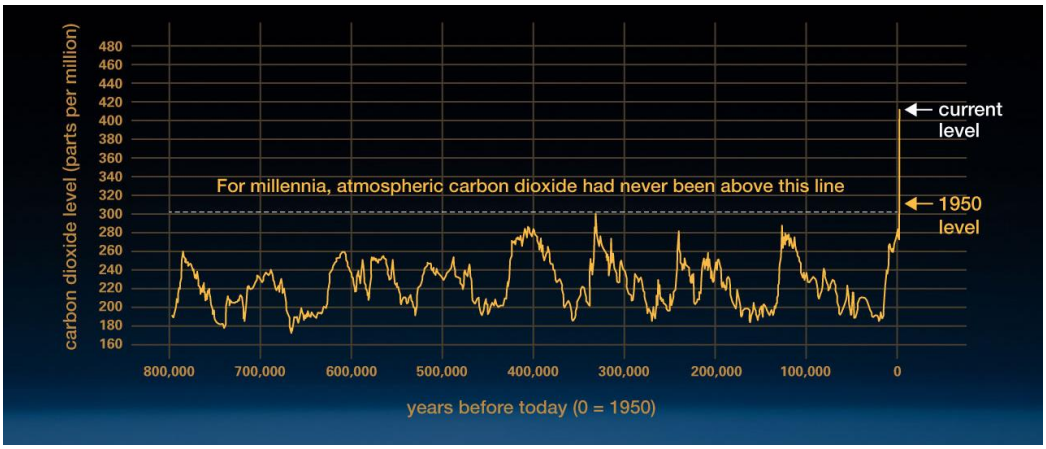

Figure 1.8 CO_2 levels now and recent history.[95]

From mid-1800's to 2019, the cumulative CO_2 emissions are estimated to be 2,400 ± 240 Gt CO_2 where 1,000 ± 900 Gt CO_2 (42%) has occurred in the last 119 years, from late 1900's to 2019. Only through the 9 years of 2010 to 2019, 410 ± 30 Gt CO_2 – or 410 ± 30 billion tons of CO_2 has been pumped into the atmosphere.[87] So even though CO_2 retains a small volumetric percentage of the atmosphere, it is billions upon billions of CO_2 molecules added to atmospheric layers trapping heat and warming our planet.

1.1.9 CO_2 emission sources

Scientists have reported that the main contributors to the CO_2 increase are generation and use of energy for transportation and built environment, deforestation, agriculture, waste handling and chemical production.[80,96,97] The annual absolute values of CO_2 emission or contribution to CO_2 increase from these sectors vary with country and year.

The International Council on Clean Transportation (ICCT) reports the average global CO_2 emission from transportation to be ~25% of the total CO_2 emitted.[98] The International Energy Agency (IEA) reports the global CO_2 emissions from transportation in the year of 2019 to be around ~8.5 Gt CO_2, accounting for ~27% of global emissions.[99] Nearly half of

CO_2 emissions from the transportation sector is reported to be from passenger cars (personal cars and trucks, buses, motorcycles, taxis, etc.). Around 30% of CO_2 emissions from this sector is from road freight transport. Aviation contributes to ~12% of emissions from this sector, where more than ~80% is passenger air travel (where ~60% is international air travel). The rest of CO_2 emission in the transportation sector is attributed to international shipping, rail travel and transport via pipelines (transportation of water, oil , gas, etc.).[100]

The built environment contributes to CO_2 pollution both directly and indirectly. Direct CO_2 emission can be from use of appliances and equipment that rely on combustion processes, such as boilers, furnaces, heaters, generators, or turbines. Indirect emission can be from using electricity produced from coal or natural gas fired power stations. Another indirect emission source is from building material and construction known as "embodied carbon".[101,102] Only the production of material used in built environment such as concrete, steel and aluminum are responsible for 11-6%, 10-6% and ~2% of the global CO_2 emissions, respectively.[103,104] The Environment Programme of United Nations reports ~10 Gt CO_2 emission from built environment (both direct and indirect) in 2019, accounting for ~38% of total CO_2 emissions.[105]

Plants are a major sink to CO_2, as they can capture CO_2 before it reaches the troposphere and store a large amount in their leaves, branches, roots and soil as they grow. All the stored carbon is released upon purposeful clearing or burning of the plants to produce agricultural products (such as pasture for cattle, soybeans, palm oil, cocoa, coffee, etc.) and clear the land for human activities. This is known as deforestation. Earth's largest tropical forests

such as the Amazon rainforest and Congo basin are under high rates of deforestation. The United Nations Food and Agriculture Organization (FAO) estimates that between 1990 and 2015, land area equivalent to whole of south Africa has been cleared. The Climate Council reports that between 2015 and 2017, nearly 5 Gt CO_2 were emitted annually (~10% of CO_2 emissions) as the result of deforestation.[106]

Globally, up to 2 billion metric tons of waste is generated annually.[107] Generated waste is usually processed, prepared and transported to either be recycled, buried in landfills or burnt in the incinerator. Incineration of waste is performed to not only remove the non-recyclable waste from lands, but also generate electricity from the energy released in burning. However, incineration of plastics, mostly made from carbon, releases a vast amount of CO_2 and contributes to climate change.[108–110] Decomposition of organic waste in landfills depleted of oxygen generates another greenhouse gas, CH_4, and decomposition with presence of oxygen results in CO_2 pollution. The United Nations FAO reports annual 4.4 GT global CO_2 emissions from food loss and generated waste.[111]

The main industrial consumers of oil and gas are the chemical production sector. Demand growth for primary chemicals and components such as cement, iron, steel, plastics and ethanol are expected to grow with growth in population.[112] The IEA estimates 1.5 Gt CO_2 emissions as the direct result of primary chemical production in 2018.[113]

1.1.10 Direct Air Capture (DAC)

Even if we suddenly cease all GHG emissions, it will still take a very long time for the released carbon to stabilize in the atmosphere and return to the ground. We cannot wait millenniums for nature to absorb the flood of anthropogenic CO_2 released into the

atmosphere. In the Paris Agreement, signed in December 2015, 192 countries and the European Union committed to reduce GHG emissions and work on climate change adaptation. In this legally binding treaty, the goal is set to keep the global average temperature rise below 2 °C from the pre-industrial temperatures and pursue efforts to limit the global average temperature rise to 1.5 °C. So far, human activities have caused a 1.36 °C increase from average pre-industrial temperatures, and it is projected that we are on the pathway to breach 1.5 °C within next three decades without substantial cuts in emissions and removing the already emitted GHGs.[114,115] Investigations have shown significant difference between the average temperature increase of 2 °C and 1.5 °C.[116–118] Complete bleaching of 99% of tropical coral reefs is projected to occur by 2100 in the 2 °C scenario, compared to 70% of tropical coral reefs in the 1.5 °C scenario.[119] Another study shows in the 2 °C above pre-industrial temperatures scenario, 2 million km^2 more permafrost is thawed compared to the 1.5 °C scenario.[120] The IPPC estimates a carbon budget of 500 and 1150 Gt CO_2 emission for 50% and 67% possibility to stay below 1.5 °C from 2020 onward. To put this in perspective, 500 Gt CO_2 emission from 2020 onward is only 75% of the total CO_2 emitted between the nine years of 2010 – 2019.[87]

With more attention given to the climate change crisis, the rate of global GHG emissions has slowed from an increase of 2.1% per year from 2000 to 2009, to an increase of 1.3% from 2010 to 2019.[87,88] The IPCC reports two dozen countries have successfully reduced CO_2 emissions in the last decade and deforestation in the Amazon rainforest has declined in the past decade. Electric vehicles have advanced to compete with and replace CO_2 emitting vehicles. However, with continued emissions, the net amount of CO_2 in the

atmosphere is still increasing. Many – not enough – countries and companies have pledged to develop net zero emission in the near future, but no solid policies are in place to enforce them.[121–123] Internationally coordinated human effort is required to overcome many barriers, significantly reduce emissions and also, remove billions of tons of CO_2 from the atmosphere to stay below the designated temperature rise threshold.[124] An estimated ~1 Gt CO_2 per year should be removed from the atmosphere until 2030 to attain the targets in the Paris Agreement.[125] If we don't move fast and effectively, even the 2 °C target will be unattainable.

Various climate change mitigation strategies are discussed throughout literature to stay withing the temperature rise threshold and halt climate change. One strategy is targeting reducing or preventing GHG emissions to the atmosphere or decarbonization of processes and technologies. Examples of this strategy include replacing fossil fuel energy with "cleaner" renewable energy sources such as nuclear, solar and wind power, and biomass. Replacing coal with less carbon-intensive fuels such as natural gas is also a target withing this strategy. Another approach within this strategy is increasing efficiency of energy conversion and utilization, and carbon storage and utilization within the process to eliminate emissions.

A second strategy is removal of existing GHGs, typically CO_2, in the atmosphere with novel capture and sequester processes to attain negative emission technologies (NETs). Given the world's reliance on fossil fuels, and the inability to completely halt CO_2 emissions worldwide, NETs are designed to counterbalance the unavoidable emissions and slow climate change. Direct air capture (DAC), cloud and ocean alkalinity treatment,

mineral carbonation (enhanced weathering), enhanced ocean productivity, “blue carbon” habitat restoration, afforestation and reforestation, bioenergy coupled with carbon capture and storage, biomass construction, biochar, and soil carbon sequestration are innovative approaches to NETs.

A third strategy involves manipulating Earth’s atmosphere to reflect a larger portion of the incoming solar radiation. This is projected to cool the planet without altering the GHG composition and is known as solar radiation management or solar geoengineering. Examples for this approach include marine cloud brightening (marine cloud seeding or marine cloud engineering), stratospheric aerosol injection, Cirrus cloud thinning (CCT), Space mirrors and surface brightening.[126–128] These technologies are not yet deployed in large-scale and are still in theoretical-level or early trial level of evaluations.[129]

Direct air capture (DAC) can be the solution to counter the unavoidable CO_2 emissions and the already emitted CO_2 residing in Earth’s atmosphere. DAC technology is a promising approach to complement traditional CO_2 capture technologies, to capture CO_2 directly from the air. DAC can compensate for mobile/distributed CO_2 emissions and can potentially avoid the costs and energy requirements of CO_2 compression for transportation since installations are not location specific (in DAC, there is no need to be in proximity to the source of emission, since CO_2 concentration is roughly the same everywhere, because the air is well mixed). Using DAC to produce sustainable, net-zero carbon fuels is a potential strategy to decarbonize sectors of our economy with no viable decarbonization strategy. DAC can provide a renewable CO_2 feedstock to produce non-fossil-based fuels (such as algae farms for production of biofuels) and chemicals (polycarbonate, polyurethane, etc.)

from recycled atmospheric CO_2.[130,131] However, DAC faces technical challenges to reach CO_2 capture targets needed to fight climate change. Financial limitations and higher energy requirements exist for DAC as separating dilute mixtures (i.e., CO_2 in the atmosphere) requires higher energy input than more concentrated mixtures (i.e., CO_2 in flue gas). DAC, depending on the process technology utilized, may be energy intensive and create a new source of CO_2 pollution. Sorbents and capture technology designed for point source capture also have to be reimagined to be useful for DAC, as CO_2 concentrations in air (~ 0.04%) are more than 300-fold lower than CO_2 concentrations in point source exhaust streams (15% – 60%).[132]

Scientists have been looking into pathways to remove the dilute CO_2 from air for over 80 years.[133] Capture of CO_2 from air was investigated in efforts such as removing breathed CO_2 by astronauts and submariners inside their confined environments where fresh air is limited[133] and removing CO_2 from air fed to cryogenic distillation columns producing nitrogen (N_2), oxygen (O_2) and Argon (Ar) to inhibit solid CO_2 formation on the heat exchanges.[134] However, the developed technologies are not on a comparable scale to what is envisioned for DAC. For space stations and submarines, effectively removing CO_2 is necessary at any cost, with no obligation to store and/or reuse the CO_2. Additionally, extraction of CO_2 from air is not intended to be absolute. Therefore, existing processes need to be reimagined for DAC.

1.2 Dissertation Overview

In **Chapter 1**, this dissertation highlights the critical imperative to combat climate change, identifying CO_2 as the principal driver behind this global challenge. Within this context,

the chapter introduces Direct Air Capture (DAC) technology as a pivotal solution, underlining its significance in achieving net-zero, or potentially net-negative, emissions.

Building on this introduction, **Chapter 2** presents a comprehensive literature review on DAC, focusing on the methods and sorbents developed for this purpose. This detailed examination investigates the advancements and potential of different approaches in contributing to the overarching goal of mitigating climate change.

In the following chapter, **Chapter 3**, a novel quaternary ammonium functionalized poly(arylene ether sulfone) copolymeric sorbent is explored for moisture swing DAC. This polymeric sorbent, prepared through step-growth polymerization and subsequent post-polymerization modification, demonstrates promise in capturing atmospheric CO_2 in dry conditions and releasing it when exposed to moisture. This study highlights the development of a specialized polymeric structure engineered for DAC.

Chapter 4 investigates the performance of moisture swing sorbents across a range of form factors, including free-standing dense membranes and thin film composite membranes. This assessment also revisits the polymer powders discussed in Chapter 3, providing a comprehensive comparison. The goal is to understand how variations in sorbent form factors impact the moisture swing DAC outcome, thereby guiding the optimization of this promising technology for future applications.

This dissertation extends the modifications of poly(arylene ether sulfones), a polymer extensively utilized in membrane-based desalination processes, to address the pressing challenge of water scarcity. **Chapter 5** focuses on enhancing hydrophilicity and reducing

the fouling tendency of desalination membranes through functionalization with zwitterionic groups. A study on the alterations in mechanical properties and water uptake of these modified membranes is presented in this chapter, demonstrating their improved hydrophilicity in desalination applications. Transitioning from enhancing poly(arylene ether sulfones) for desalination, this dissertation takes a step toward sustainable materials science by exploring the synthesis of poly(arylene ether sulfone) polymers from lignin-derivable monomers. In **Chapter 5**, the polymers produced from lignin-derivable compounds are analyzed and compared with conventional polysulfones used in desalination, which are increasingly scrutinized for their environmental and health impacts due to toxic and non-renewable components. The findings demonstrate the promising potential of lignin as a source for the eco-friendly production of polysulfone polymers with enhanced hydrophilicity. Finally, a hybrid system of desalination and direct ocean capture is explored, providing a dual approach to mitigate water scarcity while reducing CO_2 levels.

1.3 References

(1) Proceedings of the World Climate Conference -- a Conference of Experts on Climate and Mankind. Secretariat of the World Meteorological Organisation; Geneva, 1979.

(2) Centre for Research on the Epidemiology of Disasters. Extreme Events Defining Our Lives Executive Summary. **2021**. https://doi.org/10.1787/eee82e6e-en.

(3) Barry, R.; Gan, T. Y. *The Global Cryosphere*; Cambridge University Press, 2011; Vol. 74. https://doi.org/10.1017/CBO9780511977947.

(4) Ding, Y.; Zhang, S.; Zhao, L.; Li, Z.; Kang, S. Global Warming Weakening the Inherent Stability of Glaciers and Permafrost. *Sci. Bull.* **2019**, *64* (4), 245–253. https://doi.org/10.1016/j.scib.2018.12.028.

(5) Cazenave, A.; Palanisamy, H.; Ablain, M. Contemporary Sea Level Changes from Satellite Altimetry: What Have We Learned? What Are the New Challenges? *Adv. Sp. Res.* **2018**, *62* (7), 1639–1653. https://doi.org/10.1016/j.asr.2018.07.017.

(6) Mouginot, J.; Rignot, E.; Scheuchl, B. Continent-Wide, Interferometric SAR Phase, Mapping of Antarctic Ice Velocity. *Geophys. Res. Lett.* **2019**, *46* (16), 9710–9718. https://doi.org/10.1029/2019GL083826.

(7) Mouginot, J.; Rignot, E.; Bjørk, A. A.; van den Broeke, M.; Millan, R.; Morlighem, M.; Noël, B.; Scheuchl, B.; Wood, M. Forty-Six Years of Greenland Ice Sheet Mass Balance from 1972 to 2018. *Proc. Natl. Acad. Sci. U. S. A.* **2019**, *116* (19), 9239–9244. https://doi.org/10.1073/pnas.1904242116.

(8) Rignot, E.; Mouginot, J.; Scheuchl, B.; Van Den Broeke, M.; Van Wessem, M. J.; Morlighem, M. Four Decades of Antarctic Ice Sheet Mass Balance from 1979–2017. *Proc. Natl. Acad. Sci. U. S. A.* **2019**, *116* (4), 1095–1103. https://doi.org/10.1073/pnas.1812883116.

(9) Schröder, L.; Horwath, M.; Dietrich, R.; Helm, V. Four Decades of Surface Elevation Change of the Antarctic Ice Sheet from Multi-Mission Satellite Altimetry. *Cryosph. Discuss.* **2018**, *2018*, 1–25. https://doi.org/10.5194/tc-2018-49.

(10) Zemp, M.; Huss, M.; Thibert, E.; Eckert, N.; McNabb, R.; Huber, J.; Barandun, M.; Machguth, H.; Nussbaumer, S. U.; Gärtner-Roer, I.; Thomson, L.; Paul, F.; Maussion, F.; Kutuzov, S.; Cogley, J. G. Global Glacier Mass Changes and Their Contributions to Sea-Level Rise from 1961 to 2016. *Nature*. 2019, pp 382–386. https://doi.org/10.1038/s41586-019-1071-0.

(11) *Historic low sea ice in the Bering sea*. NASA Earth Observatory. https://earthobservatory.nasa.gov/images/92084/historic-low-sea-ice-in-the-bering-sea.

(12) *Visualizing the 2012 Sea Ice Minimum*. NASA Earth Observatory. https://earthobservatory.nasa.gov/images/79256/visualizing-the-2012-sea-ice-minimum.

(13) Chadwick, A. J.; Steele, S.; Silvestre, J.; Lamb, M. P. More Extensive Land Loss Expected on Coastal Deltas Due to Rivers Jumping Course during Sea-Level Rise. *Proc. Natl. Acad. Sci.* **2022**, *119* (31). https://doi.org/10.1073/pnas.2119333119.

(14) Sitzia, F.; Peters, M. J. H.; Lisci, C. Climate Change and Its Outcome on the Archaeological Areas and Their Building Materials. The Case Study of Tharros (Italy). *Digit. Appl. Archaeol. Cult. Herit.* **2022**, *25*, e00226. https://doi.org/10.1016/j.daach.2022.e00226.

(15) Li, Y.; Jia, X.; Liu, Z.; Zhao, L.; Sheng, P.; Storozum, M. J. The Potential Impact of Rising Sea Levels on China's Coastal Cultural Heritage: A GIS Risk Assessment. *Antiquity* **2022**, *96* (386), 406–421. https://doi.org/10.15184/aqy.2022.1.

(16) Anwar, M. S.; Rahman, K.; Bhuiyan, M. A. E.; Saha, R. Assessment of Sea Level and Morphological Changes along the Eastern Coast of Bangladesh. *J. Mar. Sci. Eng.* **2022**, *10* (4), 527. https://doi.org/10.3390/jmse10040527.

(17) Ji, T.; Yao, Y.; Dou, Y.; Deng, S.; Yu, S.; Zhu, Y.; Liao, H. The Impact of Climate Change on Urban Transportation Resilience to Compound Extreme Events. *Sustainability* **2022**, *14* (7), 3880. https://doi.org/10.3390/su14073880.

(18) Boone, W. W.; McCleery, R. A. Climate Change Likely to Increase Co-Occurrence of Island Endemic and Invasive Wildlife. *Clim. Chang. Ecol.* **2023**, *4* (January 2022), 100061. https://doi.org/10.1016/j.ecochg.2022.100061.

(19) Magnan, A. K.; Oppenheimer, M.; Garschagen, M.; Buchanan, M. K.; Duvat, V. K. E.; Forbes, D. L.; Ford, J. D.; Lambert, E.; Petzold, J.; Renaud, F. G.; Sebesvari, Z.; van de Wal, R. S. W.; Hinkel, J.; Pörtner, H.-O. Sea Level Rise Risks and Societal Adaptation Benefits in Low-Lying Coastal Areas. *Sci. Rep.* **2022**, *12* (1), 10677. https://doi.org/10.1038/s41598-022-14303-w.

(20) Sánchez-García, E. A.; López-Rosas, H.; Sosa, V. J.; Lindig-Cisneros, R.; Moreno-Casasola, P. Effect of Water Level and Salinity on the Growth of Annona Glabra L. Seedlings. *Wetl. Ecol. Manag.* **2022**, *30* (3), 579–593.

(21) Galbraith, H.; Jones, R.; Park, R.; Clough, J.; Herrod-Julius, S.; Harrington, B.; Page, G. Global Climate Change and Sea Level Rise: Potential Losses of Intertidal Habitat for Shorebirds. *Waterbirds* **2002**, *25* (2), 173–183. https://doi.org/10.1675/1524-4695(2002)025[0173:gccasl]2.0.co;2.

(22) Martins, S.; Patino−Martinez, J.; Abella, E.; de Santos Loureiro, N.; Clarke, L. J.; Marco, A. Potential Impacts of Sea Level Rise and Beach Flooding on Reproduction of Sea Turtles. *Clim. Chang. Ecol.* **2022**, *3* (April 2021), 100053. https://doi.org/10.1016/j.ecochg.2022.100053.

(23) DeConto, R. M.; Pollard, D.; Alley, R. B.; Velicogna, I.; Gasson, E.; Gomez, N.; Sadai, S.; Condron, A.; Gilford, D. M.; Ashe, E. L.; Kopp, R. E.; Li, D.; Dutton, A. The Paris Climate Agreement and Future Sea-Level Rise from Antarctica. *Nature* **2021**, *593* (7857), 83–89. https://doi.org/10.1038/s41586-021-03427-0.

(24) *Special Report on the Ocean and Cryosphere in a Changing Climate*; 2019; Vol. 9781107025. https://doi.org/10.1017/CBO9781139177245.003.

(25) Climate Change Initiative Coastal Sea Level team. Coastal Sea Level Anomalies and Associated Trends from Jason Satellite Altimetry over 2002-2018. *Nat. Sci. DATA* **2020**, *7* (1), 357. https://doi.org/10.1038/s41597-020-00694-w.

(26) Hancock, L. *Six ways loss of Arctic ice impacts everyone*. World Wildlife Fund (WFF).

(27) Amores, A.; Marcos, M.; Le Cozannet, G.; Hinkel, J. Coastal Flooding and Mean Sea-Level Rise Allowances in Atoll Island. *Sci. Rep.* **2022**, *12* (1), 1281. https://doi.org/10.1038/s41598-022-05329-1.

(28) Veron, S.; Mouchet, M.; Govaerts, R.; Haevermans, T.; Pellens, R. Vulnerability to Climate Change of Islands Worldwide and Its Impact on the Tree of Life. *Sci. Rep.* **2019**, *9* (1), 14471. https://doi.org/10.1038/s41598-019-51107-x.

(29) Farbotko, C. The Global Warming Clock Is Ticking so See These Places While You Can': Voyeuristic Tourism and Model Environmental Citizens on Tuvalu's Disappearing Islands. *Singap. J. Trop. Geogr.* **2010**, *31* (2), 224–238. https://doi.org/10.1111/j.1467-9493.2010.00392.x.

(30) Bellard, C.; Leclerc, C.; Courchamp, F. Potential Impact of Sea Level Rise on French Islands Worldwide. *Nat. Conserv.* **2013**, *5*, 75–86. https://doi.org/10.3897/natureconservation.5.5533.

(31) Albert, S.; Leon, J. X.; Grinham, A. R.; Church, J. A.; Gibbes, B. R.; Woodroffe, C. D. Interactions between Sea-Level Rise and Wave Exposure on Reef Island Dynamics in the Solomon Islands. *Environ. Res. Lett.* **2016**, *11* (5), 054011. https://doi.org/10.1088/1748-9326/11/5/054011.

(32) Spencer, N.; Strobl, E.; Campbell, A. Sea Level Rise under Climate Change: Implications for Beach Tourism in the Caribbean. *Ocean Coast. Manag.* **2022**, *225* (June), 106207. https://doi.org/10.1016/j.ocecoaman.2022.106207.

(33) Raj, N.; Gharineiat, Z.; Ahmed, A. A. M.; Stepanyants, Y. Assessment and Prediction of Sea Level Trend in the South Pacific Region. *Remote Sens.* **2022**, *14* (4), 986. https://doi.org/10.3390/rs14040986.

(34) Martínez-Asensio, A.; Wöppelmann, G.; Ballu, V.; Becker, M.; Testut, L.; Magnan, A. K.; Duvat, V. K. E. Relative Sea-Level Rise and the Influence of Vertical Land Motion at Tropical Pacific Islands. *Glob. Planet. Change* **2019**, *176* (March), 132–143. https://doi.org/10.1016/j.gloplacha.2019.03.008.

(35) *Early Melt on the Greenland Ice Sheet*. NASA Earth Observatory. https://earthobservatory.nasa.gov/images/88288/early-melt-on-the-greenland-ice-sheet.

(36) Observatory, L. G. The Great Ocean Conveyor Belt Drops Hints before It Slows. *New Sci.* **2008**, *198* (2656), 18. https://doi.org/10.1016/S0262-4079(08)61198-7.

(37) Döös, K.; Nilsson, J.; Nycander, J.; Brodeau, L.; Ballarotta, M. The World Ocean Thermohaline Circulation*. *J. Phys. Oceanogr.* **2012**, *42* (9), 1445–1460. https://doi.org/10.1175/JPO-D-11-0163.1.

(38) Tillinger, D. Physical Oceanography of the Present Day Indonesian Throughflow. *Geol. Soc. London, Spec. Publ.* **2011**, *355* (1), 267–281. https://doi.org/10.1144/SP355.13.

(39) Liggett, D.; Storey, B.; Cook, Y.; Meduna, V. *Exploring the Last Continent*; Liggett, D., Storey, B., Cook, Y., Meduna, V., Eds.; Springer International Publishing: Cham, 2015. https://doi.org/10.1007/978-3-319-18947-5.

(40) Onarheim, I. H.; Eldevik, T.; Smedsrud, L. H.; Stroeve, J. C. Seasonal and Regional Manifestation of Arctic Sea Ice Loss. *J. Clim.* **2018**, *31* (12), 4917–4932. https://doi.org/10.1175/JCLI-D-17-0427.1.

(41) Overland, J. E. Less Climatic Resilience in the Arctic. *Weather Clim. Extrem.* **2020**, *30* (May), 100275. https://doi.org/10.1016/j.wace.2020.100275.

(42) Meijer, P. T.; Dijkstra, H. A. The Response of Mediterranean Thermohaline Circulation to Climate Change: A Minimal Model. *Clim. Past* **2009**, *5* (4), 713–720. https://doi.org/10.5194/cp-5-713-2009.

(43) Boers, N. Observation-Based Early-Warning Signals for a Collapse of the Atlantic Meridional Overturning Circulation. *Nat. Clim. Chang.* **2021**, *11* (8), 680–688. https://doi.org/10.1038/s41558-021-01097-4.

(44) Åkesson, H.; Morlighem, M.; Nilsson, J.; Stranne, C.; Jakobsson, M. Petermann Ice Shelf May Not Recover after a Future Breakup. *Nat. Commun.* **2022**, *13* (1). https://doi.org/10.1038/s41467-022-29529-5.

(45) Biskaborn, B. K.; Smith, S. L.; Noetzli, J.; Matthes, H.; Vieira, G.; Streletskiy, D. A.; Schoeneich, P.; Romanovsky, V. E.; Lewkowicz, A. G.; Abramov, A.; Allard, M.; Boike, J.; Cable, W. L.; Christiansen, H. H.; Delaloye, R.; Diekmann, B.; Drozdov, D.; Etzelmüller, B.; Grosse, G.; Guglielmin, M.; Ingeman-Nielsen, T.; Isaksen, K.; Ishikawa, M.; Johansson, M.; Johannsson, H.; Joo, A.; Kaverin, D.; Kholodov, A.; Konstantinov, P.; Kröger, T.; Lambiel, C.; Lanckman, J.-P.; Luo, D.; Malkova, G.; Meiklejohn, I.; Moskalenko, N.; Oliva, M.; Phillips, M.; Ramos, M.; Sannel, A. B. K.; Sergeev, D.; Seybold, C.; Skryabin, P.; Vasiliev, A.; Wu, Q.; Yoshikawa, K.; Zheleznyak, M.; Lantuit, H. Permafrost Is Warming at a Global Scale. *Nat. Commun.* **2019**, *10* (1), 264. https://doi.org/10.1038/s41467-018-08240-4.

(46) Fouché, J.; Christiansen, C. T.; Lafrenière, M. J.; Grogan, P.; Lamoureux, S. F. Canadian Permafrost Stores Large Pools of Ammonium and Optically Distinct Dissolved Organic Matter. *Nat. Commun.* **2020**, *11* (1), 4500. https://doi.org/10.1038/s41467-020-18331-w.

(47) Peng, D.; Zhang, L.; Jiang, R.; Zhang, S.; Shen, P.; Lu, W.; He, X. Initiation Mechanisms and Dynamics of a Debris Flow Originated from Debris-Ice Mixture Slope Failure in Southeast Tibet, China. *Eng. Geol.* **2022**, *307*. https://doi.org/10.1016/j.enggeo.2022.106783.

(48) da Silva, T. H.; Queres Gomes, E. C.; Gonçalves, V. N.; da Costa, M. C.; Valério, A. D.; de Assis Santos, D.; Johann, S.; Convey, P.; Rosa, C. A.; Rosa, L. H. Does Maritime Antarctic Permafrost Harbor Environmental Fungi with Pathogenic Potential? *Fungal Biol.* **2022**, *126* (8), 488–497. https://doi.org/10.1016/j.funbio.2022.04.003.

(49) Magnússon, R. Í.; Hamm, A.; Karsanaev, S. V.; Limpens, J.; Kleijn, D.; Frampton, A.; Maximov, T. C.; Heijmans, M. M. P. D. Extremely Wet Summer Events Enhance Permafrost Thaw for Multiple Years in Siberian Tundra. *Nat. Commun.* **2022**, *13* (1), 1556. https://doi.org/10.1038/s41467-022-29248-x.

(50) Miner, K. R.; Turetsky, M. R.; Malina, E.; Bartsch, A.; Tamminen, J.; McGuire, A. D.; Fix, A.; Sweeney, C.; Elder, C. D.; Miller, C. E. Permafrost Carbon Emissions in a Changing Arctic. *Nat. Rev. Earth Environ.* **2022**, *3* (1), 55–67. https://doi.org/10.1038/s43017-021-00230-3.

(51) Chapman, E. J.; Byron, C. J.; Lasley-Rasher, R.; Lipsky, C.; Stevens, J. R.; Peters, R. Effects of Climate Change on Coastal Ecosystem Food Webs: Implications for Aquaculture. *Mar. Environ. Res.* **2020**, *162* (July), 105103. https://doi.org/10.1016/j.marenvres.2020.105103.

(52) Zandalinas, S. I.; Fritschi, F. B.; Mittler, R. Global Warming, Climate Change, and Environmental Pollution: Recipe for a Multifactorial Stress Combination Disaster. *Trends Plant Sci.* **2021**, *26* (6), 588–599. https://doi.org/10.1016/j.tplants.2021.02.011.

(53) Alaerts, L.; Dobbelaere, T.; Gravinese, P. M.; Hanert, E. Climate Change Will Fragment Florida Stone Crab Communities. *Front. Mar. Sci.* **2022**, *9*. https://doi.org/10.3389/fmars.2022.839767.

(54) Hansen, J.; Kharecha, P.; Sato, M.; Masson-Delmotte, V.; Ackerman, F.; Beerling, D. J.; Hearty, P. J.; Hoegh-Guldberg, O.; Hsu, S.-L.; Parmesan, C.; Rockstrom, J.; Rohling, E. J.; Sachs, J.; Smith, P.; Steffen, K.; Van Susteren, L.; von Schuckmann, K.; Zachos, J. C. Assessing "Dangerous Climate Change": Required Reduction of Carbon Emissions to Protect Young People, Future Generations and Nature. *PLoS One* **2013**, *8* (12), e81648. https://doi.org/10.1371/journal.pone.0081648.

(55) INOUE, H. Y.; MATSUEDA, H.; ISHII, M.; FUSHIMI, K.; HIROTA, M.; ASANUMA, I.; TAKASUGI, Y. Long-Term Trend of the Partial Pressure of Carbon Dioxide (PCO2) in Surface Waters of the Western North Pacific, 1984-1993. *Tellus B* **1995**, *47* (4), 391–413. https://doi.org/10.1034/j.1600-0889.47.issue4.2.x.

(56) Bushek, D.; Ford, S. E. Anthropogenic Impacts on an Oyster Metapopulation: Pathogen Introduction, Climate Change and Responses to Natural Selection. *Elem. Sci. Anthr.* **2016**, *4*, 1–13. https://doi.org/10.12952/journal.elementa.000119.

(57) Silverstein, T. P. Rising Atmospheric Carbon Dioxide Could Doom Ocean Corals and Shellfish: Simple Thermodynamic Calculations Show Why. *J. Chem. Educ.* **2022**, *99* (5), 2020–2025. https://doi.org/10.1021/acs.jchemed.2c00149.

(58) Shier, B. La. Ocean Acidifcation, Warming Waters Endanger Global Fisheries. *Sea Technol.* **2018**, *59* (1), 41–42.

(59) Atwood, T. C.; Marcot, B. G.; Douglas, D. C.; Amstrup, S. C.; Rode, K. D.; Durner, G. M.; Bromaghin, J. F. Forecasting the Relative Influence of Environmental and Anthropogenic Stressors on Polar Bears. *Ecosphere* **2016**, *7* (6), 1–22. https://doi.org/10.1002/ecs2.1370.

(60) Regehr, E. V.; Laidre, K. L.; Akçakaya, H. R.; Amstrup, S. C.; Atwood, T. C.; Lunn, N. J.; Obbard, M.; Stern, H.; Thiemann, G. W.; Wiig, Ø. Conservation Status of Polar Bears (Ursus Maritimus) in Relation to Projected Sea-Ice Declines. *Biol. Lett.* **2016**, *12* (12), 20160556. https://doi.org/10.1098/rsbl.2016.0556.

(61) Regehr, E. V.; Runge, M. C.; Von Duyke, A.; Wilson, R. R.; Polasek, L.; Rode, K. D.; Hostetter, N. J.; Converse, S. J. Demographic Risk Assessment for a Harvested Species Threatened by Climate Change: Polar Bears in the Chukchi Sea. *Ecol. Appl.* **2021**, *31* (8), 1–13. https://doi.org/10.1002/eap.2461.

(62) Hoegh-Guldberg, O. Climate Change, Coral Bleaching and the Future of the World's Coral Reefs. *Mar. Freshw. Res.* **1999**, *50* (8), 839–866. https://doi.org/10.1071/MF99078.

(63) Maingey, Y.; Opondo, M.; Olago, D.; Ouma, G. The Impacts of Increasing Water Scarcity and the Potential for Water-Related Conflict in Lamu, Kenya. *Water Supply* **2022**, *22* (2), 1983–1994. https://doi.org/10.2166/ws.2021.299.

(64) Pinho, P. F.; Canova, M. T.; Toledo, P. M.; Gonzalez, A.; Lapola, D. M.; Ometto, J. P.; Smith, M. S. Climate Change Affects Us in the Tropics: Local Perspectives on Ecosystem Services and Well-Being Sensitivity in Southeast Brazil. *Reg. Environ. Chang.* **2022**, *22* (3), 89. https://doi.org/10.1007/s10113-022-01938-8.

(65) Martin, L.; Zhang, Y.; Mustieles, V.; Souter, I.; Petrozza, J.; Messerlian, C. Reproductive Medicine in the Face of Climate Change: A Call for Prevention through Leadership. *Fertil. Steril.* **2022**, *118* (2), 239–246. https://doi.org/10.1016/j.fertnstert.2022.06.010.

(66) Anderko, L.; Pennea, E. Climate Changes Children's Health: Improving Clinical Practice to Address Changing Health Needs. *J. Nurse Pract.* **2022**, *18* (4), 395–398. https://doi.org/10.1016/j.nurpra.2021.09.005.

(67) Gasper, R.; Blohm, A.; Ruth, M. Social and Economic Impacts of Climate Change on the Urban Environment. *Curr. Opin. Environ. Sustain.* **2011**, *3* (3), 150–157. https://doi.org/10.1016/j.cosust.2010.12.009.

(68) Torres, J. M.; Casey, J. A. The Centrality of Social Ties to Climate Migration and Mental Health. *BMC Public Health* **2017**, *17* (1), 1–10. https://doi.org/10.1186/s12889-017-4508-0.

(69) Amelung, B.; Nicholls, S.; Viner, D. Implications of Global Climate Change for Tourism Flows and Seasonality. *J. Travel Res.* **2007**, *45* (3), 285–296. https://doi.org/10.1177/0047287506295937.

(70) Carrillo, J.; González, A.; Pérez, J. C.; Expósito, F. J.; Díaz, J. P. Projected Impacts of Climate Change on Tourism in the Canary Islands. *Reg. Environ. Chang.* **2022**, *22* (2). https://doi.org/10.1007/s10113-022-01880-9.

(71) Wang, S.; Tan, C.; Du, J.; Tang, Z.; Liu, C.; Wang, Y. A Responsible Tourism System at Glacier Tourism Sites: Reducing the Impacts of Tourism Activities on Glaciers. *J. Resour. Ecol.* **2022**, *13* (4), 697–707. https://doi.org/10.5814/j.issn.1674-764x.2022.04.015.

(72) Dube, K.; Nhamo, G.; Chikodzi, D. Climate Change-Induced Droughts and Tourism: Impacts and Responses of Western Cape Province, South Africa. *J. Outdoor Recreat. Tour.* **2022**, *39* (August 2020), 100319. https://doi.org/10.1016/j.jort.2020.100319.

(73) De Sherbinin, A.; Schiller, A.; Pulsipher, A. The Vulnerability of Global Cities to Climate Hazards. *Environ. Urban.* **2007**, *19* (1), 39–64. https://doi.org/10.1177/0956247807076725.

(74) Andreoni, V.; Miola, A. Climate Change and Supply-Chain Vulnerability. *Int. J. Emerg. Serv.* **2015**, *4* (1), 6–26. https://doi.org/10.1108/IJES-09-2014-0012.

(75) Ghadge, A.; Wurtmann, H.; Seuring, S. Managing Climate Change Risks in Global Supply Chains: A Review and Research Agenda. *Int. J. Prod. Res.* **2020**, *58* (1), 44–64. https://doi.org/10.1080/00207543.2019.1629670.

(76) Wright, K. M.; Hogan, C. *The Potential Impacts of Global Sea Level Rise on Transportation Infrastructure*; 2009. papers2://publication/uuid/7EC657D2-646C-4DDC-8A7A-C64A9648E3AD.

(77) Kirshen, P.; Watson, C.; Douglas, E.; Gontz, A.; Lee, J.; Tian, Y. Coastal Flooding in the Northeastern United States Due to Climate Change. *Mitig. Adapt. Strateg. Glob. Chang.* **2008**, *13* (5–6), 437–451. https://doi.org/10.1007/s11027-007-9130-5.

(78) Rae, J. W. B.; Zhang, Y. G.; Liu, X.; Foster, G. L.; Stoll, H. M.; Whiteford, R. D. M. Atmospheric CO 2 over the Past 66 Million Years from Marine Archives. *Annu. Rev. Earth Planet. Sci.* **2021**, *49* (1), 609–641. https://doi.org/10.1146/annurev-earth-082420-063026.

(79) Meyer, A. L. S.; Bentley, J.; Odoulami, R. C.; Pigot, A. L.; Trisos, C. H. Risks to Biodiversity from Temperature Overshoot Pathways. *Philos. Trans. R. Soc. B Biol. Sci.* **2022**, *377* (1857). https://doi.org/10.1098/rstb.2021.0394.

(80) Rossing, T. D.; Chiaverina, C. J. *Sources of CO2*; Springer International Publishing: Cham, 2019. https://doi.org/10.1007/978-3-030-27103-9_8.

(81) Totterdill, A.; Kovács, T.; Feng, W.; Dhomse, S.; Smith, C.; Carlos Gómez-Martín, J.; Chipperfield, M.; Forster, P.; Plane, J. Atmospheric Lifetimes, Infrared Absorption Spectra, Radiative Forcings and Global Warming Potentials of NF3 and CF3CF2Cl (CFC-115). *Atmos. Chem. Phys.* **2016**, *16* (17), 11451–11463. https://doi.org/10.5194/acp-16-11451-2016.

(82) *Montreal Protocol on Substances That Deplete the Ozone Layer*; 1989.

(83) Turner, A. J.; Frankenberg, C.; Kort, E. A. Interpreting Contemporary Trends in Atmospheric Methane. *Proc. Natl. Acad. Sci.* **2019**, *116* (8), 2805–2813. https://doi.org/10.1073/pnas.1814297116.

(84) Boucher, O.; Friedlingstein, P.; Collins, B.; Shine, K. P. The Indirect Global Warming Potential and Global Temperature Change Potential Due to Methane Oxidation. *Environ. Res. Lett.* **2009**, *4* (4), 044007. https://doi.org/10.1088/1748-9326/4/4/044007.

(85) Law, Y.; Ye, L.; Pan, Y.; Yuan, Z. Nitrous Oxide Emissions from Wastewater Treatment Processes. *Philos. Trans. R. Soc. B Biol. Sci.* **2012**, *367* (1593), 1265–1277. https://doi.org/10.1098/rstb.2011.0317.

(86) Griffis, T. J.; Chen, Z.; Baker, J. M.; Wood, J. D.; Millet, D. B.; Lee, X.; Venterea, R. T.; Turner, P. A. Nitrous Oxide Emissions Are Enhanced in a Warmer and Wetter World. *Proc. Natl. Acad. Sci.* **2017**, *114* (45), 12081–12085. https://doi.org/10.1073/pnas.1704552114.

(87) Working Group III contribution to the IPCC 6th assessment report (AR6). *Climate Change 2022, Mitigation of Climate Change*; 2022. https://doi.org/10.1201/9781003264705-7.

(88) Metz, B.; Davidson, O.; Coninck, H.; Loos, M.; Meyer, L. *IPCC Special Report on Carbon Dioxide Capture and Storage. . Prepared by Working Group III of the Intergovernmental Panel on Climate Change*; 2005.

(89) Falkowski, P.; Scholes, R. J.; Boyle, E.; Canadell, J.; Canfield, D.; Elser, J.; Gruber, N.; Hibbard, K.; Högberg, P.; Linder, S.; Mackenzie, F. T.; Moore III, B.; Pedersen, T.; Rosenthal, Y.; Seitzinger, S.; Smetacek, V.; Steffen, W. The Global Carbon Cycle: A Test of Our Knowledge of Earth as a System. *Science (80-.).* **2000**, *290* (5490), 291–296. https://doi.org/10.1126/science.290.5490.291.

(90) Howe, J. P. This Is Nature; This Is Un-Nature: Reading the Keeling Curve. *Environ. Hist. Durh. N. C.* **2015**, *20* (2), 286–293. https://doi.org/10.1093/envhis/emv005.

(91) Thoning, K. W.; Tans, P. P.; Komhyr, W. D. Atmospheric Carbon Dioxide at Mauna Loa Observatory: 2. Analysis of the NOAA GMCC Data, 1974-1985. *J. Geophys. Res. Atmos.* **1989**, *94* (D6), 8549–8565. https://doi.org/10.1029/JD094iD06p08549.

(92) Berger, A.; Loutre, M. F. Climate 400,000 Years Ago, a Key to the Future? *Geophys. Monogr. Ser.* **2003**, *137*, 17–26. https://doi.org/10.1029/137GM02.

(93) Wikipedia. *Keeling Curve*. wikipedia.org/wiki/Keeling_Curve.

(94) *Carbon dioxide now more than 50% higher than pre-industrial levels*. National Oceanic and Atmospheric Administration (NOAA). https://www.noaa.gov/news-release/carbon-dioxide-now-more-than-50-higher-than-pre-industrial-levels.

(95) NASA. *The relentless rise of carbon dioxide*. science.nasa.gov.

(96) Yoro, K. O.; Daramola, M. O. *CO_2 Emission Sources, Greenhouse Gases, and the Global Warming Effect*; Elsevier Inc., 2020. https://doi.org/10.1016/b978-0-12-819657-1.00001-3.

(97) Huang, L.; Krigsvoll, G.; Johansen, F.; Liu, Y.; Zhang, X. Carbon Emission of Global Construction Sector. *Renew. Sustain. Energy Rev.* **2018**, *81* (June), 1906–1916. https://doi.org/10.1016/j.rser.2017.06.001.

(98) The International Council on Clean Transportation (ICCT). *Real Impact*. https://theicct.org/.

(99) the international energy agency. *Data and Statistics*. iea.org.

(100) Ritchie, H. *Cars, planes, trains: where do CO_2 emissions from transport come from?*. Our World in Data. ourworldindata.org.

(101) Chastas, P.; Theodosiou, T.; Kontoleon, K. J.; Bikas, D. Normalising and Assessing Carbon Emissions in the Building Sector: A Review on the Embodied CO_2 Emissions of Residential Buildings. *Build. Environ.* **2018**, *130* (November 2017), 212–226. https://doi.org/10.1016/j.buildenv.2017.12.032.

(102) Min, J.; Yan, G.; Abed, A. M.; Elattar, S.; Amine Khadimallah, M.; Jan, A.; Elhosiny Ali, H. The Effect of Carbon Dioxide Emissions on the Building Energy Efficiency. *Fuel* **2022**, *326*, 124842. https://doi.org/10.1016/j.fuel.2022.124842.

(103) Kuruscu, A. O.; Z., Kc. G. Effective Use of Structural Materials in Sustainable Design. In *Sustainable Construction Materials and Technologies*; Kyoto, 2013.

(104) International Energy Agency. *World Energy Balances Database*; 2018.

(105) *2020 Global Status Report for Buildings and Construction*. globalabc.org.

(106) Contosta, A. R.; Asbjornsen, H.; Orefice, J.; Perry, A.; Smith, R. G. Climate Consequences of Temperate Forest Conversion to Open Pasture or Silvopasture. *Agric. Ecosyst. Environ.* **2022**, *333* (April), 107972. https://doi.org/10.1016/j.agee.2022.107972.

(107) Wiedinmyer, C.; Yokelson, R. J.; Gullett, B. K. Global Emissions of Trace Gases, Particulate Matter, and Hazardous Air Pollutants from Open Burning of Domestic Waste. *Environ. Sci. Technol.* **2014**, *48* (16), 9523–9530. https://doi.org/10.1021/es502250z.

(108) Chung, J.; Jung, I.; Song, J. Development of CO_2 Emission Factors and Evaluation of Emissions from Municipal Solid Waste Incineration Facility. *Asian J. Chem.* **2013**, *25* (12), 6515–6520. https://doi.org/10.14233/ajchem.2013.14261B.

(109) Christensen, T. H.; Bisinella, V. Climate Change Impacts of Introducing Carbon Capture and Utilisation (CCU) in Waste Incineration. *Waste Manag.* **2021**, *126*, 754–770. https://doi.org/10.1016/j.wasman.2021.03.046.

(110) Shakya, P. R.; Shrestha, P.; Tamrakar, C. S.; Bhattarai, P. K. Studies on Potential Emission of Hazardous Gases Due to Uncontrolled Open-Air Burning of Waste Vehicle Tyres and Their Possible Impacts on the Environment. *Atmos. Environ.* **2008**, *42* (26), 6555–6559. https://doi.org/10.1016/j.atmosenv.2008.04.013.

(111) Food and Agricultural of the United Nations. Food Wastage Footprint & Climate Change. **2011**, No. 1, 1–4.

(112) Rissman, J.; Bataille, C.; Masanet, E.; Aden, N.; Morrow, W. R.; Zhou, N.; Elliott, N.; Dell, R.; Heeren, N.; Huckestein, B.; Cresko, J.; Miller, S. A.; Roy, J.; Fennell, P.; Cremmins, B.; Koch Blank, T.; Hone, D.; Williams, E. D.; de la Rue du Can, S.; Sisson, B.; Williams, M.; Katzenberger, J.; Burtraw, D.; Sethi, G.; Ping, H.; Danielson, D.; Lu, H.; Lorber, T.; Dinkel, J.; Helseth, J. Technologies and Policies to Decarbonize Global Industry: Review and Assessment of Mitigation Drivers through 2070. *Appl. Energy* **2020**, *266* (November 2019), 114848. https://doi.org/10.1016/j.apenergy.2020.114848.

(113) *Chemicals*. the international energy agency (IEA). https://www.iea.org/fuels-and-technologies/chemicals.

(114) Fawzy, S.; Osman, A. I.; Doran, J.; Rooney, D. W. Strategies for Mitigation of Climate Change: A Review. *Environ. Chem. Lett.* **2020**, *18* (6), 2069–2094. https://doi.org/10.1007/s10311-020-01059-w.

(115) Dvorak, M. T.; Armour, K. C.; Frierson, D. M. W.; Proistosescu, C.; Baker, M. B.; Smith, C. J. Estimating the Timing of Geophysical Commitment to 1.5 and 2.0 °C of Global Warming. *Nat. Clim. Chang.* **2022**, *12* (6), 547–552. https://doi.org/10.1038/s41558-022-01372-y.

(116) Warren, R.; Andrews, O.; Brown, S.; Colón-González, F. J.; Forstenhäusler, N.; Gernaat, D. E. H. J.; Goodwin, P.; Harris, I.; He, Y.; Hope, C.; Manful, D.; Osborn, T. J.; Price, J.; Van Vuuren, D.; Wright, R. M. Quantifying Risks Avoided by Limiting Global Warming to 1.5 or 2 °C above Pre-Industrial Levels. *Clim. Change* **2022**, *172* (3–4), 39. https://doi.org/10.1007/s10584-021-03277-9.

(117) Qu, Y.; Liu, Y.; Jevrejeva, S.; Jackson, L. P. Future Sea Level Rise along the Coast of China and Adjacent Region under 1.5 °C and 2.0 °C Global Warming. *Adv. Clim. Chang. Res.* **2020**, *11* (3), 227–238. https://doi.org/10.1016/j.accre.2020.09.001.

(118) Martins, F. B.; Benassi, R. B.; Torres, R. R.; de Brito Neto, F. A. Impacts of 1.5 °C and 2 °C Global Warming on Eucalyptus Plantations in South America. *Sci. Total Environ.* **2022**, *825*, 153820. https://doi.org/10.1016/j.scitotenv.2022.153820.

(119) Schleussner, C. F.; Lissner, T. K.; Fischer, E. M.; Wohland, J.; Perrette, M.; Golly, A.; Rogelj, J.; Childers, K.; Schewe, J.; Frieler, K.; Mengel, M.; Hare, W.; Schaeffer, M. Differential Climate Impacts for Policy-Relevant Limits to Global Warming: The Case of 1.5 °C and 2 °C. *Earth Syst. Dyn.* **2016**, *7* (2), 327–351. https://doi.org/10.5194/esd-7-327-2016.

(120) Chadburn, S. E.; Burke, E. J.; Cox, P. M.; Friedlingstein, P.; Hugelius, G.; Westermann, S. An Observation-Based Constraint on Permafrost Loss as a Function of Global Warming. *Nat. Clim. Chang.* **2017**, *7* (5), 340–344. https://doi.org/10.1038/nclimate3262.

(121) Chaichaloempreecha, A.; Chunark, P.; Hanaoka, T.; Limmeechokchai, B. Thailand's Mid-Century Greenhouse Gas Emission Pathways to Achieve the 2 Degrees Celsius Target. *Energy. Sustain. Soc.* **2022**, *12* (1), 22. https://doi.org/10.1186/s13705-022-00349-1.

(122) Zheng, J.; Duan, H.; Yuan, Y. Perspective for China's Carbon Capture and Storage under the Paris Agreement Climate Pledges. *Int. J. Greenh. Gas Control* **2022**, *119*, 103738. https://doi.org/10.1016/j.ijggc.2022.103738.

(123) Shivanna, K. R. Climate Change and Its Impact on Biodiversity and Human Welfare. *Proc. Indian Natl. Sci. Acad.* **2022**, *88* (2), 160–171. https://doi.org/10.1007/s43538-022-00073-6.

(124) Santos, F. D.; Ferreira, P. L.; Pedersen, J. S. T. The Climate Change Challenge: A Review of the Barriers and Solutions to Deliver a Paris Solution. *Climate* **2022**, *10* (5), 75. https://doi.org/10.3390/cli10050075.

(125) van Soest, H. L.; de Boer, H. S.; Roelfsema, M.; den Elzen, M. G. J.; Admiraal, A.; van Vuuren, D. P.; Hof, A. F.; van den Berg, M.; Harmsen, M. J. H. M.; Gernaat, D. E. H. J.; Forsell, N. Early Action on Paris Agreement Allows for More Time to Change Energy Systems. *Clim. Change* **2017**, *144* (2), 165–179. https://doi.org/10.1007/s10584-017-2027-8.

(126) Xie, M.; Moore, J. C.; Zhao, L.; Wolovick, M.; Muri, H. Impacts of Three Types of Solar Geoengineering on the Atlantic Meridional Overturning Circulation. *Atmos. Chem. Phys.* **2022**, *22* (7), 4581–4597. https://doi.org/10.5194/acp-22-4581-2022.

(127) Wood, R. Assessing the Potential Efficacy of Marine Cloud Brightening for Cooling Earth Using a Simple Heuristic Model. *Atmos. Chem. Phys.* **2021**, *21* (19), 14507–14533. https://doi.org/10.5194/acp-21-14507-2021.

(128) Roy, K. The Solar Shield Concept: Current Status and Future Possibilities. *Acta Astronaut.* **2022**, *197*, 368–374. https://doi.org/10.1016/j.actaastro.2022.02.022.

(129) Low, S.; Baum, C. M.; Sovacool, B. K. Taking It Outside: Exploring Social Opposition to 21 Early-Stage Experiments in Radical Climate Interventions. *Energy Res. Soc. Sci.* **2022**, *90*, 102594. https://doi.org/10.1016/j.erss.2022.102594.

(130) Goldberg, D. S.; Lackner, K. S.; Han, P.; Slagle, A. L.; Wang, T. Co-Location of Air Capture, Subseafloor CO_2 Sequestration, and Energy Production on the Kerguelen Plateau. *Environ. Sci. Technol.* **2013**, *47* (13), 7521–7529. https://doi.org/10.1021/es401531y.

(131) Hou, C.; Wu, Y.; Jiao, Y.; Huang, J.; Wang, T.; Fang, M.; Zhou, H. Integrated Direct Air Capture and CO_2 Utilization of Gas Fertilizer Based on Moisture Swing Adsorption. *J. Zhejiang Univ. A* **2017**, *18* (10), 819–830. https://doi.org/10.1631/jzus.A1700351.

(132) Shi, X.; Xiao, H.; Azarabadi, H.; Song, J.; Wu, X.; Chen, X.; Lackner, K. S. Sorbents for the Direct Capture of CO_2 from Ambient Air. *Angew. Chemie Int. Ed.* **2020**, *59* (18), 6984–7006. https://doi.org/10.1002/anie.201906756.

(133) Ranjan, M.; Herzog, H. J. Feasibility of Air Capture. *Energy Procedia* **2011**, *4* (2010), 2869–2876. https://doi.org/10.1016/j.egypro.2011.02.193.

(134) Rege, S. U.; T. Yang, R.; Buzanowski, M. A. Sorbents for Air Prepurification in Air Separation. *Chem. Eng. Sci.* **2000**, *55* (21), 4827–4838. https://doi.org/10.1016/S0009-2509(00)00122-6.

2 CHAPTER 2: LITERATURE REVIEW

Direct air capture (DAC) is developing at a fast pace following the urgent need for net zero and negative emission technologies. A wide variety of materials have been studied for DAC, in the quest to find a system with optimum selectivity, working capacity, kinetics, energetics, and stability. Membrane separation and sorbents (can be liquid or solid) undergoing physisorption, chemisorption and moisture swing sorption are among the popular methods actively being investigated for DAC. This chapter is a summary of the most acknowledged systems investigated for DAC. Sorption chemistry, active functional groups and some of the pros and cons of each system are explored in this chapter.

2.1 CO_2 sorption mechanisms

CO_2 sorption mechanisms for DAC are divided into three groups of physi-sorption, chemi-sorption, and moisture swing sorption. Physisorption or physical adsorption, is when the sorbate (CO_2) only binds with the sorbent through weak intermolecular attractions such as van der Waals forces, hydrogen bonding, electrostatic forces, and hydrophobic interactions. Physisorption is a reversible process, and no electron transfer takes place or chemical bond is formed between the sorbent and sorbate, although polarization may occur. Many solid sorbents performing DAC via adsorption are explored such as activated carbon (AC), Metal-Organic Frameworks (MOFs) and Hybrid ultra-microporous materials (HUMs) and zeolites. Chemisorption or chemical adsorption is when the sorbate (CO_2) irreversibly binds with the sorbent through transfer, exchange or share of electrons forming

a strong chemical bond. Solid sorbents are most functionalized with amines to promote CO_2 adsorption via chemisorption in DAC.

When evaluating their use in DAC, physi-sorption and chemi-sorption present a mixed bag of benefits and drawbacks (**Table 2.1**). Chemi-sorbents, with their stronger affinity for CO_2 due to higher binding energies, outperform physi-sorbents in terms of CO_2 selectivity and absorption capacity. This allows them to capture CO_2 more efficiently from the atmosphere. Nonetheless, the strong chemical bonds in chemi-sorption necessitate significant energy for sorbent regeneration, posing a challenge for DAC applications. On the other hand, physi-sorbents offer an advantage during regeneration, requiring less energy to sever the weaker CO_2 bonds. However, this weaker bonding decreases the driving force for adsorption, leading to poorer selectivity and lower capacity for CO_2 capture from low-concentration sources, which is less ideal for extracting CO_2 from ambient air.

Table 2.1 Physisorption vs. Chemisorption

Physi-sorption	Chemi-sorption
CO_2 is adhered to the sorbent via weak intermolecular attractions	CO_2 is adhered to the sorbent via strong chemical bonds
Low enthalpy (heat) of adsorption (order of 20 kJ/mol)	High enthalpy (heat) of adsorption (order of 200 kJ/mol)
Favorable at low temperatures	Favorable at high temperatures
Reversible	Often irreversible
Monolayer of multilayer (multi-molecular) sorption	Monolayer sorption (uni-molecular)

A class of sorption has been recently introduced for DAC that seeks a compromise between chemisorption and physisorption for CO_2 capture, called moisture swing sorption.[1–3] In this approach, the sorbent's affinity for CO_2 alters with the introduction of moisture (humidity). Moisture swing sorbents are compounds with fixed hydroxide, carbonate, or bicarbonate

sites. Without moisture, the balance between carbonate and bicarbonate (**Equation 2.1**) moves towards the formation of bicarbonate and hydroxide ions. These hydroxides act as selective chemisorption sites for CO_2, capturing it from the air and converting it into bicarbonates. Upon the addition of moisture to a CO_2 saturated moisture swing sorbent, CO_2 is released as bicarbonate bind and transform into carbonate. Upon dehydration, the carbonates destabilize and revert back to bicarbonate and hydroxide.

$$2(\mathrm{HCO_3^-}\ \mathbf{R^+}.xH_2O) + (\mathrm{y} - 2\mathrm{x} - 1)\mathrm{H_2O}_{(g)} \leftrightarrow \mathrm{CO_3^{2-}}(\mathbf{R^+})_2.yH_2O + {CO_2}_{(g)} \qquad \textbf{(Eq. 2.1)}$$

Various materials have been functionalized with a carbonate-bicarbonate-hydroxide system and studied for DAC, such as anion exchange resins[45], porous polymers[6], ionic liquids[7], and cellulose[8].

2.2 Popular sorbents for DAC

2.2.1 Activated Carbon

Activated carbon (AC), also known as activated charcoal or carbon active, is an affordable, highly porous solid sorbent made from carbon-rich materials, utilized in numerous purification and separation processes. The production of AC involves a two-step process: carbonization followed by oxidation of the starting material. The oxidation step may be performed through gas or chemical treatment (also known as physical or chemical activation, respectively). In gas treatment, the carbonized material is initially prepared by heating the precursor material to 600 to 900 °C in an inert environment, and then is fed an oxidizing agent (such as steam, air, or $CO_{2(g)}$) at 600 to 1200 °C to bind and activate the carbons. In chemical treatment, carbonization and oxidation occurs simultaneously, with

submerging the precursor material inside an activating chemical bath (such as KOH, NaOH, H_3PO_4, $ZnCl_2$, Na_2CO_3 and H_2SO_4) and heated to 450 to 900 °C.[9] AC may be post-processed, modified and impregnated with different groups for different separation applications. Surface area and capacity of ACs depend on the nature of the precursor material and carbonization/oxidization process utilized to make the AC.

Initially, coal and petroleum residues were explored as precursor materials for AC. However, the focus has shifted towards deriving highly porous ACs from abundant and renewable bio-wastes, which are rich in carbon and low in inorganic and volatile substances. Lignin[10], sugarcane bagasse[11], tea leaves[12], rice[13] and chickpea[14] or sunflower[15] husk, fruit peels[15,16], coffee grounds[15], coconut shells[17], bamboo[18] are among the natural raw materials used to make AC.

ACs capture CO_2 through physisorption, locking the CO_2 molecules in their porous structures (**Figure 2.1**). Because of weak physical interactions between CO_2 and ACs, these sorbents have low energy requirements for sorbent regeneration. However, as the result of these weak interactions, ACs often exhibit low selectivity towards CO_2. ACs are more commonly considered for CO_2 capture for flue gas having higher CO_2 concentration compared to DAC. Scientists have evaluated the potential of ACs for DAC and observed that due to the sorption competition between CO_2 and H_2O in the atmosphere, ACs generally perform poorly in humid environments. However, studies are being conducted to enhance CO_2 selectivity and capacity with optimization in pore size and pore chemistry, for use in dilute and impure CO_2 streams such as DAC.[19]

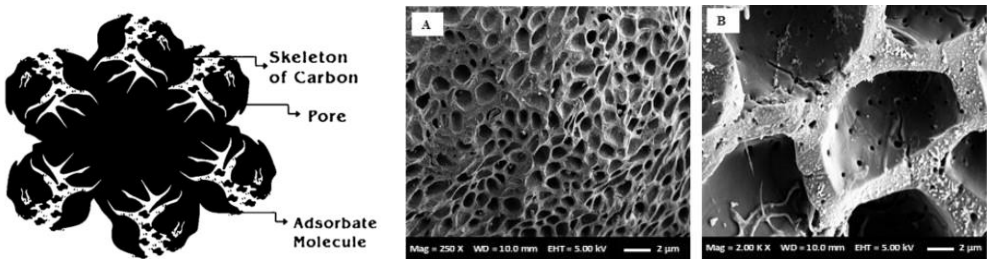

Figure 2.1 CO_2 physisorption in porous AC (left)[20] (A) 250X and (B) 2000X magnified image of AC porous structure (right)[21]

2.2.2 Metal-Organic Frameworks and Hybrid ultra-microporous materials

Metal-Organic frameworks (MOFs) are a class of versatile materials compromised of metal ions (nodes) and organic linker molecules (**Figure 2.2**). The organic linkers assemble the metal cations to form 1D, 2D or 3D structures. Hybrid ultra-microporous materials (HUMs) are newly introduced porous physi-sorbents like MOFs but have both organic and inorganic linkers (hence, "hybrid") which enable greater pore tunability. As seen in **Figure 2.3**, the organic linkers bind to a divalent metal cation (such as Cu^{2+} Ni^{2+}, Cd^{2+} or Zn^{2+}) to form a cationic square lattice (sql net) and inorganic linkers, like pillars, link the divalent metal cation on the sql net to form a 3D network.

MOFs and HUMs find various applications in gas separation and storage as the result of their hollow crystalline 3D "cage" structure providing ultrahigh porosity, and their stability and tunability. Varying the length and chemistry of the organic linkers and inorganic pillars in MOFs and HUMs enables fine-tuning of pore size (ranging from mesoporous (2-50 nm) to ultra-microporous (<7 nm) and chemistry for DAC. They can soak up large quantities of CO_2 molecules like a sponge and perform incomparably when exposed to concentrated CO_2 streams.

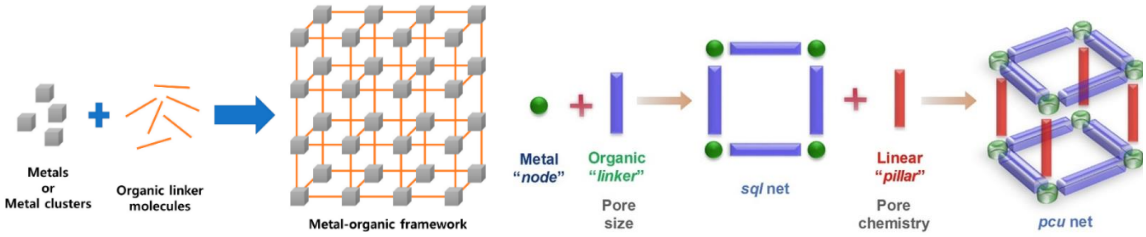

Figure 2.2 Metal-organic framework structure (left)[22] and Hybrid ultra-microporous materials (right)[23]

High efficiencies are obtained for CO_2 selective MOFs and HUMs with varying pore size and open-metal sites for CO_2 capture from precombustion and post-combustion flue gas, biogas, and natural gas.[24] A few reports have evaluated the performance of these materials for ultra-dilute concentrations and DAC **(Figure 2.3**). HUMs have shown great success in capturing trace levels of CO_2 from various gas mixtures and DAC (**Figure 2.4**).[25,26] M(4,4′-Bipyridine and/or pyrazine)$_2SiF_6$ (M being copper pore size = 3.5 Å)[27], nickel (pore size = 3.8 Å)[28], or zinc (pore size = 3.84 Å)[29] metals) with considerable uptake at dilute concentrations are reported. By replacing SiF_6^{2-} with shorter TiF_6^{2-}, Ni(pyrazine)$_2TiF_6$ (pore size = 3.5 Å)[30] HUM performed favorably for DAC.[26] Incorporation of amine groups into the MOF structure (**Figure 2.3**), mimicking amine scrubbing, has led to even higher CO_2 capacity at dilute concentrations. MOFs such as secondary amine functionalized M_2(4,4'-dioxido-3,3'-biphenyldicarboxylate) (M being Zinc or Magnesium metals) [31] and primary amine functionalized Mg_2(2′,5′-dimethyl-3,3″- dihydroxy-[1,1′:4′,1″-terphenyl]-4,4″-dicarboxylic acid)[32] have shown great promise for DAC.

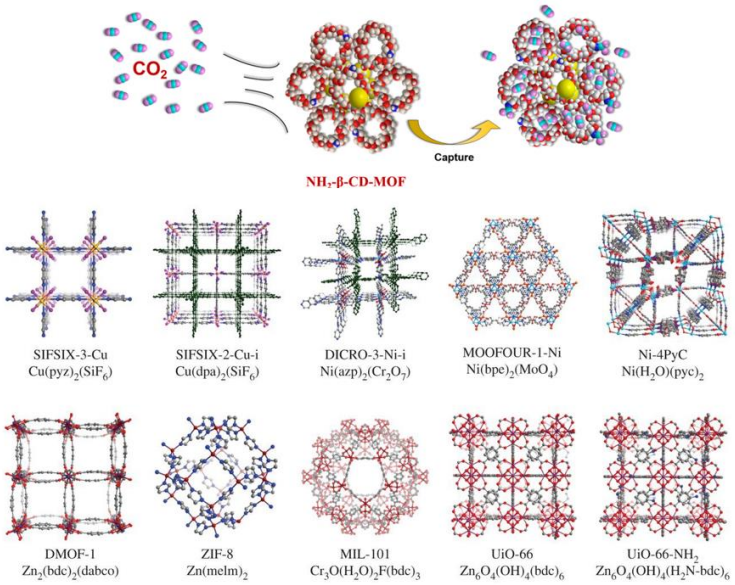

Figure 2.3 CO_2 sorption with amine functionalized-MOF (top)[33] and some MOF structures evaluated for DAC (bottom)[34]

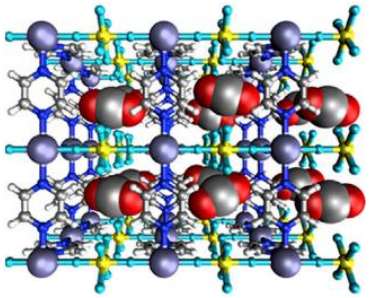

Figure 2.4 CO_2 physisorption with Ni(pyrazine)$_2$SiF$_6$ HUM[35]

Use of these materials are also generally reported to be limited to dry environments, as extended exposure to moisture causes CO_2 uptake interference.[19] Under humid conditions, the pores are occupied by water molecules (diameter of H_2O molecule= 2.75 Å, CO_2 molecule =3.3 Å), decreasing available sites for CO_2 molecules. Appending amine sites to MOFs is a pathway shown to maintain high CO_2 capacity at elevated humidity, as CO_2 uptake may occur at the newly added amine linkers.[32] Challenges however, are that elevated temperatures (80 to 120 °C) are required sorbent regeneration and decreased porosity and thermal stability is observed for the amine functionalized MOFs.[36]

2.2.3 Zeolites

Zeolites are highly porous crystalline solids made of SiO_4 and AlO_4 compounds connected tetrahedrally through shared oxygens (**Figure 2.5**). They can be found in nature, as the product of the reaction between volcanic material and saline water or synthesized in a laboratory. These materials are commonly used as sorbents. Zeolites carry a net negative charge, counterbalanced by basic alkali or alkaline earth metals like sodium, potassium, calcium, or magnesium. This negative charge, stemming from aluminum within the zeolite, exhibits a strong attraction to CO_2, a molecule with a quadrupole moment. The characteristics of the cation, including its size, charge density, and distribution within the zeolite framework, play crucial roles in defining the pore size and the efficiency of CO_2 sorption.

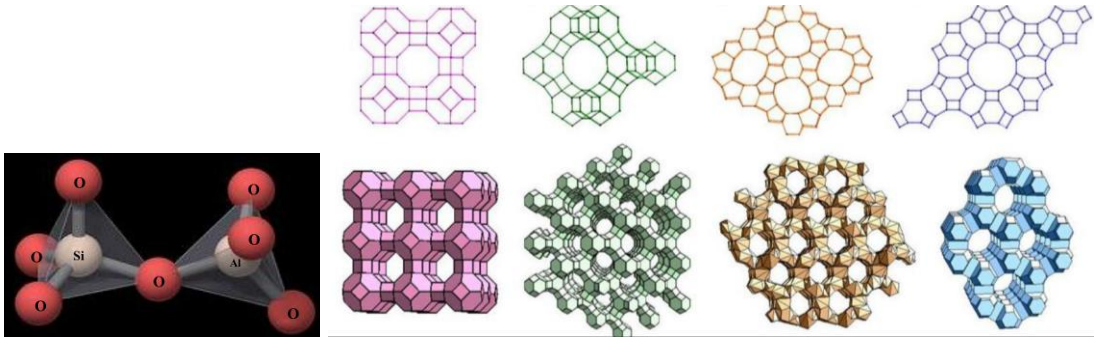

Figure 2.5 Tetrahedral structure of SiO_4 and AlO_4 compounds (left)[37] zeolite structures of different types of zeolites (right)[38]

Pure and impregnated zeolites have been subjected to extensive research for CO_2 adsorption from concentrated CO_2 streams for many years and show great performance.[39] Researchers have recently investigated DAC capabilities of various types of zeolites, working under dilute CO_2 concentrations. Investigations show zeolite affinity in the order of $H_2O>CO_2>N_2>O_2$ for the constituents in air.[40] Experimental evaluations on various

types of zeolites such as 13X (pore size = 9-10 Å), 3A (pore size 3 Å), 4A (pore size 3.8 Å) and 5A (pore size = 4.8 Å)[41–43] and computational modelling of alumino-phosphate and Gallo-phosphate and 5A have been carried out for DAC.[44,45] Generally, inefficient DAC performance is observed with zeolite sorbents due to weak bonds with CO_2 and adsorption competition with H_2O (excessive humidity uptake observed by the hydrophilic zeolite material).[46] Investigations report decent DAC performance by zeolites upon the addition of a gas dehydration or cooling (up to -20 °C) stage prior to sorption.[45,47,48]

2.2.4 Hydroxide sorbents

CO_2 capture utilizing hydroxide solutions are among the most studied processes.[49] CO_2, an acid gas, can be chemically absorbed inside a strong base solution. Employing this method for DAC was initially evaluated by Lackner[1], where he demonstrated DAC using a calcium hydroxide ($Ca(OH)_2$ – slaked lime) solution. The product of CO_2 and $Ca(OH)_2$ is $CaCO_3$ (limestone or chalk) (**Reaction 2.1**). Upon feeding the separated and dried $CaCO_3$ oxygen (O_2) at elevated temperatures (up to 900°C) calcium oxide (CaO) is produced, and the captured carbon is released as a concentrated stream (**Reaction 2.2**). CaO is then hydrated to regenerate $Ca(OH)_2$ to reuse as CO_2 capture sorbent (**Reaction 2.3)**. The cycle of change of calcium between its carbonate and oxide form is known as calcination, calcium looping or regenerative calcium cycle.

$$Ca(OH)_2 + CO_2 \rightarrow CaCO_3 + H_2O \qquad \textbf{R. 2.1}$$

$$CaCO_3 \rightarrow CaO + CO_2 \qquad \textbf{R. 2.2}$$

$$CaO + H_2O \rightarrow Ca(OH)_2 \qquad \textbf{R. 2.3}$$

Solubility of $Ca(OH)_2$ in water is limited, limiting CO_2 binding sites (OH^-) for DAC.[50] The substitution of calcium hydroxide ($Ca(OH)_2$) with sodium hydroxide (NaOH – also known as caustic soda) and potassium hydroxide (KOH – known as caustic potash) has been explored, with a greater emphasis on NaOH due to KOH being a more expensive alternative. Both are shown to be as affective at capturing CO_2, producing sodium carbonate (Na_2CO_3, soda ash or washing soda) and potassium carbonate (K_2CO, pearl ash, or potash carbonate) after reacting with CO_2, respectively. In using NaOH, the product, Na_2CO_3, is fed $Ca(OH)_2$ and $CaCO_3$ is formed while simultaneously NaOH sorbent is regenerated (**Reactions 2.4** and **2.5**). This process is known as causticization. The $CaCO_3$ is converted back to $Ca(OH)_2$ via the calcination process mentioned above (**Reactions 2.2 and 2.3**).

$$2NaOH + CO_2 \rightarrow Na_2CO_3 + H_2O \quad \textbf{R. 2.4}$$

$$Na_2CO_3 + Ca(OH)_2 \rightarrow 2NaOH + CaCO_3 \quad \textbf{R. 2.5}$$

In utilizing KOH, sulfuric acid (H_2SO_4) is introduced to the K_2CO_3 formed from the reaction between KOH and CO_2 (**Reactions 2.6** and **2.7**). This is known as acidification, $KHSO_4$ is produced, and CO_2 is released. KOH and H_2SO_4 are regenerated via electrodialysis.

$$2KOH + CO_2 \rightarrow K_2CO_3 + H_2O \quad \textbf{R. 2.6}$$

$$K_2CO_3 + H_2SO_4 \rightarrow KHSO_4 + H_2O + CO_2 \quad \textbf{R. 2.7}$$

Generally, these hydroxide absorbents exhibit great DAC performance with excellent CO_2 capture capacities.[51,52] Compounds like CaO can be sourced from natural and eco-friendly reserves, including limestone or dolomite. Yet, their extraction and utilization require significant energy input and they exhibit corrosive properties. For example, temperatures

of 900 °C to 950 °C is required for decomposition of $CaCO_3$.[53] Pure O_2 gas is preferred in the calcination process over use of air, to obtain a pure CO_2 product, necessitating an air separation unit. Solid alkali carbonates and supported alkali carbonates are also being investigated for DAC application. Effect of moisture was observed to be significant in these materials, and temperatures of 200 – 450 °C were required.[50] More investigation on these class of materials is required to assess the use in DAC.

2.2.5 Amine-based sorbents

First introduced in the 1930s and nowadays among the most studied and commercially available large-scale technologies for CO_2 removal is amine scrubbing.[54] A low-cost organic liquid amine system known for its high chemical absorption capacities, is employed for the removal of CO_2. As shown in **Figure 2.6(a)**, in absence of water, 1 mol of CO_2 reacts with 2 mol of a primary amine, forming a zwitterion and then a carbamate through deprotonation of the zwitterion by the second amine. In the case of a secondary amine, 1 mol of CO_2 reacts with 1 mol of secondary amine. In the presence of moisture, bicarbonate is formed (**Figure 2.6(b)**). CO_2 can also react with tertiary amines and form bicarbonates (**Figure 2.6(c)**). Generally, primary amines outperform secondary and tertiary amines in DAC due to favorable entropic factors.[55,56]

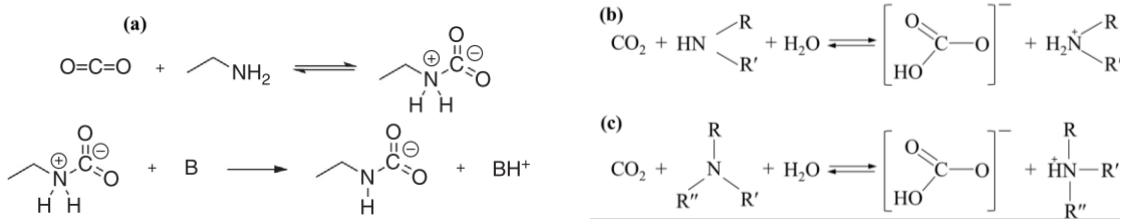

Figure 2.6 CO_2 chemisorption mechanism by primary amine (a), where B is a base (a second amine)[57] and CO_2 chemisorption mechanism by primary (R'=H) and secondary amine with presence of water (b), and by tertiary amine with presence of water (c)[58]

The reactivity and selectivity of amines towards CO_2 remain relatively unchanged by CO_2 concentration levels, and they can operate efficiently under ambient conditions, unlike hydroxide chemi-sorbents. This adaptability has also led to their increased consideration for DAC applications. Monoethanolamine (MEA)[59,60], pyrrolizidine-based diamines[59], pentaethylenehexamine[61], and so many other amine compounds[62,63] have been both experimentally and computationally studied for DAC. Results show that aqueous amine solutions are more effective than non-aqueous (organic solvents such as ethylene glycol) solutions, where more stable carbamate is formed.[63]

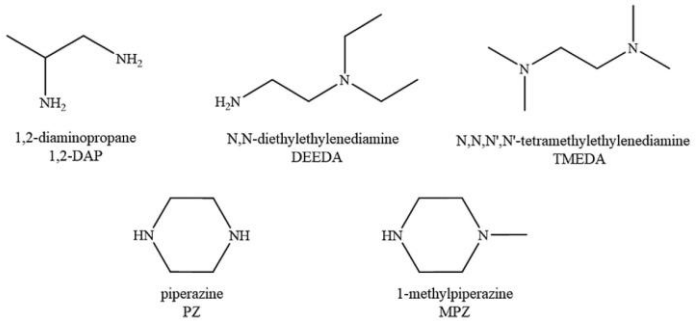

Figure 2.7 Structures of some of the amine compounds studied for DAC[62]

Despite amine scrubbing being among the most researched, refined, and commercially applied methods for CO_2 capture, it faces significant challenges. These include amine loss due to high volatility or entrainment, along with concerns related to its toxicity, corrosivity,

and instability, which includes issues with oxidative degradation.[64] Amine regeneration, due to high heat of absorption and high water content, requires high energy input for desorption deeming unfavorable for DAC. Blends of liquid amines with high boiling point and nitrogen content are expected to be evaluated in the near future for DAC to overcome some of these challenges.[63]

Due to the mentioned shortcomings for liquid amines, scientists have also looked at utilizing immobilized primary, secondary, or tertiary amines or combinations of them, on solid porous material to make high capacity, stable and less energy intensive DAC adsorbents. Physically impregnating porous media with pre-synthesized amine molecule or polymer (**Figure 2.8**, class 1), chemically (covalently) tethering amine groups on supports (**Figure 2.8**, class 2), or polymerizing polyamines in situ to a porous support (**Figure 2.8**, class 3) are some of these alternative forms.

Class 1 sorbents: small molecule or polymeric amine groups are physically impregnated (loaded) inside the available porous window of a meso-/macro- porous solid to form class 1 sorbents. From short and long alkylamines or alkanolamines to branched polymers containing amines (**Figure 2.9**) have been impregnated into porous support materials such as silica (gels, capsules, monoliths, etc.), alumina, AC, MOFs, or polymeric supports and studied for DAC.

Class 1 sorbents are usually easy to prepare and show great CO_2 capture performance. However, since amine groups are attached to the porous support via weak physical interaction and not chemical bonds, amine loss via leaching is observed during repeated regeneration cycles. Other shortcomings associated with use of amines, most of them

which are mutual with class 2 and 3 amine sorbents, are loss of amine by evaporation and thermal and oxidative degradation, especially when short amine chains such as diethylenetriamine[65,66] and tetraethylenepentamine[67,68] are used. More viscous high molecular weight and highly branched amine polymers undergo less leaching, have less volatility and enhanced thermal stability, however, they can lead to pore obstruction, reducing CO_2 diffusivity and devastating CO_2 uptake capacity and kinetics.[69] Also, in DAC, water condensation from atmospheric humidity can degrade class 1 sorbents due to solubilization.[70] Regeneration processes for these adsorbents also exhibit challenges, such as poly (ethylene imine) PEI decomposition (PEI is one of the most commonly utilized amine in class 1 sorbents) to urea which occurs at elevated temperatures and dry conditions. Adding humidity during regeneration to avoid PEI decomposition will deform the silica porous support, most utilized in class 1 sorbents.

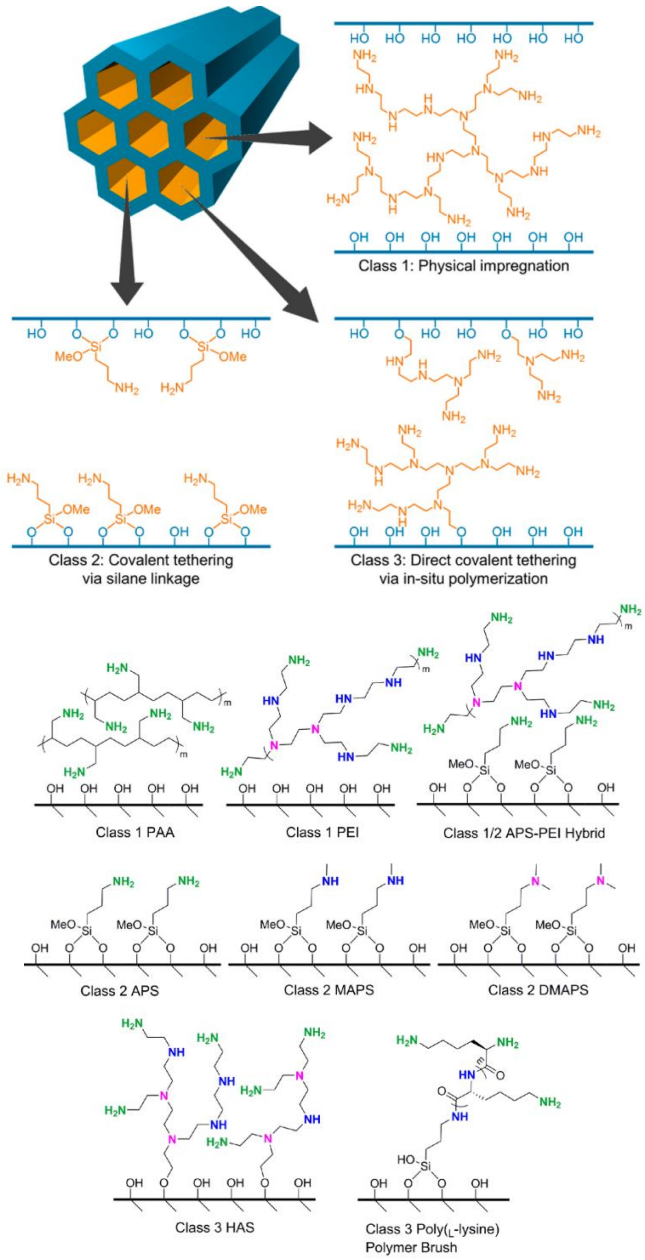

Figure 2.8 Classes of amine-functionalized sorbents[71]

The aggregation of amines and the produced ammonium carbamates on the supports can restrict CO_2 diffusion to deeper amine sites and lower process kinetics. In face of these challenges, careful tuning of amine molecular weight and structure, impregnation method,

amine distribution pattern, support nature, structure and porosity, and regeneration conditions has shown to produce DAC operable sorbents.

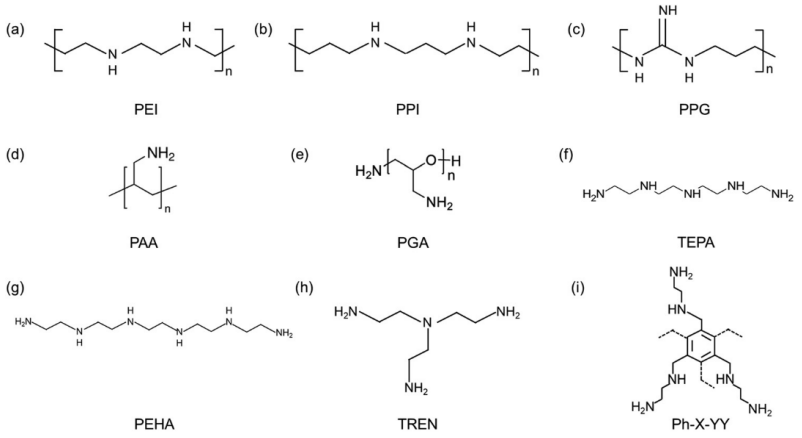

Figure 2.9 Most common amines impregnated in porous media for class 1 amine-based sorbents investigated for DAC.[69] (a) polyethyleneimine, (b) poly(propylene imine), (c) poly(propylene glycol), (d) poly(allylamine), (e) Polyglycolide or poly(glycolic acid), (f) Tetraethylenepentamine, (g) Pentaethylenehexamine, (h) Tris(2-aminoethyl)amine and (i) alkyl–aryl amine- rich small molecules

A computational study shows that tuning of the pore structure can allow the fabrication of stable class 1 sorbent with high capacity for DAC.[72] In this study, 800 Da PEI (**Figure 2.9a**) was impregnated inside a hierarchical bimodal pore (meso-/macro- pore) silica structure, and negligible leaching is observed. Another study reported that the modification of the amine compound led to increased thermal stability of class 1 sorbents. Here, PEI was modified with tetrapropyl orthotitanate and (3-aminopropyl)triethoxysilane groups and impregnated inside silica, and promising DAC performance and enhanced thermal stability was observed.[70] Impregnation with poly(propylene imine) (PPI - **Figure 2.9b**) is shown to enhance DAC performance and reduce oxidative degradation compared to PEI.[73] Another research has shown that the impregnation of hydrophobically modified branched amine polymer, fluorinated poly(allylamine) (PAA- **Figure 2.9d**) not only negates pore

obstruction, but leads to increased free volume and intermolecular diffusion pathways, drastically enhancing DAC perfromance[74]. A study has found that impregnating PEI on alumina porous support in place of silica, has shown to improve DAC performance and enable sorbent regeneration using steam.[75] Researchers have looked into adding surfactants, such as poly(ethylene glycol) (PEG), glycerol, ionic liquids, and potassium carbonate, to break the bulk ammonium carbamates and aid with deeper CO_2 diffusion,[76,77] and addition of sulfur-containing additives to decrease oxidation rate of amines.[78] But to our knowledge, there is no study on the effect of additives on DAC performance.

Class 2 sorbents: By chemically bonding amine sites to the porous support, these sorbents are synthesized to have a more ordered stacking of amine groups on the surface of the sorbent and less volatility compared to class 1 sorbents. However, the abundancy of active amine sites are reduced in class 2 sorbents compared to class 1 sorbents, where amine sites are dispersed inside the pores.[79]

Class 2 sorbents are synthesized via two pathways. In the first and most studied pathway, amininosilanes are systematically grafted to the surface of the sorbent through stable Si-O-Si bonds formed via reacting hydroxyl groups on the surface of a sorbent with aminosilanes, via a silylation reaction. In the second pathway, amines are attached to the sorbents by means of a coupling agent. The coupling agent is initially attached to the sorbent, and then functionalized with amine-containing compounds. The most commonly aminosilanes used in the first pathway are shown in **Figure 2.10**.

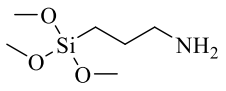

3-aminopropyltrimethoxysilane

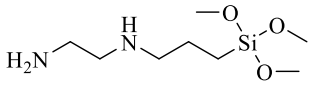

N-(2-aminoethyl)-3-aminopropyltrimethoxysilane

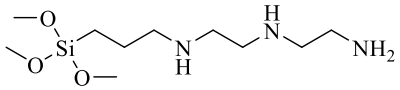

3-[2-(2-aminoethylamino)ethylamino]propyltrimethoxysilane

Figure 2.10 Common amines grafted on porous supports for class 2 amine -based sorbents.

Study shows the amine grafted silica sorbents generally have good DAC performance, however, large scale production of these materials is uneasy and expensive[69]. Same as class 1 sorbents, steam regeneration for class 2 adsorbents deforms the porous structure of the silica support. These sorbents generally require a large surface area for high CO_2 capacities, and aggregation on the surface can lead to CO_2 diffusion constraints. Amine oxidative degradation is also a challenge in class 2 sorbents. Similar to class 1 sorbents, by optimization of amine compounds, grafted surface and solvent polarity[80], DAC appropriate sorbents can be explored. A study reports DAC capable class 2 sorbent, synthesized by grafting N-(2-aminoethyl)-3-aminopropylmethyldimethoxysilane on cellulose, an abundant, inexpensive and renewable material.[81] Another reports promising results in replacing silica with alumina for DAC to enable adsorbent steam regeneration.[82]

Class 3 sorbents: To simultaneously have high sorbent stability and, high number of amine sites for higher CO_2 sorption capacities for DAC, in situ polymerization of amine-containing compounds on the pores of the support is performed (**Figure 2.11**).

Hyperbranched amino-silica sorbents (HAS), poly(l-lysine) brush-silica hybrids and melamine-dendrimer silica hybrids are recently introduced and are referred to as class 3 sorbents. [79,83–85]

In multiple studies, a class 3 sorbent synthesized from ring-opening polymerization of aziridine is reported to have higher CO_2 uptake capacity and regenerability in DAC[86] compared to class 1 and 2 amine-based sorbents.[83] Class 3 sorbents are indifferent to steam regeneration, as no capacity loss is observed after 3 cycles for aziridine polymerized on a silica foam.[87] Further investigations are required on these novel sorbents to reveal the potential for large-scale DAC.

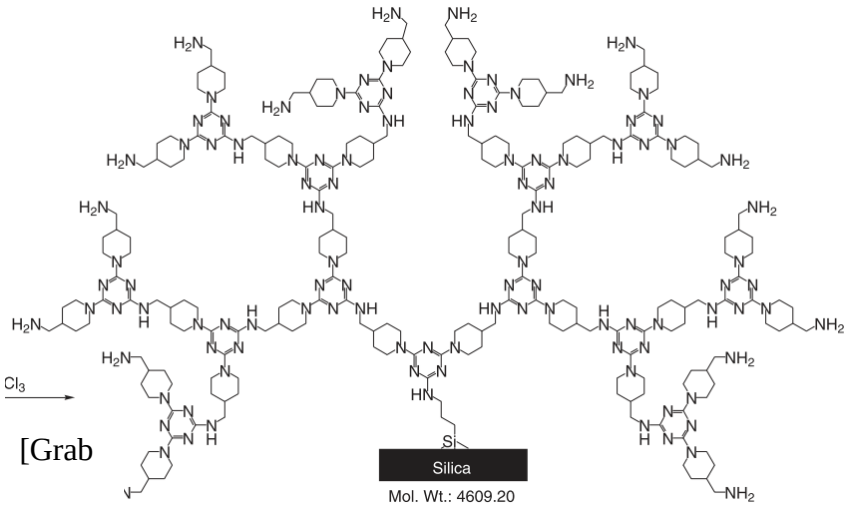

[Grab

Figure 2.11 Structure of a class 3 sorbent[84]

2.2.6 Ionic Liquids

Ionic liquids (ILs) are non-volatile and non-flammable stable organic salts that are liquid near room temperature. These recyclable liquids can be tailored for various applications to potentially replace volatile organic compounds used in industry and lower environmental pollution. The tunability of ILs allows the fabrication of sorbents with high CO_2 affinity

and selectivity. Some of the most common cation and anions making up ILs for CO_2 capture are shown in Figure **2.12**.

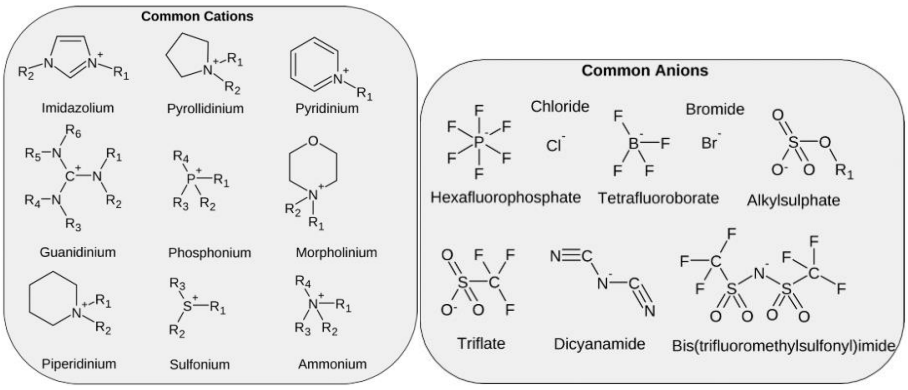

Figure 2.12 Common cation and anions making up ILs[88]

Good CO_2 capture performance from post- and pre- combustion stages is reported with ILs.[88,89] The main mechanism behind CO_2 capture with ionic liquids is believed to be a combination of CO_2 reaction with the IL anion and the added amine moiety (chemi-sorption), and CO_2 imprisonment in the cavities (free volume) in ILs (physisorption).[90,91] ILs are generally expensive viscous liquids that due to their water solubility, may result in aquatic toxicity.[92] Their high viscosity reduces CO_2 mass transfer inside the IL, and result in decreased diffusion and uptake. Further investigations into the many structural compositions in ILs can lead to a good task-specific DAC sorbent.[93]

With lower number of functionalities that undergo hydrogen bonding, lower viscosity ILs allowing higher CO_2 diffusion is obtained.[94] ILs have been investigated in various forms, such as liquids, dispersed on porous supports, encapsulated in polymeric or carbonaceous shells to increase the gas-liquid interface for higher CO_2 diffusion and higher working capacities at low concentrations.[95] ILs derived from 3 common amino acids, leucine, isoleucine, and valine derived from bio waste (in this case feathers, fur and human hair)

were studied for DAC to obtain environmentally friendly sorbents and show promising results.[96] IL functionalized with quaternary ammonium groups were also investigated for DAC via the moisture swing process.

2.2.7 Moisture Swing Sorbents

Ion exchange resins or charged polymers with positively charged groups (such as quaternary ammonium groups) that are neutralized by carbonate/bicarbonate system can effectively capture and release atmospheric CO_2 by a process known as moisture swing or humidity swing.[4] Moisture swing sorption (MSS) was first introduced by Lackner as a viable method for DAC and was further studied with experimental and computational modeling work by Yang et al. and Shi et al.[97–101] In the MSS process, CO_2 is captured by a chemi-sorption process. However, with the addition of a second sorbate, water (humidity), the CO_2 affinity for the sorbent changes, and the adsorbed CO_2 is released, seeking a compromise between physi-sorption and chemi-sorption mechanisms. In thermodynamic analysis, the free energy required for regeneration is provided by water evaporation, so a swing in moisture replaces the conventional thermal or pressure swings used for sorbent regeneration.[4]

The simplified moisture swing mechanism is illustrated in **Figure 2.13** for a polymer with positively charged quaternary ammoniums (QA) neutralized with OH^-, HCO_3^- or CO_3^{2-} ions. In "dry" conditions, the carbonate-bicarbonate equilibrium favors the presence of hydroxide and bicarbonate ions since carbonate ions are less stable in dry environments. This is shown as state I in **Figure 2.13**. The CO_2 in the atmosphere reacts with hydroxide forming a bicarbonate saturated sorbent (state II). Due to the high affinity of CO_2 for

hydroxide, this reaction occurs even at low CO_2 partial pressures (i.e., low atmospheric CO_2 concentrations). When humidity is introduced, the bicarbonate is hydrated (state III) and dissociates to release CO_2 to the environment, leaving the surface saturated with carbonates stabilized by water (state IV). Destabilization of carbonate occurs during dehumidification, returning to state I, and the MSS cycle is closed. The MSS is also demonstrated through **Reaction 2.8**, where R^+, *x* and *y* represent the QA groups, moles of water associated with bicarbonate, and moles of water associated with carbonate, respectively.[102]

$$2(HCO_3^- \mathbf{R}^+ . xH_2O) + (y - 2x - 1)H_2O_{(g)} \leftrightarrow CO_3^{2-}(\mathbf{R}^+)_2 . yH_2O + CO_{2(g)} \qquad \textbf{R. 2.8}$$

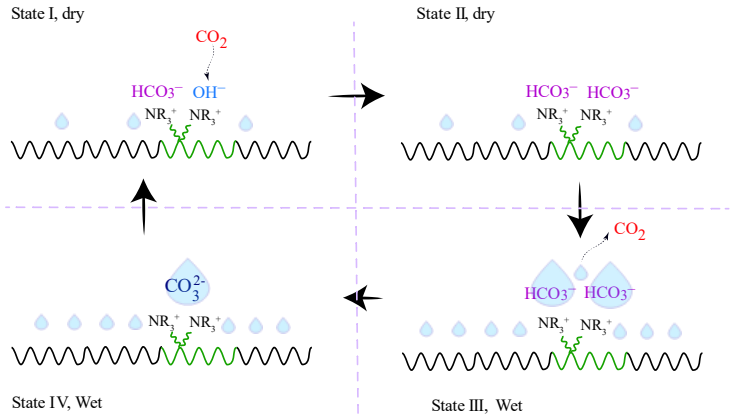

Figure 2.13 Moisture swing sorption mechanism.[103]

Porous polymers, amine-based anion exchange resins, QA functionalized ionic liquids, cellulose and chitosan/PVA aerogels, ammonium modified silica, colloidal crystal templates and sorbent containing electrospun fibers have been evaluated as sorbents.[6,7,110–113,8,101,104–109] For example, He and coworkers tested DAC via MSS (20-95% RH) with three QA-functionalized porous materials and reported CO_2 uptakes between 0.13 and 0.49 mmol/g (they also compared their performance to two commercially available materials).[104] Song and coworkers investigated QA chitosan/PVA systems and reported a

maximum uptake of 0.18 mmol/g at room temperature with a 3-95% RH humidity swing.[107] Hou and coworkers studied QA-modified bamboo cellulose and reported a maximum uptake of 0.19 mmol/g at 25 °C and a relative humidity swing of 60-80%.[8] The aforementioned investigations on DAC sorbents show that the adsorption and desorption capacities for CO_2 are significantly improved compared to commercial resins by increasing porosity, gas diffusivity and reduced sorbent size, but those DAC sorbents are generally used on organic supports.

2.3 Choosing Moisture Swing Sorption

A wide array of physi- and chemi-sorbents is under investigation for DAC. Chemisorption, in particular, is deemed highly promising for DAC, offering advantages such as superior capacity, selectivity, and stability under DAC conditions. Additionally, the regeneration of sorbents (CO_2 desorption) plays a pivotal role in the DAC process. However, the high energy demands associated with regenerating chemi-sorbents, depending on the energy source, could lead to potentially introduce a new source of CO_2 pollution. Various CO_2 sorption and desorption processes are explored for DAC sorbents such as thermal-(heat[43] and microwave[114]), pressure-[115], moisture-[3], vaccum-[116], electro-[117], alkalinity-[118], and photo-[119] swing or the combination of these, that vary in terms of operating conditions and energy requirements.

The moisture swing process is considered highly promising for DAC because the energy needed for sorbent regeneration is supplied through water evaporation. This area of research is still in the early stages, and of the objectives of this dissertation is to enhance our understanding of the MSS and the development of a polymeric structure for MSS.

Generally, these processes reported in literature are batchwise, having consecutive sorption and desorption cycles. Assuming the same performance, continuous CO_2 capture is preferred over batch processes in large-scale applications. To date, continuous MSS processes investigated in literature utilize commercial anion exchange membranes and pump CO_2 through the membrane with the assistance of a potential field.[120,121] Membrane technology has long been explored for CO_2 capture from concentrated streams (such as flue gas), but is at initial stages of evaluation for DAC.[122] The target sorbent material in is a dense membrane designed specifically for continuous DAC via the moisture swing process.

2.4 References

(1) Lackner, K. S.; Grimes, P.; Ziock, H. Carbon Dioxide Extraction from Air: Is It an Option? In *24th Annual Technical Conference on Coal Utilization and Fuel Systems*; 1999.

(2) Kaneko, Y.; Lackner, K. S. Isotherm Model for Moisture-Controlled CO_2 Sorption. *Phys. Chem. Chem. Phys.* **2022**, *24* (24), 14763–14771. https://doi.org/10.1039/D2CP01131J.

(3) Kaneko, Y.; Lackner, K. S. Kinetic Model for Moisture-Controlled CO_2 Sorption. *Phys. Chem. Chem. Phys.* **2022**, *24* (35), 21061–21077. https://doi.org/10.1039/D2CP02440C.

(4) Wang, T.; Lackner, K. S.; Wright, A. B. Moisture-Swing Sorption for Carbon Dioxide Capture from Ambient Air: A Thermodynamic Analysis. *Phys. Chem. Chem. Phys.* **2013**, *15* (2), 504–514. https://doi.org/10.1039/c2cp43124f.

(5) Song, J.; Zhu, L.; Shi, X.; Liu, Y.; Xiao, H.; Chen, X. Moisture Swing Ion-Exchange Resin-PO4 Sorbent for Reversible CO_2 Capture from Ambient Air. *Energy and Fuels* **2019**, *33* (7), 6562–6567. https://doi.org/10.1021/acs.energyfuels.9b00863.

(6) He, H.; Li, W.; Lamson, M.; Zhong, M.; Konkolewicz, D.; Hui, C. M.; Yaccato, K.; Rappold, T.; Sugar, G.; David, N. E.; Damodaran, K.; Natesakhawat, S.; Nulwala, H.; Matyjaszewski, K. Porous Polymers Prepared via High Internal Phase Emulsion Polymerization for Reversible CO_2 Capture. *Polymer (Guildf).* **2014**, *55* (1), 385–394. https://doi.org/10.1016/j.polymer.2013.08.002.

(7) Wang, T.; Ge, K.; Chen, K.; Hou, C.; Fang, M. Theoretical Studies on CO_2 Capture Behavior of Quaternary Ammonium-Based Polymeric Ionic Liquids. *Phys. Chem. Chem. Phys.* **2016**, *18* (18), 13084–13091. https://doi.org/10.1039/c5cp07229h.

(8) Hou, C.; Wu, Y.; Wang, T.; Wang, X.; Gao, X. Preparation of Quaternized Bamboo Cellulose and Its Implication in Direct Air Capture of CO_2. *Energy & Fuels* **2019**, *33* (3), 1745–1752. https://doi.org/10.1021/acs.energyfuels.8b02821.

(9) Raut, E. R.; Thakur, M. A. B.; Chaudhari, A. R. A Review on Activated Carbon Preparation from Natural and Eco-Friendly Raw Materials. In *AIP Conference Proceedings*; 2021; Vol. 2417, p 020011. https://doi.org/10.1063/5.0072755.

(10) Yang, Z.; Gleisner, R.; H. Mann, D.; Xu, J.; Jiang, J.; Zhu, J. Y. Lignin Based Activated Carbon Using H_3PO_4 Activation. *Polymers (Basel).* **2020**, *12* (12), 2829. https://doi.org/10.3390/polym12122829.

(11) da Costa, W. K. O. C.; Gavazza, S.; Duarte, M. M. M. B.; Freitas, S. K. B.; de Paula, N. T. G.; Paim, A. P. S. Preparation of Activated Carbon from Sugarcane Bagasse and Removal of Color and Organic Matter from Real Textile Wastewater. *Water, Air, Soil Pollut.* **2021**, *232* (9), 358. https://doi.org/10.1007/s11270-021-05306-w.

(12) Akar, E.; Altinişik, A.; Seki, Y. Using of Activated Carbon Produced from Spent Tea Leaves for the Removal of Malachite Green from Aqueous Solution. *Ecol. Eng.* **2013**, *52*, 19–27. https://doi.org/10.1016/j.ecoleng.2012.12.032.

(13) Le Van, K.; Luong Thi, T. T. Activated Carbon Derived from Rice Husk by NaOH Activation and Its Application in Supercapacitor. *Prog. Nat. Sci. Mater. Int.* **2014**, *24* (3), 191–198. https://doi.org/10.1016/j.pnsc.2014.05.012.

(14) Hayashi, J.; Horikawa, T.; Muroyama, K.; Gomes, V. G. Activated Carbon from Chickpea Husk by Chemical Activation with K_2CO_3: Preparation and Characterization. *Microporous Mesoporous Mater.* **2002**, *55* (1), 63–68. https://doi.org/10.1016/S1387-1811(02)00406-7.

(15) Kamińska, A.; Miądlicki, P.; Kiełbasa, K.; Kujbida, M.; Sreńscek-Nazzal, J.; Wróbel, R. J.; Wróblewska, A. Activated Carbons Obtained from Orange Peels, Coffee Grounds, and Sunflower Husks—Comparison of Physicochemical Properties and Activity in the Alpha-Pinene Isomerization Process. *Materials (Basel).* **2021**, *14* (23), 7448. https://doi.org/10.3390/ma14237448.

(16) Vimalkumar, A.; Thilagan, J.; Rajasekaran, K.; Raja, C.; Flora, M. N. Preparation of Activated Carbon from Mixed Peels of Fruits with Chemical Activation (K_2CO_3) - Application in Adsorptive Removal of Methylene Blue from Aqueous Solution. *Int. J. Environ. Waste Manag.* **2018**, *22* (1/2/3/4), 260. https://doi.org/10.1504/IJEWM.2018.094112.

(17) Gratuito, M. K. B.; Panyathanmaporn, T.; Chumnanklang, R.-A.; Sirinuntawittaya, N.; Dutta, A. Production of Activated Carbon from Coconut Shell: Optimization Using Response Surface Methodology. *Bioresour. Technol.* **2008**, *99* (11), 4887–4895. https://doi.org/10.1016/j.biortech.2007.09.042.

(18) Liu, Q.-S.; Zheng, T.; Wang, P.; Guo, L. Preparation and Characterization of Activated Carbon from Bamboo by Microwave-Induced Phosphoric Acid Activation. *Ind. Crops Prod.* **2010**, *31* (2), 233–238. https://doi.org/10.1016/j.indcrop.2009.10.011.

(19) Kumar, A.; Madden, D. G.; Lusi, M.; Chen, K. J.; Daniels, E. A.; Curtin, T.; Perry, J. J.; Zaworotko, M. J. Direct Air Capture of CO_2 by Physisorbent Materials. *Angew. Chemie - Int. Ed.* **2015**, *54* (48), 14372–14377. https://doi.org/10.1002/anie.201506952.

(20) Hertz, P. Vapour Intrusion Prevention through Activated Carbon Systems. *ResearchGate* **2017**, No. October 2015, 0–59. https://doi.org/10.13140/RG.2.2.15371.28964.

(21) Aboua, K. N.; Yobouet, Y. A.; Yao, K. B.; Goné, D. L.; Trokourey, A. Investigation of Dye Adsorption onto Activated Carbon from the Shells of Macoré Fruit. *J. Environ. Manage.* **2015**, *156*, 10–14. https://doi.org/10.1016/j.jenvman.2015.03.006.

(22) Liu, X.; Song, J. Metal-Organic Framework Materials for Supercapacitors. *J. Phys. Conf. Ser.* **2021**, *2021* (1), 012008. https://doi.org/10.1088/1742-6596/2021/1/012008.

(23) Mukherjee, S.; Kumar, N.; Bezrukov, A. A.; Tan, K.; Pham, T.; Forrest, K. A.; Oyekan, K. A.; Qazvini, O. T.; Madden, D. G.; Space, B.; Zaworotko, M. J. Amino-Functionalised Hybrid Ultramicroporous Materials That Enable Single-Step Ethylene Purification from a Ternary Mixture. *Angew. Chemie Int. Ed.* **2021**, *60* (19), 10902–10909. https://doi.org/10.1002/anie.202100240.

(24) Liang, W.; Bhatt, P. M.; Shkurenko, A.; Adil, K.; Mouchaham, G.; Aggarwal, H.; Mallick, A.; Jamal, A.; Belmabkhout, Y.; Eddaoudi, M. A Tailor-Made Interpenetrated MOF with Exceptional Carbon-Capture Performance from Flue Gas. *Chem* **2019**, *5* (4), 950–963. https://doi.org/10.1016/j.chempr.2019.02.007.

(25) Khraisheh, M.; Mukherjee, S.; Kumar, A.; Al Momani, F.; Walker, G.; Zaworotko, M. J. An Overview on Trace CO_2 Removal by Advanced Physisorbent Materials. *J. Environ. Manage.* **2020**, *255* (April 2019), 109874. https://doi.org/10.1016/j.jenvman.2019.109874.

(26) Kumar, A.; Hua, C.; Madden, D. G.; O'Nolan, D.; Chen, K.-J.; Keane, L.-A. J.; Perry, J. J.; Zaworotko, M. J. Hybrid Ultramicroporous Materials (HUMs) with Enhanced Stability and Trace Carbon Capture Performance. *Chem. Commun.* **2017**, *53* (44), 5946–5949. https://doi.org/10.1039/C7CC02289A.

(27) Shekhah, O.; Belmabkhout, Y.; Chen, Z.; Guillerm, V.; Cairns, A.; Adil, K.; Eddaoudi, M. Made-to-Order Metal-Organic Frameworks for Trace Carbon Dioxide Removal and Air Capture. *Nat. Commun.* **2014**, *5* (May), 1–7. https://doi.org/10.1038/ncomms5228.

(28) Shekhah, O.; Belmabkhout, Y.; Adil, K.; Bhatt, P. M.; Cairns, A. J.; Eddaoudi, M. A Facile Solvent-Free Synthesis Route for the Assembly of a Highly CO_2 Selective and H_2S Tolerant NiSIFSIX Metal–Organic Framework. *Chem. Commun.* **2015**, *51* (71), 13595–13598. https://doi.org/10.1039/C5CC04487A.

(29) Nugent, P.; Belmabkhout, Y.; Burd, S. D.; Cairns, A. J.; Luebke, R.; Forrest, K.; Pham, T.; Ma, S.; Space, B.; Wojtas, L.; Eddaoudi, M.; Zaworotko, M. J. Porous Materials with Optimal Adsorption Thermodynamics and Kinetics for CO_2 Separation. *Nature* **2013**, *495* (7439), 80–84. https://doi.org/10.1038/nature11893.

(30) Warfsmann, J.; Tokay, B.; Champness, N. R. Thin Film Synthesis of Hybrid Ultramicroporous Materials (HUMs)- a Comparative Approach. *Microporous Mesoporous Mater.* **2021**, *311* (July 2020), 110686. https://doi.org/10.1016/j.micromeso.2020.110686.

(31) McDonald, T. M.; Lee, W. R.; Mason, J. A.; Wiers, B. M.; Hong, C. S.; Long, J. R. Capture of Carbon Dioxide from Air and Flue Gas in the Alkylamine-Appended Metal–Organic Framework Mmen-Mg 2 (Dobpdc). *J. Am. Chem. Soc.* **2012**, *134* (16), 7056–7065. https://doi.org/10.1021/ja300034j.

(32) Peralta, R. A.; Alcántar-Vázquez, B.; Sánchez-Serratos, M.; González-Zamora, E.; Ibarra, I. A. Carbon Dioxide Capture in the Presence of Water Vapour in InOF-1. *Inorg. Chem. Front.* **2015**, *2* (10), 898–903. https://doi.org/10.1039/C5QI00077G.

(33) Xu, L.; Xing, C.-Y.; Ke, D.; Chen, L.; Qiu, Z.-J.; Zeng, S.-L.; Li, B.-J.; Zhang, S. Amino-Functionalized β-Cyclodextrin to Construct Green Metal–Organic Framework Materials for CO_2 Capture. *ACS Appl. Mater. Interfaces* **2020**, *12* (2), 3032–3041. https://doi.org/10.1021/acsami.9b20003.

(34) Madden, D. G.; Scott, H. S.; Kumar, A.; Chen, K.; Sanii, R.; Bajpai, A.; Lusi, M.; Curtin, T.; Perry, J. J.; Zaworotko, M. J. Flue-Gas and Direct-Air Capture of CO_2 by Porous Metal–Organic Materials. *Philos. Trans. R. Soc. A Math. Phys. Eng. Sci.* **2017**, *375* (2084), 20160025. https://doi.org/10.1098/rsta.2016.0025.

(35) Chen, K.-J.; Scott, H. S.; Madden, D. G.; Pham, T.; Kumar, A.; Bajpai, A.; Lusi, M.; Forrest, K. A.; Space, B.; Perry, J. J.; Zaworotko, M. J. Benchmark C_2H_2/CO_2 and CO_2/C_2H_2 Separation by Two Closely Related Hybrid Ultramicroporous Materials. *Chem* **2016**, *1* (5), 753–765. https://doi.org/10.1016/j.chempr.2016.10.009.

(36) Chen, X. Y.; Hoang, V.-T.; Rodrigue, D.; Kaliaguine, S. Optimization of Continuous Phase in Amino-Functionalized Metal–Organic Framework (MIL-53) Based Co-Polyimide Mixed Matrix Membranes for CO_2/CH_4 Separation. *RSC Adv.* **2013**, *3* (46), 24266. https://doi.org/10.1039/c3ra43486a.

(37) Xiem Nguyen Thang. Influence of Curing and Water to the Mechanical Properties of Geopolymer Mortar. *Int. J. Eng. Res. Technol.* **2016**, *5* (2), 49–52. https://doi.org/10.17577/IJERTV5IS020082.

(38) Zheng, Y.; Li, X.; Dutta, P. K. Exploitation of Unique Properties of Zeolites in the Development of Gas Sensors. *Sensors* **2012**, *12* (4), 5170–5194. https://doi.org/10.3390/s120405170.

(39) Karka, S.; Kodukula, S.; Nandury, S. V.; Pal, U. Polyethylenimine-Modified Zeolite 13X for CO_2 Capture: Adsorption and Kinetic Studies. *ACS Omega* **2019**, *4* (15), 16441–16449. https://doi.org/10.1021/acsomega.9b02047.

(40) Barkakaty, B.; Sumpter, B. G.; Ivanov, I. N.; Potter, M. E.; Jones, C. W.; Lokitz, B. S. Emerging Materials for Lowering Atmospheric Carbon. *Environ. Technol. Innov.* **2017**, *7*, 30–43. https://doi.org/10.1016/j.eti.2016.12.001.

(41) Abaza, A. Direct Air Capture of CO_2 by Adsorption on Zeolites, 2021.

(42) Santori, G.; Charalambous, C.; Ferrari, M.-C.; Brandani, S. Adsorption Artificial Tree for Atmospheric Carbon Dioxide Capture, Purification and Compression. *Energy* **2018**, *162*, 1158–1168. https://doi.org/10.1016/j.energy.2018.08.090.

(43) Stuckert, N. R.; Yang, R. T. CO_2 Capture from the Atmosphere and Simultaneous Concentration Using Zeolites and Amine-Grafted SBA-15. *Environ. Sci. Technol.* **2011**, *45* (23), 10257–10264. https://doi.org/10.1021/es202647a.

(44) Wang, H.; Qu, Z. G.; Bai, J. Q.; Qiu, Y. S. Combined Grand Canonical Monte Carlo and Finite Volume Method Simulation Method for Investigation of Direct Air Capture of Low Concentration CO_2 by 5A Zeolite Adsorbent Bed. *Int. J. Heat Mass Transf.* **2018**, *126*, 1219–1235. https://doi.org/10.1016/j.ijheatmasstransfer.2018.06.052.

(45) Wilson, S. M. W.; Tezel, F. H. Direct Dry Air Capture of CO_2 Using VTSA with Faujasite Zeolites. *Ind. Eng. Chem. Res.* **2020**, *59* (18), 8783–8794. https://doi.org/10.1021/acs.iecr.9b04803.

(46) Findley, J. M.; Sholl, D. S. Computational Screening of MOFs and Zeolites for Direct Air Capture of Carbon Dioxide under Humid Conditions. *J. Phys. Chem. C* **2021**, *125* (44), 24630–24639. https://doi.org/10.1021/acs.jpcc.1c06924.

(47) Song, M.; Rim, G.; Kong, F.; Priyadarshini, P.; Rosu, C.; Lively, R. P.; Jones, C. W. Cold-Temperature Capture of Carbon Dioxide with Water Coproduction from Air Using Commercial Zeolites. *Ind. Eng. Chem. Res.* **2022**, *61* (36), 13624–13634. https://doi.org/10.1021/acs.iecr.2c02041.

(48) Sinha, A.; Thakkar, H.; Rezaei, F.; Kawajiri, Y.; Realff, M. J. Direct Air Capture of CO_2 in Enclosed Environments: Design under Uncertainty and Techno-Economic Analysis. In *Computer Aided Chemical Engineering*; Elsevier Masson SAS, 2018; Vol. 44, pp 2179–2184. https://doi.org/10.1016/B978-0-444-64241-7.50358-X.

(49) Astarita, G. Absorption of Carbon Dioxide into Alkaline Solutions in Packed Towers. *Ind. Eng. Chem. Fundam.* **1963**, *2* (4), 294–297. https://doi.org/10.1021/i160008a009.

(50) Sanz-Pérez, E. S.; Murdock, C. R.; Didas, S. A.; Jones, C. W. Direct Capture of CO_2 from Ambient Air. *Chem. Rev.* **2016**, *116* (19), 11840–11876. https://doi.org/10.1021/acs.chemrev.6b00173.

(51) Bandi, A.; Specht, M.; Weimer, T.; Schaber, K. CO_2 Recycling for Hydrogen Storage and Transportation —Electrochemical CO2 Removal and Fixation. *Energy Convers. Manag.* **1995**, *36* (6–9), 899–902. https://doi.org/10.1016/0196-8904(95)00148-7.

(52) McQueen, N.; Gomes, K. V.; McCormick, C.; Blumanthal, K.; Pisciotta, M.; Wilcox, J. A Review of Direct Air Capture (DAC): Scaling up Commercial Technologies and Innovating for the Future. *Prog. Energy* **2021**, *3* (3), 0–22. https://doi.org/10.1088/2516-1083/abf1ce.

(53) Han, R.; Wang, Y.; Xing, S.; Pang, C.; Hao, Y.; Song, C.; Liu, Q. Progress in Reducing Calcination Reaction Temperature of Calcium-Looping CO2 Capture Technology: A Critical Review. *Chem. Eng. J.* **2022**, *450* (P2), 137952. https://doi.org/10.1016/j.cej.2022.137952.

(54) Khodadadi, M. J.; Abbasi, M.; Riahi, S.; Shokrollahzadeh, H. Investigation on Kinetics of Carbon Dioxide Absorption in Aqueous Solutions of Monoethanolamine + 1, 3-Diaminopropane. *Sep. Sci. Technol.* **2019**, *54* (17), 2800–2808. https://doi.org/10.1080/01496395.2018.1553984.

(55) Didas, S. A.; Kulkarni, A. R.; Sholl, D. S.; Jones, C. W. Role of Amine Structure on Carbon Dioxide Adsorption from Ultradilute Gas Streams Such as Ambient Air. https://doi.org/10.1002/cssc.201200196.

(56) Alkhabbaz, M. A.; Bollini, P.; Foo, G. S.; Sievers, C.; Jones, C. W. Important Roles of Enthalpic and Entropic Contributions to CO 2 Capture from Simulated Flue Gas and Ambient Air Using Mesoporous Silica Grafted Amines. **2014**, 8–11.

(57) Darunte, L. A.; Walton, K. S.; Sholl, D. S.; Jones, C. W. CO_2 Capture via Adsorption in Amine-Functionalized Sorbents. *Curr. Opin. Chem. Eng.* **2016**, *12*, 82–90. https://doi.org/10.1016/j.coche.2016.03.002.

(58) Wang, C.; Ma, B.; Zhang, L. Experimental Study on CO_2 Capture by Using N-Butylamine to Plug the Gas Channeling to Enhanced Oil Recovery. *J. Pet. Explor. Prod. Technol.* **2022**, *12* (9), 2523–2531. https://doi.org/10.1007/s13202-022-01503-3.

(59) Hanusch, J. M.; Kerschgens, I. P.; Huber, F.; Neuburger, M.; Gademann, K. Pyrrolizidines for Direct Air Capture and CO_2 Conversion. *Chem. Commun.* **2019**, *55* (7), 949–952. https://doi.org/10.1039/C8CC08574A.

(60) Kiani, A.; Jiang, K.; Feron, P. Techno-Economic Assessment for CO_2 Capture From Air Using a Conventional Liquid-Based Absorption Process. *Front. Energy Res.* **2020**, *8* (May), 1–13. https://doi.org/10.3389/fenrg.2020.00092.

(61) Kothandaraman, J.; Goeppert, A.; Czaun, M.; Olah, G. A.; Prakash, G. K. S. Conversion of CO_2 from Air into Methanol Using a Polyamine and a Homogeneous Ruthenium Catalyst. *J. Am. Chem. Soc.* **2016**, *138* (3), 778–781. https://doi.org/10.1021/jacs.5b12354.

(62) Barzagli, F.; Peruzzini, M.; Zhang, R. Direct CO_2 Capture from Air with Aqueous and Nonaqueous Diamine Solutions: A Comparative Investigation Based on 13C NMR Analysis. *Carbon Capture Sci. Technol.* **2022**, *3* (March), 100049. https://doi.org/10.1016/j.ccst.2022.100049.

(63) Barzagli, F.; Giorgi, C.; Mani, F.; Peruzzini, M. Screening Study of Di Ff Erent Amine-Based Solutions as Sorbents for Direct CO_2 Capture from Air. **2020**. https://doi.org/10.1021/acssuschemeng.0c03800.

(64) Luis, P. Use of Monoethanolamine (MEA) for CO_2 Capture in a Global Scenario: Consequences and Alternatives. *Desalination* **2016**, *380*, 93–99. https://doi.org/10.1016/j.desal.2015.08.004.

(65) Martín, C. F.; Sweatman, M. B.; Brandani, S.; Fan, X. Wet Impregnation of a Commercial Low Cost Silica Using DETA for a Fast Post-Combustion CO_2 Capture Process. **2016**, *183*, 1705–1721. https://doi.org/10.1016/j.apenergy.2016.09.081.

(66) Wei, J.; Liao, L.; Xiao, Y.; Zhang, P.; Shi, Y. Capture of Carbon Dioxide by Amine-Impregnated as-Synthesized MCM-41. *J. Environ. Sci.* **2010**, *22* (10), 1558–1563. https://doi.org/10.1016/S1001-0742(09)60289-8.

(67) Jo, D. H.; Jung, H.; Shin, D. K.; Lee, C. H.; Kim, S. H. Effect of Amine Structure on CO_2 Adsorption over Tetraethylenepentamine Impregnated Poly Methyl Methacrylate Supports. *Sep. Purif. Technol.* **2014**, *125*, 187–193. https://doi.org/10.1016/j.seppur.2014.01.048.

(68) Park, S.; Choi, K.; Yu, H. J.; Won, Y.; Kim, C.; Choi, M.; Cho, S.; Lee, J.; Lee, S. Y.; Lee, J. S. Thermal Stability Enhanced Tetraethylenepentamine / Silica Adsorbents for High Performance CO_2 Capture. **2018**. https://doi.org/10.1021/acs.iecr.7b04912.

(69) Zhu, X.; Xie, W.; Wu, J.; Miao, Y.; Xiang, C.; Hare, D. O.; Li, J.; Wang, R. Recent Advances in Direct Air Capture by Adsorption. **2022**, 6574–6651. https://doi.org/10.1039/d1cs00970b.

(70) Choi, S.; Gray, M. L.; Jones, C. W. Amine-Tethered Solid Adsorbents Coupling High Adsorption Capacity and Regenerability for CO_2 Capture From Ambient Air. https://doi.org/10.1002/cssc.201000355.

(71) Didas, S. A.; Choi, S.; Chaikittisilp, W.; Jones, C. W. Amine–Oxide Hybrid Materials for CO_2 Capture from Ambient Air. *Acc. Chem. Res.* **2015**, *48* (10), 2680–2687. https://doi.org/10.1021/acs.accounts.5b00284.

(72) Kwon, H. T.; Sakwa-novak, M. A.; Pang, S. H.; Sujan, A. R.; Ping, E. W.; Jones, C. W. Aminopolymer-Impregnated Hierarchical Silica Structures : Unexpected Equivalent CO_2 Uptake under Simulated Air Capture and Flue Gas Capture Conditions. **2019**. https://doi.org/10.1021/acs.chemmater.9b01474.

(73) Pang, S. H.; Lee, L.; Sakwa-novak, M. A.; Lively, R. P.; Jones, C. W. Design of Aminopolymer Structure to Enhance Performance and Stability of CO_2 Sorbents: Poly(Propylenimine) vs Poly(Ethylenimine). **2017**, 8–11. https://doi.org/10.1021/jacs.7b00235.

(74) Koutsianos, A.; Hamdy, L. B.; Yoo, C.-J.; Lee, J. J.; Taddei, M.; Urban-Klaehn, J. M.; Dryzek, J.; Jones, C. W.; Barron, A. R.; Andreoli, E. Drastic Enhancement of Carbon Dioxide Adsorption in Fluoroalkyl-Modified Poly(Allylamine). *J. Mater. Chem. A* **2021**, *9* (17), 10827–10837. https://doi.org/10.1039/D1TA00879J.

(75) Chaikittisilp, W.; Kim, H.; Jones, C. W. Mesoporous Alumina-Supported Amines as Potential Steam-Stable Adsorbents for Capturing CO_2 from Simulated Flue Gas and Ambient Air. **2011**, 5528–5537.

(76) Wang, J.; Wang, M.; Zhao, B.; Qiao, W.; Long, D.; Ling, L. Mesoporous Carbon-Supported Solid Amine Sorbents for Low-Temperature Carbon Dioxide Capture. *Ind. Eng. Chem. Res.* **2013**, *52* (15), 5437–5444. https://doi.org/10.1021/ie303388h.

(77) Yue, M. B.; Sun, L. B.; Cao, Y.; Wang, Z. J.; Wang, Y.; Yu, Q.; Zhu, J. H. Promoting the CO_2 Adsorption in the Amine-Containing SBA-15 by Hydroxyl Group. *Microporous Mesoporous Mater.* **2008**, *114* (1–3), 74–81. https://doi.org/10.1016/j.micromeso.2007.12.016.

(78) Vu, Q. T.; Yamada, H.; Yogo, K. Inhibitors of Oxidative Degradation of Polyamine-Modified Silica Sorbents for CO_2 Capture. *Ind. Eng. Chem. Res.* **2019**, *58* (34), 15598–15605. https://doi.org/10.1021/acs.iecr.9b02742.

(79) Chaikittisilp, W.; Lunn, J. D.; Shantz, D. F.; Jones, C. W. Poly(L-lysine) Brush–Mesoporous Silica Hybrid Material as a Biomolecule-Based Adsorbent for CO_2 Capture from Simulated Flue Gas and Air. *Chem. – A Eur. J.* **2011**, *17* (38), 10556–10561. https://doi.org/10.1002/chem.201101480.

(80) Li, H.; Wang, K.; Hu, Z.; Chen, Y.; Verdegaal, W.; Zhao, D.; Zhou, H. Harnessing Solvent Effects to Integrate Alkylamine into Metal–Organic Frameworks for Exceptionally High CO_2 Uptake. **2019**, 7867–7874. https://doi.org/10.1039/c8ta11300a.

(81) Gebald, C.; Wurzbacher, J. A.; Tingaut, P.; Zimmermann, T.; Steinfeld, A. Amine-Based Nanofibrillated Cellulose As Adsorbent for CO_2 Capture from Air. **2011**, 9101–9108.

(82) Bali, S.; Leisen, J.; Foo, G. S.; Sievers, C.; Jones, C. W. Aminosilanes Grafted to Basic Alumina as CO 2 Adsorbents-Role of Grafting Conditions on CO_2 Adsorption Properties. *ChemSusChem* **2014**, *7* (11), 3145–3156. https://doi.org/10.1002/cssc.201402373.

(83) Choi, S.; Drese, J. H.; Eisenberger, P. M.; Jones, C. W. Application of Amine-Tethered Solid Sorbents for Direct CO_2 Capture from the Ambient Air. *Environ. Sci. Technol.* **2011**, *45* (6), 2420–2427. https://doi.org/10.1021/es102797w.

(84) Acosta, E. J.; Carr, C. S.; Simanek, E. E.; Shantz, D. F. Engineering Nanospaces: Iterative Synthesis of Melamine-Based Dendrimers on Amine-Functionalized SBA-15 Leading to Complex Hybrids with Controllable Chemistry and Porosity. *Adv. Mater.* **2004**, *16* (12), 985–989. https://doi.org/10.1002/adma.200306323.

(85) Yoo, S.; Lunn, J. D.; Gonzalez, S.; Ristich, J. A.; Simanek, E. E.; Shantz, D. F. Engineering Nanospaces: OMS/Dendrimer Hybrids Possessing Controllable Chemistry and Porosity. *Chem. Mater.* **2006**, *18* (13), 2935–2942. https://doi.org/10.1021/cm0520564.

(86) Hicks, J. C.; Drese, J. H.; Fauth, D. J.; Gray, M. L.; Qi, G.; Jones, C. W. Designing Adsorbents for CO_2 Capture from Flue Gas-Hyperbranched Aminosilicas Capable of Capturing CO_2 Reversibly. *J. Am. Chem. Soc.* **2008**, *130* (10), 2902–2903. https://doi.org/10.1021/ja077795v.

(87) Li, W.; Choi, S.; Drese, J. H.; Hornbostel, M.; Krishnan, G.; Eisenberger, P. M.; Jones, C. W. Steam-Stripping for Regeneration of Supported Amine-Based CO2 Adsorbents. *ChemSusChem* **2010**, *3* (8), 899–903. https://doi.org/10.1002/cssc.201000131.

(88) Ramdin, M.; de Loos, T. W.; Vlugt, T. J. H. State-of-the-Art of CO_2 Capture with Ionic Liquids. *Ind. Eng. Chem. Res.* **2012**, *51* (24), 8149–8177. https://doi.org/10.1021/ie3003705.

(89) Shukla, S. K.; Khokarale, S. G.; Bui, T. Q.; Mikkola, J.-P. T. Ionic Liquids: Potential Materials for Carbon Dioxide Capture and Utilization. *Front. Mater.* **2019**, *6*. https://doi.org/10.3389/fmats.2019.00042.

(90) Klähn, M.; Seduraman, A. What Determines CO_2 Solubility in Ionic Liquids? A Molecular Simulation Study. *J. Phys. Chem. B* **2015**, *119* (31), 10066–10078. https://doi.org/10.1021/acs.jpcb.5b03674.

(91) Cadena, C.; Anthony, J. L.; Shah, J. K.; Morrow, T. I.; Brennecke, J. F.; Maginn, E. J. Why Is CO_2 So Soluble in Imidazolium-Based Ionic Liquids? *J. Am. Chem. Soc.* **2004**, *126* (16), 5300–5308. https://doi.org/10.1021/ja039615x.

(92) Luis, P.; Ortiz, I.; Aldaco, R.; Irabien, A. A Novel Group Contribution Method in the Development of a QSAR for Predicting the Toxicity (Vibrio Fischeri EC50) of Ionic Liquids. *Ecotoxicol. Environ. Saf.* **2007**, *67* (3), 423–429. https://doi.org/10.1016/j.ecoenv.2006.06.010.

(93) Bates, E. D.; Mayton, R. D.; Ntai, I.; Davis, J. H. CO_2 Capture by a Task-Specific Ionic Liquid. *J. Am. Chem. Soc.* **2002**, *124* (6), 926–927. https://doi.org/10.1021/ja017593d.

(94) Gurkan, B.; Goodrich, B. F.; Mindrup, E. M.; Ficke, L. E.; Massel, M.; Seo, S.; Senftle, T. P.; Wu, H.; Glaser, M. F.; Shah, J. K.; Maginn, E. J.; Brennecke, J. F.; Schneider, W. F. Molecular Design of High Capacity, Low Viscosity, Chemically Tunable Ionic Liquids for CO_2 Capture. *J. Phys. Chem. Lett.* **2010**, *1* (24), 3494–3499. https://doi.org/10.1021/jz101533k.

(95) Lee, Y.-Y.; Edgehouse, K.; Klemm, A.; Mao, H.; Pentzer, E.; Gurkan, B. Capsules of Reactive Ionic Liquids for Selective Capture of Carbon Dioxide at Low Concentrations. *ACS Appl. Mater. Interfaces* **2020**, *12* (16), 19184–19193. https://doi.org/10.1021/acsami.0c01622.

(96) Recker, E. A.; Green, M.; Soltani, M.; Paull, D. H.; McManus, G. J.; Davis, J. H.; Mirjafari, A. Direct Air Capture of CO_2 via Ionic Liquids Derived from "Waste" Amino Acids. *ACS Sustain. Chem. Eng.* **2022**, *10* (36), 11885–11890. https://doi.org/10.1021/acssuschemeng.2c02883.

(97) Lackner, K. S.; Brennan, S. Envisioning Carbon Capture and Storage: Expanded Possibilities Due to Air Capture, Leakage Insurance, and C-14 Monitoring. *Clim. Change* **2009**, *96* (3), 357–378. https://doi.org/10.1007/s10584-009-9632-0.

(98) Lackner, K.; Ziock, H.-J.; Grimes, P. Capturing Carbon Dioxide from Air. In *First International Sequestration Conference*; Alexandria, VA, 2001; pp 1–15.

(99) Yang, H.; Singh, M.; Schaefer, J. Humidity-Swing Mechanism for CO_2 Capture from Ambient Air. *Chem. Commun.* **2018**, *54* (39), 4915–4918. https://doi.org/10.1039/C8CC02109K.

(100) Shi, X.; Xiao, H.; Lackner, K. S.; Chen, X. Capture CO_2 from Ambient Air Using Nanoconfined Ion Hydration. *Angew. Chemie Int. Ed.* **2016**, *55* (12), 4026–4029. https://doi.org/10.1002/anie.201507846.

(101) Shi, X.; Xiao, H.; Kanamori, K.; Yonezu, A.; Lackner, K. S.; Chen, X. Moisture-Driven CO_2 Sorbents. *Joule* **2020**, *4* (8), 1823–1837. https://doi.org/10.1016/j.joule.2020.07.005.

(102) Wang, T.; Lackner, K. S.; Wright, A. Moisture Swing Sorbent for Carbon Dioxide Capture from Ambient Air. *Environ. Sci. Technol.* **2011**, *45* (15), 6670–6675. https://doi.org/10.1021/es201180v.

(103) Shokrollahzadeh Behbahani, H.; Mithaiwala, H.; Lopez Marques, H.; Wang, W.; Freeman, B. D.; Green, M. D. Quaternary Ammonium-Functionalized Poly(Arylene Ether Sulfone) Random Copolymers for Direct Air Capture. *Macromolecules* **2023**, *56* (16), 6470–6481. https://doi.org/10.1021/acs.macromol.3c00760.

(104) He, H.; Zhong, M.; Konkolewicz, D.; Yacatto, K.; Rappold, T.; Sugar, G.; David, N. E.; Gelb, J.; Kotwal, N.; Merkle, A.; Matyjaszewski, K. Three-Dimensionally Ordered Macroporous Polymeric Materials by Colloidal Crystal Templating for Reversible CO_2 Capture. *Adv. Funct. Mater.* **2013**, *23* (37), 4720–4728. https://doi.org/10.1002/adfm.201300401.

(105) Chintapalli, M.; Meckler, S.; Iftime, G.; Pandey, R.; Louie, M.; Shin Ming Beh, E. Tunable, Rapid Uptake, Aminopolymer Aerogel Sorbent for Direct Air Capture of Co2. US20210370226A1, 2021.

(106) Meckler, S. M.; Iftime, G.; Nallapaneni, A.; Van Overmeere, Q.; Keoshkerian, B.; Bulger, E.; Ho, A. S.; Zhu, C.; Rivest, J. B.; Chintapalli, M. Optically Transparent Polymer Aerogels Via Controlled Radical Polymerization. *ACS Appl. Polym. Mater.* **2022**, *4* (3), 1565–1569. https://doi.org/10.1021/acsapm.1c01854.

(107) Realff, M. J.; Min, Y. J.; Jones, C. W.; Lively, R. P. Perspective - the Need and Prospects for Negative Emission Technologies - Direct Air Capture through the Lens of Current Sorption Process Development. *Korean J. Chem. Eng.* **2021**, *38* (12), 2375–2380. https://doi.org/10.1007/s11814-021-0957-3.

(108) He, H.; Li, W.; Zhong, M.; Konkolewicz, D.; Wu, D.; Yaccato, K.; Rappold, T.; Sugar, G.; David, N. E.; Matyjaszewski, K. Reversible CO_2 Capture with Porous Polymers Using the Humidity Swing. *Energy Environ. Sci.* **2013**, *6* (2), 488–493. https://doi.org/10.1039/C2EE24139K.

(109) Wang, T.; Liu, J.; Fang, M.; Luo, Z. A Moisture Swing Sorbent for Direct Air Capture of Carbon Dioxide: Thermodynamic and Kinetic Analysis. *Energy Procedia* **2013**, *37*, 6096–6104. https://doi.org/10.1016/j.egypro.2013.06.538.

(110) Wang, T.; Ge, K.; Chen, K.; Hou, C.; Fang, M. Theoretical Studies on CO_2 Capture Behavior of Quaternary Ammonium-Based Polymeric Ionic Liquids. *Phys. Chem. Chem. Phys.* **2016**, *18* (18), 13084–13091. https://doi.org/10.1039/C5CP07229H.

(111) Song, J.; Liu, J.; Zhao, W.; Chen, Y.; Xiao, H.; Shi, X.; Liu, Y.; Chen, X. Quaternized Chitosan/PVA Aerogels for Reversible CO_2 Capture from Ambient Air. *Ind. Eng. Chem. Res.* **2018**, *57* (14), 4941–4948. https://doi.org/10.1021/acs.iecr.8b00064.

(112) Armstrong, M.; Shi, X.; Shan, B.; Lackner, K.; Mu, B. Rapid CO_2 Capture from Ambient Air by Sorbent-containing Porous Electrospun Fibers Made with the Solvothermal Polymer Additive Removal Technique. *AIChE J.* **2019**, *65* (1), 214–220. https://doi.org/10.1002/aic.16418.

(113) Parzuchowski, P. G.; Świderska, A.; Roguszewska, M.; Rolińska, K.; Wołosz, D. Moisture- and Temperature-Responsive Polyglycerol-Based Carbon Dioxide Sorbents—The Insight into the Absorption Mechanism for the Hydrophilic Polymer. *Energy & Fuels* **2020**, *34* (10), 12822–12832. https://doi.org/10.1021/acs.energyfuels.0c02174.

(114) Shi, X.; Xiao, H.; Azarabadi, H.; Song, J.; Wu, X.; Chen, X.; Lackner, K. S. Sorbents for the Direct Capture of CO_2 from Ambient Air. *Angew. Chemie Int. Ed.* **2020**, *59* (18), 6984–7006. https://doi.org/10.1002/anie.201906756.

(115) Rege, S. U.; T. Yang, R.; Buzanowski, M. A. Sorbents for Air Prepurification in Air Separation. *Chem. Eng. Sci.* **2000**, *55* (21), 4827–4838. https://doi.org/10.1016/S0009-2509(00)00122-6.

(116) Wurzbacher, J. A.; Gebald, C.; Piatkowski, N.; Steinfeld, A. Concurrent Separation of CO_2 and H_2O from Air by a Temperature-Vacuum Swing Adsorption/Desorption Cycle. *Environ. Sci. Technol.* **2012**, *46* (16), 9191–9198. https://doi.org/10.1021/es301953k.

(117) Wilcox, J. An Electro-Swing Approach. *Nat. Energy* **2020**, *5* (2), 121–122. https://doi.org/10.1038/s41560-020-0554-4.

(118) Rinberg, A.; Bergman, A. M.; Schrag, D. P.; Aziz, M. J. Alkalinity Concentration Swing for Direct Air Capture of Carbon Dioxide. *ChemSusChem* **2021**, *14* (20), 4439–4453. https://doi.org/10.1002/cssc.202100786.

(119) Lyndon, R.; Konstas, K.; Ladewig, B. P.; Southon, P. D.; Kepert, P. C. J.; Hill, M. R. Dynamic Photo-Switching in Metal-Organic Frameworks as a Route to Low-Energy Carbon Dioxide Capture and Release. *Angew. Chemie Int. Ed.* **2013**, *52* (13), 3695–3698. https://doi.org/10.1002/anie.201206359.

(120) Muroyama, A. P.; Beard, A.; Pribyl-Kranewitter, B.; Gubler, L. Separation of CO_2 from Dilute Gas Streams Using a Membrane Electrochemical Cell . *ACS ES&T Eng.* **2021**, *1* (5), 905–916. https://doi.org/10.1021/acsestengg.1c00048.

(121) Prajapati, A.; Sartape, R.; Rojas, T.; Dandu, N. K.; Dhakal, P.; Thorat, A. S.; Xie, J.; Bessa, I.; Galante, M. T.; Andrade, M. H. S.; Somich, R. T.; Rebouças, M. V.; Hutras, G. T.; Diniz, N.; Ngo, A. T.; Shah, J.; Singh, M. R. Migration-Assisted, Moisture Gradient Process for Ultrafast, Continuous CO_2 Capture from Dilute Sources at Ambient Conditions. *Energy Environ. Sci.* **2022**, *15* (2), 680–692. https://doi.org/10.1039/D1EE03018C.

(122) Castel, C.; Bounaceur, R.; Favre, E. Membrane Processes for Direct Carbon Dioxide Capture From Air: Possibilities and Limitations. *Front. Chem. Eng.* **2021**, *3* (April), 1–15. https://doi.org/10.3389/fceng.2021.668867.

3 CHAPTER 3: POLYSULFONES FOR DIRECT AIR CAPTURE

.

This chapter begins with a comprehensive overview of polysulfones, emphasizing their distinctive features and the step-growth polymerization process used in their synthesis. It then investigates a novel series of polysulfone-based polymers developed for Direct Air Capture (DAC) by the moisture swing sorption (MSS) process. This polymer is a quaternary ammonium functionalized poly(arylene ether sulfone) random copolymer (PAES-co-QAPAES). This chapter details the synthesis and characterization techniques used to analyze these materials, as well as their atmospheric CO_2 capture and release performance with varying humidity levels for MSS DAC analysis.

3.1 Poly(Arylene ether)s (PAE)

Polyphenylenes are polymers consisting of unsubstituted aromatic rings connected with carbon-carbon single bonds (**Scheme 3.1.a**). Polyphenylene has excellent thermal and chemical stability and outstanding mechanical properties. However, pure polyphenylene polymers are not easily processible. Consequently, various functional groups are inserted into the polyphenylene polymer backbone to disturb chain regularity and enhance chain mobility, flexibility and processibility. Poly(arylene ether)s (PAE) are classified as polyphenylene polymers with additional oxygen, carbonyl, or sulfonyl groups inserted in the backbone. (**Scheme 3.1.b**). PAE's are also high-performance thermoplastics, which exhibit high thermal and oxidative stability and are processible. Some classes of PAE's are shown in **Table 3.1**.

(a)

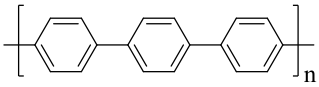

Polyphenylene

(b)

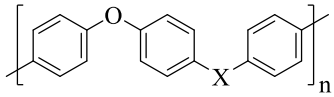

X = O, CO, SO_2, ...

Poly(arylene ether)

(c)

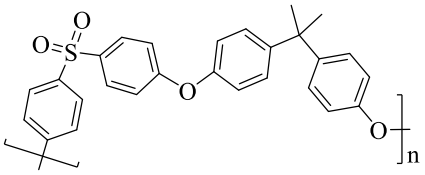

Poly(arylene ether sulfone)

Scheme 3.1 Repeat unit structure of polyphenylene, poly(arylene ether) and poly(arylene ether sulfone).

Table 3.1 Various popular poly(arylene ether)s

X*	Polymer
$-O-$	Poly(arylene ether)
$-CO-$	Poly(arylene ether ketone)
$-SO_2-$	Poly(arylene ether sulfone), poly(ether sulfone) or polysulfone

*X are compounds in Scheme 3.1.b

3.2 Poly(Arylene ether sulfone)s (PAES)

Poly(arylene ether) sulfones (PAES) were independently introduced in the 1960's by three institutions of Union Carbide Corporation (trade name Udel®) and 3M Corporation in the US and the Imperial Chemical Industries (ICI) in the UK. As shown in **Scheme 3.1.c**, they are a family of organic chemical compounds in which the backbone consists of unsubstituted aromatics (polyphenylenes) linked together with sulfonyl ($-SO_2-$) and ether ($-O-$) functional groups. As the result of the combination of these structural units, these polymers exhibit high thermal, chemical, hydrolytic, and oxidative stability, strength, transparency, processibility and, flame retardancy. PAES exhibits T_g in the range of 150 -

230 °C. PAES are polymers that do not crystallize as the result of the angled structure of polysulfone, thus have an amorphous morphology. Commercial PAES contains isopropylidene groups for additional chain flexibility.

PAES is used in a variety of applications including components within households (like microwaves, cookware, and electronics), office equipment (such as photocopy machines, battery cases, and cameras), as well as in aircraft and aerospace gadgets (**Figure 3.1**).

In the medical field, PAES is favored for fabricating equipment and devices that must endure sterilization processes (such as dry heat, autoclaving, chemical treatment, and radiation) without deteriorating. Furthermore, PAES is extensively utilized in the membrane industry for fabricating membranes aimed at water treatment and gas separation. This widespread use is attributed not only to PAES's excellent mechanical, hydrolytic, and thermal stability but also to its processability. This characteristic facilitates the production of membranes with precisely controllable and reproducible pore sizes. The synthesis of PAES typically involves a nucleophilic aromatic substitution step growth reaction (SGR) or polycondensation reaction, engaging an aromatic dihalide and a bisphenolate salt, a process that will be explored in further detail in subsequent sections.

Figure 3.1 Examples of PAES applications.

3.3 Step Growth Polymerization of poly(arylene ether sulfone)s

Step growth polymerization reaction (SGR) is a commonly used synthesis route to produce polyesters, polyamides (nylon), polycarbonates, polyurethanes and polyethers. SGR occurs when bi- or multi- functional monomers react and create dimers, trimers, oligomers, and large polymer chains. A bi-functional monomer is a monomer compound with two reactive sites per molecule. In SGR, Bi-functional monomers can create linear, and multi-functional monomers create branched polymers.

3.3.1 Condensation polymerization and Addition polymerization

Condensation polymerization and addition polymerization are two distinct terms that can be used in place of SGR. If the SGR results in the production of small molecules such as water, alcohol, or an acid molecule (shown as X in **Table 3.2**), it can be referred to as condensation polymerization. If no small molecules are produced, it is referred to as addition polymerization. This distinction was initially introduced by Wallace Carothers in 1929.[1]

Table 3.2 Condensation polymerization and addition polymerization

	$nA + nB \rightarrow (A-B)_n$
Condensation polymerization	$nA + nB \rightarrow (A-B)_n$ + X

Addition polymerization	$nA + nB \rightarrow (A - B)_n$

3.3.2 Step growth polymerization theory.

A simplified 2D array mechanism of step growth polymerization is shown in **Figure 3.2** with two bi-functional monomers shown in black (A) and pink (B). The reaction proceeds from left to right, in a stepwise manner with a slow increase in molecular weight. Dimers and trimers are initially formed and continue to react with themselves and other chains with time and produce tetramers, octamers, and eventually a single macromolecule. Since in SGR, nearly all monomers are consumed in the early stages, kinetic studies have been carried out on the change of reactive functional group concentration with time, and not the monomer concentration. For simplicity, "equal reactivity of functional groups" is assumed. This consideration regulates that the reactivity of functional groups on both A and B bi-functional monomers are identical. In addition, the reactivity of all functional groups on A and B remain identical, regardless of whether any side has reacted or is attached to any-sized chain.*

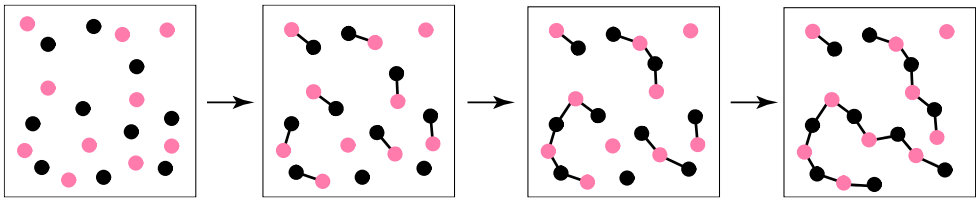

Figure 3.2 Step growth polymerization mechanism in 2D array of bi-functional monomers.

The polymer product's average molecular weight is of prime concern from a practical viewpoint, and high average molecular weights are required to obtain desirable thermal

*Functional groups attached to larger chains exhibit lower diffusion rates, but reactivity depends on the collision frequency and not the diffusion of the molecule.

and mechanical properties. The degree of polymerization, D_p, is defined as the number of monomer segments inside polymer chain and is calculated as the ratio of polymer average molecular weight ($\overline{Mw_p}$) to the molecular weight of the repeating unit (Mw_{ru}) as seen in **Equation 3.1**.

$$D_p = \frac{\overline{Mw_p}}{Mw_{ru}} \qquad \textbf{Eq. 3.1}$$

Carother's equation, named after Wallace Carother, the inventor of nylon, estimates the degree of polymerization with a given fractional monomer conversion or yield, p for SGR. For a bi-functional monomer, the number average degree of polymerization can be calculated with the **Equation 3.2**.

$$D_p = \frac{1}{1-p} \qquad \textbf{Eq. 3.2}$$

Fractional monomer conversion is defined as **Equation 3.3**.

$$p = \frac{N_0 - N}{N_0} \qquad \textbf{Eq. 3.3}$$

Where N_0 is the number of monomers present initially, and N is the number of unreacted monomers at time t. As can be seen from the above equation, high conversion is required to achieve high degree of polymerization and high molecular weight in SGR. As an example, 90% conversion gives a D_p of 10, 99% gives D_p of 100 and 99.9% gives a D_p of 1000. For this reason, to achieve high molecular weights in SGR, it is necessary that we have:

1. High reaction conversions: conversion of >99.9% based on Carothers's theory.
2. 1:1 stoichiometry for functional groups: any imbalance would terminate SGR.
3. Bi-functionality (f = 2): lower functionality would terminate SGR, and higher functionality would result in branching.

4. No side reactions: Side reactions will result in monomer loss and imbalance in 1:1 stoichiometry.
5. High monomer purity: impurities may disrupt 1:1 stoichiometry or cause side reactions.
6. Accessibility of mutual reactive sites.

3.3.3 Nucleophilic Aromatic Substitution (SnAr) of PAES

As noted above, PAES is synthesized through nucleophilic aromatic substitution (S_nAr) reaction between a bisphenolate salt (phenoxide) and an aromatic dihalide. The phenoxide is produced through phenol deprotonation with a suitable base. The polymerization is then initiated by the formation of the Meisenheimer complex. The arrow moving mechanism for the SnAr reaction to produce polysulfone is explained in detail.

3.3.4 Phenol deprotonation

Addition of an alkali metal carbonate or hydroxide (basic salt) to bisphenol A (BPA) results in the deprotonation (removing of most acidic protons) of BPA. As shown in **Scheme 3.2**, BPA is the proton donor, and therefore an acid in the Brønsted–Lowry principle and is deprotonated by a base. According to the principle, an acid-base reaction occurs when the product is a weaker acid and a base. The acid strength can be determined with the pKa value. The pKa of BPA is 9.6, and the conjugate base of any compound with higher pKa value may deprotonate BPA.[2] As an example, pKa value of HCO_3^- is 10.25, and its conjugate base (K_2CO_3) may be used.[3] The produced phenolate is a good nucleophile (electron giving) group that will react with an aromatic dihalide to form the polysulfone polymer.

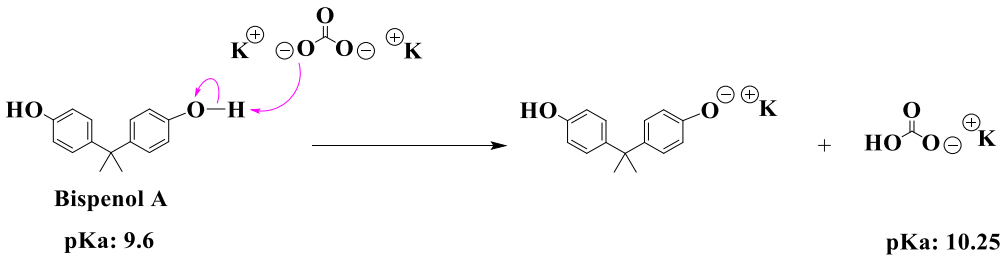

Scheme 3.2 Deprotonation of Bisphenol A (BPA)

3.3.5 The Meisenheimer Complex

The Meisenheimer complex, discovered in 1902 by J. Meisenheimer, is a negatively charged intermediate compound formed during the nucleophilic aromatic substitution reaction.[4] They are formed when a nucleophile (electron rich compound) attacks an aromatic ring carbon that has electron withdrawing groups and a leaving group in ortho or para positions to each other. In the case of reaction between the BPA and DFPDS, sulfone electron withdrawing groups in para position give rise to the S_nAr reaction. The resonance stability of the Meisenheimer complex depends on the reaction solvent and the nature of the nucleophile and leaving group.[5]

3.3.6 S_nAr Mechanism

The nucleophilic aromatic substitution is composed of steps as depicted in **Scheme 3.3**. Step a and b show the mechanism of the attack of the nucleophile (phenoxide) to the halide substituted carbon on Bis(4-fluorophenyl) sulfone (DFDPS). The resonance stabilized carbanions or the Meisenheimer complex is then formed, shown as steps b-e in **Scheme 3.3**. In the final step, the halide (F) is eliminated by the re-aromatization of the phenyl ring. The rate determining step in S_nAr reactions is the attack of the nucleophile to the aromatic ring (formation of the Meisenheimer complex).

These reactions are performed in polar aprotic solvents such as dimethyl sulfoxide (DMSO) or N-Methyl-2-pyrrolidone (NMP) to further increase the nucleophilicity of phenoxides. A dry reaction environment is required for the described mechanism, as water may hydrolyze the alkali metal phenolates and form basic solutions. Potassium hydroxide formed in aqueous environments may react with the aromatic di-halide and alter the stoichiometry of functional groups present in the reaction which prevents achieving high molecular weight polymers. The reactions should be carried out in an inert atmosphere, as oxygen may oxidize the bisphenolate compound and result in stoichiometric imbalance.[6]

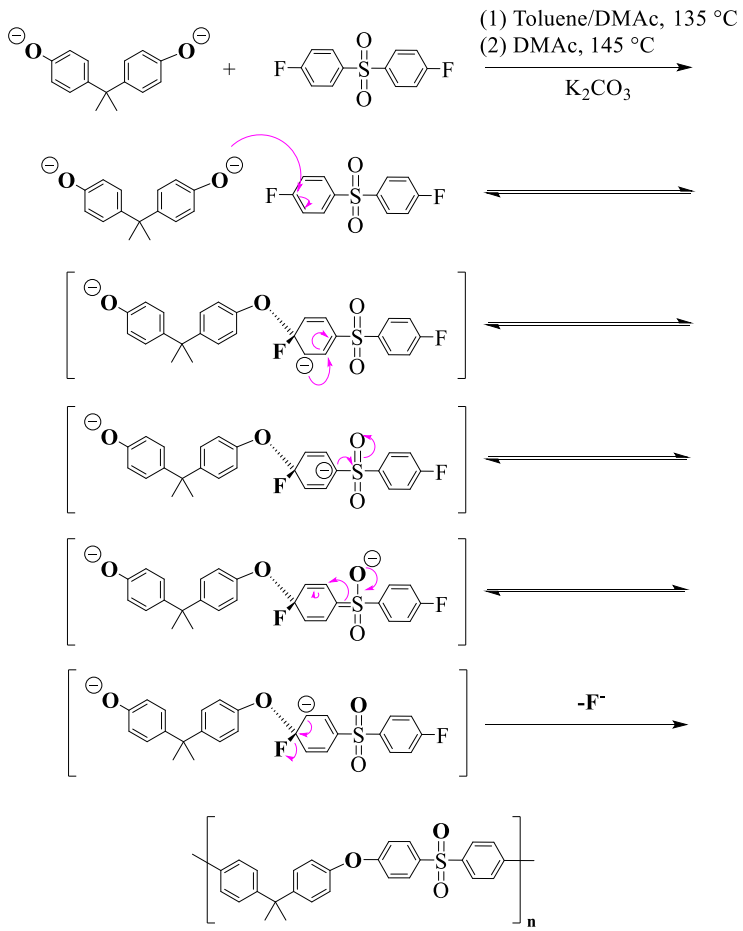

Scheme 3.3 Nucleophilic aromatic substitution reaction between Bisphenol A (BPA) and Bis(4-fluorophenyl) sulfone (DFDPS) to make poly(arylene ether sulfone)

3.4 Quaternary Ammonium Functionalized Poly(Arylene Ether Sulfone) Random Copolymers For Direct Air Capture

A series of novel quaternary ammonium (QA) functionalized poly(arylene ether sulfone) random copolymer (PAES-co-QAPAES) is prepared for DAC. The polymer backbone is constructed via an SGR reaction and is modified by two consecutive steps of thiol-ene "click" reaction and Menshutkin reaction. Allyl-modified poly(arylene ether sulfone) (PAES-co-APAES) is utilized to leverage the excellent mechanical strength, high thermal and chemical stability, and processibility of polysulfones.[7] The quaternary ammonium cation ($-NR_3^+$) attached to the polymer backbone is initially balanced by bicarbonate ions to undergo DAC via the MSS process. Polymers with varying ion exchange capacities (IEC) are synthesized, characterized, and tested for MSS performance. Kinetic modeling studies evaluate the potential of this novel material to be used as a sorbent and, in future studies, be a processible standalone membrane, for continuous DAC.

3.4.1 Experimental

3.4.1.1 Materials and reagents

Bisphenol A (BPA, ≥99%) was purchased from Sigma-Aldrich and recrystallized from acetic acid/water (1:1 v/v) before use. Bis(4-fluorophenyl) sulfone (DFDPS, 99%) was purchased from VWR and recrystallized from toluene before use. 2,2'-Diallylbisphenol A

(DABA, 85%) was purchased from Sigma-Aldrich and purified by liquid-liquid extraction.[8] Potassium carbonate (K_2CO_3, ≥99%) was purchased from Sigma-Aldrich and kept inside an oven operating at 130 °C before use. Toluene (99.8%) and THF Optima™ were purchased from Fisher Scientific and used after passing through an MBraun SPS-800 solvent purification system. N,N-Dimethylacetamide (DMAc, 99.5%), deuterated dimethyl sulfoxide, (DMSO-d6, 99.9 atom% D, 0.03% (v/v) TMS), diatomaceous earth (Celite® 545) and 2,2-dimethoxy-2-phenylaceto-phenone (DMPA, 99%) were purchased from Sigma-Aldrich and used as received. 2-(Dimethylamino)-ethanethiol hydrochloride (95%) and deuterated chloroform ($CDCl_3$, 99.8 atom% D, 0.03% (v/v) TMS) were purchased from Acros Organics and used as received. N,N-Dimethylformamide (DMF, ≥99.8%) was purchased from BDH® VWR and used as received. Hydrochloric acid (HCl, 36.5–38%) was purchased from BDH® VWR and diluted with THF before use. Iodomethane (≥99.5%) was purchased from Beantown Chemical and used as received. Narrowly distributed (Đ ~1) 200 kDa and 30 kDa polystyrene (PS) standards were purchased from Pressure Chemical Company, and 482 kDa, 91,450 Da, 9,820 Da and 4,910 Da PS standards were purchased from Agilent technologies and used as received. Udel® P-1700 NT 11 polysulfone (PSU) pellets were purchased from Solvay specialty polymers and used as received.

3.4.1.2 Synthesis

The production of QA-functionalized poly(arylene ether sulfone) sorbent with basic counterions is a 4-step process (**Scheme 3.4**). The first step is a step growth reaction to form the allyl-modified poly(arylene ether sulfone) (PAES-co-APAES) copolymer, the

second step is a post-polymerization modification reaction to create the tertiary amine-modified PAES (PAES-co-TAPAES) copolymer, the third step is quaternization of the amine to form the QA-modified ((PAES)-co-[QAPAES][I]) copolymer, and the fourth step is counterion exchange ((PAES)-co-[QAPAES][HCO_3^-]).

PAES-co-APAES(25) was synthesized via the following established step growth reaction.[9–11] DABA (2.0 g, 6.5 mmol), BPA (4.4 g, 19.5 mmol), DFDPS (6.6 g, 25.9 mmol) and K_2CO_3 (4.3 g, 31.1 mmol) were weighed and added to a two-neck 250 mL round-bottom flask along with a magnetic stir bar. The flask was equipped with a Dean-Stark apparatus, a reflux condenser, and a nitrogen inlet/outlet and the complete apparatus was lowered into an oil bath equipped with a thermometer. Different BPA/DABA ratios were used to manipulate the charge content on the polymer backbone, and the molar ratio for other components were kept constant (e.g., DABA/BPA ratio of 3/1, 1/1 and 1/3 refer to 75%, 50% and 25% mol functionalized polymer, respectively). 52 mL DMAc was added to dissolve the monomers, and 26 mL toluene was added as an azeotropic agent to remove water during the polycondensation reaction. The solution was purged with nitrogen for 15 min, then refluxed at 135 °C for 2 h to dehydrate the reaction mixture through the water-toluene azeotrope. The mixture was then heated to 145 °C to remove the residual toluene, and the reaction was continued under static nitrogen atmosphere at 145 °C for 6 h. The reaction mixture was then cooled to room temperature and diluted with THF. The mixture was stirred with dilute HCl in THF for 2 h for neutralization to occur and pulled through diatomaceous earth to filter inorganic salts with a Büchner funnel. The polymer was then isolated through precipitation by addition, while stirring, of a 50/50 vol.% solution of DI

water and methanol. The polymer was dried under vacuum at 60 °C, redissolved in THF and precipitated once again in DI water. The product, PAES-co-APAES(25), was dried under vacuum at 60 °C overnight.

The second step, which involves the incorporation of the tertiary amine functional groups via the thiol-ene "click" reaction, consisted of dissolving PAES-co-APAES(25) copolymer (11.0 g, 10.7 mmol ene), 2-(dimethylamino)-ethanethiol (7.6 g, 5 equiv. to ene) and DMPA (0.8 g, 0.3 equiv. to ene) in 70 mL DMF.[12,13] The mixture was poured into a 100 mL round-bottom flask, purged with nitrogen for 15 min, and irradiated with a compact UV lamp (Analytik Jena US UVL-28 EL series at 365 nm) at room temperature for 2 h. The product (PAES-co-TAPAES(25)) was isolated by precipitation in DI water and was then dried under vacuum at 60 °C, redissolved in DMF, reprecipitated in DI water, and dried under vacuum at 60 °C overnight.

In the third step, tertiary amine groups were converted to quaternary ammoniums via the established Menshutkin reaction.[14] To a solution of PAES-co-TAPAES(25) (10.5 g, 10.1 mmol tertiary amine) in 70 mL DMF, iodomethane (7.2 g, 5 equiv. to tertiary amine) was added. The reaction mixture was stirred at room temperature and the product (PAES-co-QAPAES(25)[I]) was isolated via precipitation in stirring DI water and then dried under vacuum at 60 °C overnight. The polymers were redissolved in DMF and reprecipitated in DI water. To substitute the iodide counterions with bicarbonate counterions, as the fourth step, PAES-co-QAPAES(25)[I] was placed inside a stirring solution of 1 M $KHCO_3$ in DI water at room temperature for 48 h, and then washed 3 times with DI water.

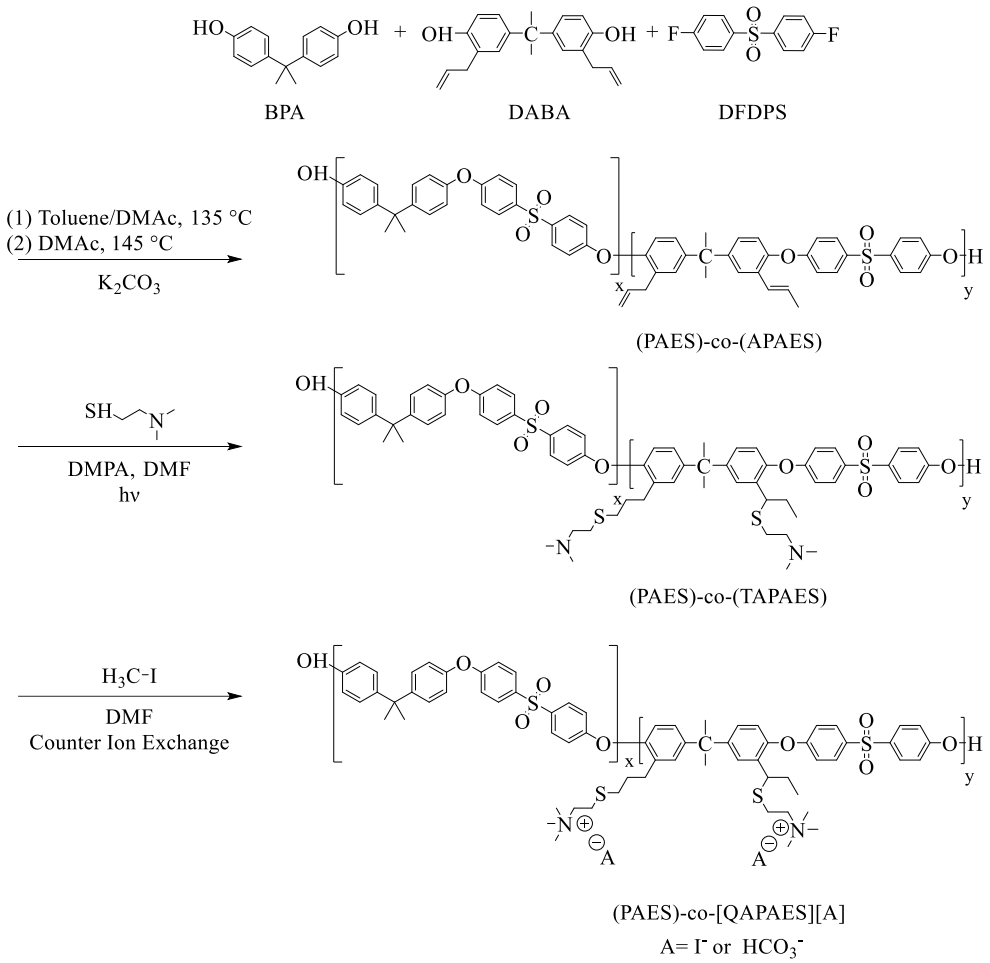

Scheme 3.4 Reaction pathway for production of PAES-co-QAPAES[HCO_3^-]

3.4.1.3 Copolymer structure

To confirm the polymer structure, ^{1}H NMR spectra were recorded on Bruker Ascend 500 MHz spectrometer. For this characterization, 20 mg of dried polymer was dissolved in 0.7 g of deuterated solvent. $CDCl_3$ was used as solvent for Udel® P-1700 PSU and PAES-co-APAES, and DMSO-d_6 for PAES-co-TAPAES and PAES-co-QAPAES.

3.4.1.4 Polymer molecular weight

Size exclusion chromatography (SEC) was carried out using a Waters Alliance e2695 HPLC system interfaced to a Wyatt miniDAWN TREOS light scattering detector and a

Wyatt Optilab T-rEX differential refractive index (dRI) detector connected to Astra v6.1 software to determine the molecular weight of the polymers. The mobile phase was THF Optima^{TM} with a flow rate of 1.0 mL/min. The molecular weights of synthesized polymers were measured from a calibration curve obtained from 6 low dispersity PS. The testing solutions were prepared by dissolving polymers in THF to a concentration of 5 mg/mL and passing through a 0.45 µm filter. The cyclic oligomer content in SEC traces was measured from the ratio of area under curve of cyclic shoulder vs. the total area in the elution trace.

3.4.1.5 Thermogravimetric analysis (TGA)

The decomposition temperature of the synthesized polymers was investigated to evaluate the thermal stability using TA Instruments TGA 5500. ~20 mg of sample was inserted into a platinum HT pan and heated up to 120 °C under nitrogen, at a rate of 10 °C/min to evaporate any water or solvents that may be present. Then, the sample was cooled to room temperature followed by thermal scanning up to 750 °C with the same rate under inert N_2 atmosphere. The TGA thermogram and the first derivative curves are plotted. The temperature at which 5% weight loss ($T_{d5\%}$) was observed is reported as thermal stability.

3.4.1.6 Differential scanning calorimetry (DSC)

To determine the glass transition temperatures (T_g) of the polymers, a TA Instruments Q2000 calorimeter was used. The polymer samples were heated under N_2 at a rate of 10 °C/min to 190 °C, held isothermally for 10 min, cooled to -80 °C, held isothermally for 10 min, and finally heated again at a rate of 10 °C/min to 200 °C. The polymer samples were loaded into a non-hermetically sealed aluminum pan, and the T_g of the polymers were

determined from the midpoint T_g function in the TA instruments Universal Analysis 2000 software (Version 4.5A) from the second heating scan.

3.4.1.7 Water vapor gravimetric sorption

A McBain quartz spring balance was used to perform the water vapor gravimetric sorption measurements.[15,16] The polymer sample was placed in a small aluminum foil pouch which is suspended from a sensitive quartz spring (Deerslayer Quartz Springs) inside a water-jacketed glass chamber at 25 °C. DI water contained in a glass reservoir was used to generate water vapor. Before the measurements, the DI water in the reservoir was degassed under full vacuum (<0.01 Torr) to remove dissolved gasses from the water. Water partial pressure was monitored using an MKS Baratron 626B transducer (full scale = 100 Torr). Prior to each test, the sample was degassed under full vacuum until no further displacement of the spring is observed. Then, sorption experiments were performed by exposing the sample to water vapor at 100% RH. The spring position was monitored using a digital camera, and the images were processed using ImageJ software.[17,18] Blank experiments were performed to determine the amount of water adsorbed by the aluminum foil pouch. This amount is subtracted from the water uptake in all sorption experiments.

3.4.1.8 Polymer density, molar volume, and fractional free volume

The true density of the polymers was measured in the powder form. The polymers were initially dried in a vacuum oven at 50 °C for 24 h. The weight of the sample was measured using an Accuris Instruments W3100-120 analytical balance. The volume of the samples was measured as the average of 10 volume displacements using a Micromeritics AccuPyc II 1340 Gas Pycnometer operating with helium gas.

The polymer molar volume, v (mL/mol), was calculated by dividing the molar mass of polymer repeat unit, Mw_{ru} (g/mol) by the true density, ρ (g/mL) as shown below:

$$v = \frac{Mw_{ru}}{\rho} \quad \textbf{(Eq. 3.4)}$$

The fractional free volume of polymers, f, was calculated using **Equation 3.5**, where v is the molar volume, and v_0 is the volume occupied per one mole of repeat unit at 0 K (zero-point molar volume).[19] An approximation for the zero point molar volume is reported by Bondi to be 1.3 times the van der Waals volume (v_{VDW}).[20] The v_{VDW} per one mole of polymer repeat unit can be calculated by the sum of v_{VDW} of composing structural groups, and the v_{VDW} of each structural group was derived from literature.[21]

$$f = \frac{v - v_0}{v} \quad \textbf{(Eq. 3.5)}$$

The v_{VDW} of Udel® P-1700, PAES-co-QAPAES[HCO_3^-](25), PAES-co-QAPAES[HCO_3^-](50) and PAES-co-QAPAES[HCO_3^-](75) is calculated to be 234.2, 1042.6, 574.2 and 1254.3 mL/mol, respectively.

3.4.1.9 Membrane preparation

Dense membranes were fabricated to investigate the hydrophilicity change of the (PAES)-co-[QAPAES][HCO_3^-] polymers via water contact angle measurements. All polymers were dried inside a vacuum oven operating at 100 °C for 24 h. The dried polymers were dissolved in DMF achieving a concentration of 2.5 wt.%, and the homogeneous solution was passed through a 0.45 μm syringe filter and poured inside a VWR® petri dish. The dish was covered with a non-hermetically sealed lid and placed under atmospheric conditions for 24 h. Gradual DMF removal was carried out by leaving the solution inside

a vacuum oven (Fisherbrand™ Isotemp™ Model 281A) operating at room temperature, 40 °C and 100 °C, each for 24 h. The dried dense membrane was removed from the petri dish by addition of DI water to the petri dish and peeling off the membrane once it had swelled.

In the protocol to fabricate dense membranes, a high boiling point solvent was used (DMF T_b = 153 °C). The boiling point controls the evaporation rate and volatility of the solvent and affects the membrane morphology. The higher the boiling point, the slower the removal of the solvent, which gives the polymer more time to relax and obtain a dense structure. The solution concentration used, 2.5 wt.%, helps generate a denser membrane. This is because by having a viscous polymer solution, the solvent evaporation process is hindered by the polymer chains and can result in micro-voids inside the membrane structure. The drying time of the membrane was spread throughout 3 days (22 °C, 40 °C and 100 °C). Slower drying time results in slower solvent removal to give the polymer more time to relax and can result in a denser structure.

3.4.1.10 Water contact angle (WCA)

Water contact angle measurements were carried out at room temperature using a Ramé-Hart automated goniometer (model 230-U1) equipped with a microscope and illumination system. The images were analyzed with DROPimage advanced® (version 2.7.03) software to investigate the hydrophilicity change of the (PAES)-co-[QAPAES][HCO_3^-] polymers. Membranes were adhered on glass slides with double-sided Scotch™ tape. A ~5 µL DI water droplet was deposited on the membrane using a Hamilton model 1750 Luer Tip threaded plunger syringe. The data reported is the average value taken

from at least 6 different locations on the respective membrane. Photos of the droplets were captured immediately after their initial placement on the membrane surface.

3.4.1.11 CO_2 sorption/desorption experimental setup

An experimental setup, as shown in **Figure 3.3,** was utilized to investigate the performance of synthesized polymers for MSS. The materials were dried, weighed and directly placed inside a sample chamber. The sample chamber consists of a cylindrical acrylic vessel, capped with PTFE (polytetrafluoroethylene) side locks. The air from the sample chamber (initially atmospheric air, containing ~415 ppm CO_2) is channeled through a Li-Cor model Li-840A infrared gas analyzer (IRGA) which measures the CO_2 and H_2O (humidity) concentration in real time in parts per million (ppm) and parts per thousand (ppt), respectively. The H_2O concentration in the closed system (system volume of 145 mL) is adjusted by cycling the air through a humidity controller. The humidity controller consists of a 1 mL water bath, copper tubing, and a Peltier element. To maintain the desired humidity level, the system adjusts the temperature of the water bath through a feedback loop: it continuously compares the actual humidity level in the IRGA with the target humidity level, and accordingly regulates the electrical current supplied to the Peltier element. Blank tests were performed to confirm competitive sorption of CO_2 and H_2O onto the sample chamber and tubing does not influence the results. For our experiments, gas flow rate is set to 1 L/min, and we fluctuated the humidity between 8 ppt, equivalent to 30% relative humidity (RH) at 22 °C, and 25 ppt, which corresponds to 95% relative humidity at the same temperature of 22 °C for moisture-swing DAC.

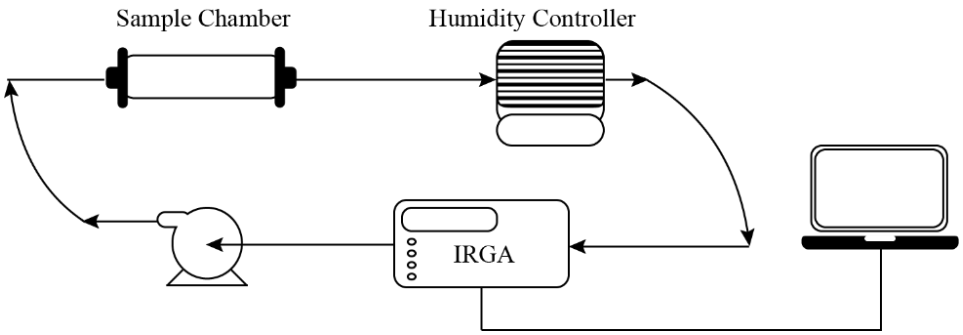

Figure 3.3 Experimental setup for moisture swing sorption analysis[22]

The IRGA reports the mole fraction of gases, which results in a systematic error in reading CO_2 levels when the humidity inside the chamber changes. For this reason, **Equation 3.6** is used to correct the error on the raw data received from the IRGA.

$$x = x_0 \times \left(1 + \frac{y}{1000} \times \frac{1}{1-\frac{y}{1000}}\right) \quad \textbf{(Eq. 3.6)}$$

In the equation above, x and x_0 are the corrected and raw CO_2 data in ppm, and y is the humidity reading in ppt.

Equation 3.7 is used to convert ppm values to µmol/g.

$$CO_2 \text{ sorbed} \frac{\text{mol } CO_2}{10^6 \text{ mol air}} \times \frac{1 \text{ mol air}}{22400 \text{ ml air}} \times 145 \text{ ml cell volume} \times \frac{1}{\text{weight of sorbent (g)}} =$$
$$\text{IEC } \frac{10^{-6} \text{ mol}}{\text{g}} = \text{ µmo l/g} \quad \textbf{(Eq. 3.7)}$$

3.4.1.12 Sorption kinetics

For the synthesized polymers, sorption kinetics were investigated through fitting experimental sorption data with kinetic models. The linear form of adsorption isotherm models evaluated are shown in **Table 3.3**. PFO[23] and PSO[24] models are the two main models used to described kinetics in the gas sorption processes.

Table 3.3 Kinetic models investigated.

Kinetic model	Integrated/Linear equation
Pseudo First Order (PFO)[23]	$q_t = q_e(1 - \exp(-k_f t))$
Pseudo Second Order (PSO)[24]	$q_t = \frac{k_s q_e^2 t}{1 + k_s q_e t}$

In **Table 3.3**, q_e is the equilibrium sorption capacity (μmol/g), q_t is the amount of sorbed CO_2 at time t (μmol/g), k_f and k_s are the PFO and PSO rate constants (1/h), respectively.

3.4.2 Results and Discussion

3.4.2.1 Synthesis of random QA-functionalized poly(arylene ether sulfone) copolymers

The ultimate objective in the synthesis of these QA-functionalized PAES copolymers is to maximize the ammonium content while maintaining good thermomechanical stability. The PAES copolymers are prepared using the multi-step synthetic protocol shown in **Scheme 3.4**. First, the copolymer is prepared using step-growth polymerization. The addition of allyl pendant groups on the polysulfone backbone enables post-polymerization functionalization to introduce chemical moieties and deliver new functionality to the traditional polysulfone polymer. The allyl concentration is tuned by controlling the DABA and BPA monomer ratio in the feed when performing step-growth polymerization (i.e., PAES-co-APAES(25) indicates a DABA/BPA ratio of 1/3 or 0.25 mol of DABA with respect to 1 mol of the repeat unit). Allyl functionalities (PAES-co-APAES) are then converted to tertiary amines (PAES-co-TAPAES) through the thiol-ene "click" reaction and quaternized to create QA-functionalized polysulfone polymers (PAES-co-QAPAES) using the Menshutkin reaction. **Scheme 3.4** shows the ^{1}H NMR spectra of Udel® P-1700 PSU (an unfunctionalized control) and our synthesized polymers. Allyl functionalities are

successfully incorporated on the backbone, as seen by the appearance of peaks at 3.24, 6.21, and 4.94 ppm belonging to protons on the non-isomerized allyl group (h, g and f, respectively) and peaks at 6.47, 5.81, and 1.78 ppm corresponding to protons on the isomerized allyl group (i, j and k, respectively). These values agree with a spectrum from literature with the same polymer backbone.[25] The ratio between the integral of peaks f-k and peak a is used to assess the percentage of functionalization. Upon analysis, the theoretical percentage of functionalization agrees with the actual amount within ±2% accuracy for all allyl modified poly(arylene ether sulfones) (i.e., PAES-co-APAES(25), PAES-co-APAES(50), PAES-co-APAES(75)) (**Figure 3.4**). The ratio between the integrals of peaks i-k to f-k is used to calculate the extent of isomerization of the allyl functionality, with 30%-60% isomerization observed for all polymers. Nonetheless, the ^{1}H NMR spectrum of tertiary amine-modified polysulfone confirms that isomerization of the allyl group does not interfere with the extent of post-polymerization functionalization. Peaks corresponding to allyl sites completely disappear after the thiol-ene "click" reaction, and new peaks are observed at 1.15 ppm, and 2.68 - 3.91 ppm which correspond to k' and l, m, n, h', i' and j' functionalities in **Figure 3.5**. The ratio of integrals of peaks n and k' with respect to peak a validates complete conversion of the allyl group to thiol-ether with the thiol-ene "click" reaction. The molar concentration – ratio of integrals – of peaks n and k' with respect to peak a – is used to confirm that the amine concentration matches the allyl concentration noted above. Upon quaternarization of tertiary amines with methyl iodide (PAES-co-QAPAES in **Figure 3.5**), the peak at 2.68 ppm shifts to 2.75 ppm, indicating the successful conversion to quaternary ammonium. The ratio of integrals of peaks n' and

k’ with respect to signal a confirms full conversion and is used to calculate the experimental IEC.

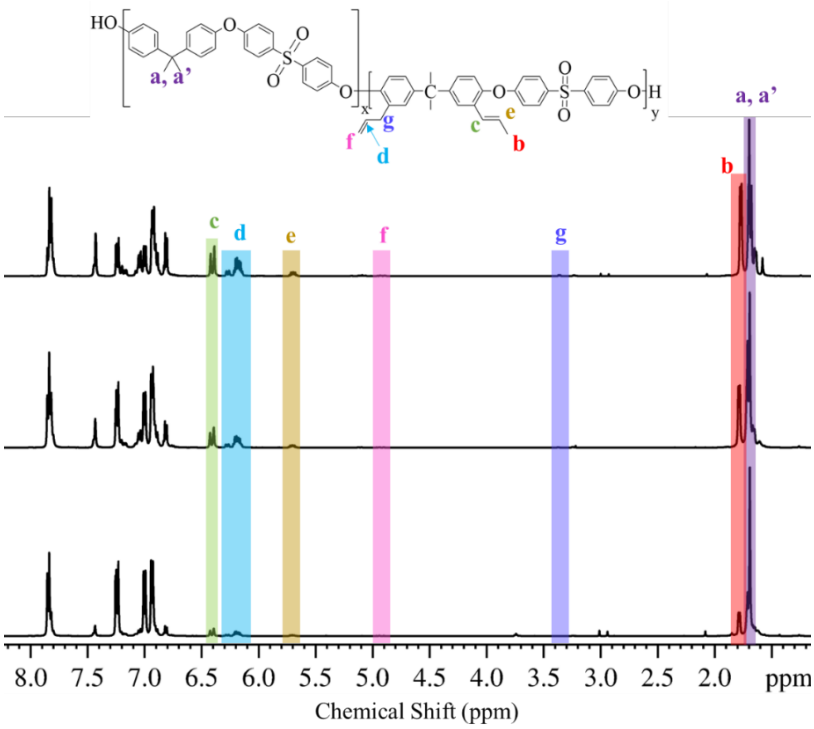

Figure 3.4 ^{1}H NMR spectra of PAES-co-APAES(25) (bottom), PAES-co-APAES(50) (middle) and PAES-co-APAES(75) (top) in C*D*Cl$_3$.

An established method of counterion exchange is employed to exchange the counterion from iodide to bicarbonate.[26–28] [26–28] To substitute the iodide counterions with bicarbonate counterions, PAES-co-QAPAES(25)[I] was placed inside a stirring solution of 1 M $KHCO_3$ in DI water at room temperature for 48 h, and then washed 3 times with fresh DI water, as this protocol has proven successful in literature.[29] A hydroxide, carbonate, or bicarbonate ions may replace iodide and the starting counterion has no effect on the outcome of MSS process.[30] Bicarbonate ions are superior to carbonate ions for ion exchange, because carbonate’s divalent charge results in a larger hydrated-ion size that is

unfavorable for ion exchange. A larger hydrated-ion size obstructs its diffusion into the polymer structure.[31] Hydroxides are less favorable than bicarbonates because they have the potential to initiate Hofmann elimination during storage, sonication and the drying process thereby requiring a more complicated polymer preparation protocol.[32,33]

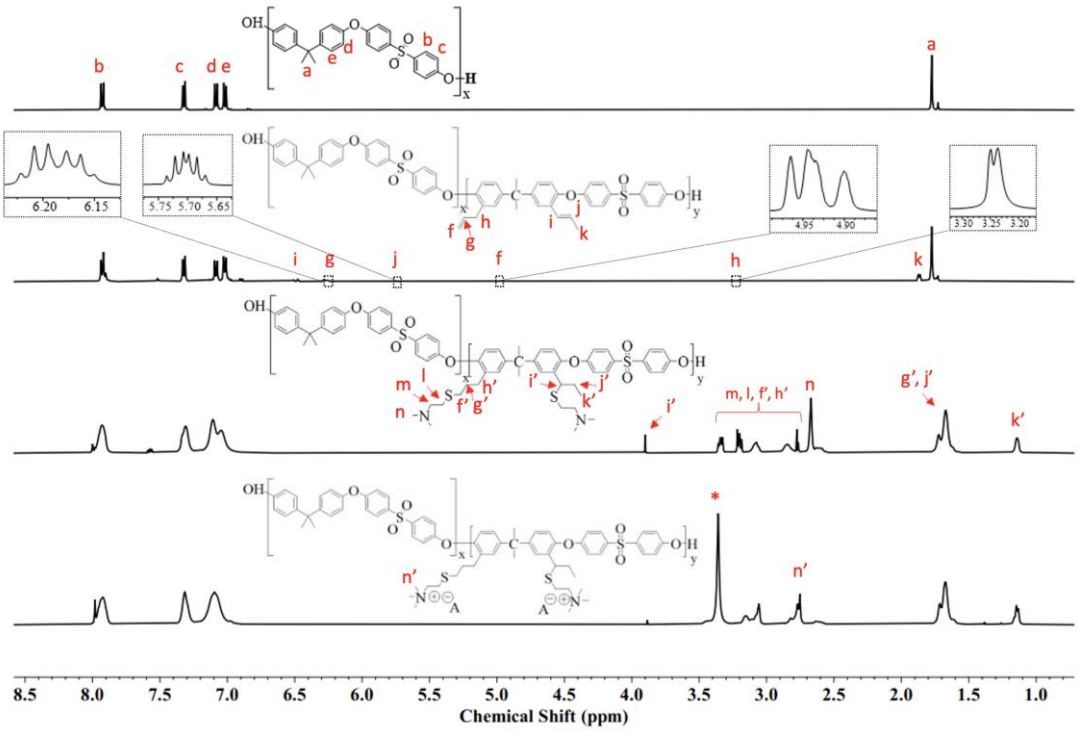

Figure 3.5 From top to bottom: ^{1}H NMR spectra of Udel® P-1700 PSU in $CDCL_3$, PAES-co-APAES(25) in $CDCL_3$, PAES-co-TAPAES(25) in DMSO-d_6, PAES-co-QAPAES(25) in DMSO-d_6.

The molecular weights of the allyl-modified polysulfones are determined using SEC (**Figure 3.6 and Table 3.4**). The number-average molecular weights for Udel® P-1700 PSU, PAES-co-APAES(25), PAES-co-APAES(50) and PAES-co-APAES(75) without cyclic oligomers are 49.5, 23.1, 83.9, and 112.8 kDa with dispersity ($Đ$ (M_W/M_n)) values of 1.5, 1.8, 2.1, and 2.4, respectively. High molecular weights are achieved in low reaction times due to extensive monomer purification and the use of DFDPS in the step growth

reaction.[11] The SEC traces of all polymers (**Figure 3.6a**) show a bimodal molecular weight distribution with a shoulder on the right attributed to the generation of smaller molecular weight cyclic compounds. Cyclic oligomers can form from the back-biting of phenoxide end groups to the polymer backbone in the step growth reaction.[34,35] The use of DABA as a comonomer introduces concerns over cross-linking, as the unsaturated allyl groups can react through a number of different reaction pathway. The absence of a shoulder at the lower elution times in all SEC traces (**Figure 3.6**) can indicate that cross-linked products are not present. Additional investigations will be performed to evaluate how the addition of allyl groups can allow the tuning of polymer architecture. According to the classical theory by Carothers and Flory, the *Đ* of polymers in step growth reaction equals 2.0 at complete conversion of monomers.[36,37] However, further investigations into the step growth reaction showed cyclic compounds are generated at any chain length during step-growth polymerization and compete with step growth reaction linear chain growth.[39] This influences the value of *Đ*, yielding higher values (*Đ* = 2-20) at higher conversions without fractionation of polymers to remove cyclic compounds before SEC analysis.[34,38,39] As an example, a mathematical study on step growth reaction for aliphatic chains with alkane moieties generated *Đ* of 2.77 at 98% conversion.[40] Another mathematical study observed *Đ*>20 at 100% conversion in the polycondensation reaction between silylated tetrahydroxy-tetramethylspirobisindane with 1,4-dicyanotetrafluorobenzene.[41] A series of experimental studies carried out by Kricheldorf et al. for step growth reactions of aromatic monomers yielded *Đ* values between 3-15 at above 97% conversion.[42–44] Thus, high *Đ* values obtained are validated and show high reactant conversion. The cyclic content

(weight fraction) in Udel® P-1700 PSU, PAES-co-APAES(25), PAES-co-APAES(50) and PAES-co-APAES(75) is calculated to be 1.7%, 5.2%, 5.7% and 20.9%, respectively. An increasing trend in cyclic content is observed with increasing DABA content, which we think may be because of a higher propensity for back-biting of polymer chains in the step growth reaction. This backbiting may be the result of greater segmental motion caused by added free volume from the pendant allylic groups on DABA. Alternatively, increased steric hinderance in the step growth reaction for DABA addition could cause slower reaction rate constants for DABA compared to BPA. Thus, at higher DABA monomer content, the propensity for side reactions would be higher. In the same reaction time (6 h) and with similar reaction conditions, a higher DABA/BPA ratio results in a higher molecular weight. Future kinetic and viscosity studies will better understand this trend. The combination of molecular weight data from SEC and ^{1}H NMR spectra confirms the successful synthesis of high molecular weight QA-functionalized poly(arylene ether sulfones).

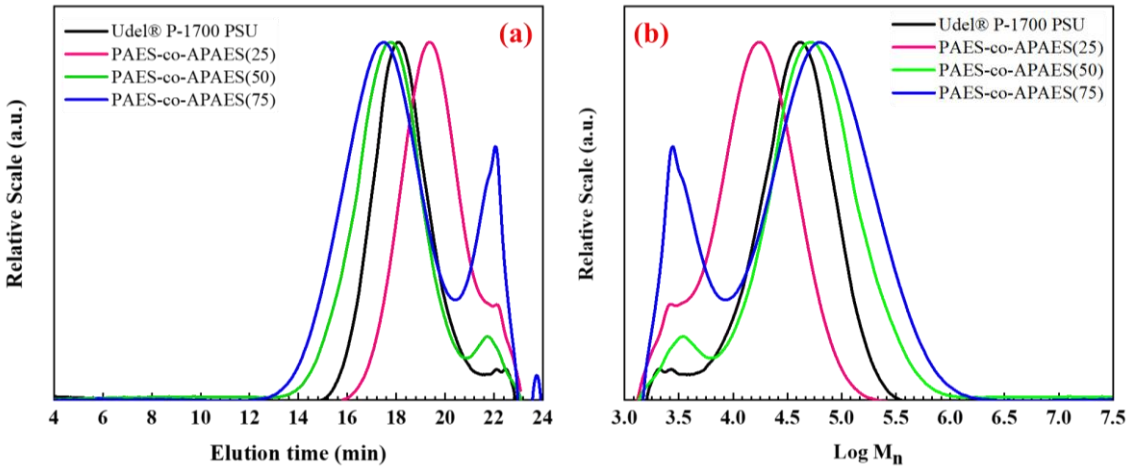

Figure 3.6 SEC traces of a) elution time b) Log M_n for Udel® P-1700 PSU, PAES-co-APAES(25), PAES-co-APAES(50) and PAES-co-APAES(75)

Table 3.4 Molecular weight, dispersity values and cyclic content of Udel® P-1700 and synthesized QA-functionalized poly(arylene ether sulfone) copolymers

Polymer	SEC M_n (kDa)	SEC M_w (kDa)	*Đ*	SEC M_n without cyclic (kDa)	SEC M_w without cyclic (kDa)	*Đ* without cyclic	Total area under curve	Area of cyclic	% cyclic
Udel® P-1700	48.9	79.4	1.62	49.5	79.4	1.53	2.661	0.045	1.70
PAES-co-APAES(25)	21.7	43.1	1.99	23.1	41.6	1.80	2.941	0.154	5.24
PAES-co-APAES(50)	73.5	146.2	2.23	83.9	178.4	2.13	3.314	0.190	5.73
PAES-co-APAES(75)	83.1	246.6	2.98	112.8	268.3	2.38	4.631	0.968	20.93

3.4.2.2 Thermogravimetric analysis (TGA) and Differential Scanning Calorimetry (DSC) of the synthesized random copolymers

Thermal stability of polymers is studied, and the TGA curves are shown in **Figure 3.7**. Udel® P-1700 PSU exhibits a one-step weight loss at ~470 °C, corresponding to backbone degradation[45] The QA-functionalized polysulfones remain stable up to a temperature of ~120 °C and show a multi-step weight loss with onset temperatures of 122-127 °C, 203-211 °C, 330-384 °C and ~470 °C, as shown as a, b, c and d in the 1st derivative plot in **Figure 3.7**. The first weight loss is the evaporation of solvent (DMF) and water held by the counterion. The next steps are the chemical degradation of counterions and initiation of Hofmann elimination of quaternary ammonium hydroxides, degradation of sulfur bonds (-S-) and decomposition of the main chain.[46] As also observed in literature, all polymers show a large residual mass (25-30%) at 800 °C, which is due to the large number of aromatic compounds.[47] The multi-step weight loss observed agrees with TGA profiles reported in literature for similarly functionalized backbones.[48,49] The $T_{d5\%}$ of QA-

functionalized polysulfone is 241-262 °C , which is up to 53% lower than Udel® P-1700 PSU as a result of incorporated structures. However, these values are still well beyond atmospheric temperatures where DAC is envisioned to be conducted.

The DSC thermograms and glass transition temperature (T_g) of Udel® P-1700 PSU and the synthesized QA-functionalized polysulfones are shown in **Figure 3.7**. The T_g of Udel® P-1700 PSU agrees with literature.[50] In comparison to Udel® P-1700 PSU, the T_g of PAES-co-APAES(25), PAES-co-APAES(50) and PAES-co-APAES(75) decrease by 9%, 17% and 21%, respectively.

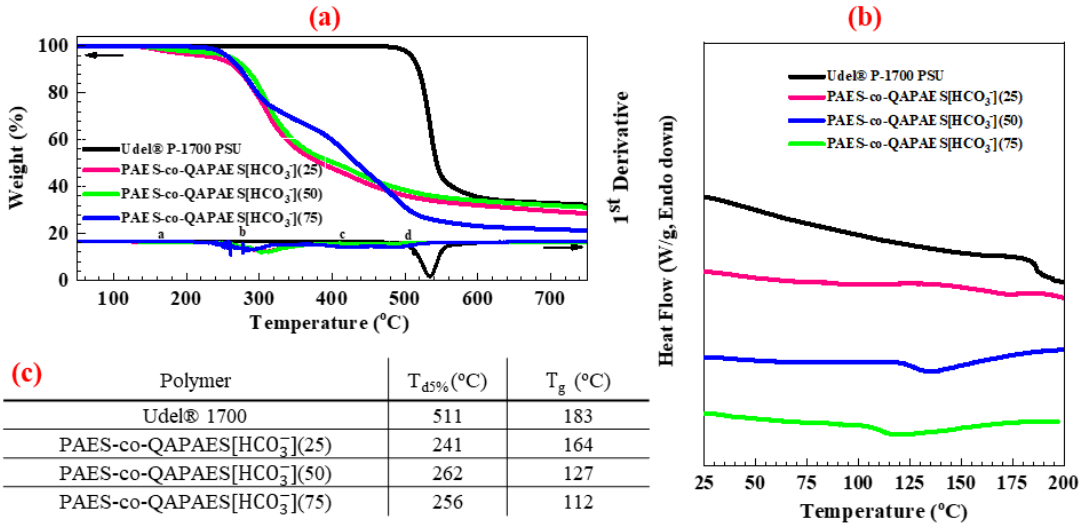

(c)

Polymer	$T_{d5\%}$(°C)	T_g (°C)
Udel® 1700	511	183
PAES-co-QAPAES[HCO_3^-](25)	241	164
PAES-co-QAPAES[HCO_3^-](50)	262	127
PAES-co-QAPAES[HCO_3^-](75)	256	112

Figure 3.7 Thermal analysis of the QA-functionalized copolymers. a) TGA and 1st derivative (DTA) plot of Udel® PSU, PAES-co-QAPAES[HCO_3^-](25), PAES-co-QAPAES[HCO_3^-](50) and PAES-co-QAPAES[HCO_3^-](75) obtained from thermal scanning up to 750 °C under N_2 and $T_{d5\%}$ of polymers. b) DSC traces from second heating scan (shifted vertically for clarity) of from top to bottom: Udel® P-1700 PSU, PAES-co-QAPAES[HCO_3^-](25), PAES-co-QAPAES[HCO_3^-](50) and PAES-co-QAPAES[HCO_3^-](75). c) $T_{d5\%}$ and T_g read from plots TGA and DSC graphs.

The entanglement molecular weight (M_e) of BPA-based polysulfone is 2,300 Da, and the molecular weight of all investigated polymers are more than 10X this value, so we can neglect the effect of molecular weight on T_g.[51] The decrease can be due to the larger free

volume between polymer chains caused by the pendant allyl functionalities causing weaker interactions.[52] When the allyl group is converted to the quaternary ammonium a further reduction in T_g is observed. The decrease in T_g is 10%, 31% and 39% for PAES-co-QPAES(25), PAES-co-QAPAES(50) and PAES-co-QPAES(75), respectively, in comparison to the allyl copolymer precursor. The larger drop in T_g observed for QA-functionalized polysulfone compared to allyl-modified polysulfone is believed to be the result of bulkier pendant sites causing larger free volume and weaker interactions between polymer chains, which enables easier cooperative segmental motion at lower temperatures. The increase in free volume hypothesis is further supported by the fractional free volume measurement ($\boldsymbol{f}$) using density values in Table 3.5, for polymers reported in Table 3.6. Increases of 3.4%, 52.0% and 71.2% are observed compared to $\boldsymbol{f}$ of 0.177 for Udel® P-1700 PSU for PAES-co-QAPAES[$\mathbf{HCO_3^-}$](25), PAES-co-QAPAES[$\mathbf{HCO_3^-}$](50) and PAES-co-QAPAES[$\mathbf{HCO_3^-}$](75), respectively.

Table 3.5 True density measurements for synthesized polymers.

Polymer	Weight of polymer (g)	Volume (mL)	Density (g/mL)
PAES-co-QAPAES[HCO_3^-](25)	0.0744 ± 0.0001	0.0554 ± 0.0001	1.3430
PAES-co-QAPAES[HCO_3^-](50)	0.0220 ± 0.0001	0.0167 ± 0.0001	1.3174
PAES-co-QAPAES[HCO_3^-](75)	0.1081 ± 0.0001	0.0812 ± 0.0001	1.3313

Table 3.6 Molar volume, van der Waals volume and fractional free volume.

polymer	v (mL/mol)	v_{VDW} (mL/mol)	f
Udel® P-1700	369.9	234.2	0.177
PAES-co-QAPAES[HCO_3^-](25)	1653.0	1042.6	0.183
PAES-co-QAPAES[HCO_3^-](50)	1020.5	574.2	0.269
PAES-co-QAPAES[HCO_3^-](75)	2338.1	1254.3	0.303

The PAES-co-APAES data fit to the Fox equation, which estimates the T_g of random copolymers.[53] Each pairwise set of data predicted a T_g of 143 °C for 100% APAES with ±2 °C standard deviation. Because of the agreement between the Fox equation and the experimental data, we can infer a random copolymer structure. No crystallization or melt transitions were observed in the DSC analysis, and a single T_g is observed meaning the polymers have an amorphous morphology with non-phase separated and randomly dispersed polymer segments.[54] This is in agreement with literature, as polysulfones inhibit crystalline morphologies due to the bond angles along the backbone.[32]

3.4.2.3 Water vapor gravimetric sorption (WU) and water contact angle (WCA)

The results for polymer water uptake (WU) on polymer powders and water contact angle (WCA) on polymeric dense membranes are shown in **Table 3.7**. WU for Udel® P-1700 PSU, PAES-co-QAPAES[HCO_3^-](25), PAES-co-QAPAES[HCO_3^-](50), and PAES-co-QAPAES[HCO_3^-](75) are 1.68%, 3.8%, 44.0%, and 9.6%, respectively. All QA-functionalized polymers have higher WU compared to Udel® P-1700 PSU. This result is as expected as QA groups are hydrophilic and should enhance the polymer's capacity to hold water. For WCA analysis on dense membranes, Udel® P-1700 PSU and PAES-co-

QAPAES[HCO_3^-](25) polymers formed dense membranes with desirable mechanical properties, meaning they were successfully removed from the petri dish as a whole. PAES-co-QAPAES[HCO_3^-](50) and PAES-co-QAPAES[HCO_3^-](75) formed brittle membranes, breaking into large and small pieces upon removal, respectively, showing less desirable mechanical properties. Inferior mechanical properties are typical for dry ionic polymers with high charge content below their T_g.[55] Nonetheless, WCA measurements were successfully performed on all dense membranes (WCA images are shown in **Figure 3.8**). The WCA for Udel® PSU is ~91° due to its inherent hydrophobic backbone. Addition of the hydrophilic QA functional groups to PAES-co-QAPAES[HCO_3^-](25), PAES-co-QAPAES[HCO_3^-](50), and PAES-co-QAPAES[HCO_3^-](75) polymers decreased the WCA by 15.2%, 22.3% and 16.9%, respectively.

Table 3.7 Water uptake and contact angle measurements for Udel® 1700 and QA-functionalized polysulfones.

Polymer	Water Uptake (%)	Water contact angle
Udel® PSU	1.68	90.9° ± 2.8
PAES-co-QAPAES[HCO_3^-](25)	3.8 ± 0.1	77.1°± 2.8
PAES-co-QAPAES[HCO_3^-](50)	44.0 ± 0.6	70.6° ± 2.0
PAES-co-QAPAES[HCO_3^-](75)	9.6 ± 0.2	75.5° ± 6.4

An intriguing trend is observed in WU and WCA results for the polymers/membranes with increasing QA content. In both investigations, increasing the QA content from PAES-co-QAPAES[HCO_3^-](25) to PAES-co-QAPAES[HCO_3^-](50) and then to PAES-co-QAPAES[HCO_3^-](75) an increase in hydrophilicity is observed followed by a decrease, but with a higher final value. T-test results (with IBM SPSS software V.27) shows statistically significant influence of QA-functionalization on WU, yielding a p-value of <0.001 for all

pairs (**Table 3.8**). T-test results for WCA shows statistically significant influence on hydrophilicity resulting from the addition of QA-functionalities for all polymers when compared to Udel® PSU (p-value of <0.001, **Table 3.8**). The increase in QA content from PAES-co-QAPAES[HCO_3^-](25) to PAES-co-QAPAES[HCO_3^-](50) also results in statistically significant increase in hydrophilicity (p-value of 0.013), however, changes from PAES-co-QAPAES[HCO_3^-](50) to PAES-co-QAPAES[HCO_3^-](75) and PAES-co-QAPAES[HCO_3^-](25) to PAES-co-QAPAES[HCO_3^-](75) did not result in statistically significant change in hydrophilicity (p-value of 0.223 and 0.593, respectively). Structural or morphological changes in the polymer matrix resulting from the added QA-functionalization may influence its ability to hold water.[55] Ionic clustering of QA groups, as reported in literature for a polymer with varying numbers of QA sites on phenylene rings in a poly(arylene ether sulfone) copolymer, can result in lower WU due to the formation of distinct hydrophobic regions[56]. Developing a deep understanding in this area will require additional studies.

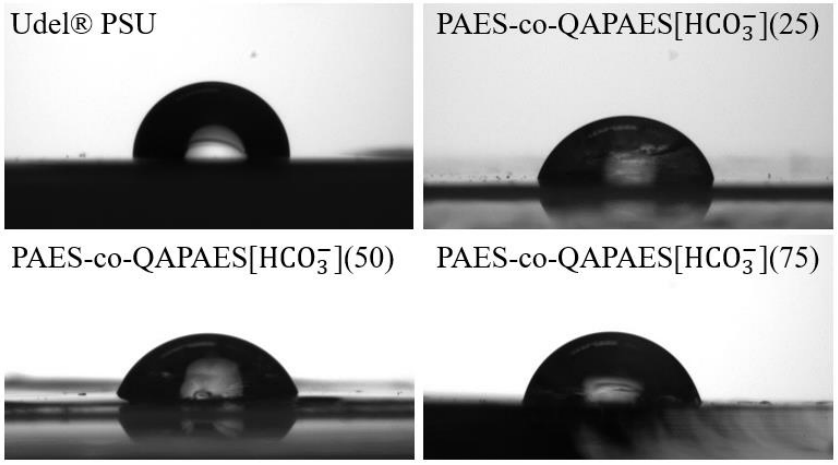

Figure 3.8 Water contact angle images on dense membranes.

Table 3.8 Paired T-test analysis for water contact angle and water uptake data.

Paired T-test for Water uptake		P value
Udel PSf	PAES-co-QAPAES(25)[HCO3-]	<0.001
Udel PSf	PAES-co-QAPAES(50)[HCO3-]	<0.001
Udel PSf	PAES-co-QAPAES(75)[HCO3-]	<0.001
PAES-co-QAPAES(25)[HCO3-]	PAES-co-QAPAES(50)[HCO3-]	<0.001
PAES-co-QAPAES(25)[HCO3-]	PAES-co-QAPAES(75)[HCO3-]	<0.001
PAES-co-QAPAES(50)[HCO3-]	PAES-co-QAPAES(75)[HCO3-]	<0.001
Paired T-test for Water contact angle		
Udel PSf	PAES-co-QAPAES(25)[HCO3-]	0.001
Udel PSf	PAES-co-QAPAES(50)[HCO3-]	<0.001
Udel PSf	PAES-co-QAPAES(75)[HCO3-]	0.001
PAES-co-QAPAES(25)[HCO3-]	PAES-co-QAPAES(50)[HCO3-]	0.013
PAES-co-QAPAES(25)[HCO3-]	PAES-co-QAPAES(75)[HCO3-]	0.593
PAES-co-QAPAES(50)[HCO3-]	PAES-co-QAPAES(75)[HCO3-]	0.223

3.4.2.4 CO_2 sorption/desorption and kinetic modelling

MSS activity of polymers are tested in the experimental setup (**Figure 3.3**). **Figure 3.9a** is a blank run showing the IRGA's reading of CO_2 levels in a closed system with varying environmental gas volume (e.g., humidity). A correction is applied on the experimental data that accounts for the dilution of CO_2 caused by the introduction of water vapor. All polymers (**Figure 3.9-d to f)** show distinct deviations from the blank run; specifically, an increase in the magnitude of the swing in CO_2 concentration occurs as the concentration of ammonium groups in the copolymer increases. The lower black curve shows the water concentration in parts per thousand, which is controlled using a dew point generator. The relative humidity is cycled between values of 8 ppt (~30% RH) and 25 ppt (~95% RH). As the water vapor concentration in the chamber increases the CO_2 concentration also rises, indicating the sample releases CO_2 under higher humidity conditions. Conversely, as the relative humidity in the chamber is decreased, the CO_2 concentration in the chamber also decreases, indicating CO_2 capture under dry conditions. Thus, the MSS mechanism is

satisfied. Also of note, desorption is performed spontaneously without extra heat supply as the system is maintained at room temperature.

Kinetic analysis is performed by fitting the data to Pseudo-first-order (PFO) and pseudo-second-order (PSO) models in a 2.4 h CO_2 uptake test at 22 °C and 30% RH (**Figure 3.9**). Better agreement is observed for PSO model for all samples, with increasing CO_2 sorption capacity with increasing IEC (QA functionalities). At this moment, we cannot be certain of the absolute values associated with reaction rates because of a lack of understanding of the moisture swing sorption process (e.g., reaction order). However, we can draw conclusions by looking at the trends in the data as discussed below.

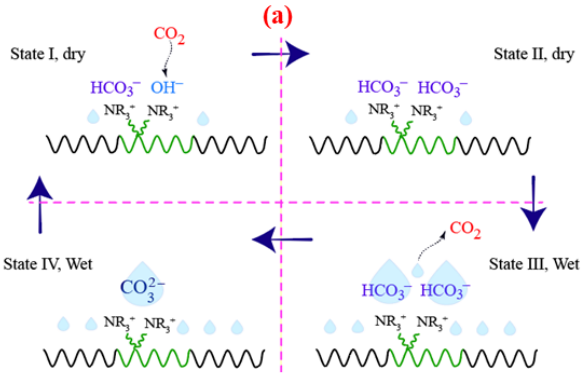

(b)

Polymer	True ρ g/mL	*f*	Effective* IEC mmol/g
Udel® 1700	1.240	0.177	n/a
PAES-co-QAPAES[HCO_3^-](25)	1.343	0.183	0.45
PAES-co-QAPAES[HCO_3^-](50)	1.317	0.269	0.75
PAES-co-QAPAES[HCO_3^-](75)	1.331	0.303	0.97

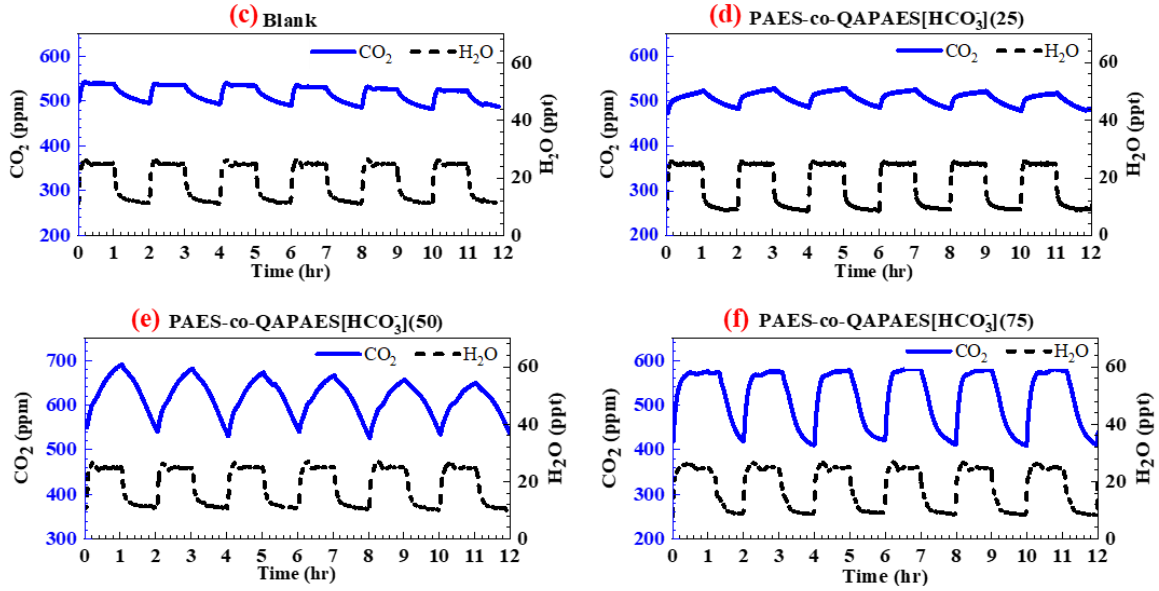

*Theoretical effective IEC is theoretical IEC/2 due to the nature of the MSS mechanism.

Figure 3.9 a) MSS mechanism (Reproduced from Shokrollahzadeh Behbahani, H.; Green, M. Direct Air Capture of CO2; ACS In Focus; American Chemical Society: Washington, DC, USA, 2023, DOI 10.1021/acsinfocus.7e7016. Copyright 2023 American Chemical Society[13]. b) copolymer density, fractional free volume, and ion exchange, and profiles for c) Udel® 1700, d) PAES-co-QAPAES[HCO_3^-](25), e) PAES-co-QAPAES[HCO_3^-](50) and f) PAES-co-QAPAES[HCO_3^-](75) ran with swing in moisture of 8 – 25 ppt (30% RH to 95% RH at 22 °C) for 6 consecutive cycles of 2 h each (1 h sorption and 1 h desorption).

PAES-co-QAPAES[HCO_3^-](25), PAES-co-QAPAES[HCO_3^-](50) and PAES-co-QAPAES[HCO_3^-](75) have theoretical effective IEC's of 0.45, 0.75, and 0.97 mmol/g,

respectively. The CO_2 uptake values are shown in **Figure 3.10**. Based on the PSO model, uptake values for PAES-co-QAPAES[HCO_3^-](25), PAES-co-QAPAES[HCO_3^-](50) and PAES-co-QAPAES[HCO_3^-](75) are 3.051 ± 0.001, 29.793 ± 0.022, and 31.579 ± 0.009 µmol/g, respectively. Uptake values observed are significantly lower than uptakes reported for point source CO_2 sorption, which are 0.001 – 0.07 mol/g[57], but this is expected as the CO_2 partial pressure in air is much lower than point source CO_2 streams. Similarly, sorbents used for DAC via the MSS in the literature also exhibit uptake capacities in the range of 0.001 mol/g, but these comparisons are not entirely practical, as the experimental conditions such as temperature (influences on kinetics and isotherms), volume of closed systems (influences desorption CO_2 partial pressure) and extent of moisture swing (influences number of sites available) either vary or are not reported (**Table 3.10**).[58,59] The rate constants for PAES-co-QAPAES[HCO_3^-](25) and PAES-co-QAPAES[HCO_3^-](75) are similar, and about an order of magnitude faster than PAES-co-QAPAES[HCO_3^-](50).

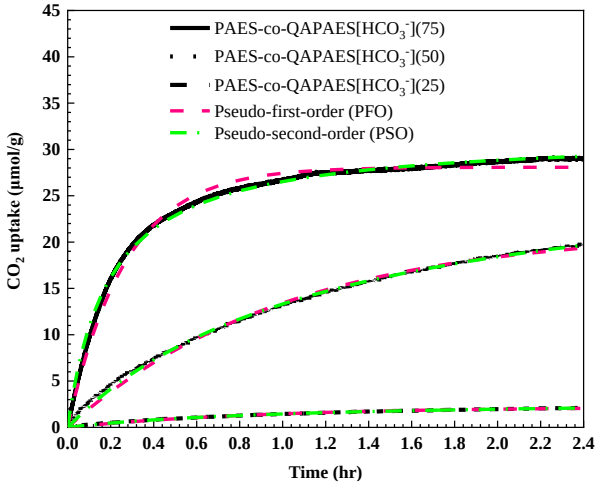

Figure 3.10 Experimental CO_2 uptake data and modeling of PFO and PSO at 22 °C and 30% RH.

Table 3.9 CO_2 uptake and release with RH swing of 30%-96%.

Polymer	PSO			PFO		
Udel® 1700	Q_e µmol/g	k_s 1/hr	R^2	Q_e µmol/g	k_f 1/hr	R^2
PAES-co-QAPAES[HCO_3^-](25)	3.051 ± 0.001	0.167	0.996	2.221 ± 0.002	1.081	0.996
PAES-co-QAPAES[HCO_3^-](50)	29.793 ± 0.022	0.027	0.998	21.318 ± 0.018	0.993	0.995
PAES-co-QAPAES[HCO_3^-](75)	31.579 ± 0.009	0.297	0.999	28.083 ± 0.009	3.761	0.987

*Theoretical effective IEC is theoretical IEC/2 due to the nature of the moisture swing mechanism.

The working capacity of the sorbents are much lower than their theoretical effective IEC, and the percent of site utilization changes with changes in the number of QA groups. We suspect the following arguments may be influencing lower working capacities and may be the foundation of future work. In general, water (humidity) can influence many aspects of the MSS process, in positive and negative ways. It may deactivate CO_2 capture sites through anion deprotonation, or the existence of a hydration layer surrounding the hygroscopic QA groups, even when exposed to dry atmosphere, may interrupt the CO_2 capture process and cause diffusion constraints.[60–62] Water present in the copolymers can promote ion transport and provide free protons for the reaction between CO_2 and sorbent. More investigations are required to elucidate the multiple roles of water on the MSS process and inform sorbent modifications to increase/decrease hydrophobicity. One way this is manifested in our work is the modest improvement in sorption capacity and kinetics exhibited by PAES-co-QAPAES[HCO_3^-](75) relative to PAES-co-QAPAES[HCO_3^-](50).

The former copolymer has a lower water uptake percentage and a higher water contact angle but a larger fractional free volume, which highlights how the interplay of water, chemical reactions between the alkaline counterions with CO_2 and the polymer thermomechanical properties will dictate the material performance for DAC. Also, in the MSS process, two QA sites are simultaneously involved. In other words, to hold a divalent CO_3^{2-} ion, the distance between two QA ions should not be much larger than the size of one carbonate ion.[30] Further evaluation is needed on the synthesized materials to explore these geometrical requirements and inform macromolecule structural features that locate ion exchange sites at appropriate distances. Finally, as shown herein, increasing the IEC does not necessarily optimize DAC performance. Block polymer structures might help retain mechanical properties while creating task-specific domains for the capture of CO_2.[63] These ideas are also employed to explain higher utilization of sites for 50% and 75% QA-functionalized (3.97% and 3.26% site utilization (calculated as working capacity divided by IEC times 100)), respectively) versus 25% QA-functionalized (0.68% site utilization), and, the discrepancy between utilization sites for 50% and 75% QA-functionalized polymer. The working capacity of the sorbents are much lower than their theoretical effective IEC, and the percentage of site utilization changes with changes in the number of QA groups. We suspect the following arguments may be influencing lower working capacities and may be the foundation of future work. In general, water (humidity) can influence many aspects of the MSS process, in positive and negative ways. It may deactivate CO_2 capture sites through anion deprotonation, or existence of a hydration layer

surrounding the hygroscopic QA groups, even when exposed to dry atmosphere, may interrupt the CO_2 capture process and cause diffusion constraints.[60–62].

Table 3.10 Summary of some experimental conditions and uptakes on sorbents for moisture swing CO_2 capture.

Material	Ion initially exchanged for MSS	IEC mmol/g	Volume of testing chamber	Uptake μmol/g	Temperature	RH%
SnowPure's Excellion™ I-200[64]	OH^-	1.5		130		20-95%
SnowPure's Excellion™ I-200[29]	HCO_3^-		1.25 L	860	25 °C	5-100 %
IONSEP-MC-A ion exchange resin[58]	CO_3^{2-}	1.9	20 L	830	22°C	Relatively low -95%
quaternary ammonium-based anion exchange resin[59]	CO_3^{2-}		1.05 L		25 °C	
porous polymers formed by HIPE polymerization (1.5% crosslinking)[65]	OH^-	1.37		230		5-25 ppt
D201 microporous polystyrene[66]	PO_4^{3-}	1.3		550	25 °C	0-100%
Quaternized bamboo cellulose[67]	CO_3^{2-}	0.55	8 L	190	25 °C	60-80%
Ammonium HBPG-modified silica[68]	OH^-	0.98		11	25 °C	0-95%
3D ordered macroporous structure (3DOM) of poly(methyl methacrylate) (PMMA) colloidal crystals[69]	OH^-	2.3		570	20 °C	20-90%
Quaternized mesoporous resin[70]	CO_3^{2-}	0.5	8 L	260	20 °C	21-100%
quaternized poly(styrene)[71]	CO_3^{2-}	1		500	20 °C	40-100%
This study	HCO_3^-	0.97	145 mL	32	22 °C	30-96%

A Water peak for "dried" PAES-co-QAPAES polymers can be observed in ^{1}H NMR analysis shown in **Figure 3.5** (the water peak is marked at 3.35 ppm with an asterisk). Water can promote ion conductivity and transport and provide free protons for the reaction between CO_2 and sorbent. More information is required on the multiple roles of water on the MSS process, and sorbent modifications can be applied accordingly (such as increasing/decreasing hydrophobicity). Also, in the MSS process, two QA sites are simultaneously involved. In other words, to hold a CO_3^{2-} divalent ion, the distance between two QA ions should not be much larger than the size of one carbonate ion.[30] Further evaluation may be performed on the synthesized materials, and modification of the macromolecule structure can be implemented to move exchange sites closer to each other, or, to increase the IEC with a block polymer structure to retain mechanical properties.[63] These ideas are also employed to explain higher utilization of sites for 50% and 75% QA-functionalized (3.97% and 3.26% site utilization (calculated as working capacity divided by IEC times 100)), respectively) versus 25% QA-functionalized (0.68% site utilization), and, the discrepancy between utilization sites for 50% and 75% QA-functionalized polymer.

3.5 Conclusion

Novel QA-functionalized poly(arylene ether sulfones) (PAES-co-QAPAES) were successfully synthesized through step growth reaction and subsequent post-polymerization modification reactions. Characterization of materials shows the successful synthesis of high molecular weights polymers with amorphous morphology and randomly dispersed polymer segments. The degradation temperature of polymers is far beyond operational

temperatures (241 °C– 262 °C) envisioned for DAC. The designed sorbents capture atmospheric CO_2 when dry and desorb CO_2 when exposed to humidity without additional energy supply. Sorption/desorption cycles show the performance of materials is stable for six consecutive cycles.

Further evaluation of the moisture swing DAC process is necessary, and anticipated modifications to the macromolecule structure of the polymeric sorbent is expected to enhance its working capacity.

3.6 References

(1) Carothers, W. H. Studies on Polymerization and Ring Formation. *J. Am. Chem. Soc.* **1929**, *51* (8), 2548–2559. https://doi.org/10.1021/ja01383a041.

(2) Zeng, G.; Zhang, C.; Huang, G.; Yu, J.; Wang, Q.; Li, J.; Xi, B.; Liu, H. Adsorption Behavior of Bisphenol A on Sediments in Xiangjiang River, Central-South China. *Chemosphere* **2006**, *65* (9), 1490–1499. https://doi.org/10.1016/j.chemosphere.2006.04.013.

(3) *Potassium Carbonate*. Common Organic Chemistry. http://www.commonorganicchemistry.com/Common_Reagents/Potassium_Carbonate/Potassium_Carbonate.htm (accessed 2022-07-01).

(4) Meizenheimer, J. Mittheilung Aux Dem Chemischen Laboratorium Der Koniglichen Akademie Der Wissenxchaften Zu Miinchen,. *Journ. chem. SOC* **1902**, *3567* (1900), 205–245. https://doi.org/10.1002/jlac.1902323020.

(5) Argyropoulos, D. S.; Sadeghifar, H.; Cui, C.; Sen, S. Synthesis and Characterization of Poly(Arylene Ether Sulfone) Kraft Lignin Heat Stable Copolymers. *ACS Sustain. Chem. Eng.* **2014**, *2* (2), 264–271. https://doi.org/10.1021/sc4002998.

(6) Odian, G. *Principles of Polymerization*; 2004.

(7) Parodi, F. Polysulfones. In *Comprehensive Polymer Science and Supplements*; Elsevier, 1989; pp 561–591. https://doi.org/10.1016/B978-0-08-096701-1.00174-9.

(8) Li, Y.; Cheng, J.; Zhang, J. A Newly Designed Dual-Functional Epoxy Monomer for Preparation of Fishbone-Shaped Heterochain Polymer with a High Damping Property at Low Temperature. *Macromol. Mater. Eng.* **2017**, *302* (5). https://doi.org/10.1002/mame.201600574.

(9) Viswanathan, R.; Johnson, B. C.; McGrath, J. E. Synthesis, Kinetic Observations and Characteristics of Polyarylene Ether Sulphones Prepared via a Potassium Carbonate DMAC Process. *Polymer (Guildf).* **1984**, *25* (12), 1827–1836. https://doi.org/10.1016/0032-3861(84)90258-1.

(10) Hedrick, J. L.; Patsiga, R. A.; McGrath, J. E. Synthesis and Characterization of Sulfonated Poly(Arylene Ether Sulfones). *Am. Chem. Soc. Polym. Prepr. Div. Polym. Chem.* **1984**, *25* (2), 88–90.

(11) Yang, Y.; Muhich, C. L.; Green, M. D. Kinetics and Mechanisms of Polycondensation Reactions between Aryl Halides and Bisphenol A. *Polym. Chem.* **2020**, *11* (31), 5078–5087. https://doi.org/10.1039/D0PY00740D.

(12) Xu, J.; Boyer, C. Visible Light Photocatalytic Thiol-Ene Reaction: An Elegant Approach for Fast Polymer Postfunctionalization and Step-Growth Polymerization. *Macromolecules* **2015**, *48* (3), 520–529. https://doi.org/10.1021/ma502460t.

(13) Christian, P. Polymer Chemistry. *Electrospinning Tissue Regen.* **2011**, 34–50. https://doi.org/10.1016/B978-1-84569-741-9.50002-1.

(14) Wang, J.; Zhao, Z.; Gong, F.; Li, S.; Zhang, S. Synthesis of Soluble Poly (Arylene Ether Sulfone) Ionomers with Pendant Quaternary Ammonium Groups for Anion Exchange Membranes. **2009**, 8711–8717. https://doi.org/10.1021/ma901606z.

(15) Burgess, S. K.; Mikkilineni, D. S.; Yu, D. B.; Kim, D. J.; Mubarak, C. R.; Kriegel, R. M.; Koros, W. J. Water Sorption in Poly(Ethylene Furanoate) Compared to Poly(Ethylene Terephthalate). Part 1: Equilibrium Sorption. *Polymer (Guildf).* **2014**, *55* (26), 6861–6869. https://doi.org/10.1016/j.polymer.2014.10.047.

(16) Singh, A.; Freeman, B. D.; Pinnau, I. Pure and Mixed Gas Acetone/Nitrogen Permeation Properties of Polydimethylsiloxane [PDMS]. *J. Polym. Sci. Part B Polym. Phys.* **1998**, *36* (2), 289–301. https://doi.org/10.1002/(SICI)1099-0488(19980130)36:2<289::AID-POLB8>3.0.CO;2-M.

(17) Dhoot, S. N.; Freeman, B. D. Kinetic Gravimetric Sorption of Low Volatility Gases and Vapors in Polymers. *Rev. Sci. Instrum.* **2003**, *74* (12), 5173–5178. https://doi.org/10.1063/1.1622978.

(18) Moon, J. D.; Galizia, M.; Borjigin, H.; Liu, R.; Riffle, J. S.; Freeman, B. D.; Paul, D. R. Water Vapor Sorption, Diffusion, and Dilation in Polybenzimidazoles. *Macromolecules* **2018**, *51* (18), 7197–7208. https://doi.org/10.1021/acs.macromol.8b01659.

(19) Yampolskii, Y.; Pinnau, I.; Freeman, B. D. *Materials Science of Membranes for Gas and Vapor Separation*; Yampolskii, Y., Pinnau, I., Freeman, B., Eds.; John Wiley & Sons, Ltd: Chichester, UK, 2006. https://doi.org/10.1002/047002903X.

(20) Bondi, A. A. *Physical Properties of Molecular Crystals Liquids, and Glasses*; New York, Wiley, 1968.

(21) Van Krevelen, D. W.; Te Nijenhuis, K. Volumetric Properties. In *Properties of Polymers*; Elsevier, 2009; pp 71–108.

(22) Shokrollahzadeh Behbahani, H.; Mithaiwala, H.; Marques, H. L.; Wang, W.; Freeman, B. D.; Green, M. D. Quaternary Ammonium-Functionalized Poly(Arylene Ether Sulfone) Random Copolymers for Direct Air Capture. *Macromolecules* **2023**, *56* (16), 6470–6481. https://doi.org/10.1021/acs.macromol.3c00760.

(23) Zur Theorie Der Sogenannten Adsorption Gelöster Stoffe. *Zeitschrift für Chemie und Ind. der Kolloide* **1907**, *2* (1), 15–15. https://doi.org/10.1007/BF01501332.

(24) Ho, Y. .; McKay, G. Pseudo-Second Order Model for Sorption Processes. *Process Biochem.* **1999**, *34* (5), 451–465. https://doi.org/10.1016/S0032-9592(98)00112-5.

(25) Yang, Y.; Ramos, T. L.; Heo, J.; Green, M. D. Zwitterionic Poly(Arylene Ether Sulfone) Copolymer/Poly(Arylene Ether Sulfone) Blends for Fouling-Resistant Desalination Membranes. *J. Memb. Sci.* **2018**, *561*, 69–78. https://doi.org/10.1016/J.MEMSCI.2018.05.025.

(26) Mielby, J.; Kegnæs, S. Epoxidation of Alkenes with Aqueous Hydrogen Peroxide and Quaternary Ammonium Bicarbonate Catalysts. *Catal. Letters* **2013**, *143* (11), 1162–1165. https://doi.org/10.1007/s10562-013-1088-1.

(27) Kim, J. M.; Lin, Y.; Hunter, B.; Beckingham, B. S. Transport and Co-Transport of Carboxylate Ions and Ethanol in Anion Exchange Membranes. *Polymers (Basel).* **2021**, *13* (17), 2885. https://doi.org/10.3390/polym13172885.

(28) Dischinger, S. M.; Gupta, S.; Carter, B. M.; Miller, D. J. Transport of Neutral and Charged Solutes in Imidazolium-Functionalized Poly(Phenylene Oxide) Membranes for Artificial Photosynthesis. *Ind. Eng. Chem. Res.* **2020**, *59* (12), 5257–5266. https://doi.org/10.1021/acs.iecr.9b05628.

(29) Wang, T.; Liu, J.; Fang, M.; Luo, Z. A Moisture Swing Sorbent for Direct Air Capture of Carbon Dioxide: Thermodynamic and Kinetic Analysis. *Energy Procedia* **2013**, *37*, 6096–6104. https://doi.org/10.1016/j.egypro.2013.06.538.

(30) Wang, T.; Lackner, K. S.; Wright, A. Moisture Swing Sorbent for Carbon Dioxide Capture from Ambient Air. *Environ. Sci. Technol.* **2011**, *45* (15), 6670–6675. https://doi.org/10.1021/es201180v.

(31) Rieman, W.; Walton, H. F. *Ion Exchange in Analytical Chemistry*; Elsevier, 1970. https://doi.org/10.1016/C2013-0-05561-2.

(32) Hofmann, A. W. Von. XIV. Researches into the Molecular Constitution of the Organic Bases. *Philos. Trans. R. Soc. London* **1851**, *141*, 357–398. https://doi.org/10.1098/rstl.1851.0017.

(33) Mohanty, A. D.; Tignor, S. E.; Krause, J. A.; Choe, Y.-K.; Bae, C. Systematic Alkaline Stability Study of Polymer Backbones for Anion Exchange Membrane Applications. *Macromolecules* **2016**, *49* (9), 3361–3372. https://doi.org/10.1021/acs.macromol.5b02550.

(34) Kricheldorf, H. R.; Böhme, S.; Schwarz, G.; Krüger, R.-P.; Schulz, G. Macrocycles. 18. The Role of Cyclization in Syntheses of Poly(Ether−sulfone)S. *Macromolecules* **2001**, *34* (26), 8886–8893. https://doi.org/10.1021/ma010218l.

(35) Savariar, S.; Underwood, G. S.; Dickinson, E. M.; Schielke, P. J.; Hay, A. S. Polysulfone with Lower Levels of Cyclic Dimer: Use of MALDI-TOF in the Study of Cyclic Oligomers. *Desalination* **2002**, *144* (1–3), 15–20. https://doi.org/10.1016/S0011-9164(02)00282-5.

(36) Carothers, W. H. Polymers and Polyfunctionality. *Trans. Faraday Soc.* **1936**, *32*, 39. https://doi.org/10.1039/tf9363200039.

(37) Flory, P. J. Molecular Size Distribution in Linear Condensation Polymers 1. *J. Am. Chem. Soc.* **1936**, *58* (10), 1877–1885. https://doi.org/10.1021/ja01301a016.

(38) Kricheldorf, H. *Polycondensation*; Springer Berlin Heidelberg: Berlin, Heidelberg, 2014; Vol. 9783642394. https://doi.org/10.1007/978-3-642-39429-4.

(39) Wutz, C.; Kricheldorf, H. R. Molecular Weight Distribution of Linear Chains in Step-Growth Polymerization Under the Influence of Cyclization Reactions. *Macromol. Theory Simulations* **2012**, *21* (4), 266–271. https://doi.org/10.1002/mats.201100084.

(40) Fawcett, A. H.; Mee, R. A. W.; McBride, F. V. A Monte-Carlo Study of Ring Formation and Molecular Configurations during Step Growth on a Lattice in Three Dimensions. *Macromolecules* **1995**, *28* (5), 1481–1490. https://doi.org/10.1021/ma00109a020.

(41) Kricheldorf, H. R.; Fritsch, D.; Vakhtangishvili, L.; Schwarz, G. Cyclic Ladder Polymers by Polycondensation of Silylated Tetrahydroxy-Tetramethylspirobisindane with 1,4-Dicyanotetrafluorobenzene. *Macromol. Chem. Phys.* **2005**, *206* (22), 2239–2247. https://doi.org/10.1002/macp.200500280.

(42) Kricheldorf, H. R.; Schwarz, G. Cyclic Polymers by Kinetically Controlled Step-Growth Polymerization. *Macromol. Rapid Commun.* **2003**, *24* (56), 359–381. https://doi.org/10.1002/marc.200390063.

(43) Kricheldorf, H. R.; Weidner, S. M. Copolyesters of Lactide, Isosorbide, and Terephthalic Acid-Biobased, Biodegradable, High- T g Engineering Plastics. *Macromol. Chem. Phys.* **2013**, *214* (6), 726–733. https://doi.org/10.1002/macp.201200612.

(44) Kricheldorf, H. R.; Mix, R.; Weidner, S. M. Poly(Ester Urethane)s Derived from Lactide, Isosorbide, Terephthalic Acid, and Various Diisocyanates. *J. Polym. Sci. Part A Polym. Chem.* **2014**, *52* (6), 867–875. https://doi.org/10.1002/pola.27069.

(45) Udel® Polysulfone Design Guide. *Solvay Specialty Polymers*; 2015; pp 1–84.

(46) Zhang, Q.; Zhang, Q.; Wang, J.; Zhang, S.; Li, S. Synthesis and Alkaline Stability of Novel Cardo Poly(Aryl Ether Sulfone)s with Pendent Quaternary Ammonium Aliphatic Side Chains for Anion Exchange Membranes. *Polymer (Guildf).* **2010**, *51* (23), 5407–5416. https://doi.org/10.1016/j.polymer.2010.09.049.

(47) Ramgobin, A.; Fontaine, G.; Bourbigot, S. Thermal Degradation and Fire Behavior of High Performance Polymers. *Polym. Rev.* **2019**, *59* (1), 55–123. https://doi.org/10.1080/15583724.2018.1546736.

(48) Choi, J.; Byun, Y. J.; Lee, S. Y.; Jang, J. H.; Henkensmeier, D.; Yoo, S. J.; Hong, S. A.; Kim, H. J.; Sung, Y. E.; Park, J. S. Poly(Arylene Ether Sulfone) with Tetra(Quaternary Ammonium) Moiety in the Polymer Repeating Unit for Application in Solid Alkaline Exchange Membrane Fuel Cells. *Int. J. Hydrogen Energy* **2014**, *39* (36), 21223–21230. https://doi.org/10.1016/j.ijhydene.2014.10.007.

(49) Strasser, D. J.; Graziano, B. J.; Knauss, D. M. Base Stable Poly(Diallylpiperidinium Hydroxide) Multiblock Copolymers for Anion Exchange Membranes. *J. Mater. Chem. A* **2017**, *5* (20), 9627–9640. https://doi.org/10.1039/c7ta00905d.

(50) El-Hibri, M. J. Sulfone Polymer Composition. EP1524297A1, 2005. https://patents.google.com/patent/EP1524297A1/en.

(51) Polymer Processes Database. *Bisphenol A Polysulfone*. https://polymerdatabase.com/polymers/bisphenolapolysulfone.html.

(52) Pu, Z.; Xia, J.; Liu, X.; Wang, Q.; Liu, J.; He, X.; Zhong, J. Novel Polyethersulfone Dielectric Films with High Temperature Resistance, Intrinsic Low Dielectric Constant and Low Dielectric Loss. *J. Mater. Sci. Mater. Electron.* **2020**. https://doi.org/10.1007/s10854-020-04873-8.

(53) Fox, T. G. Influence of Diluent and of Copolymer Composition on the Glass Temperature of a Polymer System. *Bull. Am. Phys. Soc.* **1956**, *1*, 123–132.

(54) Dennis, J. M.; Fahs, G. B.; Moore, R. B.; Turner, S. R.; Long, T. E. Synthesis and Characterization of Polysulfone-Containing Poly(Butylene Terephthalate) Segmented Block Copolymers. *Macromolecules* **2014**, *47* (23), 8171–8177. https://doi.org/10.1021/ma501903h.

(55) Khan, W. *Quaternary ammonium functionalizaed poly(arylene ether sulfone) copolymer ionomers: synthesis, processing, and structure-property relationships*; The Graduate College at the University of Nebraska, 2019.

(56) Weiber, E. A.; Jannasch, P. Ion Distribution in Quaternary-Ammonium-Functionalized Aromatic Polymers: Effects on the Ionic Clustering and Conductivity of Anion-Exchange Membranes. *ChemSusChem* **2014**, *7* (9), 2621–2630. https://doi.org/10.1002/cssc.201402223.

(57) Osman, A. I.; Hefny, M.; Abdel Maksoud, M. I. A.; Elgarahy, A. M.; Rooney, D. W. Recent Advances in Carbon Capture Storage and Utilisation Technologies: A Review. *Environ. Chem. Lett.* **2021**, *19* (2), 797–849. https://doi.org/10.1007/s10311-020-01133-3.

(58) Wang, T.; Huang, J.; He, X.; Wu, J.; Fang, M.; Cheng, J. CO_2 Fertilization System Integrated with a Low-Cost Direct Air Capture Technology. *Energy Procedia* **2014**, *63*, 6842–6851. https://doi.org/10.1016/j.egypro.2014.11.718.

(59) Hou, C.; Wu, Y.; Jiao, Y.; Huang, J.; Wang, T.; Fang, M.; Zhou, H. Integrated Direct

Air Capture and CO_2 Utilization of Gas Fertilizer Based on Moisture Swing Adsorption. *J. Zhejiang Univ. A* **2017**, *18* (10), 819–830. https://doi.org/10.1631/jzus.A1700351.

(60) Wang, T.; Lackner, K. S.; Wright, A. B. Moisture-Swing Sorption for Carbon Dioxide Capture from Ambient Air: A Thermodynamic Analysis. *Phys. Chem. Chem. Phys.* **2013**, *15* (2), 504–514. https://doi.org/10.1039/c2cp43124f.

(61) Wang, T.; Liu, J.; Lackner, K. S.; Shi, X.; Fang, M.; Luo, Z. Characterization of Kinetic Limitations to Atmospheric CO_2 Capture by Solid Sorbent. *Greenh. Gases Sci. Technol.* **2016**, *6* (1), 138–149. https://doi.org/10.1002/ghg.1535.

(62) Hsiao, E.; Barnette, A. L.; Bradley, L. C.; Kim, S. H. Hydrophobic but Hygroscopic Polymer Films-Identifying Interfacial Species and Understanding Water Ingress Behavior. *ACS Appl. Mater. Interfaces* **2011**, *3* (11), 4236–4241. https://doi.org/10.1021/am200894h.

(63) Li, Y.; Liu, Y.; Savage, A. M.; Beyer, F. L.; Seifert, S.; Herring, A. M.; Knauss, D. M. Polyethylene-Based Block Copolymers for Anion Exchange Membranes. *Macromolecules* **2015**, *48* (18), 6523–6533. https://doi.org/10.1021/acs.macromol.5b01457.

(64) He, H.; Li, W.; Zhong, M.; Konkolewicz, D.; Wu, D.; Yaccato, K.; Rappold, T.; Sugar, G.; David, N. E.; Matyjaszewski, K. Reversible CO_2 Capture with Porous Polymers Using the Humidity Swing. *Energy Environ. Sci.* **2013**, *6* (2), 488–493. https://doi.org/10.1039/C2EE24139K.

(65) He, H.; Li, W.; Lamson, M.; Zhong, M.; Konkolewicz, D.; Hui, C. M.; Yaccato, K.; Rappold, T.; Sugar, G.; David, N. E.; Damodaran, K.; Natesakhawat, S.; Nulwala, H.; Matyjaszewski, K. Porous Polymers Prepared via High Internal Phase Emulsion Polymerization for Reversible CO_2 Capture. *Polymer (Guildf).* **2014**, *55* (1), 385–394. https://doi.org/10.1016/j.polymer.2013.08.002.

(66) Song, J.; Zhu, L.; Shi, X.; Liu, Y.; Xiao, H.; Chen, X. Moisture Swing Ion-Exchange Resin-PO4 Sorbent for Reversible CO_2 Capture from Ambient Air. *Energy and Fuels* **2019**, *33* (7), 6562–6567. https://doi.org/10.1021/acs.energyfuels.9b00863.

(67) Hou, C.; Wu, Y.; Wang, T.; Wang, X.; Gao, X. Preparation of Quaternized Bamboo Cellulose and Its Implication in Direct Air Capture of CO_2. *Energy & Fuels* **2019**, *33* (3), 1745–1752. https://doi.org/10.1021/acs.energyfuels.8b02821.

(68) Parzuchowski, P. G.; Świderska, A.; Roguszewska, M.; Rolińska, K.; Wołosz, D. Moisture- and Temperature-Responsive Polyglycerol-Based Carbon Dioxide Sorbents—The Insight into the Absorption Mechanism for the Hydrophilic Polymer. *Energy & Fuels* **2020**, *34* (10), 12822–12832. https://doi.org/10.1021/acs.energyfuels.0c02174.

(69) He, H.; Zhong, M.; Konkolewicz, D.; Yacatto, K.; Rappold, T.; Sugar, G.; David, N. E.; Gelb, J.; Kotwal, N.; Merkle, A.; Matyjaszewski, K. Three-Dimensionally Ordered Macroporous Polymeric Materials by Colloidal Crystal Templating for Reversible CO_2 Capture. *Adv. Funct. Mater*. **2013**, *23* (37), 4720–4728. https://doi.org/10.1002/adfm.201300401.

(70) Wang, T.; Wang, X.; Hou, C.; Liu, J. Quaternary Functionalized Mesoporous Adsorbents for Ultra - High Kinetics of - Capture from Air. *Sci. Rep.* **2020**, No. 0123456789, 1–8. https://doi.org/10.1038/s41598-020-77477-1.

(71) Hou, C.; Kumar, D. R.; Jin, Y.; Wu, Y.; Lee, J. J.; Jones, C. W.; Wang, T. Porosity and Hydrophilicity Modulated Quaternary Ammonium-Based Sorbents for CO_2 Capture. *Chem. Eng. J.* **2021**, *413* (October), 127532. https://doi.org/10.1016/j.cej.2020.127532.

4 CHAPTER 4: POLYSULFONE-BASED MEMBRANES FOR DIRECT AIR CAPTURE

This chapter presents an exploration of the fabrication and performance assessment of dense membranes functionalized with moisture swing active sites, aimed at advancing the development of an artificial tree concept (**Figure 4.1**) and how variations in sorbent form factors impact the moisture swing sorption (MSS) direct air capture (DA)C process.

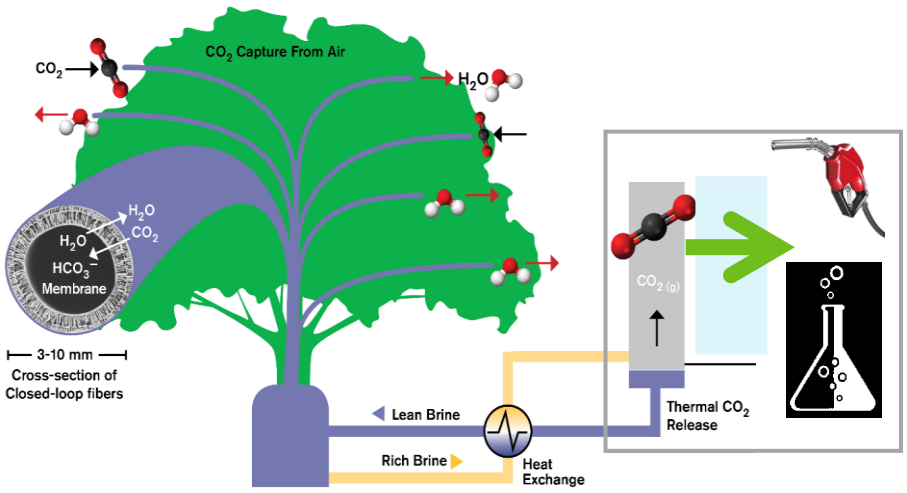

Figure 4.1 Concept for an artificial tree from the Mining Air for Fuels and Fine Chemicals (MAFF) project[1]

Dense membranes were fabricated from Udel® P-1700 PSU as reported in **section 3.4.1.9**. Scanning Electron Microscopy (SEM) imaging of the cross section was performed to probe the microstructure of the fabricated dense membrane. The cross-section was analyzed using a Philips, Model XL30 ESEM-FEG SEM operating at 15 kV. The membrane was inserted in liquid nitrogen, and then fractured to create a clean break. SEM sample was sputter coated with a thin layer of gold (30 s) to impart electric conductivity before testing. The

left image in **Figure 4.2** shows an image of the Udel® P-1700 PSU membrane being visually dense. Very small pores of <1 µm are observed at some areas in the cross section in SEM imaging (**Figure 4.2**, right).

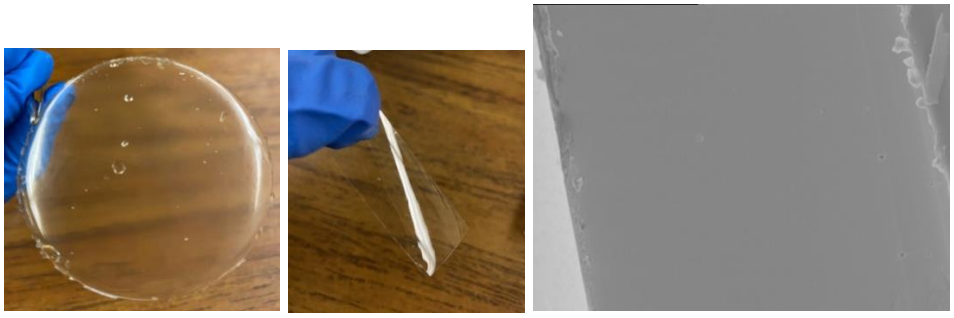

Figure 4.2 PSf membrane made following the dense membrane casting protocol (left and middle) and SEM image of the cross section (right).

Following the successful confirmation of fabrication of dense membrane, the established protocol was similarly applied to the QA-functionalized polysulfones. In this examination, it was observed that Udel® P-1700 PSU and PAES-co-QAPAES[HCO_3^-](25) polymers exhibited favorable mechanical properties, allowing them to be cleanly removed from the petri dish intact. However higher charge content polymers produced membranes that were brittle, resulting in either large or small pieces upon removal, indicating less satisfactory mechanical characteristics (**Figure 4.3**). Such diminished mechanical performance is commonly observed in dry ionic polymers with high charge content below their glass transition temperature (T_g).

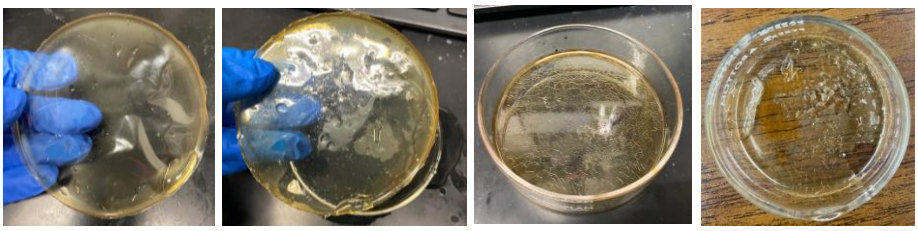

Figure 4.3 From left to right, dense membranes casted with progressively increasing QA content, specifically 12, 20, 34, and 75 mol% QAPAES segment in PAES-co-QAPAES.

In order to overcome the issue of limiting ion exchange capacity (IEC), which adversely affects the mechanical properties and structural integrity of the modified dense membranes, particularly those with higher concentrations of ion exchange groups, several strategies aimed at enhancing the mechanical robustness while maintaining or improving the IEC were explored. The approaches included:

1. Blending PAES-co-QAPAES with commercial polysulfone.
2. Adding PAES-co-QAPAES on a polysulfone-based support using spin coating method.
3. Adding PAES-co-QAPAES on a polysulfone-based support using automated draw down machine.
4. Investigating a multi block polymeric structure as opposed to the random copolymer structure.

4.1 Blending PAES-co-QAPAES with commercial polysulfone

To improve the mechanical properties of PAES-co-QAPAES, a series of blends were prepared with membrane grade commercial polysulfone polymer (Udel® P-1700 PSU) as listed in **Table 4.1**. The table shows the mass of uncharged polysulfone, weight percent of PAES-co-QAPAES, mole fraction of charge species within the polymer repeat unit

compared to all potential substituent sites, ion exchange capacity (IEC) and membrane properties.

Table 4.1 QA-functionalized poly(arylene ether sulfone) blended with membrane grade polysulfone.

#	QAPAES (g)	Polysulfone (g)	Wt. %	Mol. % charge	IEC (mol/kg)	Properties
1	0.5622 PAES(75)-co-[QAPAES][I](25)	0.7489	-	-	-	did not dissolve
2	0.2955 PAES(25)-co-[QAPAES][I](75)	0	100%	75%	2.91	Very brittle
3	0.2304 PAES(25)-co-[QAPAES][I](75)	0.0830	74%	31%	2.14	Very brittle
4	0.1596 PAES(25)-co-[QAPAES][I](75)	0.1583	50%	14%	1.46	brittle
5	0.0292 PAES(25)-co-[QAPAES][OH](75)	0.0649	31%	7%	0.90	brittle
6	0.1999 PAES(25)-co-[QAPAES][I](75)	0.4664	30%	6%	0.87	Ductile membrane (discolored)
7	0.1035 PAES(25)-co-[QAPAES][I](75)	0.3230	24%	5%	0.71	Ductile membrane
8	0 PAES(25)-co-[QAPAES][I](75)	0.5	0%	0%	0	Ductile membrane

One of the polymers did not redissolve in dimethylformamide (DMF) which is suspected to have crosslinked in storage (#1 in **Table 4.1** and **Figure 4.4**). For the rest, as the weight percentage of QA with respect to commercial polysulfone is decreased, an increase in membrane ductility was observed which is as expected. At 24 wt.%, a uniform ductile membrane was obtained (#7 in **Figure 4.4 and Table 4.1**) and at 0% PAES-co-QAPAES, the membrane was ductile (#8 in **Figure 4.4 and Table 4.1**). . At 30 wt.%, the membrane came out ductile, but with a two phased discoloration (#6 in **Figure 4.4 and Table 4.1**).

With this method, a limit in adding QA groups whilst having a homogeneous and ductile membrane was observed.

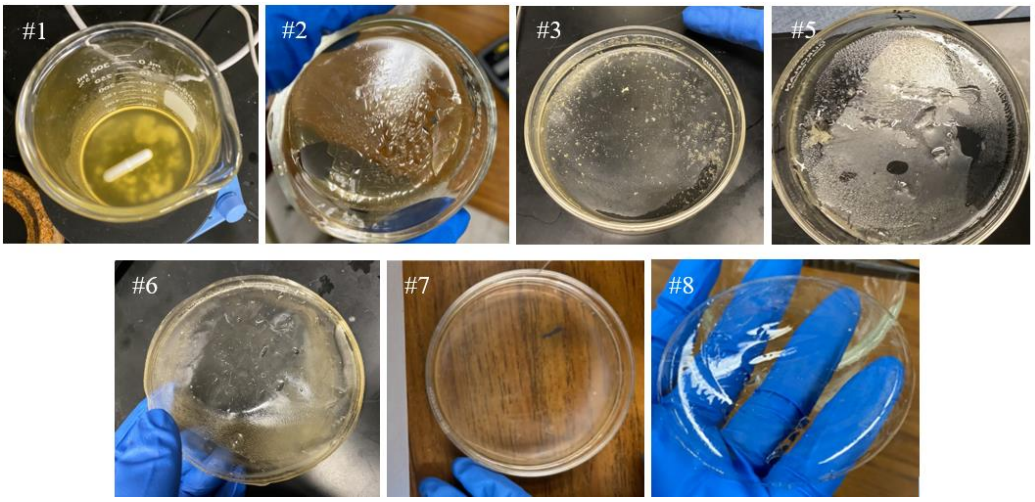

Figure 4.4 QA-functionalized poly(arylene ether sulfone) blended with commercial polysulfone.

4.2 Adding PAES-co-QAPAES on a support using spin coating method

The spin coating technique is a common and simple process used to uniformly deposit thin coatings over a substrate. A solution of PAES-co-QAPAES in DMF can be spin coated on a ductile polysulfone (PSf)-based support membrane to make a thin film composite (TFC) membrane. In this process (**Figure 4.5**), the solvent is spread and removed by the centrifugal force through rotation of the spin coating equipment at high speed, and with that, the PAES-co-QAPAES polymer is attached to the support membrane at the interface.

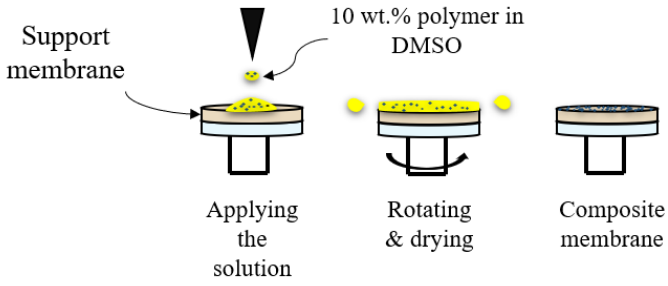

Figure 4.5 Spin coating PAES-co-QAPAES on top of PSf membrane.

For this method to work, a solvent must be identified that dissolves PAES-co-QAPAES but not the PSf support. To find this solvent, the Hansen solubility parameters (HSP) have been studied. HSP is a useful tool in predicting if a pure material will dissolve in another and form a solution.[2] **Figure 4.6** shows the parameters used in HSP analysis. In this analysis, if the RED (relative energy difference) of the system is above 1, the system will not dissolve, i.e., PSf will not dissolve in the solvent and can be considered as a candidate for adding PAES-co-QAPAES on PSf, if it dissolves the charged polymer. A list of solvents was collected with an RED>1 for PSf and were tested for their performance in dissolving PAES-co-QAPAES.[3] The PAES-co-QAPAES Polymer beads with bicarbonate counter ion were chosen for these experiments.

$$R_a^2 = 4(\delta_{d2} - \delta_{d1})^2 + (\delta_{p_2} - \delta_{p_1})^2 + (\delta_{h_2} - \delta_{h_2})^2$$

$$R_0 = solubility\ radius\ of\ polymer$$

R_a = HSP Distance between two molecules
δ_d = energy from dispersion forces between molecules
δ_p = energy from dipolar intermolecular force between molecule
δ_h = energy from hydrogen bonds between molecules

$R_{a/}R_0 > 1$ polymer non soluble in solvent
$R_{a/}R_0 < 1$ polymer soluble in solvent
$R_{a/}R_0 = 1$ polymer partially soluble in solvent

$R_{a/}R_0$: relative energy difference (RED)

Figure 4.6 Hansen solubility parameter calculation.

The tests revealed that dimethyl sulfoxide (DMSO) is an appropriate solvent, as it fully dissolves PAES-co-QAPAES but does not effectively dissolve the PSf-based support at room temperature. The polymers were shipped to our collaborators at the University of Texas at Austin, Dr. Benny Freeman's group, which undertook the task of fabricating the membranes. They were dissolved in a 10 wt.% concentration in DMSO, stirred for 4 h, filtered, sonicated for 10 min, and then spin coated on a poly(ether sulfone) (PES) support for 1 minute.

4.3 Depositing PAES-co-QAPAES on a support using automated draw down machine

Automated draw down machines or film applicators are widely used in industries for evenly applying coatings or films onto panels or substrates with large-scale production. This process allows for customizable coatings by adjusting speed, pressure, and film thickness. By utilizing the same solvent, DMSO, the PAES-co-[QAPAES][I](25) polymer was deposited on a commercial PSf membrane (PS-20) by our collaborators at UT Austin (**Figure 4.8**) with an automated draw down machine. A Gardco automatic drawdown M machine with a rod size of 10 inch was utilized for this process. A 5 wt.% solution of PAES-co-[QAPAES][I](25) in DMSO was used as the casting solution. The TFC membranes were dried overnight inside a fume hood, followed by drying under vacuum at 100 °C for 48 h prior to delivery.

4.4 Multi-block copolymer structure

Investigations into block polymeric structures have demonstrated that incorporating a higher number of charged sites into the polymer backbone can still preserve mechanical integrity. To develop a ductile membrane suitable for MSS, collaboration was established with Dr. Dan Knauss and Dr. Alison Biery from the Colorado School of Mines. A series of multiblock copolymers containing polydiallyldimethylammonium (PDADMA) and polysulfone (PSf) blocks were synthesized. The PSf blocks contribute to mechanical strength, whereas the PDADMA blocks facilitate the moisture swing DAC. Multiblock copolymers were synthesized at high yield, and PDADMA(OH)-PSf multi block copolymer films with good flexibility and strength were formed with IECs of 424 μmol/g (17 mol% PDADMA(OH)), 1,407 μmol/g (44 mol% PDADMA(OH)) and 1,726 μmol/g (50 mol% PDADMA(OH)) (**Figure 4.7**). The production of dense films and the subsequent exchange of counterions were conducted in the laboratory of our collaborators, who then supplied the finished materials to study for moisture swing DAC.[4] A schematic of the MSS process for these block polymers is shown in **Figure 4.8**.

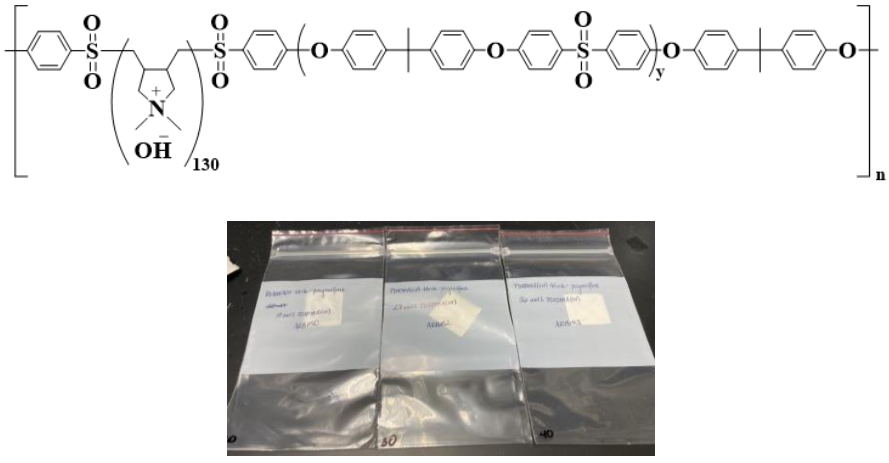

Figure 4.7 PDADMA(OH)-PSf multi block copolymers structure (top) and membranes (bottom).

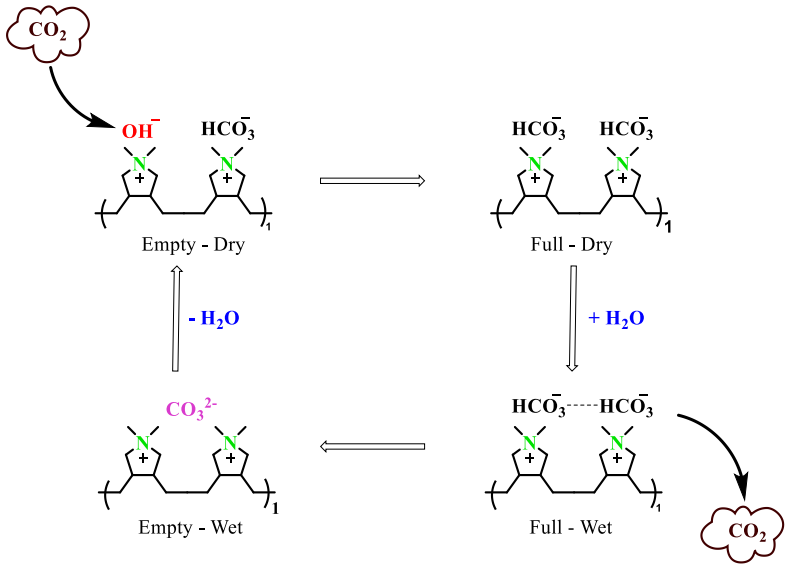

Figure 4.8 Moisture swing DAC for PDADMA(OH)-PSf multi block copolymers[4]

4.4.1 Experimental

4.4.1.1 Thermogravimetric Analysis (TGA)

Thermogravimetric analysis (TGA) was carried out on a TA Instruments TGA 5500. Samples were heated under N_2 to 100 °C at 40 °C/min, held at 100 °C for 30 min, then heated to 800 °C at 10 °C/min before being cooled to room temperature. All runs were performed in a platinum HT pan with an empty platinum HT pan as reference.

4.4.1.2 Differential scanning calorimetry (DSC)

Differential scanning calorimetry (DSC) was performed on a TA Instruments Q20 DSC to measure thermal transitions. A manual quench cooling accessory and liquid nitrogen coolant was used. Samples in non-hermetically sealed T-zero aluminum pans were heated from 0 °C to 210 °C at a rate of 10 °C/min then cooled back down to -150 °C at the same rate. Two heating cycles were completed and data from the second cycle was used to determine glass transition (T_g) temperatures. All runs were completed under a 50 mL/min

flow of N_2 with an empty T-zero aluminum pan as reference. TA instruments Universal Analysis software (V 4.5A) was used to report the midpoint T_g.

4.4.1.3 Atomic force microscopy (AFM)

Atomic force microscopy (AFM) was performed on a Bruker MultiMode 8 using a Tap150-G probe (force constant of 5 N/m and resonance frequency of 150 kHz) at room temperature.

4.4.2 Result and discussion: PDADMA(OH)-PSf multi block thermal and morphological properties

Given that the end objective for these materials is to use for DAC purposes the thermal stability of the polymers was studied. The TGA results show that even at the highest incorporation of PDADMA(OH) studied (50 mol% PDADMA(OH)-PSf), no significant degradation of the copolymer is observed at ambient temperatures. Degradation temperatures at 5% weight loss ($T_{d5\%}$) of polymers occurs at 345-383 °C, which is only up to a 32% decrease from $T_{d5\%}$ of a homo-PSf polymer such as Udel® P-1700 PSU (**Figure 4.9**).

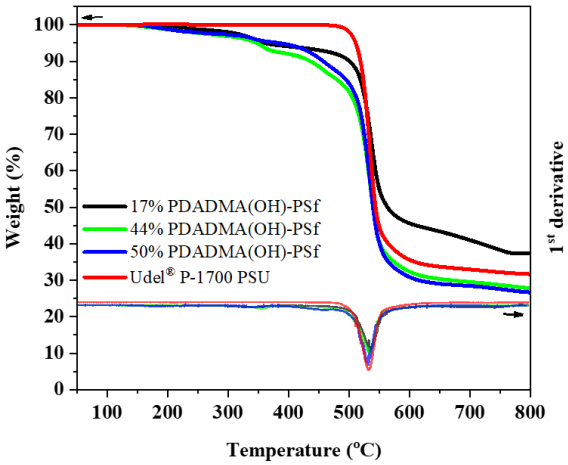

Polymer	$T_{d,5\%}$
Udel® P-1700 PSU	511 °C
17% PDADMA(OH)-PSf	360 °C
44% PDADMA(OH)-PSf	345 °C
50% PDADMA(OH)-PSf	383 °C

Figure 4.9 TGA thermograms for Udel® P-1700 PSU and 17 mol%, 44 mol% and 50 mol% PDADMA(OH)-PSf (top) and their corresponding derivative curve (bottom) obtained from thermal scanning up to 800 °C under N_2. The table on the right summarizes the degradation temperature at 5% weight loss.[4]

In addition to the thermal stability of the polymers, determining the glass transition temperature provides useful insight into the material properties. The copolymers with 17 mol% and 44 mol% PDADMA(OH) were characterized to only have one T_g at 185 °C, whereas the 50 mol% PDADMA(OH)-PSf showed a T_g at 183 °C and a second T_g at 16 °C (**Figure 4.10**). A polysulfone homopolymer, such as Udel® P-1700 PSU, has a T_g of 183 °C.[5] The observation of one T_g value equivalent to the T_g of a polysulfone homopolymer, for 17 mol% and 44 mol% PDADMA(OH)-PSf multiblock copolymers, provides support for a microphase separated microstructure. The smaller and dispersed PDADMA(OH) blocks in 17 mol% and 44 mol% PDADMA(OH)-PSf multiblock copolymers do not substantially affect the T_g of the dominant PSf block. In contrast, once enough PDADMA(OH) microdomain is present a small T_g signal at 16 °C is observed (i.e., for the 50 mol% copolymer) while the T_g at 183 ˚C remains for the PSf microdomain. The

T_g of PDADMA(Cl) homopolymer has been observed to largely vary in literature from 23 °C to above 275 °C, greatly influenced by the quantity of free and bound water.[6–8] Additionally, the T_g of polyelectrolytes is difficult to determine by DSC, which may result in these transitions being difficult to see in the DSC curves of the 17 and 44 mol% copolymers. Microphase separation is confirmed through the AFM phase images (**Figure 4.11**). The presence of high concentrations of charged species causes interactions with the AFM tip that result in changes in tip oscillation.[9] As a result, areas enriched in charged and uncharged blocks appear as different phases in the AFM images. Although no long range order develops, this behavior is common for multiblock copolymers. Increasing concentrations in the PDADMA block correspond to increasing dark areas in the AFM images, indicating the dark areas are enriched in PDADMA chains, which corresponds to previous result for similar materials.[10,11]

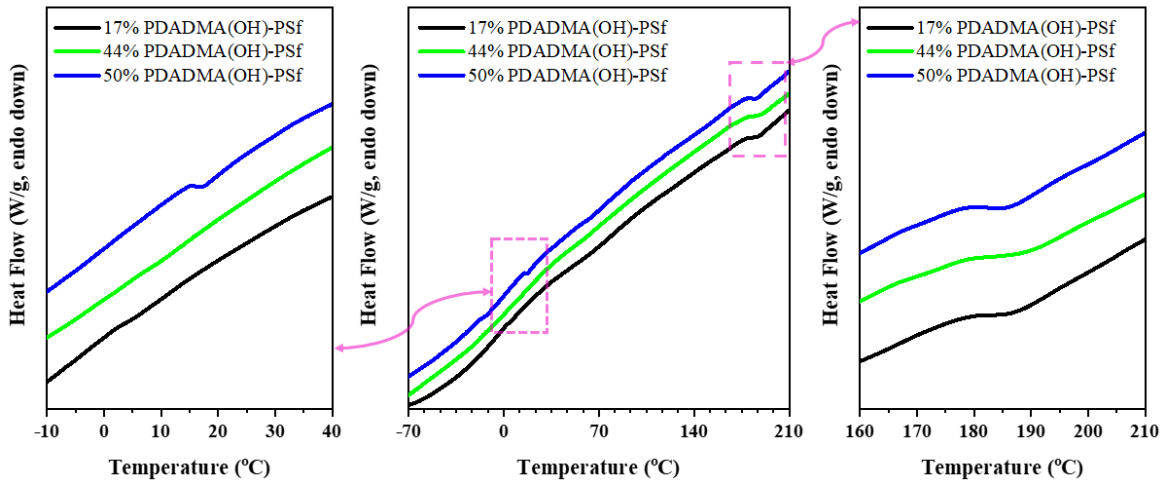

Figure 4.10 DSC curves from the second heating scan showing the T_g for the 17 mol%, 44 mol% and 50 mol% PDADMA(OH)-PSf multi block copolymer. The DSC traces are shifted vertically for clarity.[4]

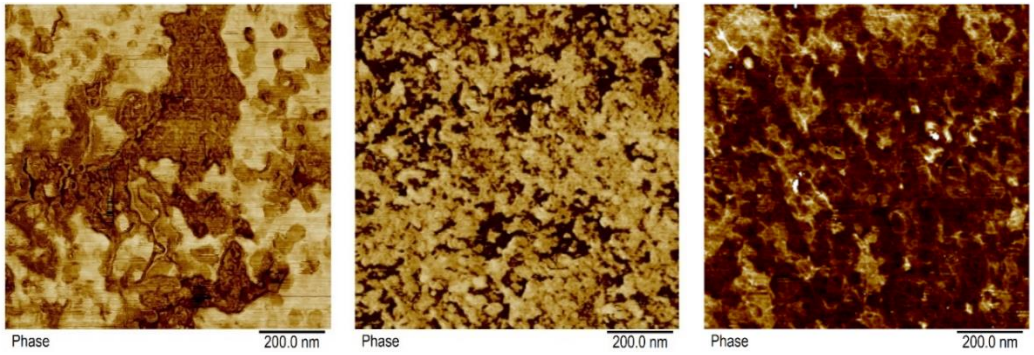

Figure 4.11 AFM images of 17 mol% (left), 44 mol% (middle), and 50 mol% (right) PDADMA(OH)-PSf multi block copolymer, displaying disordered phase separation.[4]

4.5 Result and discussion: MSS performance

To address the challenge of limited ductility associated with increased IEC, the driver of MSS sorption, in the PAES-co-QAPAES polymers discussed in Chapter 3, alternative strategies were explored. One approach involved blending the PAES-co-QAPAES polymer with commercial polysulfone (Udel® P-1700 PSU); however, this method faced limitations due to discoloration and non-homogeneity issues that arose with increased content of the charged polymer and was discontinued. Subsequently, TFC membranes were fabricated in collaboration with Dr. Benny Freeman's group at the University of Texas at Austin, utilizing techniques such as spin coating and an automated draw down machine. Furthermore, the potential of multi block copolymer structures was investigated. The ductile membranes, both free-standing and composite, were subsequently tested for their MSS activity. All films exhibited the capability for capturing and releasing atmospheric CO_2 via the moisture swing mechanism. For all tests, the sample sizes were 10 – 15 mg.

4.5.1 Spin coated TFC membrane

The TFC membrane fabricated using the spin coating technique reported to have a uniform thickness of approximately 1 µm through SEM analysis by our collaborators (**Figure 4.12**).

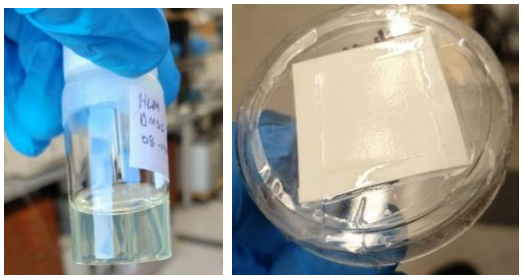

Figure 4.12 PAES-co-QAPAES[I](25) in DMSO (left) and the thin film composite membrane fabricated with spin coating technique (right).

Counterion exchange of iodide to bicarbonate was carried out on the membranes fabricated with PAES-co-QAPAES(25)[I] with a 1 M sodium bicarbonate solution in DI water at room temperature for 2 days. The ion exchanged samples were tested in the MSS setup described in **section 3.4.1.11** for a total cycle time of 4 h. **Figure 4.13** shows the CO_2 change inside the closed system in response to a swing in humidity. In this graph, the black line represents the CO_2 levels in parts per million (ppm) and the blue line represents the moisture level in parts per thousand (ppt). The sample CO_2 swing observed was 105.5 µmol/g with a 5-25 ppt (19% – 95% RH at 22 °C) moisture swing. Comparing the CO_2 swing to the calculated effective capacity, approximately 23.4% of the QA sites were utilized in the moisture swing DAC process.

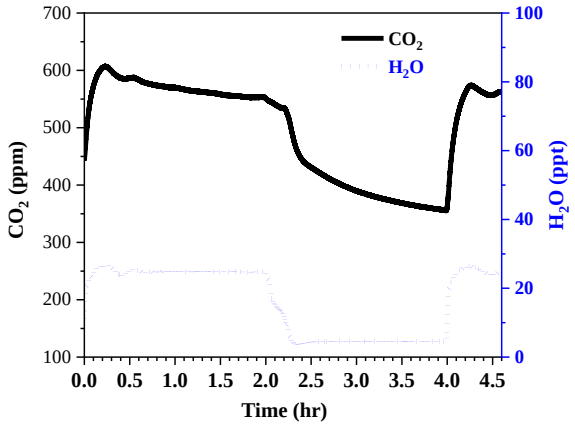

Figure 4.13 MSS results QA-functionalized poly(arylene ether sulfone) spin-coated on PES membrane.

4.5.2 TFC membrane fabricated with automated draw-down machine

Defect-free membrane were fabricated with a total area of with an area of 3.5 m^2 (or 1 ft by 38 ft) to demonstrate the scalability of material preparation (**Figure 4.14**).

Figure 4.14 TFC membrane fabricated with automated draw down machine.

After successful preparation of the TFC membrane using the automated draw down machine, the iodide counterions in PAES-co-QAPAES(25)[I] were exchanged with bicarbonates (1 M Sodium bicarbonate in DI, room temperature, 2 days) and tested in the MSS setup described in **section 3.4.1.11**. For these tests, a total cycle time of 4 h and 8 hr

was investigated, both with an 8-25 ppt (30% – 95% RH at 22 °C) humidity swing. **Figure 4.15** shows this TFC membrane's MSS performance upon the swing in humidity. The TFC membrane showed 42.5 µmol/g and 62.4 µmol/g swing for the 4 and 8 h tests, respectively. Compared to the IEC of sorbent, this amounts to a 9.4 % and 13.9% utilization of the theoretical DAC available sites in the MSS process.

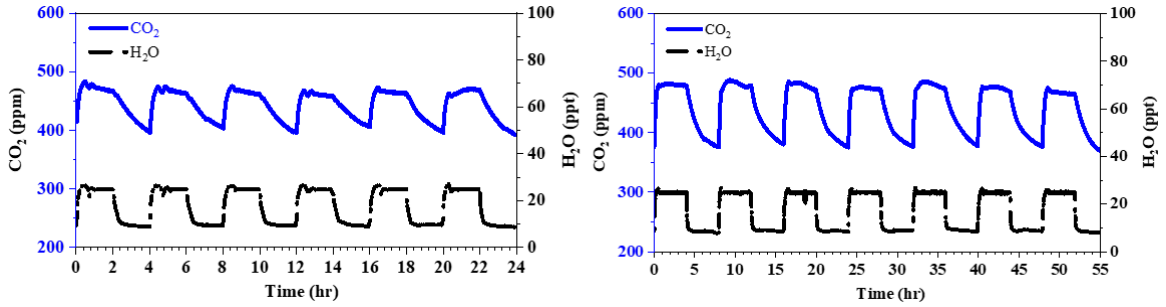

Figure 4.15 MSS results of QA-functionalized poly(arylene ether sulfone) on PS-20 membrane using draw-down machine.

4.5.3 PDADMA(OH)-PSf multi-block copolymeric membrane

The free-standing dense membranes were subjected to moisture swing DAC evaluations with the MSS setup described in **section 3.4.1.11**. CO_2 capture and release for a moisture swing of 8 ppt (30% RH) to 25 ppt (95% RH) at 22 °C and total cycle time of 2 h and 8 h was investigated. The moisture swing CO_2 sorption and desorption of the dense films with 17, 44, and 50 mol% PSf-PDADMA(OH) were recorded at negligible, 15.0, and 36.0 for 2 h cycle time, and 9.9, 25.0, and 48.3 µmol/g for a 8 hr cycle time, respectively (**Figure 4.16**). The data indicates that for dense films containing 17, 44, and 50 mol% of PSf-PDADMA(OH), the observed working capacities for CO_2 uptake and release during 8-hour cycles were 4.7%, 3.6%, and 5.6%, respectively, when compared to the membranes' theoretical capacities.

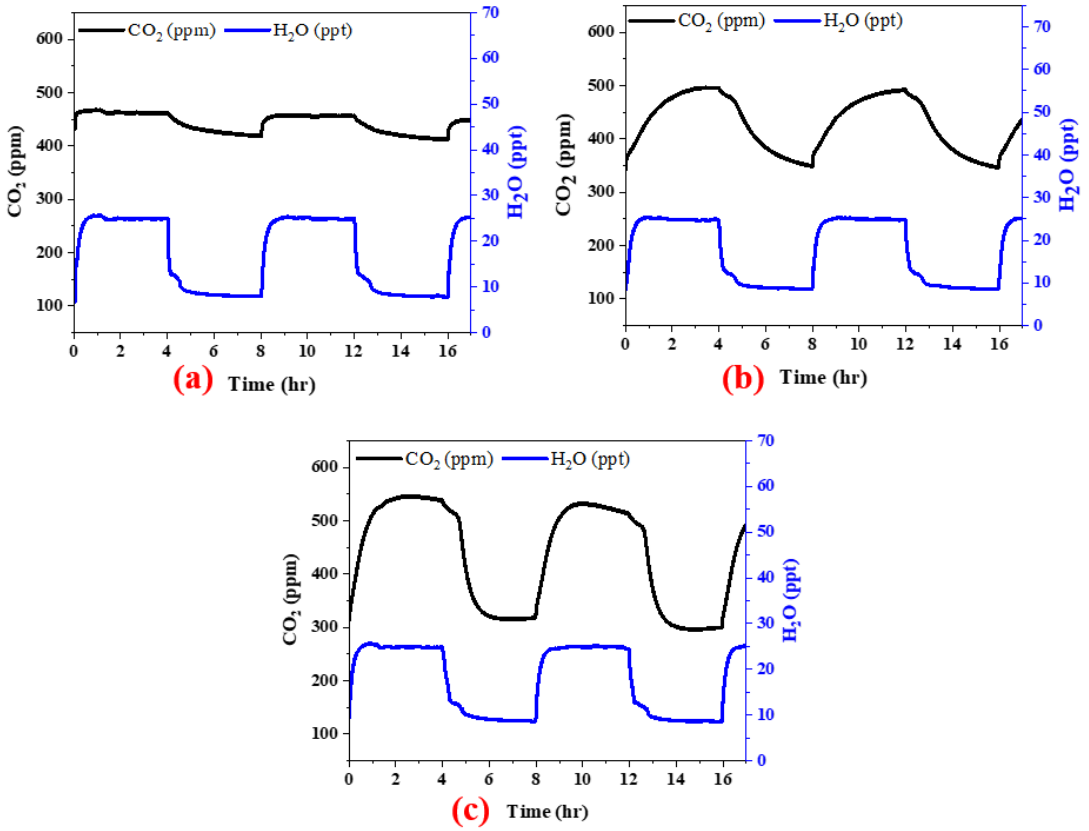

Figure 4.16 MSS results of 17 (a), 44 (b), and 50 (c) mol% multiblock DADMA(OH)-PSf copolymer films.[4]

4.5.4 Comparative analysis of MSS data

Investigations show that all materials examined can capture and release CO_2 from the atmosphere as the result of a humidity swing. The working capacity of the materials examined is lower than theoretical expectations. Comparative analyses of all MSS performance data (**Table 4.2**) highlights that the composite membranes, featuring a thin (~1 µm) active layer on top a support structure, demonstrated superior working capacities compared to powders and dense membranes (thickness ~30 µm). These findings hint at potential limitations related to CO_2 permeation within the bulk polymer, indicating a surface-dominant capture process. Future research should delve into the density and

transport properties of these membranes, focusing on the mobility and conductivity of carbonate and bicarbonate ions, to improve material performance and evaluate the efficacy of counterion exchange across all membrane types. Additionally, permeation limitations may be due to formation of hydration layer from the water molecules present in the process. High humidity content can heighten the resistance to CO_2 diffusion and surface reactions.[12] A future direction could involve assessing the MSS by testing it with a variety of polymers that span a range of hydrophilic to hydrophobic properties. In the study of PDADMA(OH)-PSf, the oligomer content on the polymer backbone was varied and effectiveness in increasing DAC efficiency was observed. Alternatively, changing the length of the oligomer could be a focus in future studies, as alterations in oligomer length can significantly influence the microstructure of the block copolymers, potentially affecting the accessibility of active groups, which in turn may impact the DAC performance. Additionally, flat films may "bury" DAC active sites within the material, lowering the material's DAC capability. Given that materials are robust thermoplastics and have the potential as a thermoplastic elastomer, exploring hierarchical structures could be a promising direction to enhance surface accessibility of DAC active sites.

Table 4.2 Summary of moisture swing DAC performance

Sorbent	Effective IEC (mmol/g)	Cycle time (h)	Moisture Swing	Working capacity
PAES-co-QAPAES[HCO_3^-](25)	0.45	2	30% – 95% RH	0.7%
PAES-co-QAPAES[HCO_3^-](50)	0.75	2	30% – 95% RH	4.0%
PAES-co-QAPAES[HCO_3^-](75)	0.97	2	30% – 95% RH	3.3%
Spin coated PAES-co-QAPAES[HCO_3^-](25)	0.45	4	19% – 95% RH	23.4%
Drawdown PAES-co-QAPAES[HCO_3^-](25)	0.45	4	30% – 95% RH	9.4%
Drawdown PAES-co-QAPAES[HCO_3^-](25)	0.45	8	30% – 95% RH	13.9%
17 mol% PDADMA(OH)-block-PSf – 2 hr	0.453	4	30% – 95% RH	-
44 mol% PDADMA(OH)-block-PSf– 2 hr	0.675	4	30% – 95% RH	2.1%
50 mol% PDADMA(OH)-block-PSf– 2 hr	0.97	4	30% – 95% RH	4.2%
17 mol% PDADMA(OH)-block-PSf– 8 hr	0.453	8	30% – 95% RH	4.7%
44 mol% PDADMA(OH)-block-PSf– 8 hr	0.675	8	30% – 95% RH	3.6%
50 mol% PDADMA(OH)-block-PSf– 8 hr	0.975	8	30% – 95% RH	5.6%

4.6 Conclusion

Thin film composite (TFC) membranes were successfully developed with PAES-co-QAPAES random polymer, and free-standing dense membranes with high IEC was developed with PDADMA(OH)-PSf multi block copolymers. All material showed

moisture swing sorption (MSS) capabilities, but with working capacities lower than their theoretical capacities. Despite the challenges associated with low working capacities, the initial demonstration of atmospheric CO_2 affinity and unique properties of PAES-co-QAPAES TFC membranes and PDADMA(OH)-PSf multiblock copolymeric membranes maintain their position as interesting materials for further investigation. This is important because it enables the application of thermoplastics for DAC of CO_2, which is a topic scarcely addressed in literature to our knowledge. Further investigation of the MSS DAC process is essential, with expected adjustments to the membrane structure likely to improve its working capacity.

4.7 References

(1) Green, M.; Lackner, K.; Behbahani, H.; Kaneko, Y.; Niimoto, K.; Mithaiwala, H.; Yang, Y.; Stirling, R.; Flory, J.; Freeman, B.; Kumar, M.; Marques, H.; Wang, W.; Bridge, A.; Gleason, K.; Wade, J.; Smith, E.; Stratton, R. *Mining Air for Fuels and Fine Chemicals*; 2022. https://doi.org/10.2172/1869810.

(2) Hansen, C. M. *Hansen Solubility Parameters*; CRC Press, 2007. https://doi.org/10.1201/9781420006834.

(3) Hansen, C. M. *Solubility Parameters for Polyphenylene Sulfide (PPS) and Polyether Sulphone (PES)*; Centre for Polymer Composites, 1991.

(4) Biery, A. R.; Shokrollahzadeh Behbahani, H.; Green, M. D.; Knauss, D. M. Polydiallylammonium-Polysulfone Multiblock Copolymers for Moisture-Swing Direct Air Capture of Carbon Dioxide. *ACS Appl. Polym. Mater.* **2024**, *6* (5), 2649–2658. https://doi.org/10.1021/acsapm.3c02850.

(5) Shokrollahzadeh Behbahani, H.; Mithaiwala, H.; Marques, H. L.; Wang, W.; Freeman, B. D.; Green, M. D. Quaternary Ammonium-Functionalized Poly(Arylene Ether Sulfone) Random Copolymers for Direct Air Capture. *Macromolecules* **2023**, *56* (16), 6470–6481. https://doi.org/10.1021/acs.macromol.3c00760.

(6) Zhang, Y.; Batys, P.; O'Neal, J. T.; Li, F.; Sammalkorpi, M.; Lutkenhaus, J. L. Molecular Origin of the Glass Transition in Polyelectrolyte Assemblies. *ACS Cent. Sci.* **2018**, *4* (5), 638–644. https://doi.org/10.1021/acscentsci.8b00137.

(7) Lyu, X.; Clark, B.; Peterson, A. M. Thermal Transitions in and Structures of Dried Polyelectrolytes and Polyelectrolyte Complexes. *J. Polym. Sci. Part B Polym. Phys.* **2017**, *55* (8), 684–691. https://doi.org/10.1002/polb.24319.

(8) Francis, S.; Varshney, L.; Sabharwal, S. Thermal Degradation Behavior of Radiation Synthesized Polydiallyldimethylammonium Chloride. *Eur. Polym. J.* **2007**, *43* (6), 2525–2531. https://doi.org/10.1016/j.eurpolymj.2007.03.009.

(9) Heinz, W. F.; Hoh, J. H. Relative Surface Charge Density Mapping with the Atomic Force Microscope. *Biophys. J.* **1999**, *76* (1 I), 528–538. https://doi.org/10.1016/S0006-3495(99)77221-8.

(10) Biery, A. R.; Knauss, D. M. Synthesis and Properties of Cationic Multiblock Polyaramides and Polyimides. *J. Polym. Sci.* **2022**. https://doi.org/10.1002/pol.20220447.

(11) Strasser, D. J.; Graziano, B. J.; Knauss, D. M. Base Stable Poly(Diallylpiperidinium Hydroxide) Multiblock Copolymers for Anion Exchange Membranes. *J. Mater. Chem. A* **2017**, *5* (20), 9627–9640. https://doi.org/10.1039/c7ta00905d.

(12) Dong, H.; Wang, T.; Wang, X.; Liu, F.; Hou, C.; Wang, Z.; Liu, W.; Fu, L.; Gao, X. Humidity Sensitivity Reducing of Moisture Swing Adsorbents by Hydrophobic Carrier Doping for CO_2 Direct Air Capture. *Chem. Eng. J.* **2023**, *466*, 143343. https://doi.org/10.1016/j.cej.2023.143343.

5 CHAPTER 5: POLYSULFONES FOR WATER TREATMENT

5.1 Water crisis

Access to clean water is crucial for sustaining life on Earth, maintaining health and fostering economic development. Approximately 71% of the Earth's surface is covered by water, yet only 3% of this is freshwater, which is water containing low concentrations of dissolved salts or impurities.[1] This type of water, suitable for consumption and agriculture, is found in rivers, lakes, aquifers, and glaciers. Of this scarce amount of freshwater (3%), ~83% is sequestered within the cryosphere in a frozen state making them inaccessible for direct use, meaning only ~0.5% of Earth's water is available freshwater.[1] Climate change, population growth and suboptimal and unsustainable management have further strained the availability of freshwater in many regions, leading to a water crisis where the available resources cannot meet the demand. Climate change is further exacerbating water scarcity through unpredictable precipitation changes, drought and the contamination of water resources.[2,3] Water scarcity also impacts food security by reducing crop productivity and affecting yields, underscoring the vital link between water availability and food supply.[4] According to UNICEF, around 1 in 3 children, or about a billion globally, faced high or extremely high levels of water scarcity in 2022.[5] Additionally, approximately 2 out of 3 people or roughly 4 billion people globally undergo severe water scarcity for at least one month annually.[6] **Figure 5.1** illustrates the global physical and economic water scarcity. Physical water scarcity refers to the lack of available water resources in the region, with

consumption outpacing replenishment, and economic water scarcity refers to a situation where the region lacks the financial resources to access freshwater.

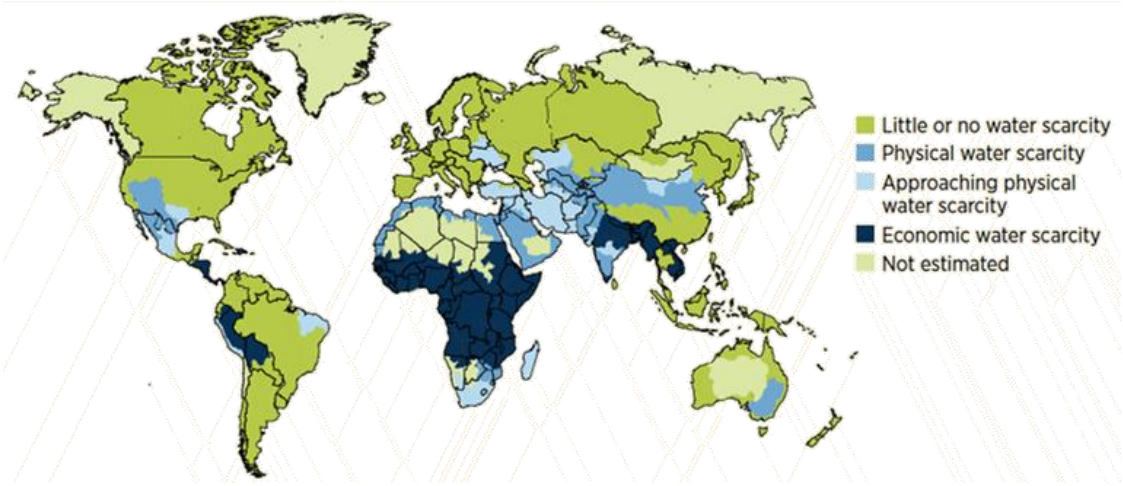

Figure 5.1 Regions facing physical and economic water scarcity in 2012.[7]

Various technological and infrastructural solutions have been developed to address water shortages worldwide.[8] Some strategies are focused on enhancing the efficiency and management of existing water resources, while others are designed to enhance water supply by generating new sources of water. Examples of methods focused on improving existing water resources include water conservation, water recycling and reuse, rainwater harvesting and improved irrigation systems.[9] Strategies focused on producing new sources of water include desalination, cloud seeding, atmospheric water harvesting, iceberg towing and water importation.[10–12] Some of these methods are in the early phases of exploration, while others have undergone further development. Depending on specific regional needs and capabilities, these strategies can be tailored, often requiring a combination of approaches for effective water shortage mitigation. Among these strategies, desalination has proven to be one of the most effective and thoroughly researched methods for

addressing water scarcity, offering the unlimited and steady supply of freshwater, though it comes with the caveat of financial and environmental expenses.

5.2 Desalination technologies

Desalination is the technological process of removing dissolved salts and minerals from saltwater. This process is becoming increasingly vital in producing freshwater and addressing global water scarcity. Historically, desalination dates back to ancient times when sailors employed simple evaporation techniques to obtain drinkable water from seawater during long voyages. These early techniques laid the groundwork for the development of desalination processes we see today. Extensive efforts in research and development have been directed towards enhancing these technologies, with an added focus on utilizing renewable energy and the utilization of waste heat as strategies to further lower financial and energy costs.[13,14] Desalination technologies today can be categorized into the primary types of thermally-driven, pressure-driven, chemical and biological and membrane-based (non pressure-driven) desalination methods.

5.2.1 Thermally-driven desalination

In thermally-driven systems, seawater is heated to produce vapor, which is then condensed into desalinated water. Examples of thermally-driven desalination include multiple-stage flash distillation, multiple-effect distillation, vapor compression distillation, solar distillation and freeze distillation.[15–17] These methods, due to their reliance on thermal energy applied to large volumes of water, can be energy intensive. This can lead to high capital and operational costs, and use of fossil fuels in some of these processes can result

in a substantial carbon footprint. They can be used independently, or combined with other desalination methods, leveraging the strengths of each to enhance efficiency, while potentially reducing energy consumption and operational costs.[18]

5.2.2 Pressure-driven desalination

Pressure-driven systems involve applying pressure to push seawater through a semipermeable membrane, effectively removing dissolved salt and minerals from water. Reverse osmosis (RO), nanofiltration and ultrafiltration are among the pressure-driven desalination methods.[19] RO is the most prevalent, using high pressure to force seawater through a semipermeable membrane, leaving salts and other impurities behind. These processes are generally less energy-intensive compared to thermal methods, however, water pre-treatment is necessary to protect the membranes from fouling. Extensive research is being conducted on pressure-driven processes for better performance and favorable energetics.[20,21]

5.2.3 Electrically-driven desalination

In electrically-driven desalination, electrical energy is utilized to remove salt and dissolved impurities from water. Electrodialysis, electrodialysis reversal and capacitive deionization are some of the desalination methods in this category.[22,23] These methods have a generally lower energy demand compared to thermal desalination techniques, but the effectiveness of these techniques can decrease as the water salinity increases. Moreover, these techniques rely on consistent availability of electrical power.

5.2.4 Chemical and microbial desalination

Chemical and microbial desalination represent desalination approaches utilizing chemical reactions and biological processes. In chemical desalination, specific chemicals are added to the water to precipitate out salts or to facilitate their removal through other processes. This method can be effective for removing specific types of salts and may also serve as a pre-treatment step or as a post-treatment process for salt recovery.[24,25] Microbial desalination, on the other hand, employs microorganisms to biologically remove salts from water. This process typically involves the use of microorganisms that can absorb and metabolize salts, effectively purifying the water.[26,27] Another notable method within this category is microbial desalination cell, which combines bio-electrochemical processes with desalination.[28] These methods generally have low energy requirements; however, the effectiveness of desalination can vary widely depending on the specific chemicals and microorganisms used and the types of salts present in the water. Additionally, microbial desalination's efficiency is highly dependent on maintaining optimal conditions for the microorganisms, which can complicate system design and operation.

5.2.5 Membrane-based desalination (non-pressure driven)

In membrane-based desalination methods that do not rely on pressure as the driving force, innovative techniques utilize gradients such as concentration or thermal, or special materials to facilitate the separation of salts from water. Forward osmosis, membrane distillation, pervaporation, biomimetic membranes, and air dehydration are some technologies within this category. These technologies potentially offer lower energy requirements, making them attractive for sustainable desalination solutions. The use of

novel materials can enhance water flux and selectivity, potentially reducing fouling and improving operational efficiency. However, the technological maturity of these methods varies, with many still in developmental or pilot stages, not yet widely implemented at commercial scales.

5.2.6 Membranes for reverse osmosis

Reverse osmosis (RO) desalination is the most reliable and widely used technique for desalination. Membranes serve as the core of the RO process, dictating the efficiency and effectiveness of the desalination process. Since the initial development of the RO membrane in 1959, the field has witnessed significant progress in various areas, including materials science (i.e. developing membranes with higher permeability) and optimization strategies (i.e. use of energy recovery systems and more efficient pumps). Investigation have shown that the power requirements to drive RO desalination has decreased significantly, and is close to the theoretical minimum free energy required for a 50% recovery.[20] **Figure 5.2** shows a notable decline in the energy requirements for the RO stage of desalination plants from 1970 to 2008. In this figure, a horizontal dashed line is used to indicate the theoretical minimum energy necessary for achieving a 50% water recovery rate from desalination of seawater with a salinity of 35 g/L, highlighting the efficiency improvements in the RO process over the years. This energy requirement does not include the energy needed for water intake, pre-treatment, post-treatment, or the disposal of brine. Given that we are close the theoretical minimum energy requirement for the reverse osmosis (RO) stage, there is opportunity to reduce the overall energy demand of the

desalination process through optimization in other stages of the desalination process, as well as through the integration of renewable energy sources.

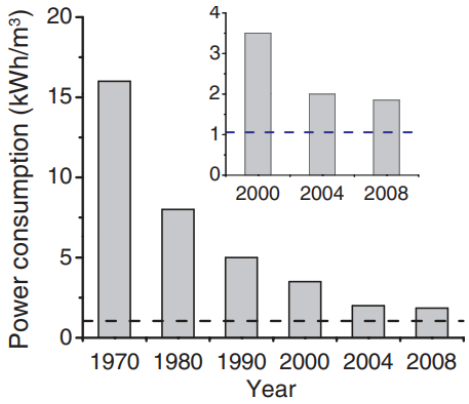

Figure 5.2 Power consumption for salt water RO plants[20]

Fouling, which is the buildup of foreign materials on the membrane surface, is a principal challenge in RO desalination.[29] It not only reduces the membrane's permeability but also significantly shortens its lifespan. The decrease in permeability requires the use of higher operating pressures to preserve water flux. Additionally, it necessitates more frequent cleaning and membrane replacement, leading to increased energy consumption and operational costs. The foreign materials contributing to fouling can include microorganisms, organic compounds, colloids, and scale-forming minerals. To address this, various strategies have been investigated such as pre-treatment of feed water, biological control, and membrane surface and chemical modification.[30–32]

5.3 Zwitterionic functionalized poly(arylene ether sulfone) copolymers

,

Reproduced with permission from: Yang, Y., Shokrollahzadeh Behbahani, H., Morgan, B. F., Beyer, B. F., Hocken, A., Green, M. D., Synthesis and thermomechanical

characteristics of zwitterionic poly (arylene ether sulfone) copolymers, Polymer, 2023, 264, 3, 125522.

To address the fouling issues associated with RO membranes, the desalination industry has turned to various strategies, among which the modification of membrane surfaces with zwitterionic compounds stands out as a particularly effective approach. Zwitterionic materials, which are compounds that possess both positive and negative charges within the same molecule, exhibit strong polarity hydrophilicity. This characteristic makes the membrane surface less attractive to fouling agents by reducing the tendency of particles, organic compounds, and microorganisms to adhere. The hydration layer formed by the zwitterionic materials on the membrane surface impedes the adhesion and accumulation of fouling agents, thereby preserving the membrane's permeability and operational lifespan.[33]

In this study, an allyl modified poly(arylene ether sulfone) backbone (PAES-co-APAES), previously evaluated for direct air capture, has been functionalized with zwitterionic groups. The effect of addition of the with zwitterionic groups on the water uptake and mechanical properties of a poly(arylene ether sulfone) backbone was investigated.[34] The zwitterionic-functionalized poly(arylene ether sulfone) (**Scheme 5.1**) with 22, 45 and 72 mol% zwitterion content were provided by Dr. Yi Yang.

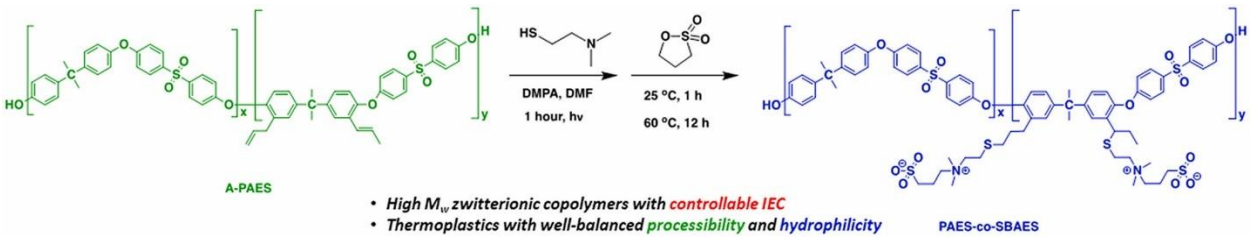

Scheme 5.1 Zwitterionic Poly(arylene ether sulfone) structure[33]

5.3.1 Experimental

5.3.1.1 Film preparation

Dense membranes were prepared from the polymers according to the procedure in **section 3.4.1.9**. The membranes were stored in DI water prior to testing.

5.3.1.2 Mechanical Testing

An Instron 5943 equipped with submersible pneumatic grips and a water bath was used to perform uniaxial tensile testing on the dense membranes. ASTM D-1708 was used to cut samples into dog bone geometry; the samples were then extended at a rate of 1 mm/min at room temperature until breakage. Replicates were analyzed, and the average values are reported.

5.3.1.3 Water uptake

To measure the water uptake, the membranes were dried using a Fisher-brand Isotemp Model 281A Vacuum Oven for 24 h at room temperature. Then, the samples were submerged and left to sit in deionized water at room temperature for 24 h. The samples were then taken out, blotted dry to remove surface droplets and weighed with a Classic MS Series Mettler Toledo scale. The water uptake is measured using **Equation 4.1**.

$$Water\ uptake\ (\%) = \left(\frac{w_w - w_d}{w_d}\right) x\ 100$$

Eq. 4.1

Here, w_w and w_d are the weights of the wet and dry sample, respectively. Replicates were analyzed and the average water uptake content was reported. The fixed charge concentration of membranes, C_x^m, is calculated using the **Equation 4.2**.

$$C_x^m = \frac{IEC \times \rho_w}{WU}$$ **Eq. 4.2**

In the above equation, IEC, which is the quantity of charged groups on the polymer backbone per weight of dry polymer is measured from the molecular weight of the repeating unit of polymers (mmol/g), WU is the water uptake (g water/g of dry polymer) and ρ_w is the density of water, assumed to be 1.0 g/mL.

5.3.2 Results and discussion

The mechanical properties and water uptakes of the zwitterionic poly(arylene ether sulfones) and are summarized in **Table 5.1**. Mechanical testing data could not be obtained for PAES-co-SBAES-22, as the films would dry and break instantly, when loading into the tensile testing apparatus. Overall, all the modified membranes exhibit good mechanical properties in aqueous environments. The Young's modulus, ultimate stress, and toughness of the membranes decreased with the addition of zwitterion content (SBAES content) from 0% to 45%, which is presumably attributed to the plasticization effect by incorporating bulky pendant chains. However, the Young's modulus, toughness, and strain at break increased as the zwitterion content increased from 45% to 72%. The ultimate stress for the 45% and 72% charge contents showed no statistically significant difference. The water uptake data report a substantial increase in absorbed water with an increase in the zwitterionic content, which is rationalized by the hydrophilic nature of the zwitterionic groups.

The water uptake data is used to calculate the fixed charge concentration of the polymers (**Table 5.1**), which decreases 14.6% as the IEC increases from 0.84 mmol/g to 1.34 mmol/g

(PAES-co-SBAES-22 to PAES-co-SBAES-45, i.e., ~60% increase in IEC) and decreases 36.6% as the IEC increases from 1.34 mmol/g to 1.67 mmol/g (PAES-co-SBAES-45 to PAES-co-SBAES-72, i.e., ~27% increase in IEC). These data provide interesting insights into the material performance, and we analyze each change in composition separately. When the charge content increases from 22% to 45% the material exhibits an increase in IEC and water sorption that are similar in magnitude (~60% and ~87%, respectively). When the charge content increases from 45% to 72%, the increase in IEC is ~27% but the water uptake is similar in magnitude to the previous jump, ~85%. This results in a similar fixed charge concentration (in mol charge/L water sorbed) for the 22% and 45% charge contents, but a much smaller fixed charge concentration at 72% zwitterionic content. Therefore, the water uptake and uniaxial tensile experiments corroborate with one another. The neutral polymer (PAES- 0) displays unique behavior: good mechanical properties and a low water uptake. However, the zwitterion copolymers have a different trend. The PAES-co-SBAES-22 copolymer could not form a stable film when hydrated, the samples broke almost instantaneously. Then, the strain at break, Young's modulus, and toughness all increase when the charge content goes from 45% to 72% and the fixed charge concentration decreases by 37%. Thus, we predict that the zwitterions form intermolecular ion bridges that serve as physical crosslinks to improve the mechanical performance from 22% to 72% charge content. As noted above, the steady increase in water uptake decreases the fixed charge concentration; but, in spite of this, the mechanical properties improve because of the physical crosslinks.

Table 5.1 Mechanical properties, water uptake, and IEC of PAES-co-SBAES copolymers.

Membrane	Young's modulus (MPa)	Ultimate Stress (MPa)	Toughness (MPa)	Strain at break (%)	Water uptake (%)	C_x^m (mol/L)	IEC (mmol/g)
PAES-co-SBAES-0	4,937.1 ± 359.5	91.8 ± 31.2	3.56 ± 2.70	3.9 ± 1.6	7.5 ± 1.3	-	0
PAES-co-SBAES-22	-	-	-	-	18.3 ± 3.9	4.8 ± 1.3	0.84
PAES-co-SBAES-45	66.8 ± 10.7	9.1 ± 4.4	0.10 ± 0.06	3.0 ± 0.4	34.3 ± 8.8	4.1 ± 1.2	1.34
PAES-co-SBAES-72	183.4 ± 86.3	8.5 ± 4.3	0.43 ± 0.13	5.7 ± 1.8	63.6 ± 5.4	2.6 ± 0.2	1.67

5.4 Lignin-derivable polysulfones as potential alternatives to bisphenol A-based water filtration membranes

To be published as: Mahajan, J., Shokrollahzadeh Behbahani, H., Green M. D., Korley, T., Epps, T., "Lignin-derivable polysulfones with increased hydrophilicity as potential alternatives to bisphenol A-based water filtration membranes"

5.4.1 Introduction

Although polysulfones (PSfs) are excellent candidates for many high-performance applications such as water treatment membranes, they are derived mainly from bisphenol A (BPA), a suspected human endocrine disruptor.[35] Because BPAs are known to leach from plastic food containers and water bottles, even at room temperature, there is reasonable concern that water separation membranes produced from PSfs could cause water contamination.[36,37] Because of the increasing health concerns associated with BPA exposure, there is desire to produce next-generation bisphenols with reduced toxicity that

can yield PSfs with comparable or better thermochemical properties. Moreover, several commercial alternatives to BPA, e.g., tetrachlorobisphenol A and bisphenol B, among others, are not necessarily safer as they can still exhibit some level of endocrine disruption potential.[38] Given that BPAs and other commercially available alternatives are non-renewable and toxic, newly produced bisphenols would ideally have reduced health risks and increased sustainability. There is growing interest in using bio-based resources for the development of next-generation materials to reduce reliance on petroleum-based feedstocks. Lignin is among the most abundant source of renewable aromatic chemicals.[39] Our collaborators at the University of Delaware have supplied us with four monomers derivable from lignin for assessment within a polysulfone framework (**Figure 5.3**).[40,41]

Bisguaiacol F (BGF) and bisguaiacol A (BGA) are to be investigated to be used in place of bisphenol F (BPF) and BPA. The lignin-derivable bisguaiacols have methoxy groups on their aromatic rings in contrast to their commercial petroleum-based structures. These methoxy groups may hinder estrogen binding, which can significantly reduce endocrine disruption potential.

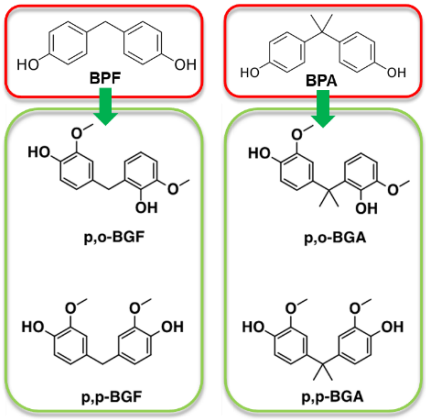

Figure 5.3 Lignin-derivable monomers as a sustainable alternative to BPA and BPF.

In this study, four polymers of BPA-based polysulfone (BPA-PSf), BGA-based polysulfone (BGA-PSf), BPF-based polysulfone (BPF-PSf), and BGF-based polysulfone (BGF-PSf), are synthesized. Their structures are evaluated with proton nuclear magnetic resonance (^{1}H NMR), and their thermal properties and hydrophilicity properties are compared. The results show comparable thermal characteristics between the lignin-based polymers versus their petroleum-based partner, with enhanced hydrophilicity.

5.4.2 Experimental

5.4.2.1 Materials and Reagents

Bisphenol A (BPA, ≥99%), 4,4'-difluorodiphenyl sulfone (DFDPS, 99%), diatomaceous earth (Celite® 545), diiodomethane (99%), and potassium carbonate (K_2CO_3, ≥99%) were purchased from Sigma-Aldrich. Bisphenol F (BPF, >99.0%) was purchased from TCI Chemicals. *N*,*N*-Dimethylacetamide (DMAc, 99.0%) and deuterated chloroform ($CDCl_3$, 99.8 atom% D, with 0.03% v/v TMS) were acquired from Acros Organics. Chloroform (≥95 %) was procured from Macron Fine Chemicals. Sodium hydroxide pellets (≥98.0%)

were purchased from LabChem. Toluene (99.8%), tetrahydrofuran (THF Optima™, ≥99.9%), HCl (36.5 - 38%) were purchased from Fisher Scientific. *N*,*N*-Dimethylformamide (DMF, ≥99.8%) and methanol (≥99.8%) were sourced from VWR. N_2 (ultra-high purity, 99.999%) was obtained from Airgas Inc., facilitated by Arizona State University gas services. BPA, BPF, and DFDPS were placed in an oven at 60 °C for 48 h before use. Toluene and THF Optima™ were purified using an MBraun SPS-800 solvent purification system prior to use. K_2CO_3 was stored in an oven at 130 °C before use. HCl was diluted in THF before use. All other chemicals were used as received.

5.4.2.2 Synthesis

PSfs were synthesized using step-growth polymerization (**Scheme 5.2**). The synthesis of BPF-PSf is reported as a representative example. The reaction setup consisted of a two-neck, round-bottomed flask (100 mL) equipped with a magnetic stirrer, reflux condenser, ultra-high purity (UHP) N_2 gas inlet and outlet, and a Dean-Stark trap. The following chemicals were added: BPF (3 g, 15 mmol), DFDPS (3.8 g, 15. mmol, 1 equiv.), K_2CO_3 (2.5 g, 18 mmol, 1.2 equiv.), DMAc (41.2 mL), and toluene (22.2 mL). Initially, the system was purged with UHP N2 for 20 min and then heated to 135 °C in an oil bath. The solution was stirred at 650 rpm for 2 h under UHP N_2 at 135 °C (i.e., at reflux) to remove water and toluene. After removing the residual toluene, the reaction continued for 24 h at 145 °C under an N_2 blanket. The solution was then cooled to ~23 °C and diluted with chloroform (~200 mL). Subsequently, the solution was neutralized by the gradual addition of 0.1 M HCl in THF in excess, with the mixture being stirred at ~23 °C for 2 h. The mixture was then vacuum- filtered through diatomaceous earth to remove salts. The solution was

concentrated using rotary evaporation (Scilogex RE 100-pro), and the product was precipitated from methanol. The isolated BPF-PSf was dried under vacuum at 80 °C for 18 h. The PSf was redissolved in THF and reprecipitated from methanol. The final product was dried under vacuum at 160 °C for 48 h. This protocol was consistently applied across all PSfs, although the lignin-derivable PSfs were synthesized using the same molar ratios but on a smaller scale (<1.9 g).

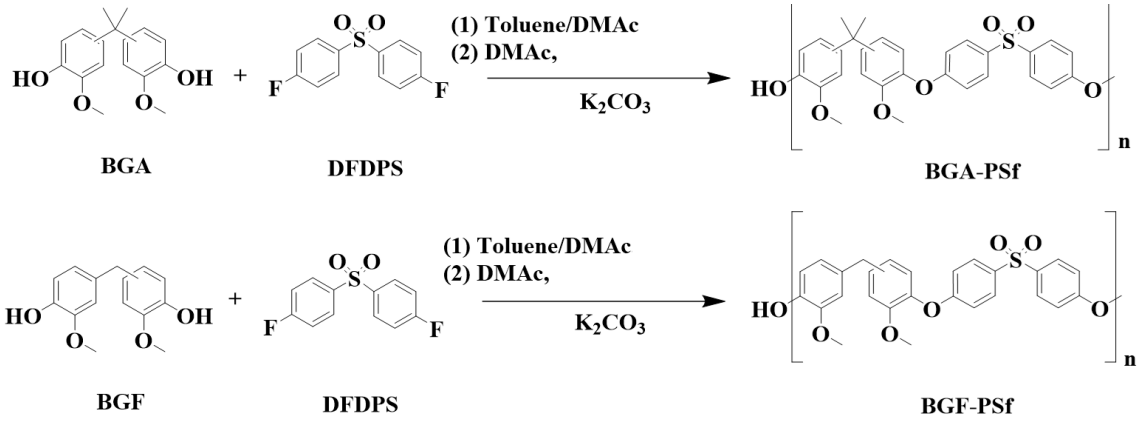

Scheme 5.2 Reactions pathways to make lignin-derivable polysulfones.

5.4.2.3 Proton nuclear magnetic resonance spectroscopy (^{1}H NMR)

^{1}H NMR analysis is performed on a Bruker Ascend 500 MHz spectrometer to study the synthesized polymers' structure. For these tests, ~20 mg of dried polymer is dissolved in ~0.7 g $CDCl_3$. ^{1}H NMR spectra were analyzed using the TopSpin v4.3.0 software package.

5.4.2.4 Size Exclusion Chromatography (SEC)

SEC was performed using a Waters Alliance e2695 HPLC system connected to a Wyatt Optilab T-rEX differential refractive index (dRI) detector. Two Waters™ Styragel® HR 5 THF and Styragel® HR 4 THF columns were used in series. This setup was linked to Astra v6.1 software, which was used for the analysis. The mobile phase was THF OptimaTM

with a flow rate of 1.0 mL/min and an injection volume of 100 µL. A calibration curve was made using five low-dispersity polystyrene (PS) samples with mid-point molecular weights (M_p) of 9.82, 30.00, 91.45, 200.0, and 482.0 kDa. PS standards (30.00 and 200 kDa) were acquired from Pressure Chemical Company, and the rest of the standards (9.82, 91.45, and 482.0 kDa) were purchased from Agilent Technologies. The SEC samples were prepared by dissolving PSfs in THF OptimaTM at ~5 mg/mL (at 23 °C). The samples were filtered using a Spectrum 0.22-µm PTFE syringe filter.

5.4.2.5 pK_a measurements

The dissociation constants (pK_a values) of BPA, BPF, BGA and BGF monomers were determined utilizing proton nuclear magnetic resonance (^{1}H NMR) spectroscopy.[42] The experiment was conducted at room temperature, 1 M and 0.1 M NaOH and HCl solutions were utilized to prepare samples of pH 0 to 12. pH measurements were carried out using Oakton PC 450 portable pH meter. Incremental adjustments of pH were achieved through the careful addition of acid and base, and the corresponding chemical shifts in the ^{1}H NMR spectra were recorded. These shifts are indicative of changes in the electronic environment surrounding the hydrogen atoms, allowing for the determination of pK_a values. Chemical shift vs pH was plotted, and the Boltzman sigmoidal fit function in Origin (version 2018) was utilized to obtain the inflection point corresponding to the pK_a value of each compound.

5.4.2.6 Differential scanning calorimetry (DSC)

The glass-transition temperatures (T_gs) of the polysulfones were measured utilizing a Q2000 calorimeter from TA Instruments. Approximately 5 mg of each sample was placed

into non-hermetically sealed aluminum pans. These pans were then heated to 190 °C at a rate of 10 °C per minute in a nitrogen atmosphere, where they were maintained at this temperature for 10 minutes. Subsequently, the samples were cooled to -80 °C at the same rate of 10 °C per minute under nitrogen and kept at this low temperature for another 10 minutes. A second heating cycle was then initiated, warming the samples back up to 200 °C at the same heating rate. The T_g values were identified at the midpoint of the inflection point, based on the data from the second heating scan, utilizing the TA Instruments Universal Analysis 2000 software (version 4.5A).

5.4.2.7 Thermogravimetric analysis (TGA)

The thermal stability of the synthesized polysulfones was assessed using a TGA 5500 from TA Instruments. Around 5 mg of each polysulfone sample was placed in a high-temperature platinum pan. This pan was initially heated to 175 °C at a rate of 10 °C per minute in a N_2 atmosphere to remove any residual moisture or solvents. After this step, the pan was cooled down to 40 °C and then reheated to 800 °C at a rate of 10 °C per minute under a continuous flow of N_2. The point of thermal stability for the polysulfones was determined and reported based on the temperature at which a 5% weight loss was observed ($T_{d5\%}$).

5.4.2.8 Dense membrane fabrication

Dense membranes were fabricated to evaluate the hydrophilicity of the polysulfones (PSfs) through contact angle measurements. The process began with dissolving the dried PSfs in DMF to achieve a concentration of 2.5% w/w. This solution was then passed through a 0.45-µm PTFE syringe filter and dispensed into a VWR petri dish with a diameter of 10

cm. The dish was covered with a loose lid and left to stand at around 23 °C for 24 hours inside a fume hood. Subsequent drying stages to evaporate DMF gradually involved placing the petri dish in a vacuum oven (Fisherbrand Isotemp Model 281A) at incrementally increasing temperatures of 23 °C, 40 °C, 100 °C, and finally 160 °C, each for 24 hours. The dried dense membrane was delaminated by introducing DI water. The membranes were dried under vacuum at 160 °C for approximately 14 hours before proceeding with the contact angle measurements.

5.4.2.9 Water Contact Angle tests (WCA)

Water contact angle measurements on the dried PSf dense membranes were conducted using a Ramé-hart automated goniometer (Model 230-U1), which is equipped with a microscope and a lighting system for observation. The DROPimage Advanced® software (version 2.7.3) was employed for analyzing the data collected during these measurements. Around 5 µL of DI water was carefully placed onto the surface of the PSf dense membranes, which had been fixed onto glass slides using Scotch™ tape. This placement of water was done using a Hamilton (model 1750TPLT) Luer tip threaded plunger syringe equipped with a 16-gauge stainless steel blunt needle. To ensure accuracy and reproducibility, each membrane was tested at six different points, with each point measured three times. The reported values represent the average of these measurements.

5.4.2.10 Surface free energy measurements

The assessment of surface free energy was performed using the Extended Fowkes's/Owens, Wendt, Rabel, and Kaelble (OWRK) model, which splits the surface energy into its polar and dispersive components. This model involves measuring the

contact angle of two liquids – one polar and one non-polar – on the membrane's surface. The known surface tensions of these liquids are then utilized to calculate the polar and dispersive components of the membrane's surface energy. A Ramé-hart automated goniometer (Model 230-U1) facilitated these measurements, and DROPimage Advanced® software (version 2.7.03) was used for data analysis. DI water was used to evaluate the polar component of surface energy, and diiodomethane was used for the dispersive component. The total surface free energy was determined by adding the values obtained for both the polar and dispersive components. For each membrane sample, five distinct areas were chosen for analysis, with each area undergoing three separate tests. The values reported represent the average of these measurements.

5.4.2.11 Water vapor uptake

The water vapor sorption (or water vapor uptake) of the PSf dense membranes were evaluated using a Q5000 sorption analyzer from TA Instruments. In these experiments, 5 to15 mg of the dense membrane was placed in quartz pans. The procedure was conducted under an ultra-high purity (UHP) N_2 atmosphere. The protocol consisted of holding the relative humidity at 0% until the weight change stabilized to less than 0.01% over a period of 5 minutes. The RH was then increased to 95% and maintained until the weight change again stabilized at less than 0.01% change for 5 minutes. Triplicates were tested for each type of membrane (BPA/BPF/BGA/BGF-PSf), and the average weight gain recorded for these tests was used to determine the water vapor uptake capacity of the membranes.

5.4.3 Results and discussion

5.4.3.1 Synthesis of lignin-derivable polysulfone

The polymers are successfully synthesized by the step-growth reaction. Analysis of ^{1}H NMR of structures (**Figures 5.4-5.7**) show the appearance of protons on the methoxy groups at 3.5-3.9 ppm for BGA-PSf and BGF-PSf when compared to BPA-PSf and BPF-PSf. The integration of peaks was used to confirm the polymer structure, indicating successful polymerization of monomers. The ^{1}H NMR spectra is as follows: BPA-PSf: ^{1}H NMR (500 MHz, $CDCl_3$) δ 7.88 – 7.82 (m, 4H), 7.26 – 7.20 (m, 4H), 7.04 – 6.97 (m, 4H), 6.97 – 6.91 (m, 4H), 1.69 (s, 6H). BPF-PSf: ^{1}H NMR (500 MHz, $CDCl_3$) δ 7.87 – 7.80 (m, 4H), 7.20 (d, J = 8.2 Hz, 4H), 7.02 – 6.92 (m, 8H), 3.98 (s, 2H). BGA-PSf: ^{1}H NMR (500 MHz, $CDCl_3$) δ 7.81 (dt, J = 6.7, 3.2 Hz, 4H), 7.21 – 6.61 (m, 9H), 3.88 – 3.61 (m, 5H), 1.82 – 1.49 (m, 6H). BGF-PSf: ^{1}H NMR (500 MHz, $CDCl_3$) δ 7.82 (dd, J = 16.8, 8.7 Hz, 4H), 7.22 – 6.70 (m, 10H), 4.09 – 3.45 (m, 8H).

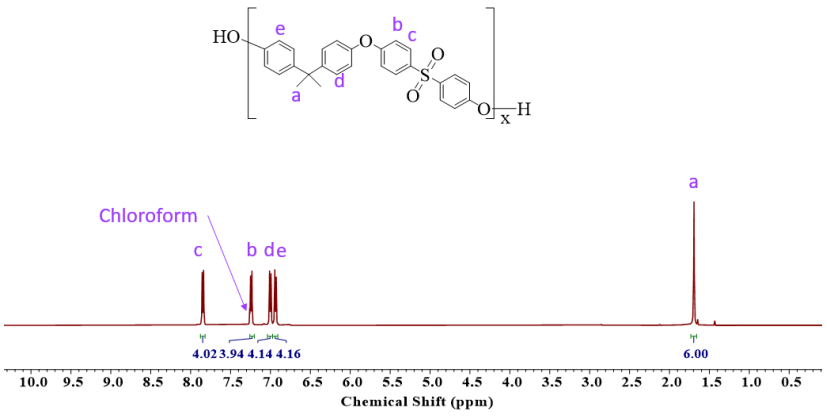

Figure 5.4 ^{1}H NMR BPA-PSf

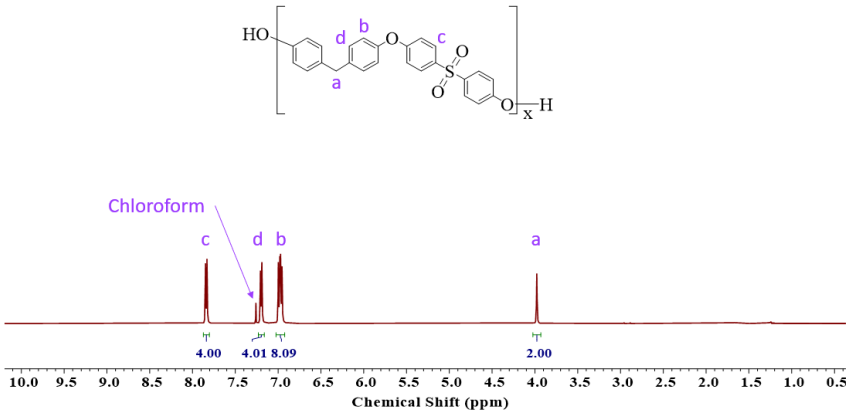

Figure 5.5 [1]H NMR BPF-PSf

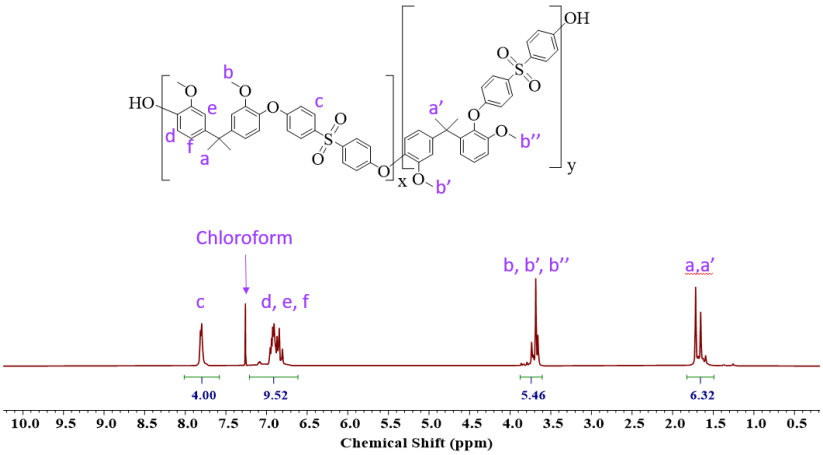

Figure 5.6 [1]H NMR of BGA-PSf

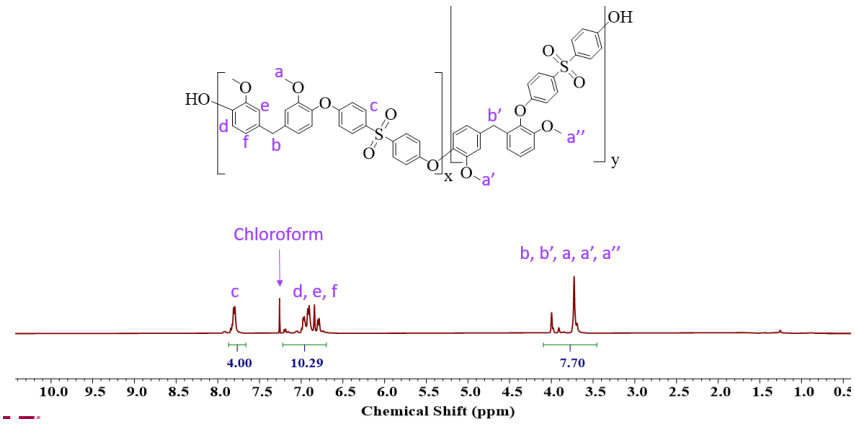

Figure 5.7 [1]H NMR of BGF-PSf

SEC traces are shown in **Figure 5.8**. The traces and dispersity values are indicative of a broader molecular weight distribution than typically aimed for in polysulfone step growth synthesis. Specifically, the number-average molecular (M_n) ranges from 14.5 to 48.0 kDa, while the dispersity values (Đ) span from 1.6 to 3.4, suggesting a wide molecular weight distribution. Utilizing the same synthesis protocols, BPA and BPF-based PSfs show approximately 20% and 70% higher M_n, respectively, compared to their lignin-derivable counterparts. The cyclic oligomer content of the polymers (the right shoulder on the SEC trace) ranges from 8.5% to 23.2% with the lignin-derivable PSfs showing up to 100% more cyclic generation. The observed variations in molecular weights and Đ values of the synthesized polymers point to an intricate interplay of factors during the polymerization process and invite further reaction kinetic studies.

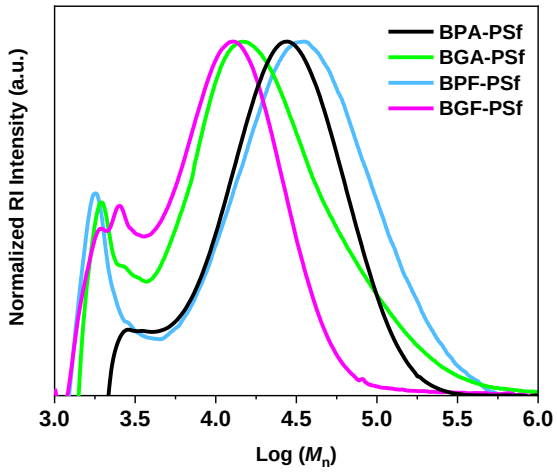

Figure 5.8 Normalized RI as a function of logarithmic molar mass (M_n) measured via SEC for PSfs.

The following may be some factors influencing the molecular weight and Đ of the polymers: The differences in monomer structures (i.e. the presence and absence of methoxy groups) and structural isomer ratios likely have a significant impact on the reactivity and

steric effects during the step-growth polymerization. Additionally, the presence of methoxy groups on lignin-derived monomers suggests potential pK_a differences compared to BPA- and BPf-based monomers, which is critical in the deprotonation step of the synthesis; this raises the question of whether K_2CO_3 is sufficiently basic to efficiently deprotonate the lignin-derivable monomers. The pK_a value is a quantitative measure of the strength of an acid, representing its ability to donate a proton.[43] The lower pK_a (more acidic) a compound, the more easily it is deprotonated with a base. Even though the exact impact of pK_a differences on deprotonation extent can vary due to several factors, generally, even a relatively small difference in pK_a can lead to significant effects on the extent of deprotonation. Changes in monomer pK_a were evaluated with ^1H NMR are shown in **Figure 5.9**. Using the Boltzman sigmoidal fit, the pK_a of BPA, BPF, BGA and BGF were measured as 10.4, 9.6, 9.5 and 9.8 respectively. The data reveals that BGA exhibits higher acidity compared to BPA, while BGF is found to be more basic relative to BPF. The reduction in the pK_a value for BGA can be attributed to the electron-withdrawing effect through induction caused by the electronegative oxygen atom in the methoxy group. Conversely, the increase in the pK_a value for BGF is likely due to the electron-donating effect facilitated by resonance. Finally, the polymer-solvent interactions, which remain undefined, could play a significant role in the polymerization and SEC analysis. These insights provide a roadmap for refining the synthesis protocol for the lignin-derivable PSfs.

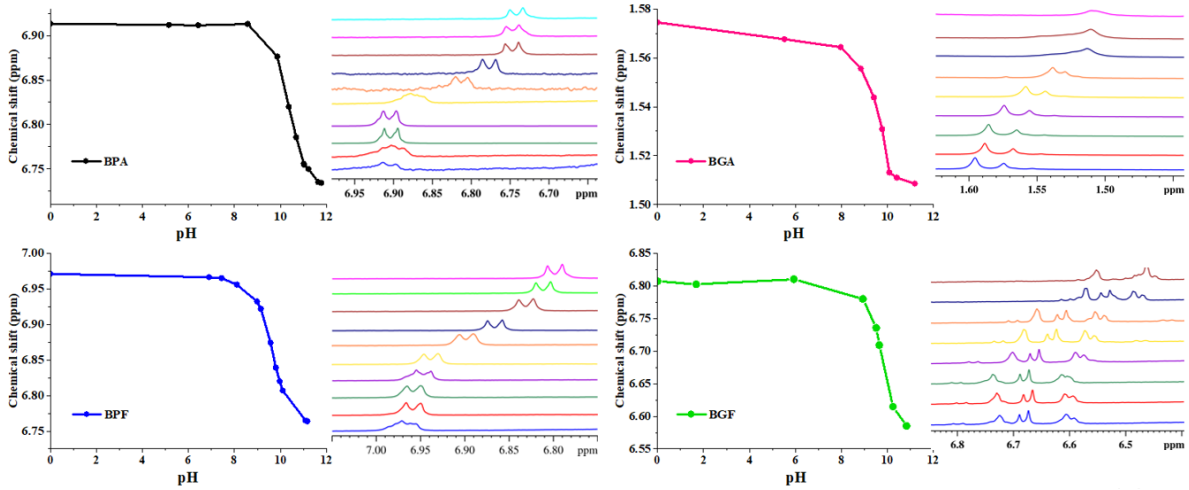

Figure 5.9 pK_a measurements of monomers using ^1H NMR.

5.4.3.2 Thermogravimetric analysis (TGA)

The thermal stability of the lignin-derived PSfs falls within the spectrum of high-performance thermoplastics. The temperatures at which a 5% weight loss was observed ($T_{d5\%}$) for BPA-PSf, BPF-PSf, BGA-PSf, and BGF-PSf were 507, 416, 425, and 395 °C, respectively, under a N_2 atmosphere (**Figure 5.10**). Insignificant changes in thermal degradation was observed for the lignin-derivable PSFs, due to the preservation of the general structure of the polymer's repeating units. Additionally, all PSfs demonstrated a char yield of approximately 30 - 45%. This is as expected, as PSfs typically undergo pyrolysis in an inert environment, leading to char formation, rather than undergoing oxidative degradation which would result in their complete breakdown.[44]

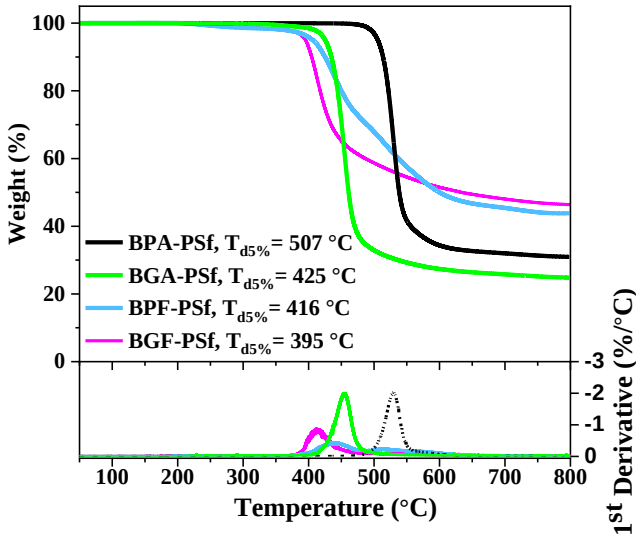

Figure 5.10 Thermogravimetric analysis and first derivative of BPA/BPF/BGA/BGF-PSfs.

5.4.3.3 Differential Scanning Calorimetry (DSC)

The glass transition temperatures (T_gs) of the lignin-derivable PSfs are comparable with those of commercial PSfs (**Figure 5.11**). Specifically, the T_gs for BPA-PSf, BPF-PSf, BGA-PSf, and BGF-PSf were approximately 185, 179, 166, and 172 °C, respectively. Comparing within the polymer series (BPA-PSf versus BGA-PSfs and BPF-PSf versus BGF-PSfs), minor shifts in T_g demonstrate the influence of methoxy groups on chain mobility and packing, with the addition of methoxy groups leading to a reduction in T_g by approximately 10% to 4% for the polymer comparisons. Nevertheless, the T_gs of the lignin-derivable PSfs remained in line with those of commercial PSfs, which are around 170 °C. This T_g value of approximately 170 °C is also well-suited for various potential applications, including water filtration membranes, microwave dishes, hemodialysis membranes, and more.[33]

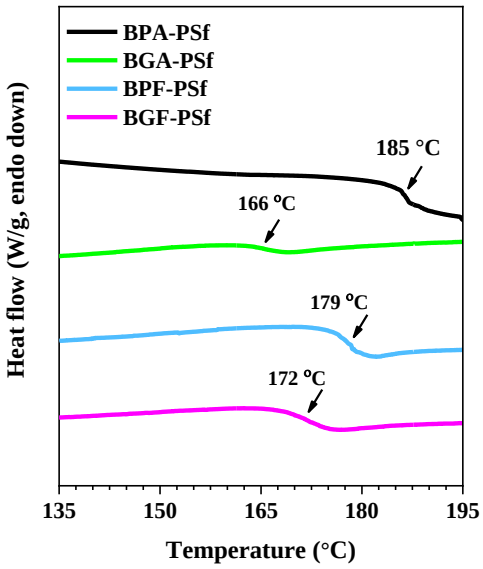

Figure 5.11 Second heating scan DSC analysis of BPA/BGA/BPF/BGF-PSfs.

5.4.3.4 Water contact angle, water uptake and polarity Changes

The hydrophilic nature of these lignin-derivable PSf dense membranes was analyzed through measurements of water vapor uptake, water contact angle, and polymer polarity studies. The water vapor sorption capability of the PSfs showed an increase alongside the number of methoxy groups, pointing towards an enhancement in the hydrophilicity of the PSfs (**Figure 5.12**). BPA-PSf, which does not contain any methoxy groups, had a water vapor uptake of 0.84% ± 0.04%, while BGA-PSf, containing two methoxy groups, exhibited a water vapor uptake of around 1.35% ± 0.15%. This increase, representing a roughly 50% higher water vapor uptake for BGA-PSf compared to BPA-PSf, was statistically significant (as confirmed by a paired T-test with a p-value of 0.048). Meanwhile, BPF-PSf (with no methoxy groups) had a water vapor uptake of 1.01% ± 0.03%, and BGF-PSf (with two methoxy groups) showed an uptake of 1.10% ± 0.04%, though this rise was not statistically significant (paired T-test, p-value = 0.080). These

lignin-derivable PSfs achieve enhanced hydrophilicity without the need for the harsh reagents or conditions often involved in PSf modifications, within the confines of dense film matrices.

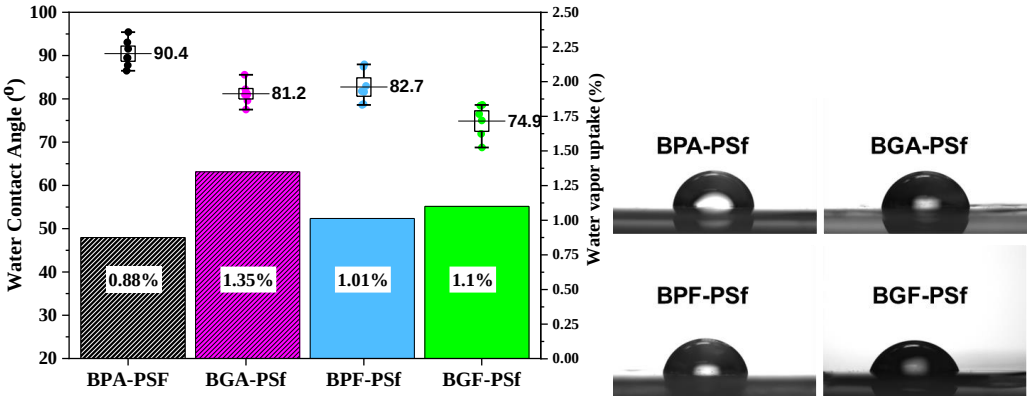

Figure 5.12 Water vapor uptake and water contact angle of dense membranes of BPA/BGA/BPF/BGF-PSfs.

As seen in Figure **5.12**, the addition of methoxy groups, due to the polar nature of methoxy, led to a decrease in water contact angle values, thus increasing the PSfs' hydrophilicity. BPA-PSf had a water contact angle of 90.4° ± 3.2°, whereas its lignin-derivable counterpart, BGA-PSf (with two methoxy groups), displayed a water contact angle of 81.2° ± 2.3°. Similarly, BPF-PSf had a water contact angle of approximately 82.7° ± 3.7°, while BGF-PSf (with two methoxy groups) presented a water contact angle of around 74.9° ± 3.9°.

The presence of methoxy groups on the aromatic rings of lignin-derivable PSfs increased the polymers' polarity, enhancing their hydrophilicity. This enhancement was validated the Extended Fowke's/Owens, Wendt, Rabel, and Kaelble model for evaluating surface energy.

For surface energy measurements, an increase in the polar component with more methoxy content was observed, underscoring the methoxy groups' inherent polarity (**Figure 5.13**).

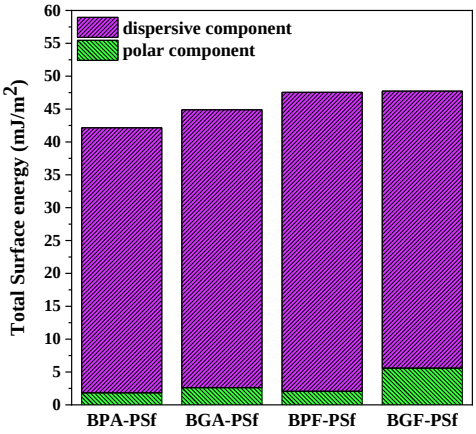

Polymer	Polar component (mJ/m^2)	Dispersive component (mJ/m^2)	Total surface energy (mJ/m^2)
BPA-PSf	2 ± 0.2	40 ± 0.8	42 ± 0.7
BGA-PSf	3 ± 0.1	42 ± 0.1	45 ± 0.1
BPF-PSf	2 ± 0.1	45 ± 0.2	47 ± 0.2
BGF-PSf	6 ± 0.2	42 ± 0.3	48 ± 0.3

Figure 5.13 Polar and dispersive components of surface free energy measurements for BPA/BGA/BPF/BGF-PSfs.

5.4.4 Conclusion

In this study, polysulfones were synthesized with petroleum-based (BPA and BPF) and lignin-derivable monomers (BGA and BGF) via step-growth polymerization. The water contact angles, water vapor absorption, material polarity, and thermal properties of lignin-derivable PSfs were compared against those derived from petroleum. A key observation was that the water contact angles decreased – indicating an increase in hydrophilicity– with a higher methoxy group content in the lignin-derivable PSfs, achieved without the need for any post-polymerization modifications, due to the polar nature of methoxy groups. The water contact angles of these lignin-derivable PSfs were on par with those of functionalized PSfs, approximately 75°, showcasing an enhanced hydrophilicity without compromising other critical polymer properties, such as glass transition temperature (T_g) and thermal stability.[34] The T_g of these bio-derivable PSfs matched commercial PSfs, around 170 °C,

and their thermal stability was at approximately 400 °C. These findings underscore the valuable role of lignin-aromatics' inherent functionalities, especially methoxy groups, in improving the characteristics of renewable polymers. Thus, lignin-derived PSfs not only offer an eco-friendly alternative to petroleum-based polymers but also maintain, and in some aspects enhance, the material properties crucial for a wide range of applications.

5.5 Hybrid desalination and direct ocean capture

5.5.1 Introduction

Each year, the oceans absorb and dissolve approximately 30% of anthropogenic emissions.[45] In fact, the concentration of CO_2 in ocean water (~ 100 mg/L) is approximately 150 times the concentration of CO_2 in the air (0.7 mg/L).[46] Direct ocean capture (DOC) is an approach to mitigating climate change by directly removing the CO_2 from oceans. DOC not only addresses the large amount of dissolved CO_2, but also decreases ocean acidification.

CO_2 from the atmosphere dissolves in ocean water, and through reaction with water form carbonic acid (H_2CO_3, **Figure 5.14**). Carbonic acid can dissociate into bicarbonate (HCO_3^-) and hydrogen ions (H^+). This bicarbonate can further dissociate into carbonates (CO_3^{2-}) and more hydrogen ions. All these reactions are reversible and form the ocean's buffering system.

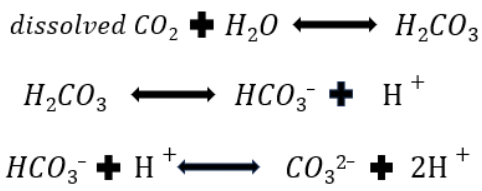

Figure 5.14 Ocean's buffering system.

When excess hydrogens are present, the reactions are reversed, and the bicarbonate and carbonate absorb these ions and produce carbonic acid. This ocean carbonate buffering system naturally helps stabilize the pH of the ocean, maintaining it between 8.1 and 8.3, despite fluctuations in atmospheric CO_2 levels. However, when excessive amounts of CO_2 are absorbed by the oceans, this buffering capacity can become overwhelmed, leading to a phenomenon known as ocean acidification.

Ocean acidification is significantly altering the world's oceanic carbonate systems. Historical mass extinctions have been associated with such acidification, and the present shift in ocean chemistry is occurring at an unprecedented rate.[47] Studies show that this change will significantly affect marine species, especially those that create skeletons, shells, and other structures from carbonates. Ocean acidification may affect species populations and distributions, impacting marine food chains.[48,49] Additionally, ocean acidification can lead to increase growth of toxic algal species and negatively impact human health.[50]

Since the onset of the industrial revolution, the pH level of surface ocean waters has decreased by approximately 0.1 pH units and projections suggest an additional decrease of up to 0.4 pH units by the end of this century (**Figure 5.15 and Figure 5.16**). As pH

scale is logarithmic, each whole unit decrease in pH corresponds to a tenfold increase in acidity.

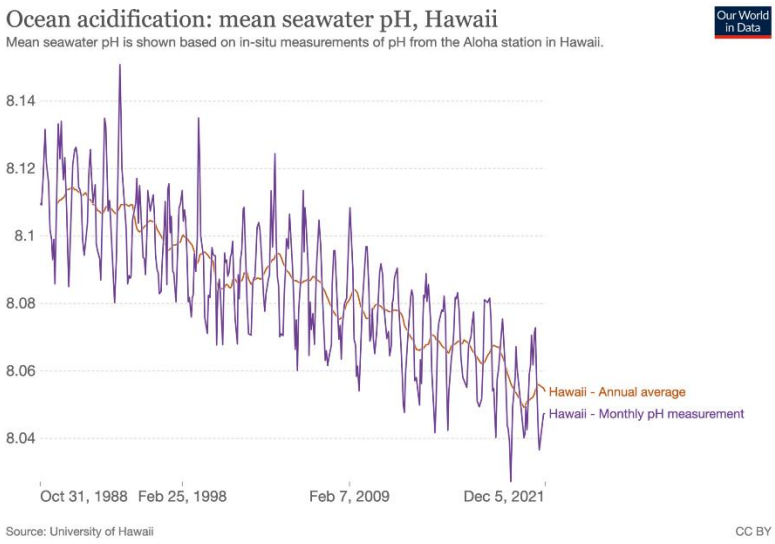

Figure 5.15 Changes in mean seawater pH from 1988 to 2021[51]

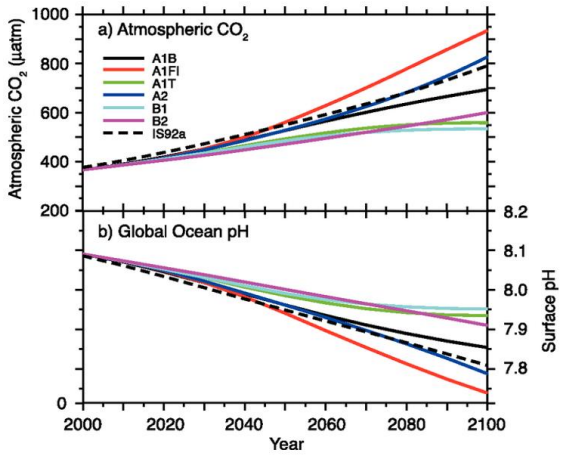

Figure 5.16 projected changes in global ocean pH in response to different scenarios of atmospheric CO_2 levels.[52]

Removing dissolved CO_2 from ocean water poses significant challenges. Handling and pumping large quantities of water can be energy-intensive and demand robust infrastructure. Desalination infrastructure, which is utilized to provide freshwater, is

equipped to handle and process larger amounts of water that can be taken advantage of for ocean capture efforts. By leveraging the established mechanisms and infrastructure of desalination plants, it may be possible to enhance their functionality to include the extraction of CO_2 from seawater alongside desalination. This approach could provide a more energy-efficient solution for ocean capture by minimizing the need for additional, separate systems to move and process seawater solely for dissolved carbon removal. One promising avenue is the integration of redox-active compounds into the desalination membranes. Redox-active compounds can facilitate chemical reactions that alter the pH levels of seawater as it passes through the desalination process. By shifting the pH levels downwards (making the water more acidic), the equilibrium can be shifted to favor the formation of dissolved CO_2 (**Figure 5.17**). This dual-functionality could significantly improve the efficiency of ocean capture technologies, offering a more integrated and potentially less energy-intensive approach to tackling global CO_2 levels.

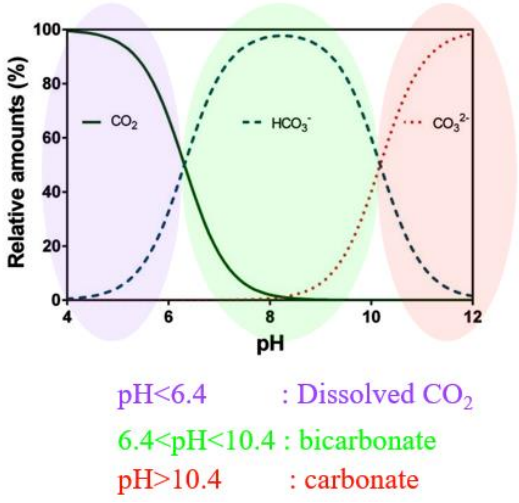

Figure 5.17 Bjerrum plot.

5.5.2 Experimental

This hybrid DOC and desalination process was modeled at Dr. Katherine Hornbostel's group at the University of Pittsburgh.[53] Additionally, the redox-active compounds (**Figure 5.18**) were supplied by Clarabella Li from Dr. Jenny Yang's group at the University of California, Irvine.[54] We investigated methods for incorporating redox-active compounds into desalination membranes.

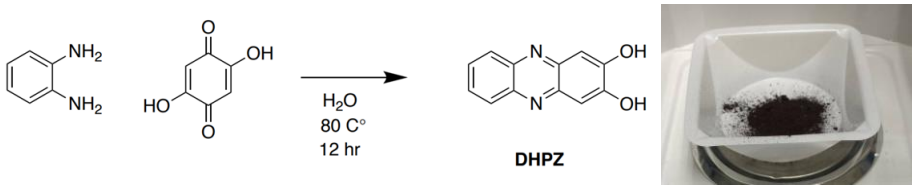

Figure 5.18 2,3-dihydroxyphenazine (DHPZ) compound.

DHPZ, or 2,3-dihydroxyphenazine (also called phenazine-2,3-diol), is the compound provided to us by our collaborators. This compound is an aqueous-soluble organic redox-active material that is particularly notable for its role in redox flow batteries, where it is used as an analyte.[55] There is potential in using DHPZ for removing CO_2 from ocean water by inducing an electrochemically driven water pH swing.

Physical addition of this compound on commercial desalination membranes of FilmTec BW30 and DeltaMem AG were studied. FilmTec BW30 8 in x 10 sheets were purchased from OctoChem and DeltaMem AG commercial membranes were generously provided by Dr. François Perreault at ASU. **Figure 5.19** shows cross sectional images of the commercial membranes thorough SEM analysis. As it is shown, BW30 membrane consists of a polyamide (PA) skin, polysulfone (PSf) substrate and a non-woven

polyethylene (PE) support. DeltaMem consists of a polyvinyl alcohol (PVA) selective layer on a polyacrylonitrile (PAN) support.

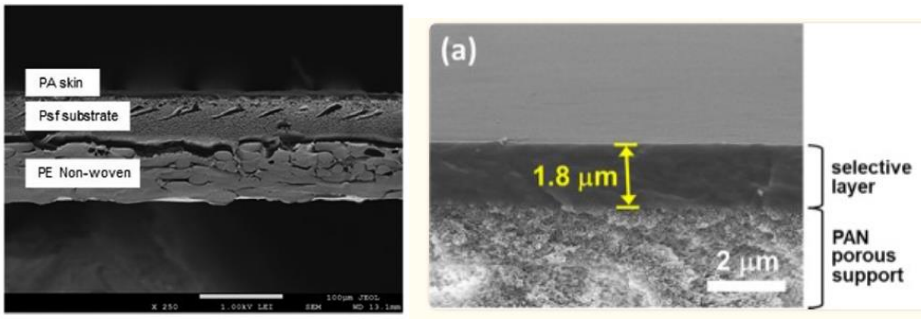

Figure 5.19 reported SEM images of BW30 (left)[56] and DeltaMem (right)[57]

Three different pathways of physical addition were investigated. The first method of addition of DOC active specie, DHPZ, was physical mixing of solution containing DHPZ in DI water and commercial membranes (**Figure 5.20**). DHPZ in DI solutions were prepared and commercial membranes were submerged and held floated inside the stirring solution. Various DHPZ in DI concentrations and stirring times were tested (examples are shown in **Figure 5.20**). Membranes were pre-weighed and washed and weighed after physical mixing to measure the content of DHPZ added.

The second process studied was the dropwise addition of a solution of DHPZ in DI water (**Figure 5.21**). After dropwise addition, sufficient time was given for water to evaporate. This was performed to add a thin and uniform layer of DHPZ on commercial membranes.

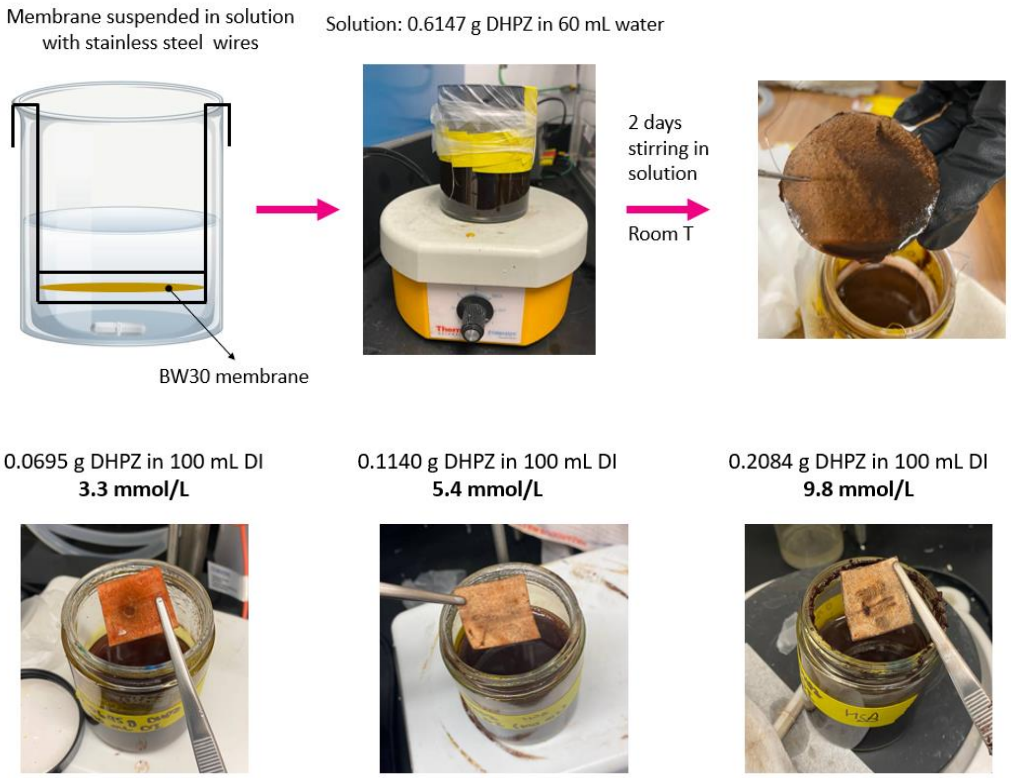

Figure 5.20 Physical mixing process for addition of DHPZ on commercial membranes with various concentrations.

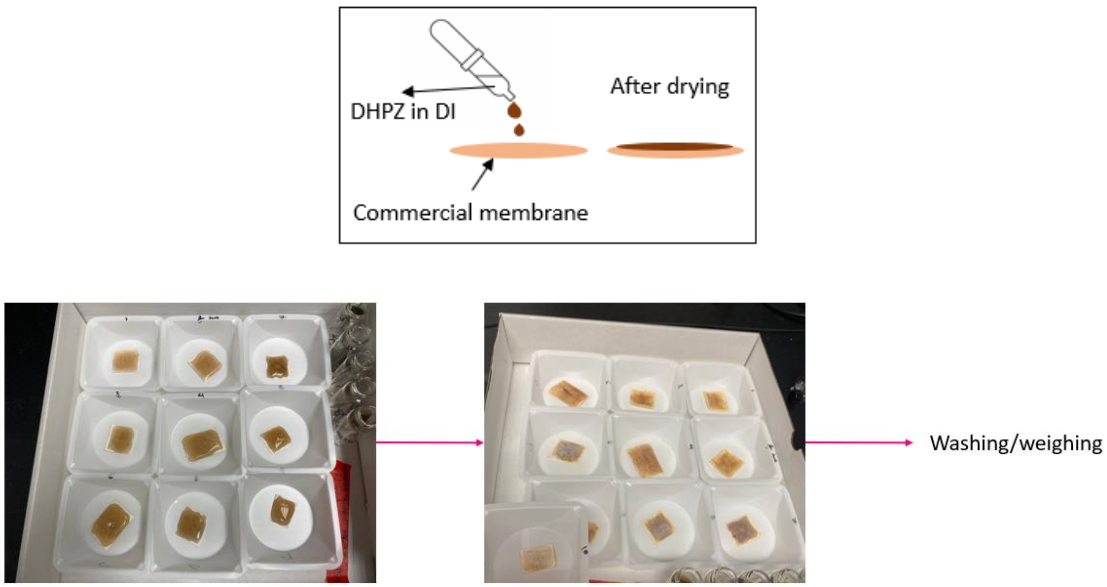

Figure 5.21 Image is the dropwise addition of DHPZ in DI solution on pre-weighed commercial membranes.

Simultaneous casting of commercial Udel Polysulfone (P-1700) and DHPZ was investigated as the third method. Initially, dense membrane casting protocol was utilized. In this process, a 2.5 wt.% solution of DHPZ in dimethylformamide (DMF) was prepared. The solution was homogenized with sufficient stirring using a vortexer. The homogenous solution was then poured inside a flat-bottom Druoplan petri dish (**Figure 5.22**). The dish was closed with a non-hermetically sealed pan and equilibrated with air overnight, to remove any bubbles that may have formed during vortexing. The petri dish containing the solution was then placed inside a vacuum oven operating at room temperature for 24 h. The vacuum oven temperature was increased to 40 °C for 24 h, and then to 70 °C for 24 h to slowly remove the DMF, to provide the polymer chains time to relax and obtain a dense structure.

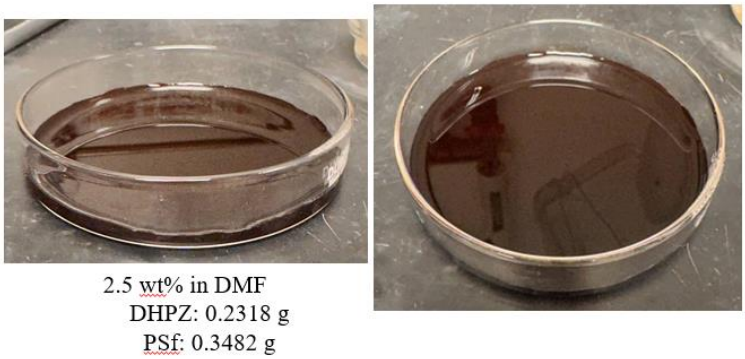

Figure 5.22 preparation of dense polysulfone membranes with DHPZ.

A second form of membrane casting was carried out to fabricate porous membranes. In the second form, 15 wt.% solutions of Udel polysulfone were prepared inside N-Methyl-2-pyrrolidone (NMP), and DHPZ was added to the solution with varying

concentrations (**Figure 5.23**). The dense membranes were cast using a doctor blade with controlled thickness and precipitated using a non-solvent bath.

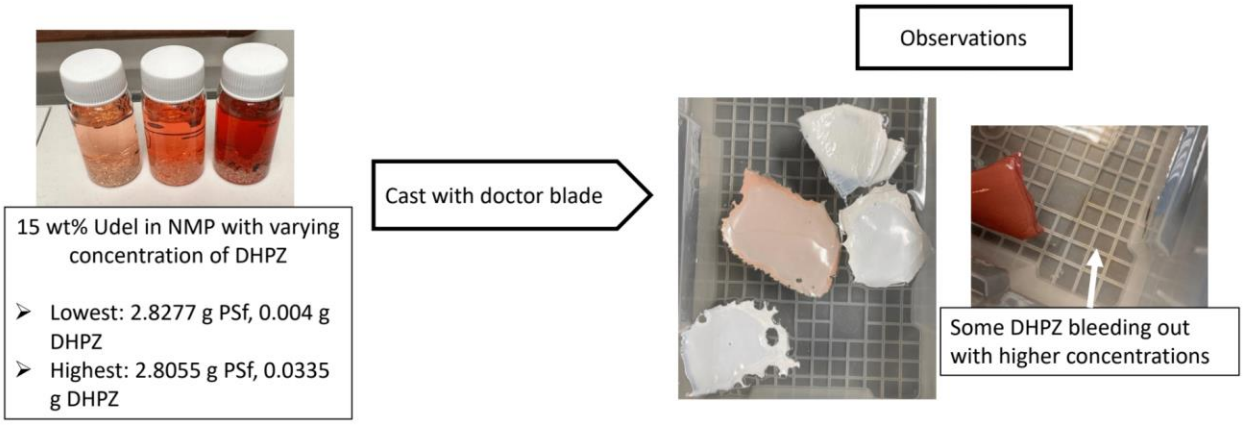

Figure 5.23 preparation of porous polysulfone membranes with DHPZ.

5.5.3 Results and Discussion

After physical mixing, membranes changed color from white to the color of DHPZ powder (dark red/dark brown). SEM images show changes on surfaces (top and bottom of membrane) and cross section of commercial membranes on a micrometer scale before after physical mixing, which is believed to be due to the addition of DHPZ compound (**Figures 5.24 - 5.27**).

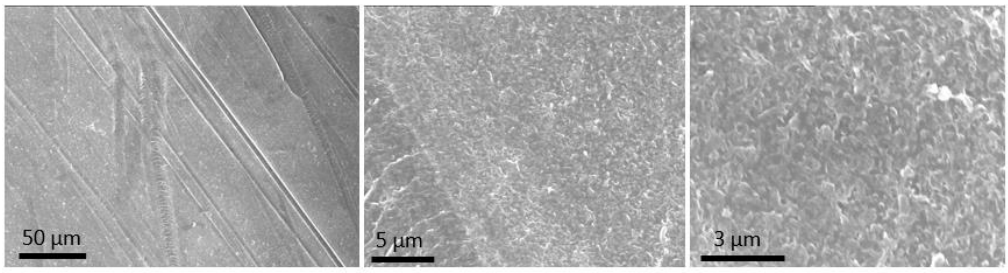

Figure 5.24 SEM images of surface of BM30 prior to addition of DHPZ.

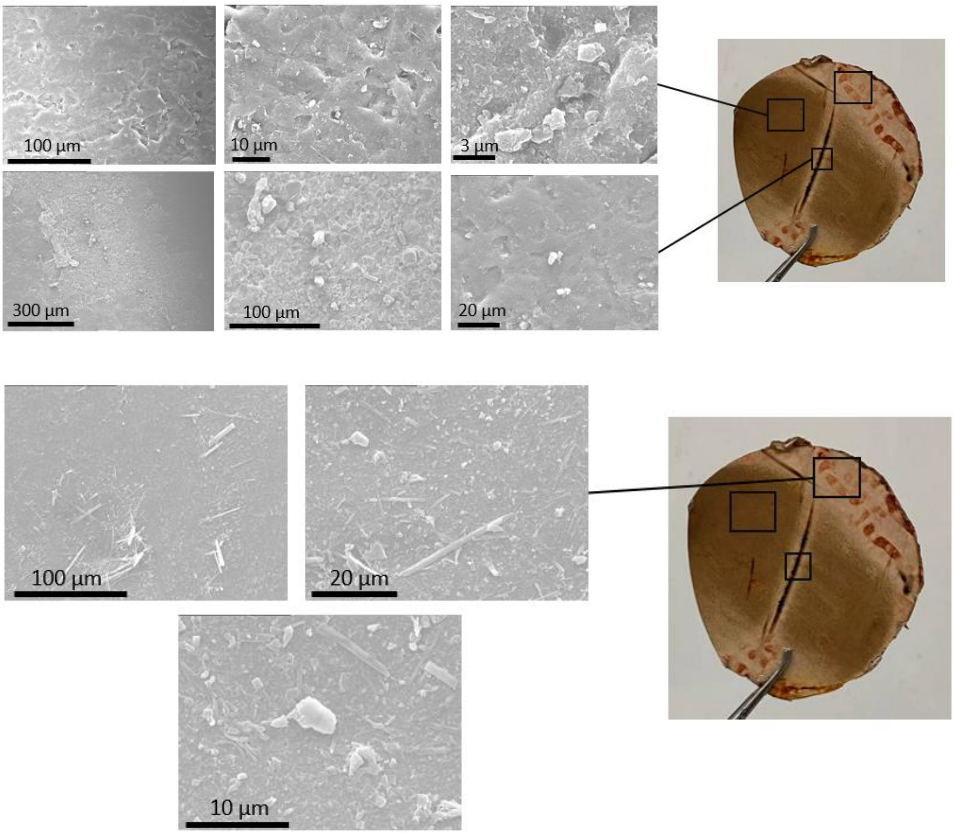

Figure 5.25 SEM images of the "top" surface of BW30 membrane after physical mixing with DHPZ and DI solution.

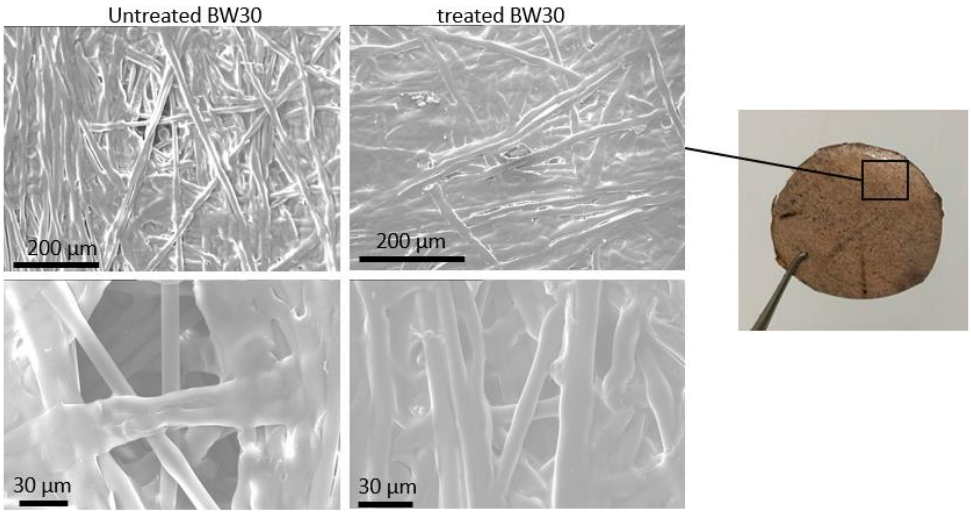

Figure 5.26 SEM images of the "bottom" of BW30 membrane before (untreated) and after (treated) physical mixing with DHPZ and DI solution.

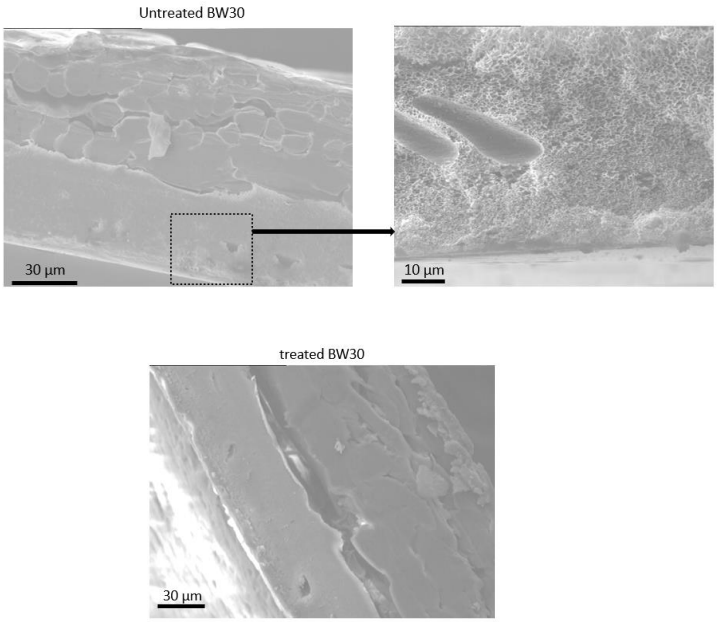

Figure 5.27 SEM images of cross section of BW30 membrane, before (top) and after (bottom) physical mixing with DHPZ in DI solution.

Figure 5.28 shows the weight of membranes after physical mixing and subsequent washing of membranes to remove excess DHPZ. An increase in weight is observed due to

the addition of DHPZ, and a continuous trend of decreasing weight was observed after multiple washes.

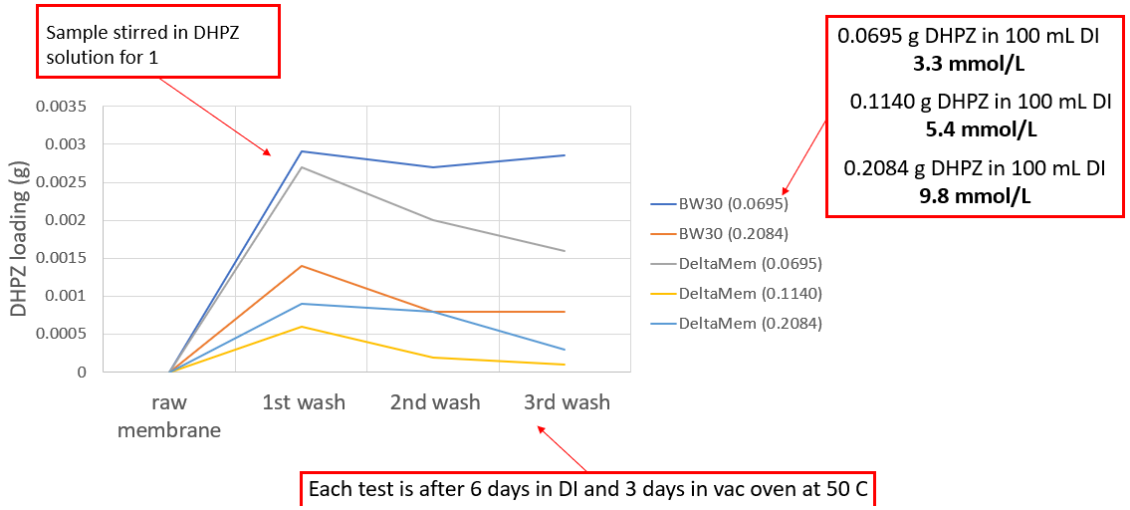

Figure 5.28 weight of BW30 and DeltaMem membranes recorded after physical mixing and subsequent washing to remove excess DHPZ.

Visible and non-uniform DHPZ addition was observed for the commercial membranes after physical mixing in all studies. We suspect the non-uniformity and continuous trend of weight decrease after subsequent washing is due to stacking of DHPZ compounds on top of each other, resulting from high concentration DHPZ and DI solutions.

The weight increase in membranes after drop-wise addition shows the adherence of DHPZ on the membranes. However, like the previous process, weight loss was observed after subsequent washing (**Figure 5.29**).

Figure 5.29 Weight of BW30 and DeltaMem membranes recorded after dropwise addition and subsequent washing to remove excess DHPZ.

The membrane fabricated through the co-casting method showed no weight loss after subsequent washes, indicating the DHPZ is locked inside the polysulfone polymer chains (**Figure 5.30**).

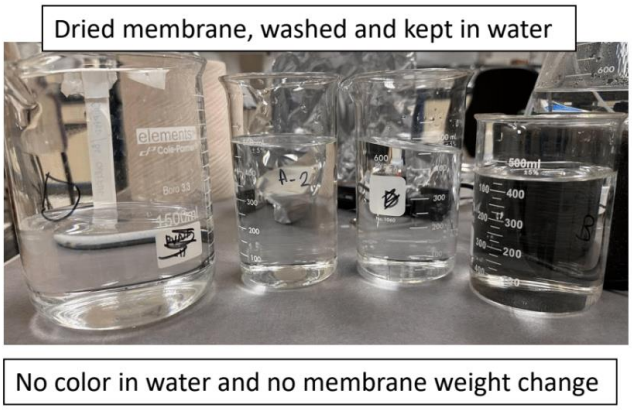

Figure 5.30 No color change observed after subsequent washing of co-cased membranes.

SEM images of porous membranes cast with DHPZ are shown in **Figure 5.31.**

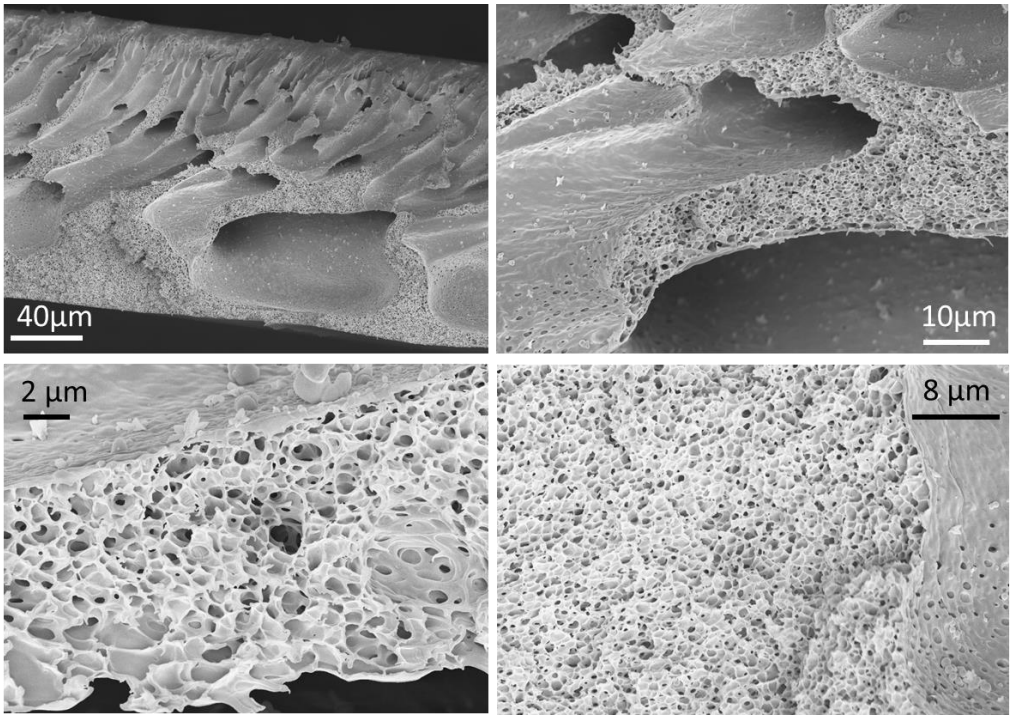

Figure 5.31 SEM images of cross section of a porous polysulfone membrane cast with DHPZ.

The third type of physical addition successfully incorporated DHPZ into the polymer matrix. Water permeation studies conducted on these membranes indicated insufficient water flow. Consequently, it is concluded that enhancing desalination membranes through the physical addition approaches examined is not feasible. Therefore, chemical modification of desalination membranes is deemed necessary. These routes can include grafting redox-active groups to monomers prior to polymer synthesis, surface modification with redox active compounds or interfacial polymerization techniques.

5.6 References

(1) Vureau of reclamation. *Water Facts - Worldwide Water Supply*. https://www.usbr.gov/.

(2) UNICEF. *Water and the global climate crisis: 10 things you should know*. https://www.unicef.org/stories/water-and-climate-change-10-things-you-should-know.

(3) Ault, T. R. On the Essentials of Drought in a Changing Climate. *Science (80-.).* **2020**, *368* (6488), 256–260. https://doi.org/10.1126/science.aaz5492.

(4) Vadez, V.; Grondin, A.; Chenu, K.; Henry, A.; Laplaze, L.; Millet, E. J.; Carminati, A. Crop Traits and Production under Drought. *Nat. Rev. Earth Environ.* **2024**. https://doi.org/10.1038/s43017-023-00514-w.

(5) UNICEF. *1 in 3 children exposed to severe water scarcity – UNICEF*. https://www.unicef.org/press-releases/1-3-children-exposed-severe-water-scarcity-unicef#:~:text=In 2022%2C 436 million children,of 10 children are exposed.

(6) UNICEF. *Water scarcity*. https://www.unicef.org/wash/water-scarcity.

(7) Wikipedia. Water Scarcity.

(8) Lopez-Gunn, E.; Ramón Llamas, M. Re-thinking Water Scarcity: Can Science and Technology Solve the Global Water Crisis? *Nat. Resour. Forum* **2008**, *32* (3), 228–238. https://doi.org/10.1111/j.1477-8947.2008.00200.x.

(9) Campisano, A.; Butler, D.; Ward, S.; Burns, M. J.; Friedler, E.; DeBusk, K.; Fisher-Jeffes, L. N.; Ghisi, E.; Rahman, A.; Furumai, H.; Han, M. Corrigendum to "Urban Rainwater Harvesting Systems: Research, Implementation and Future Perspectives" [Water Res. 115 (2017) 195–209]. *Water Res.* **2017**, *121*, 386. https://doi.org/10.1016/j.watres.2017.06.002.

(10) Gasparini, B.; McGraw, Z.; Storelvmo, T.; Lohmann, U. To What Extent Can Cirrus Cloud Seeding Counteract Global Warming? *Environ. Res. Lett.* **2020**, *15* (5), 054002. https://doi.org/10.1088/1748-9326/ab71a3.

(11) Zhou, X.; Lu, H.; Zhao, F.; Yu, G. Atmospheric Water Harvesting: A Review of Material and Structural Designs. *ACS Mater. Lett.* **2020**, *2* (7), 671–684. https://doi.org/10.1021/acsmaterialslett.0c00130.

(12) Qadir, M.; Siriwardana, N. Water Transportation via Icebergs Towing. In *Unconventional Water Resources*; Springer International Publishing: Cham, 2022; pp 199–212. https://doi.org/10.1007/978-3-030-90146-2_9.

(13) Koroneos, C.; Dompros, A.; Roumbas, G. Renewable Energy Driven Desalination Systems Modelling. *J. Clean. Prod.* **2007**, *15* (5), 449–464. https://doi.org/10.1016/j.jclepro.2005.07.017.

(14) Elsaid, K.; Taha Sayed, E.; Yousef, B. A. A.; Kamal Hussien Rabaia, M.; Ali Abdelkareem, M.; Olabi, A. G. Recent Progress on the Utilization of Waste Heat for Desalination: A Review. *Energy Convers. Manag.* **2020**, *221*, 113105. https://doi.org/10.1016/j.enconman.2020.113105.

(15) Nannarone, A.; Toro, C.; Sciubba, E. Multi-Stage Flash Desalination Process: Modeling and Simulation. *30th Int. Conf. Effic. Cost, Optim. Simul. Environ. Impact Energy Syst. ECOS 2017* **2017**, No. July.

(16) Arunkumar, T.; Sathyamurthy, R.; Denkenberger, D.; Lee, S. J. Solar Distillation Meets the Real World: A Review of Solar Stills Purifying Real Wastewater and Seawater. *Environ. Sci. Pollut. Res.* **2022**, *29* (16), 22860–22884. https://doi.org/10.1007/s11356-022-18720-2.

(17) Najim, A. A Review of Advances in Freeze Desalination and Future Prospects. *npj Clean Water* **2022**, *5* (1), 15. https://doi.org/10.1038/s41545-022-00158-1.

(18) El-Dessouky, H.; Ettouney, H.; Al-Fulaij, H.; Mandani, F. Multistage Flash Desalination Combined with Thermal Vapor Compression. *Chem. Eng. Process. Process Intensif.* **2000**, *39* (4), 343–356. https://doi.org/10.1016/S0255-2701(99)00098-7.

(19) Al-Najar, B.; Peters, C. D.; Albuflasa, H.; Hankins, N. P. Pressure and Osmotically Driven Membrane Processes: A Review of the Benefits and Production of Nano-Enhanced Membranes for Desalination. *Desalination* **2020**, *479*, 114323. https://doi.org/10.1016/j.desal.2020.114323.

(20) Elimelech, M.; Phillip, W. A. The Future of Seawater Desalination: Energy, Technology, and the Environment. *Science (80-.).* **2011**, *333* (6043), 712–717. https://doi.org/10.1126/science.1200488.

(21) Skuse, C.; Gallego-Schmid, A.; Azapagic, A.; Gorgojo, P. Can Emerging Membrane-Based Desalination Technologies Replace Reverse Osmosis? *Desalination* **2021**, *500*, 114844. https://doi.org/10.1016/j.desal.2020.114844.

(22) Al-Amshawee, S.; Yunus, M. Y. B. M.; Azoddein, A. A. M.; Hassell, D. G.; Dakhil, I. H.; Hasan, H. A. Electrodialysis Desalination for Water and Wastewater: A Review. *Chem. Eng. J.* **2020**, *380*, 122231. https://doi.org/10.1016/j.cej.2019.122231.

(23) Wu, Q.; Liang, D.; Lu, S.; Wang, H.; Xiang, Y.; Aurbach, D.; Avraham, E.; Cohen, I. Advances and Perspectives in Integrated Membrane Capacitive Deionization for Water Desalination. *Desalination* **2022**, *542*, 116043. https://doi.org/10.1016/j.desal.2022.116043.

(24) Sorour, M. H.; Hani, H. A.; Shaalan, H. F.; Al-Bazedi, G. A. Schemes for Salt Recovery from Seawater and RO Brines Using Chemical Precipitation. *Desalin. Water Treat.* **2015**, *55* (9), 2398–2407. https://doi.org/10.1080/19443994.2014.946720.

(25) Ayoub, G. M.; Zayyat, R. M.; Al-Hindi, M. Precipitation Softening: A Pretreatment Process for Seawater Desalination. *Environ. Sci. Pollut. Res.* **2014**, *21* (4), 2876–2887. https://doi.org/10.1007/s11356-013-2237-1.

(26) Sahle-Demessie, E.; Aly Hassan, A.; El Badawy, A. Bio-Desalination of Brackish and Seawater Using Halophytic Algae. *Desalination* **2019**, *465*, 104–113. https://doi.org/10.1016/j.desal.2019.05.002.

(27) Gao, L.; Zhang, X.; Fan, L.; Gray, S.; Li, M. Algae-Based Approach for Desalination: An Emerging Energy-Passive and Environmentally Friendly Desalination Technology. *ACS Sustain. Chem. Eng.* **2021**, *9* (26), 8663–8678. https://doi.org/10.1021/acssuschemeng.1c00603.

(28) Gujjala, L. K. S.; Dutta, D.; Sharma, P.; Kundu, D.; Vo, D.-V. N.; Kumar, S. A State-of-the-Art Review on Microbial Desalination Cells. *Chemosphere* **2022**, *288*, 132386. https://doi.org/10.1016/j.chemosphere.2021.132386.

(29) Ahmed, M. A.; Amin, S.; Mohamed, A. A. Fouling in Reverse Osmosis Membranes: Monitoring, Characterization, Mitigation Strategies and Future Directions. *Heliyon* **2023**, *9* (4), e14908. https://doi.org/10.1016/j.heliyon.2023.e14908.

(30) Cai, Y.-H.; Galili, N.; Gelman, Y.; Herzberg, M.; Gilron, J. Evaluating the Impact of Pretreatment Processes on Fouling of Reverse Osmosis Membrane by Secondary Wastewater. *J. Memb. Sci.* **2021**, *623*, 119054. https://doi.org/10.1016/j.memsci.2021.119054.

(31) Zhang, Z.; Li, X.; Liu, H.; Zhou, T.; Wang, Z.; Nghiem, L. D.; Wang, Q. Biofouling Control of Reverse Osmosis Membrane Using Free Ammonia as a Cleaning Agent. *J. Memb. Sci.* **2024**, *694*, 122414. https://doi.org/10.1016/j.memsci.2024.122414.

(32) Upadhyaya, L.; Qian, X.; Ranil Wickramasinghe, S. Chemical Modification of Membrane Surface — Overview. *Curr. Opin. Chem. Eng.* **2018**, *20*, 13–18. https://doi.org/10.1016/j.coche.2018.01.002.

(33) Yang, Y.; Behbahani, H. S.; Morgan, B. F.; Beyer, F. L.; Hocken, A.; Green, M. D. Synthesis and Thermomechanical Characteristics of Zwitterionic Poly(Arylene Ether Sulfone) Copolymers. *Polymer (Guildf).* **2022**, 125522. https://doi.org/10.1016/j.polymer.2022.125522.

(34) Yang, Y.; Ramos, T. L.; Heo, J.; Green, M. D. Zwitterionic Poly(Arylene Ether Sulfone) Copolymer/Poly(Arylene Ether Sulfone) Blends for Fouling-Resistant Desalination Membranes. *J. Memb. Sci.* **2018**, *561*, 69–78. https://doi.org/10.1016/J.MEMSCI.2018.05.025.

(35) Rubin, B. S. Bisphenol A: An Endocrine Disruptor with Widespread Exposure and Multiple Effects. *J. Steroid Biochem. Mol. Biol.* **2011**, *127* (1–2), 27–34. https://doi.org/10.1016/j.jsbmb.2011.05.002.

(36) Cho, S.; Choi, Y. S.; Luu, H. M.-D.; Guo, J. Determination of Total Leachable Bisphenol A from Polysulfone Membranes Based on Multiple Consecutive Extractions. *Talanta* **2012**, *101*, 537–540. https://doi.org/10.1016/j.talanta.2012.09.033.

(37) Le, H. H.; Carlson, E. M.; Chua, J. P.; Belcher, S. M. Bisphenol A Is Released from Polycarbonate Drinking Bottles and Mimics the Neurotoxic Actions of Estrogen in Developing Cerebellar Neurons. *Toxicol. Lett.* **2008**, *176* (2), 149–156. https://doi.org/10.1016/j.toxlet.2007.11.001.

(38) Bittner, G. D.; Denison, M. S.; Yang, C. Z.; Stoner, M. A.; He, G. Chemicals Having Estrogenic Activity Can Be Released from Some Bisphenol A-Free, Hard and Clear, Thermoplastic Resins. *Environ. Heal.* **2014**, *13* (1), 103. https://doi.org/10.1186/1476-069X-13-103.

(39) O'dea, R. M.; Willie, J. A.; Epps, T. H. 100th Anniversary of Macromolecular Science Viewpoint: Polymers from Lignocellulosic Biomass. Current Challenges and Future Opportunities. *ACS Macro Lett.* **2020**, *9* (4), 476–493. https://doi.org/10.1021/acsmacrolett.0c00024.

(40) Epps, T. H. I.; Korley, L. T. J.; Green, M. D.; Mahajan, J. S.; Behbahani, H. S. Bio-Based Polysulfones And Uses Thereof. US20220251300A1, 2020. https://patents.google.com/patent/WO2020252217A1/en?oq=WO%2F2020%2F252217%27.

(41) Mahajan, J. S.; O'Dea, R. M.; Norris, J. B.; Korley, L. S. T. J.; Epps, T. H. Aromatics from Lignocellulosic Biomass: A Platform for High-Performance Thermosets. *ACS Sustain. Chem. Eng.* **2020**, *8* (40), 15072–15096. https://doi.org/10.1021/acssuschemeng.0c04817.

(42) Bezençon, J.; Wittwer, M. B.; Cutting, B.; Smieško, M.; Wagner, B.; Kansy, M.; Ernst, B. PKa Determination by 1H NMR Spectroscopy – An Old Methodology Revisited. *J. Pharm. Biomed. Anal.* **2014**, *93*, 147–155. https://doi.org/10.1016/j.jpba.2013.12.014.

(43) Kütt, A.; Selberg, S.; Kaljurand, I.; Tshepelevitsh, S.; Heering, A.; Darnell, A.; Kaupmees, K.; Piirsalu, M.; Leito, I. PKa Values in Organic Chemistry – Making Maximum Use of the Available Data. *Tetrahedron Lett.* **2018**, *59* (42), 3738–3748. https://doi.org/10.1016/j.tetlet.2018.08.054.

(44) Li, X.-G.; Huang, M.-R. Thermal Degradation of Bisphenol A Polysulfone by High-Resolution Thermogravimetry. *React. Funct. Polym.* **1999**, *42* (1), 59–64. https://doi.org/10.1016/S1381-5148(98)00058-3.

(45) Le Quéré, C.; Andres, R. J.; Boden, T.; Conway, T.; Houghton, R. A.; House, J. I.; Marland, G.; Peters, G. P.; van der Werf, G. R.; Ahlström, A.; Andrew, R. M.; Bopp, L.; Canadell, J. G.; Ciais, P.; Doney, S. C.; Enright, C.; Friedlingstein, P.; Huntingford, C.; Jain, A. K.; Jourdain, C.; Kato, E.; Keeling, R. F.; Klein Goldewijk, K.; Levis, S.; Levy, P.; Lomas, M.; Poulter, B.; Raupach, M. R.; Schwinger, J.; Sitch, S.; Stocker, B. D.; Viovy, N.; Zaehle, S.; Zeng, N. The Global Carbon Budget 1959–2011. *Earth Syst. Sci. Data* **2013**, *5* (1), 165–185. https://doi.org/10.5194/essd-5-165-2013.

(46) Jayarathna, C.; Maelum, M.; Karunarathne, S.; Andrenacci, S.; Haugen, H. A. Review on Direct Ocean Capture (DOC) Technologies. *SSRN Electron. J.* **2022**, No. October, 1–12. https://doi.org/10.2139/ssrn.4282969.

(47) Guinotte, J. M.; Fabry, V. J. Ocean Acidification and Its Potential Effects on Marine Ecosystems. *Ann. N. Y. Acad. Sci.* **2008**, *1134* (1), 320–342. https://doi.org/10.1196/annals.1439.013.

(48) Koch, M.; Bowes, G.; Ross, C.; Zhang, X. Climate Change and Ocean Acidification Effects on Seagrasses and Marine Macroalgae. *Glob. Chang. Biol.* **2013**, *19* (1), 103–132. https://doi.org/10.1111/j.1365-2486.2012.02791.x.

(49) Kroeker, K. J.; Kordas, R. L.; Crim, R. N.; Singh, G. G. Meta-analysis Reveals Negative yet Variable Effects of Ocean Acidification on Marine Organisms. *Ecol. Lett.* **2010**, *13* (11), 1419–1434. https://doi.org/10.1111/j.1461-0248.2010.01518.x.

(50) Falkenberg, L. J.; Bellerby, R. G. J.; Connell, S. D.; Fleming, L. E.; Maycock, B.; Russell, B. D.; Sullivan, F. J.; Dupont, S. Ocean Acidification and Human Health. *Int. J. Environ. Res. Public Health* **2020**, *17* (12), 4563. https://doi.org/10.3390/ijerph17124563.

(51) Wikipedia. *Ocean acidification*. https://en.wikipedia.org/wiki/Ocean_acidification.

(52) IPCC: Working group I. *Climate Change 2007: The Physical Science Basis*.

(53) Hornbostel, K.; Lieber, A.; Riveroa, J.; Hildebrandt, D.; Snodgrass, C.; Gamble, W.; Neal, Z.; Davidson, S.; Usman, H.; Niepa, T. H. R. Direct Ocean Carbon Capture Using Membrane Contactors. *SSRN Electron. J.* **2022**. https://doi.org/10.2139/ssrn.4272912.

(54) Li, C. J.; Ziller, J. W.; Barlow, J. M.; Yang, J. Y. Aqueous Electrochemical and PH Studies of Redox-Active Guanidino Functionalized Aromatics for CO2 Capture. **2023**. https://doi.org/10.26434/chemrxiv-2023-fhcv4.

(55) Hollas, A.; Wei, X.; Murugesan, V.; Nie, Z.; Li, B.; Reed, D.; Liu, J.; Sprenkle, V.; Wang, W. A Biomimetic High-Capacity Phenazine-Based Anolyte for Aqueous Organic Redox Flow Batteries. *Nat. Energy* **2018**, *3* (6), 508–514. https://doi.org/10.1038/s41560-018-0167-3.

(56) Goh, G. L.; Tay, M. F.; Lee, J. M.; Ho, J. S.; Sim, L. N.; Yeong, W. Y.; Chong, T. H. Potential of Printed Electrodes for Electrochemical Impedance Spectroscopy (EIS): Toward Membrane Fouling Detection. *Adv. Electron. Mater.* **2021**, *7* (10), 2100043. https://doi.org/10.1002/aelm.202100043.

(57) Angelini, A.; Fodor, C.; Yave, W.; Leva, L.; Car, A.; Meier, W. PH-Triggered Membrane in Pervaporation Process. *ACS Omega* **2018**, *3* (12), 18950–18957. https://doi.org/10.1021/acsomega.8b03155.

6 APPENDIX A: PERMISSION

Permission is granted to the author for reuse of all material from publishers and co-authors.